2015

NANOMECHANICAL AND SCALING BEHAVIOR OF NANOPOROUS GOLD

Nicolas J. Briot
University of Kentucky, njbr222@uky.edu

Recommended Citation

Briot, Nicolas J., "NANOMECHANICAL AND SCALING BEHAVIOR OF NANOPOROUS GOLD" (2015). *Theses and Dissertations--Chemical and Materials Engineering*. 45.
https://uknowledge.uky.edu/cme_etds/45

STUDENT AGREEMENT:

I represent that my thesis or dissertation and abstract are my original work. Proper attribution has been given to all outside sources. I understand that I am solely responsible for obtaining any needed copyright permissions. I have obtained needed written permission statement(s) from the owner(s) of each third-party copyrighted matter to be included in my work, allowing electronic distribution (if such use is not permitted by the fair use doctrine) which will be submitted to UKnowledge as Additional File.

I hereby grant to The University of Kentucky and its agents the irrevocable, non-exclusive, and royalty-free license to archive and make accessible my work in whole or in part in all forms of media, now or hereafter known. I agree that the document mentioned above may be made available immediately for worldwide access unless an embargo applies.

I retain all other ownership rights to the copyright of my work. I also retain the right to use in future works (such as articles or books) all or part of my work. I understand that I am free to register the copyright to my work.

REVIEW, APPROVAL AND ACCEPTANCE

The document mentioned above has been reviewed and accepted by the student's advisor, on behalf of the advisory committee, and by the Director of Graduate Studies (DGS), on behalf of the program; we verify that this is the final, approved version of the student's thesis including all changes required by the advisory committee. The undersigned agree to abide by the statements above.

Nicolas J. Briot, Student

Dr. T. John Balk, Major Professor

Dr. Thomas Dziubla / Dr. Fuqian Yang, Director of Graduate Studies

NANOMECHANICAL AND SCALING BEHAVIOR OF NANOPOROUS GOLD

DISSERTATION

A dissertation submitted in partial fulfillment of the
requirements for the degree of Doctor of Philosophy in the
College of Engineering at the University of Kentucky

By

Nicolas Jérôme Briot

Lexington, Kentucky

Director: Dr. T. John Balk, Professor of Materials Engineering

Lexington, Kentucky

2015

ABSTRACT OF DISSERTATION

NANOMECHANICAL AND SCALING BEHAVIOR OF NANOPOROUS GOLD

Nanoporous metals have recently been drawn significant interest in various fields of research. Their high surface-to-volume ratio present a strong potential for applications in sensing, catalysis, micro-electromechanical systems (MEMS) and even in the medical field. However, the mechanical properties of nanoporous metals have not yet been well determined, as conducting mechanical tests was found to be challenging. Scaling relations linking the mechanical properties of porous materials to those of their dense counterparts are successfully and widely used for many porous metals. However, their applicability to nanoporous metals have recently been questioned, as estimations from the classic scaling relations were found no to agree with experimental determinations.

In this study, the mechanical properties of nanoporous gold will be measured by conducting tensile testing of single crystalline, millimeter-scale specimens, for the first time. Results did not agree with the predictions from the classic scaling relations. Using experimental results from these tensile tests, new nanoindentation testing and data reported in the literature, a new scaling relation for the yield strength of nanoporous gold is proposed. This new relation is found to correctly describe the mechanical properties of nanoporous gold. In addition, compression tests are conducted on polycrystalline nanoporous gold, and the results were found to agree very well with the proposed scaling relation.

KEYWORDS: Nanoporous, Gold, Scaling relations, Small-scale mechanical properties

Nicolas J. Briot

April 24th, 2015

NANOMECHANICAL AND SCALING BEHAVIOR OF NANOPOROUS GOLD

By

Nicolas Jérôme Briot

Dr. T. John Balk

Director of Dissertation

Dr. Fuqian Yang

Director of Graduate Studies

April 24th, 2015

Date

ACKNOWLEDGMENTS

I would like to start by thanking my advisor Dr. T. John Balk, whose guidance and help throughout this whole process made the completion of this work possible. Dr. Balk’s patience and confidence were immensely valuable, and his trust pushed me to go and accomplish things that I would not have thought myself to be capable of.

I also want to thank the members of my committee, Dr. Yang-Tse Cheng, Dr. Gang Cao, Dr. Matthew Beck and Dr. Todd Hastings, for their time and appreciated help.

I would like to acknowledge the National Science Foundation which supported this work (DMR-0847693).

I want to thank all the support staff, Jerry Rougeux, Floyd Taylor, Herb Mefford and Nancy Miller. I would like to thank Jerry Rougeux in particular without whom many of the experiments describe in this study would not even have been performed.

Special thanks to my labmates and friends with whom I shared many laughs and spent great times: Phillip Swartzentruber, Lei Wang, Julius Schoop, Tyler Vanover, Michael Detisch, Wayne Li and Xu Jiang.

I also want to thank all the students who collaborated with me over the years, Nathalie Werner, Jens Steiger and Michael Bürckert: some of this work would not have been possible without your help.

Finally I want to thank my family for their continuous support and patience, and Tristana for always believing in me. You have helped me every step of the way, and I would have never completed this work without you.

TABLE OF CONTENTS

Acknowledgments iii

List of tables vii

List of figures ix

Chapter 1 : Introduction 1

Chapter 2 : Background 5

- 2.1. Description of np-Au 5
- 2.2. Fabrication of np-Au: dealloying 6
- 2.3. Applications of np-Au 14
  - 2.3.1. Catalysis 15
  - 2.3.2. Sensing and actuation 15
  - 2.3.3. Energy storage 15
  - 2.3.4. Radioprotection 15
- 2.4. Deformation behavior and mechanical properties of np-Au 16
  - 2.4.1. Deformation behavior at the microscopic scale 16
  - 2.4.2. Deformation behavior at the macroscopic scale 18
  - 2.4.3. Mechanical properties of np-Au 19
  - 2.4.4. Scaling relations for porous materials 25

Chapter 3 : Materials and experimental methods 30

- 3.1. Film deposition by magnetron sputtering 30
- 3.2. Dealloying 30
- 3.3. Characterization 32
  - 3.3.1. Optical microscopy 32
  - 3.3.2. Electron microscopy 32
  - 3.3.3. Elemental analysis 33

3.4. Anelastic relaxation: damping measurements 34
    3.4.1. Internal friction 34
    3.4.2. Measurement system 36
3.5. Tension/compression testing of millimeter-scale specimens 38
3.6. Nanoindentation 45
Chapter 4 : Identification of microstructural defects by anelastic relaxation 47
4.1. Specimen fabrication and experimental details 50
    4.1.1. Nc-Ni specimens 50
    4.1.2. Np-Au specimens 51
4.2. Experimental details 56
4.3. Results and discussion 57
    4.3.1. Nc-Ni specimens 57
    4.3.2. Np-Au specimens 61
4.4. Conclusion and future work 67
Chapter 5 : Mechanical testing of pseudo-single crystalline np-Au in tension 69
5.1. Specimen fabrication and characterization 70
5.2. Experimental details and results 77
5.3. Discussion 81
Chapter 6 : Mechanical testing of single crystalline np-Au 84
6.1. Specimen fabrication and characterization 84
6.2. Experimental details and results 88
6.3. Compression testing of single crystalline np-Au 95
6.4. Fracture toughness 97
6.5. Discussion 98
    6.5.1. Deformation behavior 98

6.5.2. Yield Strength ... 102

6.5.3. Young's modulus ... 103

6.5.4. Fracture toughness ... 104

Chapter 7 : New scaling relation for the yield strength of np-Au ... 106

7.1. Specimen fabrication and characterization ... 106

7.2. Experimental details and results ... 108

7.3. New scaling relation ... 111

7.3.1. Nanoindentation vs. tensile testing ... 112

7.3.2. Ligament size effect ... 115

7.3.3. New scaling relation derivation ... 115

7.4. Discussion and applicability of the new scaling relation ... 123

Chapter 8 : Mechanical testing of polycrystalline specimens in compression ... 128

8.1. Specimen fabrication and characterization ... 129

8.2. Experimental details and results ... 130

8.3. Discussion ... 134

8.3.1. Stress strain curves ... 134

8.3.2. Plastic Poisson's ratio ... 140

8.3.3. Comparison with new yield strength scaling relation ... 142

8.3.4. Young's modulus scaling relation ... 144

Chapter 9 : Conclusions and future work ... 148

Appendix A ... 153

Appendix B ... 154

Appendix C ... 155

References ... 165

Vita ... 178

LIST OF TABLES

Table 1.1. List of np metals successfully prepared by dealloying, reported in the literature. 4

Table 2.1. Nanoindentation results reported in the literature for np-Au.......... 22

Table 3.1. List of components for the KIT small-scale mechanical testing system. 43

Table 3.2. List of components for the UK small-scale mechanical testing system. 44

Table 4.1. Summary and details of the internal friction peaks observed in nickel, after[109].......... 48

Table 4.2. Sputtering details for the deposition of the gold-silver films on silicon, for the preparation of damping samples.......... 52

Table 6.1. Summary of tensile test results for single crystalline nanoporous gold specimens. 95

Table 7.1. Sample details and nanoindentation results for np-Au with different relative densities. Ligament size was determined from the maximum of the lognormal fit of the ligament size distribution, as measured on SEM images. Hardness values are the average values calculated from indentations with different maximum loads and constant loading/unloading rate. Hardness was calculated from the maximum load applied and the residual indent area left at the surface of the sample, measured on SEM images. 111

Table 8.1. Polycrystalline np-Au compression specimen details and results from mechanical testing. The yield strength is taken as the first deviation from the linear region of the stress strain curve, during loading. For each specimen, the Young’s modulus values and the Poisson’s ratio values are averages of the values determined during the unloading portion of the test. 132

Table 8.2. Detailed results from compression testing cycles conducted on specimen 1-5. The Young’s modulus values determined during loading progressively match the value determined during unloading. 138

LIST OF FIGURES

Figure 1.1. Classification of porous structures based on their feature size, based on[12], [14]. The bottom part shows the classification as defined by the IUPAC, and the top part shows the updated classification by Mays. 2

Figure 2.1. SEM image of nanoporous gold. (Reproduced from[20] with permission of The Royal Society of Chemistry and of the PCCP Owner Societies) 6

Figure 2.2. Illustration of the dealloying process. a) LN atoms are etched at the surface exposed to the solution, b) MN element adatoms diffuse and form islands, exposing the material underneath, c) newly exposed surface is stripped of the LN element and MN adatoms diffuse to the existing islands, d) widening of the islands in hills, e) undercutting of the hills and f) creation of new islands of MN atoms once the diffusion distance becomes large. (From[65], reproduced by permission of The Electrochemical Society) 7

Figure 2.3 Pourbaix diagrams of a) silver and b) gold, in different solutions of their respective ions. (from[66], reproduced with permission from Wiley ©2000). 9

Figure 2.4. Simulated polarization curve for an AuAg alloy. In this case, the critical potential is 1.14 eV. (From[65], reproduced by permission of The Electrochemical Society) 10

Figure 2.5. SEM images of the structure after dealloying in nitric acid (6.56 mol/L, 80ºC) for initial compositions a) $Au_{0.16}Ag_{0.84}$, b) $Au_{0.36}Ag_{0.64}$ and c) $Au_{0.45}Ag_{0.55}$. (Reproduced from[67] with kind permission of Springer Science and Business Media).. 11

Figure 2.6. Gold-Silver phase diagram, from[68].. 12

Figure 2.7. Three types of grain boundaries observed in nanoporous gold. a) open grain boundary (gap), b) continuous structure along the grain boundary

and c) fused grain boundary. (Reprinted from [58] with permission from Elsevier) 13

Figure 2.8. Coarsening of the ligaments in a nanoporous gold film annealed in nitrogen at different temperatures. a) as-dealloyed, b) 100ºC, c) 200ºC, d) 300ºC, e) 400ºC and f) 500ºC. (From[69], reproduced with permission from Taylor & Francis Group) 14

Figure 2.9. SEM images of np-Au fractured by Vickers indentation. a) highly strained ligaments bridging the sides of a crack, b) extensive elongation and necking of the ligament prior to failure. (Reprinted with permission from [75]. Copyright 2005, AIP Publishing LLC) 17

Figure 2.10. TEM still image of np-Au during *in situ* indentation, showing significant dislocation activity in the ligaments. Three dislocations are clearly observable (indicated by white arrows). (Reproduced with permission from Wiley, ©2009 [78]) 18

Figure 2.11. SEM image of the fracture surface of np-Au ruptured in three-point bending. Two grains, I and II can be observed. Rupture was transgranular in grain I as indicated by the highly strained ligaments, while rupture was intergranular along grain II, which shows non deformed ligaments. (Reprinted with permission from [75]. Copyright 2005, AIP Publishing LLC) 19

Figure 2.12. a) Freestanding np-Au specimens created from a gold leaf on silicon substrate by electron beam lithography and undercut by reactive ion etching (reprinted from[96] with permission from Elsevier); b) np-Au micropillar create using a focused ion beam, after dealloying (reprinted with permission from[89]. Copyright 2006 American Chemical Society). 21

Figure 2.13. Yield strengths reported for np-Au in the literature, determined using different measurement techniques: nanoindentation (black filled

triangles adapted from [90], grey filled triangle adapted from[88], white open triangles from[89], open triangles with vertical crosses from[95], open triangle with diagonal cross from[96], open triangle with dot from[99], open triangle with vertical line from[100]); compression testing of millimeter-size samples (filled squares from[103], open square from[86]); tensile testing of millimeter-size samples (open circle from[86]); micropillar compression (diagonal cross from[101], vertical cross from[90]). 24

Figure 2.14. Schematic of a cell in Gibson and Ashby’s model. The cell is cubic, with ligaments of length l and thickness t. (From[94], reprinted with the permission of Cambridge University Press) 25

Figure 3.1. Schematic representing the electrochemical dealloying setup used for this work. 31

Figure 3.2. Damping system’s configuration. (left) schematic of the system’s elements (cross-section view), (right) schematic representing the free decay of the vibration induced by electrostatic forces in a cantilever shaped sample. 36

Figure 3.3. Photograph of the damping system, showing the main components of the setup. 37

Figure 3.4. Photographs of the small-scale testing setup at UK, in tensile testing configuration. (top) overview of the system, (bottom) close-up showing the grips and the positioning of a tensile testing, dogbone shaped specimen. 40

Figure 3.5. Shape of a typical nanoindentation curve. (From[107], reproduced with permission) 45

Figure 4.1. Damping ratio as a function of temperature for nc-Ni, measured using the Stanford system, before modifications. Experiments were conducted

by Jochen Lohmiller and reported in[109]. a) damping ratio vs. temperature for an induced vibration at 1586 Hz; b) relaxation peak after subtraction of the background from plot in a). The peak was identified as the Hasiguti peak $P\beta$; c) damping ratio vs temperature for a test with initial vibration at 440 Hz. The peak detected is identified as the Hasiguti $P\gamma$; d) Arrhenius plot allowing determination of the activation energy associated with the peak observed in a) and b). (All figures reprinted from[109] with permission from Elsevier) 49

Figure 4.2. Geometry of the nc-Ni damping samples. The samples were cut by wire EDM with various paddle sizes but constant clamping area and cantilever beam dimensions. (left) representation of a damping sample, the arrow demonstrating the direction of the cyclic deformation (vibration); (right) Typical dimensions of a sample. The base and cantilever portion were identical for all samples. 50

Figure 4.3. Details of the fabrication process for the np-Au damping specimens. a) bare silicon wafer, b) patterned photoresist on silicon, c) gold-silver sputtering, d) lift-off of the photoresist and the gold-silver film away from the damping sample geometry, e) wet etching of the silicon in HNA. The film is partly dealloyed after this step, f) complete dealloying of the gold-silver film. In e) and f), scale bars are 100 nm. 54

Figure 4.4. SEM micrographs of the np-Au film on top of silicon for the same damping sample (left) before testing (as-dealloyed state), (right) after 3 cycles below room temperature. 55

Figure 4.5. SEM micrographs of the np-Au film on top of silicon for the same damping sample (left) before testing (as-dealloyed state), (right) after 2 cycles below room temperature and 2 cycles above temperature (up to 450 K). 55

Figure 4.6. Damping ratio as a function of temperature for the same nc-Ni sample, at a resonant frequency of 2900 Hz. The tests were performed on two consecutive days, under the same conditions. The Bordoni peak's intensity was found to decrease while the Hasiguti $P\alpha$ and $P\gamma$ grew. 57

Figure 4.7. Damping ratio as a function of temperature for a nc-Ni sample with resonant frequency of 1780 Hz. (left) raw data with fitting of the exponential background; (right) after subtraction of the background, the Niblett-Wilks NW can be distinguished as the left shoulder to the Bordoni peak B. 58

Figure 4.8. Evolution of the damping ratio vs. temperature plots, for the sample nc-Ni sample tested several times, at different times. During the first tests, only the Bordoni peak was observed. This peak gradually disappeared while the Hasiguti $P\gamma$ peak's intensity gradually increased. 60

Figure 4.9. Damping ratio vs. temperature for the first set of np-Au films on silicon, created by KOH wet etching. Poor signal led to noisy data, but a damping peak can be identified at ~ 260 K. (top) Raw data obtained with an excitation frequency of 240 Hz; (bottom) data after subtraction of the exponential background. The damping peak can be fitted as a Gaussian peak. 63

Figure 4.10. Evolution of the damping ratio vs. temperature curves through several cycles from low to high temperatures. Data points were recorded during natural heating and cooling. The amplitude of the relaxation peaks stays constant and no obvious difference is determined after several cycles. For the first natural heating, hardware issues prevented recording of the data up to room temperature. 65

Figure 4.11. Comparison of damping ratio vs. temperatures curves for the sample with the np-Au film, the sample with only the Ta and Au interlayers, and

bare silicon. The relaxation above room temperature is clearly not associated with the np-Au film. 66

Figure 5.1. Grain growth based on number of grain sides (2D). With less than 6 sides, grains will shrink and disappear; with more, grains will grow. (Republished with permission of Taylor and Francis Group LLC from[125]; permission conveyed through Copyright Clearance Center, Inc.) 71

Figure 5.2. Sample ($Au_{35}Ag_{65}$) after cold-rolling and annealing steps, showing large grains obtained by AGG. The front (a) and back side (b) of the sample can be seen, with the backside oriented to allow direct comparison of the microstructure, as schematically represented below the micrographs. (From[132], reprinted with permission from Taylor & Francis Group) 74

Figure 5.3. Optical micrograph of a sample after AGG, showing regions chosen to extract tensile testing specimens by wire EDM. 75

Figure 5.4. Optical micrograph of a tensile testing specimen with dogbone shape, after extraction by wire EDM. Some grain boundaries can be seen to still be present in the gage section, despite the grain size reached by AGG. 75

Figure 5.5. Typical np-Au structure obtained after dealloying of a bulk AuAg specimen. Determination of the ligament size is based on the measurement of the narrowest diameter along individual ligaments (micrograph adapted from[132], reprinted with permission from Taylor & Francis Group) 77

Figure 5.6. (a) Stress-strain curve calculated from the data recorded during the tensile test of a pseudo-single crystalline np-Au specimen. (b) The sample fracture initiated on grain boundaries remaining in the precursor alloy after AGG, and retained during dealloying. (from[132], reprinted with permission from Taylor & Francis Group) 78

Figure 5.7. SEM micrograph of the fracture surface of a pseudo-single crystalline np-Au specimen after rupture in tension. Regions where transgranular rupture occurred appear rough with extensive ligament deformation (indicated by the white arrow). In contrast, regions where intergranular rupture took place appear smooth. (from[132], reprinted with permission from Taylor & Francis Group) 80

Figure 5.8. SEM micrograph of a specimen ruptured in tension, illustrating the difference between regions that underwent deformation and others that did not bear load. 80

Figure 5.9. SEM micrograph of an unfused grain boundary, after dealloying, observed at the rupture surface of a pseudo-single crystalline specimen tested in tension. 82

Figure 5.10. SEM micrograph of the fractured surface of a pseudo-single crystalline np-Au specimen tested in tension. Regions exhibiting ligament plasticity are colored in blue, while regions seemingly unloaded during the test are colored in red. 83

Figure 6.1. Back-reflection Laue diffraction pattern of (110) from the AuAg single crystal used to extract tensile testing specimens (photograph provided by Metal Crystals and Oxides Ltd.) 85

Figure 6.2. (top) Optical micrograph of a single crystalline np-Au small-scale tensile specimen in the grips, before testing. The grid used to track deformation through DIC can be seen superimposed on the gage section of the specimen (hatched region) (from[132], reprinted with permission from Taylor & Francis Group); (bottom) SEM micrograph of the typical np-Au structure obtained after dealloying of a AuAg specimen. 87

Figure 6.3. Typical ligament distribution within a np-Au specimen. Ligament size is determined from the maximum of the lognormal fit of the size

distribution. (from[132], reprinted with permission from Taylor & Francis Group) 88

Figure 6.4. (top) Stress-strain curve calculated from data recorded during tensile testing of a non-annealed single crystalline np-Au specimen. Young’s modulus is calculated from the linear portion of the curve, just before failure; (bottom) Transverse vs axial strain curve from which Poisson’s ratio can be extracted. The value is found to decrease as the stress-strain curve becomes linear. 89

Figure 6.5. SEM micrograph from the fracture surface of the first single crystalline np-Au specimen, not annealed prior to dealloying. 90

Figure 6.6. (a) Stress-strain curve calculated from data recorded during tensile testing of specimen 1-5; (b) corresponding transverse vs axial strain curve. Young’s modulus and Poisson’s ratio are calculated from the linear region of the curves. For both plots, only one every four datapoint is shown to improve clarity. (from[132], reprinted with permission from Taylor & Francis Group).. 91

Figure 6.7. SEM micrograph from the rupture surface of a np-Au specimen ruptured in tension. Regions only a couple cells below the rupture surface are found to be intact (indicated by white arrows).. 92

Figure 6.8. SEM micrograph of the fracture surface of a single crystalline np-Au specimen that was annealed prior to dealloying. The whole cross-section shows deformed ligaments, indicating that the load was carried by the whole gage during testing and up to rupture. Some empty regions can be seen, which were likely impurities or silver rich pockets before dealloying. 93

Figure 6.9. SEM micrograph of the fracture surface after tensile testing of a single crystalline np-Au specimen. The loading axis is indicated by the black arrow in the top right corner. Most ligaments show extensive plastic

deformation and necking in the direction of the load (typical regions indicated by a white arrow) while others, not aligned with the load axis do not (red arrows). (adapted from[132], reprinted with permission from Taylor & Francis Group).. 93

Figure 6.10. SEM micrograph of an empty pocket found at the fracture surface of a specimen tested in tension... 94

Figure 6.11. Stress-strain plot obtained during compression testing of a np-Au specimen previously tested in tension up to rupture. Although strain values were not properly determined and the specimen buckled at ~32 MPa, the load values are still valid. (from[132], reprinted with permission from Taylor & Francis Group) 96

Figure 6.12. Stress-strain curve from tensile testing of sample 1-5. The evolution of the Young’s modulus is shown, gradually increasing and becoming linear before rupture... 99

Figure 7.1. Load vs. depth nanoindentation curves obtained at different maximum loads during testing of np-Au with relative density of 0.30, with loading and unloading rates of 0.025 mN.s^{-1}. A typical indentation image is shown in the top left corner, obtained by SEM.. 109

Figure 7.2. Hardness values as a function of indentation total depth determined from experiments on np-Au with relative density of 0.30. Open markers represent values obtained by calculating hardness based on the indenter tip geometry, while values represented by filled markers were determined using the area of residual print measured on SEM images after testing. Grey markers show data obtained with constant loading/unloading rate of 0.025 mN.s^{-1} while black markers show hardness values determined with constant loading/unloading time of 20 seconds.. 110

Figure 7.3. Values reported for yield strength in the literature (obtained by nanoindentation) and obtained in the present study from nanoindentation experiments and tensile testing of single crystalline specimens. The nanoindentation values are the raw measurements, assuming the hardness and yield strengths are equal. The tensile testing values have been adjusted (11% increase) to correct the stress concentration caused by sample geometry and surface roughness. Black filled triangles adapted from[90], grey triangle from[88], white open triangles from[89], filled stars from present work's nanoindentation and filled circles from tensile testing of single crystalline specimens[132]. 117

Figure 7.4. Similar plot to the one showed in Figure 7.3, after all nanoindentation hardness values have been divided by a factor of 2.65. Markers identical to those listed in Figure 7.3. 118

Figure 7.5. Similar plot to the one showed in Figure 7.4, after all yield strength values have been normalized a similar ligament size of 50 nm. Markers identical to those listed in Figure 7.3. Using the size effect exponent m as the fiiting parameter, best fit of the values is obtained for m = 0.551. 119

Figure 7.6. Ligament size effect on yield strength, based on data reported by Hodge[90], for a relative density of 0.30. The nanoindentation hardness values have been divided by a factor of 2.65. 120

Figure 7.7. Yield strength values reported in the literature for gold micro- and nanowhiskers, and for micropillars. Values have been normalized the highest Schmid factor on the (111) <110> slip system. Data adapted from[158] (square markers),[155] (open and closed circles),[142] (triangles pointing down) and[146] (triangles pointing left). Linear fitting of the data allows determination of the size effect exponent m and of k. 122

Figure 7.8. Identical plot as shown in Figure 7.7 but a fixed slope of -0.551 was used for the linear fit in order to obtain k in units of MPa.m$^{0.551}$, in agreement with the size effect exponent m value. 122

Figure 7.9. Calculated yield strength values of individual np-Au ligaments (blue, half-filled markers) based on np-Au yield strength values reported in the literature and obtained during this work. Values have been estimated using Equation 7.9. Calculated values are in good agreement with values found in the literature for gold wires and pillars (open and filled markers, similar to Figure 7.7 and Figure 7.8. 125

Figure 7.10. Calculated values of np-Au yield strengths (blue, half-filled markers) for different relative densities. Values have been estimated using Equation 7.9 and Equation 7.10, based on the reported ligament size and relative density of the sample. Black markers show the value experimentally measured, which agrees very well with estimations from the new scaling relation. 126

Figure 7.11. Calculated yield strength values for np-Au with various ligament sizes, based on calculations using both Gibson and Ashby scaling relation and the new scaling relation. The gray region represent all the possible values calculated by the original scaling relation, depending on the value chosen for σs (between 2 and 205 MPa). 127

Figure 8.1. (left) custom made specimen holder used to clamp the specimen in proper position to ensure perpendicularity of the ends with the long axis, (middle) holder in position against angle plate and granite stand to position the specimen and (right) verification of the final polished end face using a comparator. (images reproduced from Michael Bürckert Master thesis) 130

Figure 8.2. Stress strain curves for three of the six loading/unloading cycles conducted on specimen 1-5, in compression. For all plots except the first

one, the strain values have been adjusted so as to start all plots with a strain value of ~ 0. 133

Figure 8.3. Transverse strain vs. axial strain for the first loading/unloading cycle conducted on specimen 1-5. For clarity and direct comparison, the unloading plot has been adjusted so that the strain at the start of the unloading portion is set to ~ 0. 134

Figure 8.4. Ideal stress-strain curve for a porous material, showing the three separated regions: elastic loading, plastic collapse and densification. (figure reprinted from Michael Bürckert Master thesis) 135

Figure 8.5. Stress strain curves for all loading/unloading cycles conducted on specimen 1-5, in compression. For all plots except the first one, the strain values have been adjusted so as to start all plots with a strain value of ~ 0. 137

Figure 8.6. Stress vs. strain curves for compression testing on specimen 1-6. 140

Figure 8.7. Transverse vs axial strain for the fourth loading cycle conducted on specimen 1-5. The Poisson's ratio is determined in the region that corresponds to the elastic region in the stress strain curve and in the region past the yield point. 141

Figure 8.8. Transverse vs axial strain for the fifth loading cycle conducted on specimen 1-5. The Poisson's ratio is determined in the region that corresponds to the elastic region in the stress strain curve and in the region past the yield point. 142

Figure 8.9. Comparison of the yield strength values determined during compression testing and estimations based on the new scaling relation presented in Chapter 7 and the Gibson and Ashby relation. Values of yield strength at 0.2% offset are found to agree well with the new scaling relation. 143

Figure 8.10. Determination of the scaling relation for the Young's modulus of np-Au based on results from mixed experimental techniques and structure. Filled circle markers indicate results obtained in tension while the square marker indicates results from the compression tests. 146

Figure 8.11. Determination of the scaling relation for the Young's modulus of np-Au based on results from similar experimental techniques. Filled circle markers indicates results from tensile tests while square markers indicate results from compression testing. The blue square marker comes from compression testing of polycrystalline np-Au with relative density of 0.30, reported by[86]. 147

Chapter 1 : Introduction

Porous materials have been used since Antiquity, when the filtering properties of activated carbon were utilized for water purification[1] and medicinal purposes [2], [3], sand was employed in water desalination and clay as a drying agent[4]. The Roman engineers recognized the advantages of porous rocks in construction applications and included tuff stone and pumice in the formulation of cements leading to lighter yet strong concrete for the top layers of their buildings[5] (Pantheon dome, aqueducts). In 1756, at the dawn of the Industrial Revolution, A.F. Cronstedt, as Swedish mineralogist and chemist, discovered that stilbite released steam when rapidly heated. He labeled the material a zeolite, from the Greek *zéō* (to boil) and *líthos* (stone)[6]. Because of the rarity of natural zeolites, no major advancement was made until the middle of the 19th century when, in 1862, the first synthetic replication of a natural zeolite, the levynite, was successfully produced by Sainte Claire Deville[7]. In the 1930's, R. Barrer started working on the synthesis of zeolites via hydrothermal processes, eventually creating the first synthetic zeolite with no natural equivalent in 1948[8]. This achievement opened the way to extensive industrial research for applications in oil refining, catalysis and molecular sieves (for more details, see[9], [10]). Nowadays, although the largest market by volume for synthetic zeolites is in the detergent industry (72% in 2008), the largest value market (55%) is in catalysis applications (mostly fluid catalytic cracking)[11]. Other principal uses include gas separation, ion-exchanging and petroleum industry applications.

Over the past two decades and with the emergence and development of nanotechnologies, the ability to design, control and build nanomaterials has allowed scientists to create porous materials from nanoscale building block, with feature size ranging from several to hundreds of nanometers. The International Union of Pure and Applied Chemistry (IUPAC) recommended that porous materials be classified based on their pore (channel) size, as shown in the lower half of Figure 1.1[12]. However, that classification was initially proposed to differentiate adsorption mechanisms connected to the pore size[13], and so it does not characterize the material itself. Furthermore, and especially in the material science field, the prefixes employed become confusing, as micro- typically refers to an entity whose dimensions are in the micrometer range. A new classification that would correct these issues by focusing on the material rather than its properties has recently been proposed by Mays[14], and can be seen in the top half of Figure 1.1. This new classification will be used throughout the present work, and porous materials with feature size below 100 nm will be referred to as nanoporous (np) materials.

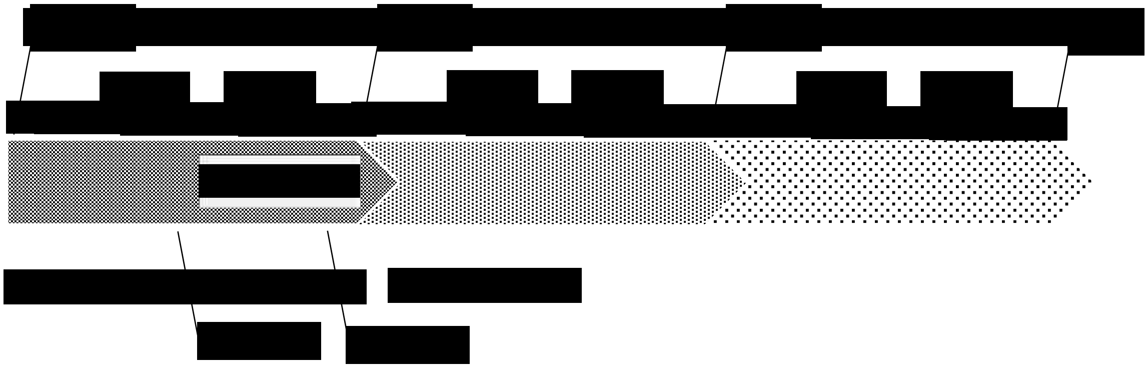

Figure 1.1. Classification of porous structures based on their feature size, based on[12], [14]. The bottom part shows the classification as defined by the IUPAC, and the top part shows the updated classification by Mays.

Np materials can be fabricated through different processes, for example using templates made of polymers[15] or porous alumina[16], using sol-gel or chemical vapor deposition techniques[17]. Research is still on-going to produce np structures with uniform, controlled pore size, and some promising techniques have been recently reported[18]. Among np materials, np metals are of particular interest as they offer opportunities in numerous fields such as catalysis[19]–[26], actuation[27]–[31], sensing[32], [33], capacitors[34], [35], batteries[36], [37], medical and biological applications[38], [39] or energy storage[40]. Because of their feature size, np metals also generate interest for novel optical applications involving surface plasmons[41]–[46]. The potential of np metals primarily arises from the very large surface area to volume ratio they exhibit. For instance, np gold (np-Au), the material of interest in the present study, has been shown to have a surface area between 3 and 7 $m^2.g^{-1}$[47].

Np metals are typically made by selective etching of an alloy, a process known as dealloying. In general, the precursor alloy is a solid solution of two elements, with one significantly more noble than the other, the latter to be selectively etched in solution. Although this binary alloy configuration has been widely viewed as a necessary condition to create np metals, dealloying has recently been successfully achieved for other types of metallic compounds. Several metals have been produced in their np form by dealloying, as detailed in Table 1.1.

This dissertation focuses on the mechanical behavior of np metals, primarily np-Au. Dealloying of bulk samples was optimized and defects within the ligaments of the structure were characterized by internal friction measurements. The relation between ligament size, determined by Scanning Electron Microscopy (SEM), and the mechanical properties was investigated by performing tension and compression testing of small-scale specimens on a custom designed system. In parallel, hardness of np metals was determined by nanoindentation experiments. Scaling relations properly linking the mechanical properties of porous materials to their dense counterparts have been derived by Gibson and Ashby. The applicability of these classic relations to np metals was evaluated in light of the new results and new scaling relations were obtained.

Table 1.1. List of np metals successfully prepared by dealloying, reported in the literature.

Np metal	Precursor alloy	References (non-exhaustive)
Ag	AgAl	[48]
Ag	AgZn	[49]
Ag	AgCu	[50]
Au	AuAg	[20], [51]–[53]
Au	AuMg	[54]
Cu	CuZn	[48]
Cu	CuAl	[48]
Ir	IrNi	[55]
Ni	NiCu	[56], [57]
Ni	NiAl	[57]
Ni	NiFe	[57]
OsRu	OsRuMg	[54]
Pd	PdAl	[48], [58]
Pd	PdCo	[59]
Pd	PdNi	[60]
Pt	PtAl	[61]

Chapter 2 : Background

Although nanotechnologies have emerged at the end of the 20th century, nanomaterials have been created and used for over 2000 years[62]. Andean smiths and later Incas used to etch the surface of *tumbaga*, gold-copper alloys with silver impurities, using the juice of a plant containing oxalic acid. This process would result in a gold layer of high purity at the surface, creating the illusion of an object made of solid gold[62], [63]. Unknowingly, they formed a porous layer of gold, selectively removing the less noble copper and silver atoms out of the alloy. The technique, sometimes referred as depletion gilding when referring to surface embellishment, is similar to dealloying, and is still the preferred technique for np metals formation.

Over the past 15 years, np-Au has been the primary np metal investigated because of the relative simplicity of preparation, from gold-silver (AuAg) alloys. Since gold is a noble metal, gold alloys can be selectively etched relatively easily. Moreover, due to its chemical stability, np-Au does not necessitate special storage conditions after dealloying. Np-Au can also be created with different relative densities, as explained in the following sections, allowing investigations on different np structures.

2.1. Description of np-Au

Np-Au has a structure made of interconnected struts generally referred to as ligaments, defining the pores of the material, and can be directly observed using a scanning electron microscope (SEM), as shown in Figure 2.1. Ligaments are randomly oriented and connect at the nodes of the structure, which are slightly larger and bulkier than the ligaments themselves. Pores and ligaments size can vary from 10 to 100 nm and even larger, to a point where the structure might not be characterized as nanoporous anymore. In opposition to polymeric foams or commercial milliporous aluminum foams (Duocel®, ERG), np metals and np-Au in particular have a larger volume fraction, or relative density, which represents the fraction of actual solid material in a given volume of np metal. It is generally expressed as ρ^*/ρ_s, with ρ^* the density of the porous material and ρ_s that of the corresponding, dense material. Typical relative densities for np-Au range between 0.25

and 0.42, whereas polymeric foams and aluminum foams usually have relative densities below 0.1. Also, the latter structures do not exhibit the enlarged nodes at which the ligaments connect. These morphological differences are of importance when considering the deformation mechanics and the mechanical properties of np metals, and comparing them to existing data and models based on other porous materials.

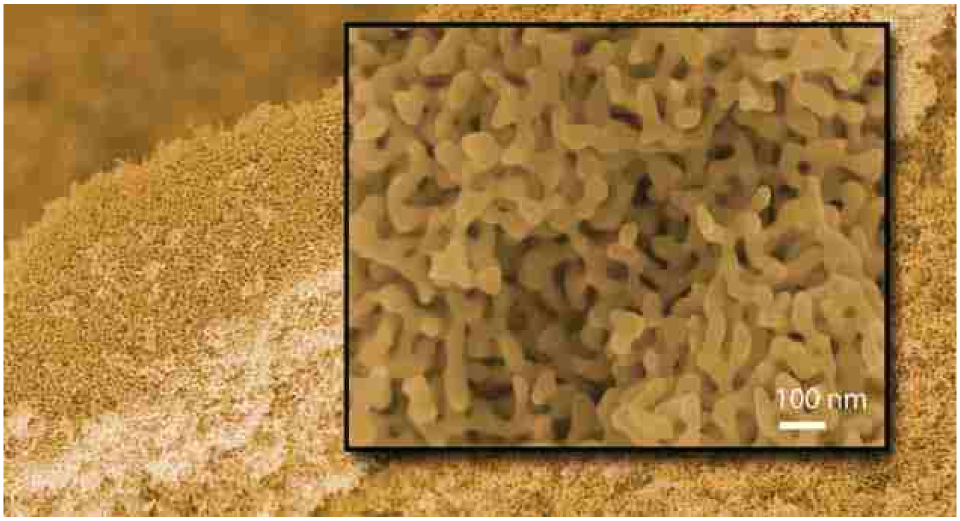

Figure 2.1. SEM image of nanoporous gold. (Reproduced from[20] with permission of The Royal Society of Chemistry and of the PCCP Owner Societies)

2.2. Fabrication of np-Au: dealloying

Np-Au has received principal attention and has been the most studied np metal, mainly because of its relative ease of fabrication, storage and characterization. Np metals are most generally made by dealloying, the selective etching of a component out of an alloy. The sacrificial element to be etched can be referred to as the less noble (LN) element whereas the element that is not etched, hence the one that will create the np structure, is the more noble (MN) element. Thus, dealloying is a selective, controlled corrosion of an alloy that will lead to the formation of the np metal.

A good description of the dealloying process has been given by Erlebacher[64]. Once in the proper solution, the LN atoms exposed at the surface of the alloy are etched out, leaving the MN atoms untouched. These adatoms (MN atoms without lateral coordination) then diffuse at the solid/electrolyte interface and agglomerate into clusters, thus exposing a fresh layer of alloy. The process repeats and more adatoms agglomerate to the existing MN element pure islands, which begins to grow larger into hills shape. These hills eventually get undercut, creation of new MN pure agglomerates become favorable over attaching to the existing ones and etching continues through the bulk of the alloy. These steps have been schematically illustrated by Erlebacher[65] and are shown in Figure 2.2.

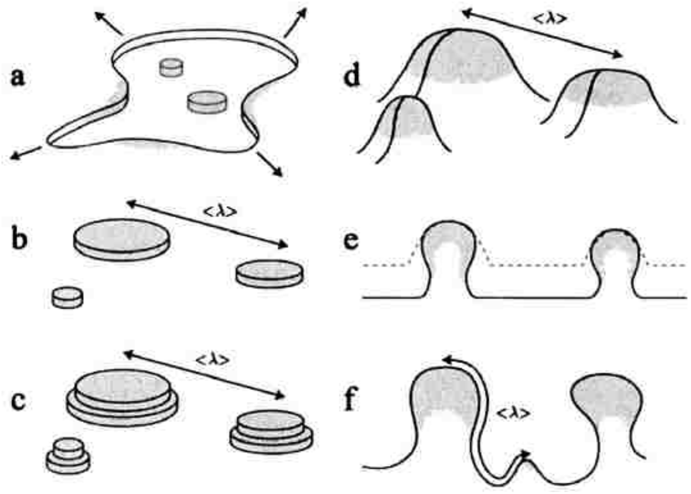

Figure 2.2. Illustration of the dealloying process. a) LN atoms are etched at the surface exposed to the solution, b) MN element adatoms diffuse and form islands, exposing the material underneath, c) newly exposed surface is stripped of the LN element and MN adatoms diffuse to the existing islands, d) widening of the islands in hills, e) undercutting of the hills and f) creation of new islands of MN atoms once the diffusion distance becomes large. (From[65], reproduced by permission of The Electrochemical Society)

Selection of the precursor alloy is critical, and it usually has to possess specific characteristics to be suitable for creating a np metal, as described by Erlebacher[65]:

(1) the potentials required to etch the components of the precursor alloy in their pure form must be separated, preferably by a hundreds of millivolt, so that the element that is to be etched is clearly the LN,
(2) the precursor alloy is typically rich in the LN element (over 50 at%),
(3) preferably, the precursor alloy does not present any phase separation (solid solution),
(4) diffusion of the MN atoms at the interface with the dealloying solution must be fast.

In the case of np-Au, alloys of gold and silver ($Au_xAg_{(1-x)}$) are usually used. Based on the table of standard electrode potentials, there is a difference of potential of ~ 0.7 V between silver and gold: 0.8 V and 1.52 V vs. standard hydrogen electrode (SHE) for silver and gold, respectively. Nitric acid is generally used because silver can be readily etched by nitric whereas gold cannot. Therefore, dealloying of AuAg by simple immersion in a nitric acid solution is possible, although relatively slow. This method is known as free dealloying, in contrast to electrochemical dealloying where the alloy is set to a potential by an external power supply. The latter method leads to faster dealloying as the dissolution rate of the LN element is increased. Determination of a suitable potential for fast dealloying can be guided by the standard electrode potentials, as well as by the Pourbaix diagrams of each of the elements in the alloy. The Pourbaix diagrams of gold and silver are reproduced in Figure 2.3. It can be seen that in a nitric acid solution ($0 < \mathrm{pH} < 1$), silver exists as Ag^+ cations when a potential above 0.8 V is applied. This threshold decreases as the concentration of Ag^+ ions in the solution increases. On the other hand, gold can only exist as Au^{3+} cations in solution of its own ions, which is only possible if a potential above 1.5 V is applied and the concentration gold ions in the acid solution rises. It can also be seen that at a pH of nearly zero, gold can exist in a solid $Au(OH)_3$ form (gold trihydroxide). Therefore, by applying a potential between 0.8 and 1.4 V, silver can be etched while gold remains intact. As the dealloying solution becomes increasingly concentrated in silver ions, the potential required to etch silver decreases towards lower values.

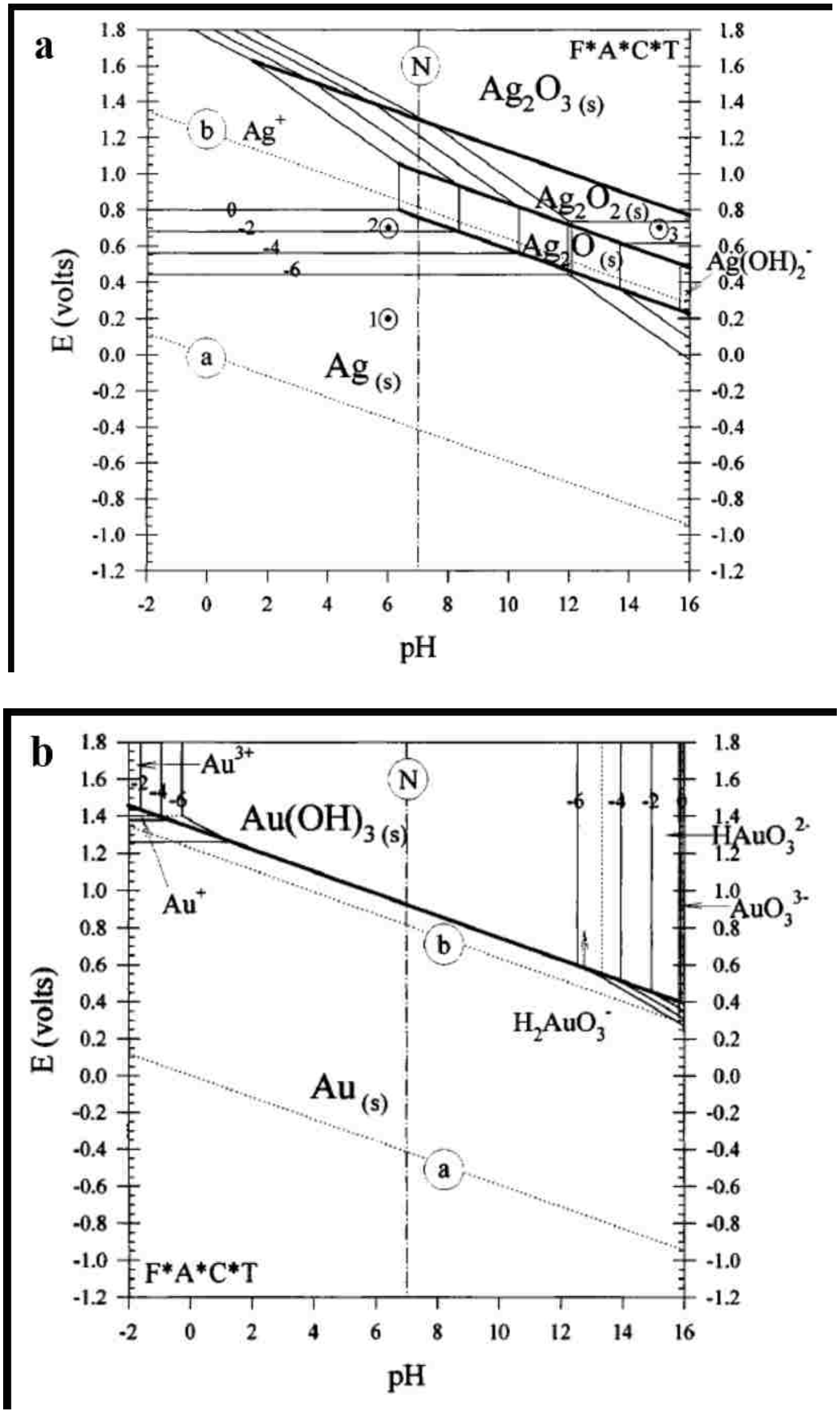

Figure 2.3 Pourbaix diagrams of a) silver and b) gold, in different solutions of their respective ions. (from[66], reproduced with permission from Wiley ©2000).

A practical method used to verify (and confirm) the value of the potential to apply for electrochemical dealloying is to conduct a linear sweep of potential, using a potentiostat system. In this method, the precursor alloy is immersed in the dealloying solution (nitric acid for AuAg) and the applied potential varies over time. At low potentials, both elements of the alloy are in the passivation region and no dissolution current can be measured. Once the potential reaches a value high enough to etch the LN element, a current will be measured. Beyond a certain potential value, commonly called the critical potential, the dissolution current typically rises quickly, as show for AuAg in Figure 2.4.

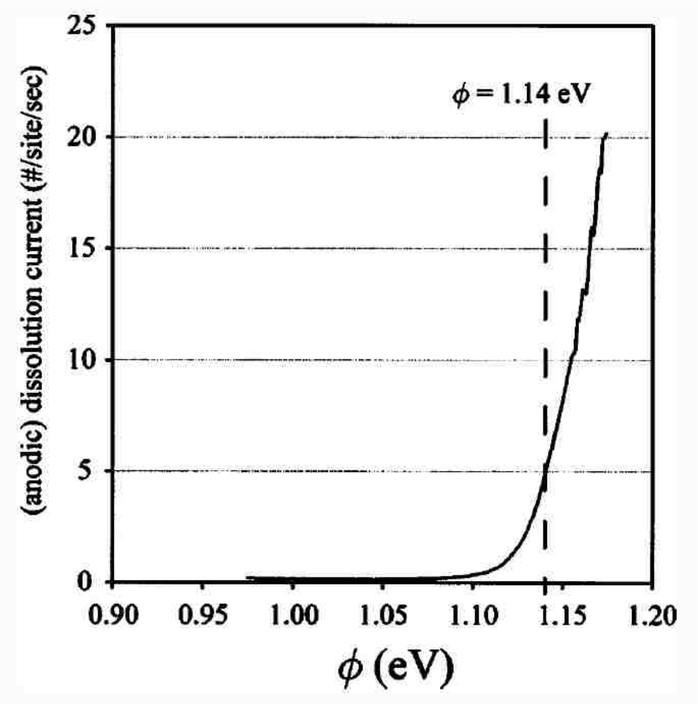

Figure 2.4. Simulated polarization curve for an AuAg alloy. In this case, the critical potential is 1.14 eV. (From[65], reproduced by permission of The Electrochemical Society)

Composition of the precursor alloy determines whether the material can be fully dealloyed or not. If the alloy is too rich in the sacrificial element, etching of the LN atoms can be faster than diffusion and construction of the porous structure by the MN atoms, hence leading to the apparition of cracks. If the alloy composition is too poor in the sacrificial element, the MN element can passivate the surface of the material before more LN atoms can be etched and removed in solution. The dealloying therefore comes to a stop, and only a few pores can be seen at the surface of the material, as can be observed in Figure

2.5. The lowest content of MN element that can lead to successful dealloying is called the parting limit. The reported range of gold content suitable for creating np-Au from AuAg is from 25 to 42 at%. Because this range is relatively large, np-Au can be created with various relative densities which is critical for the experimental determination of the influence of this parameter on the mechanical properties.

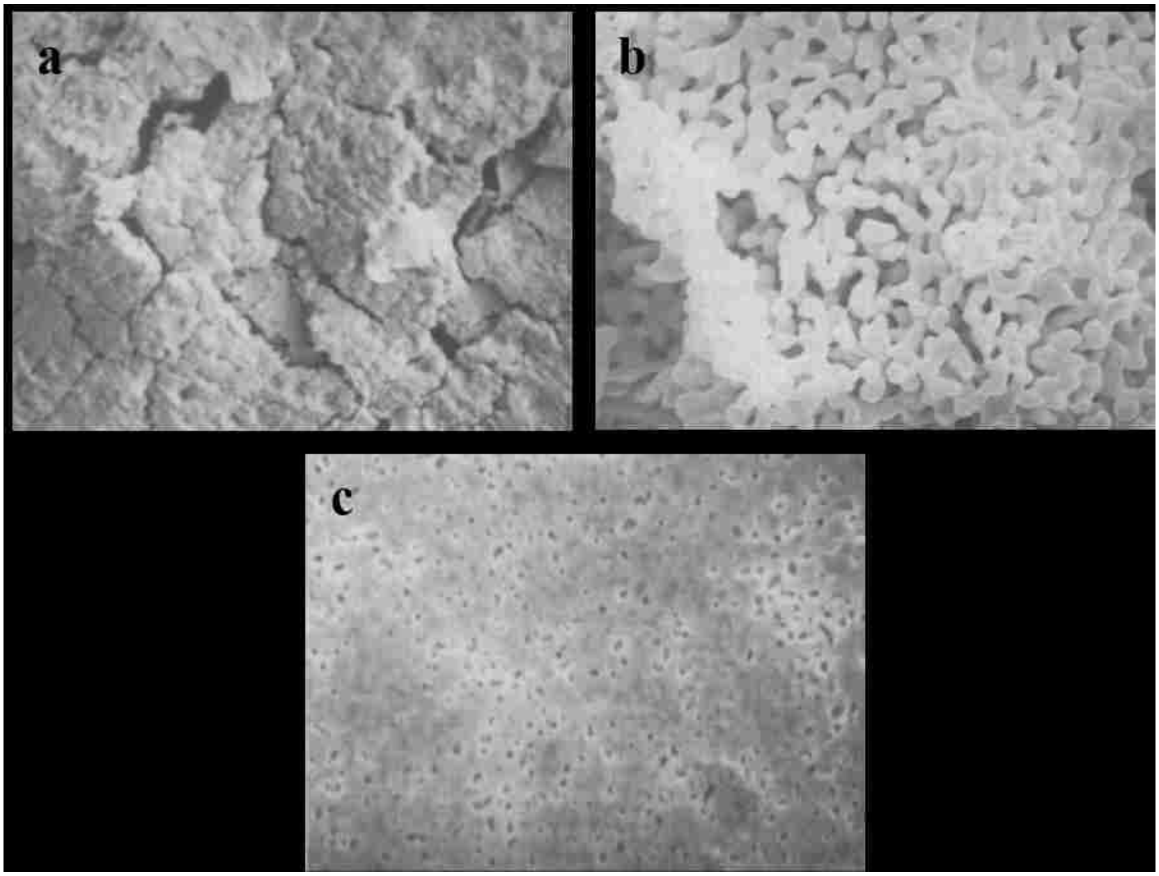

Figure 2.5. SEM images of the structure after dealloying in nitric acid (6.56 mol/L, 80ºC) for initial compositions a) $Au_{0.16}Ag_{0.84}$, b) $Au_{0.36}Ag_{0.64}$ and c) $Au_{0.45}Ag_{0.55}$. (Reproduced from[67] with kind permission of Springer Science and Business Media)

Because compositional variations can lead to different np structures, cracking or even no dealloying, one has to make sure that the precursor alloy is homogeneous. The AuAg phase diagram reproduced in Figure 2.6 shows that for a 35 at% gold rich AuAg alloy, the liquidus and solidus lines are separated by no more than 3ºC and the variation in composition expected in the alloy from rapid cooling should be no more than 2 at%. It can also be seen on the phase diagram that gold and silver a miscible over the whole composition range, satisfying characteristic (3) stated above. This does not always have to be the case though, and np metals made from non-miscible elements have been reported.

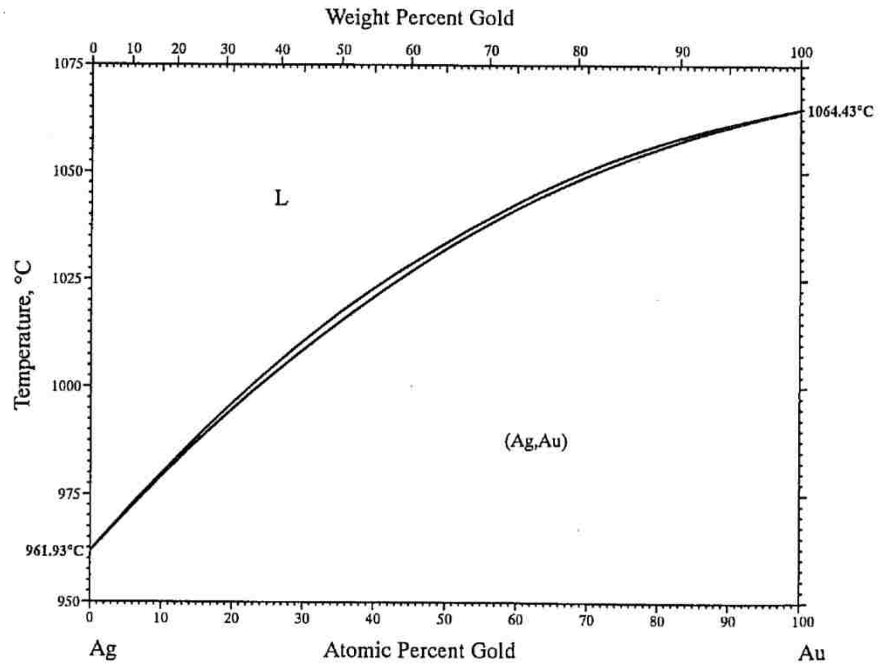

Figure 2.6. Gold-Silver phase diagram. (Reproduced from [68], with permission from ASM International)

During dealloying, the MN atoms diffuse at the alloy/electrolyte interface and agglomerate into islands in an epitaxial manner, so that individual ligaments in the np structure retain the crystalline orientation of the original alloy, regardless of their random spatial orientation in the final structure. In a similar way, original defects in the alloy will remain in the ultimate np material. For example, grain boundaries are still present after dealloying, although it has been reported by Sun and Balk[53] that grain boundaries can evolve as gaps (ligament size wide), be fused or even that the np structure can be continuous throughout the grain boundary, as shown in Figure 2.7. The fact that defects such as grain boundaries are still present in the material after dealloying presents a challenge for the evaluation of the mechanical properties of np-Au by mechanical testing of millimeter size samples, as will be detailed in following chapters.

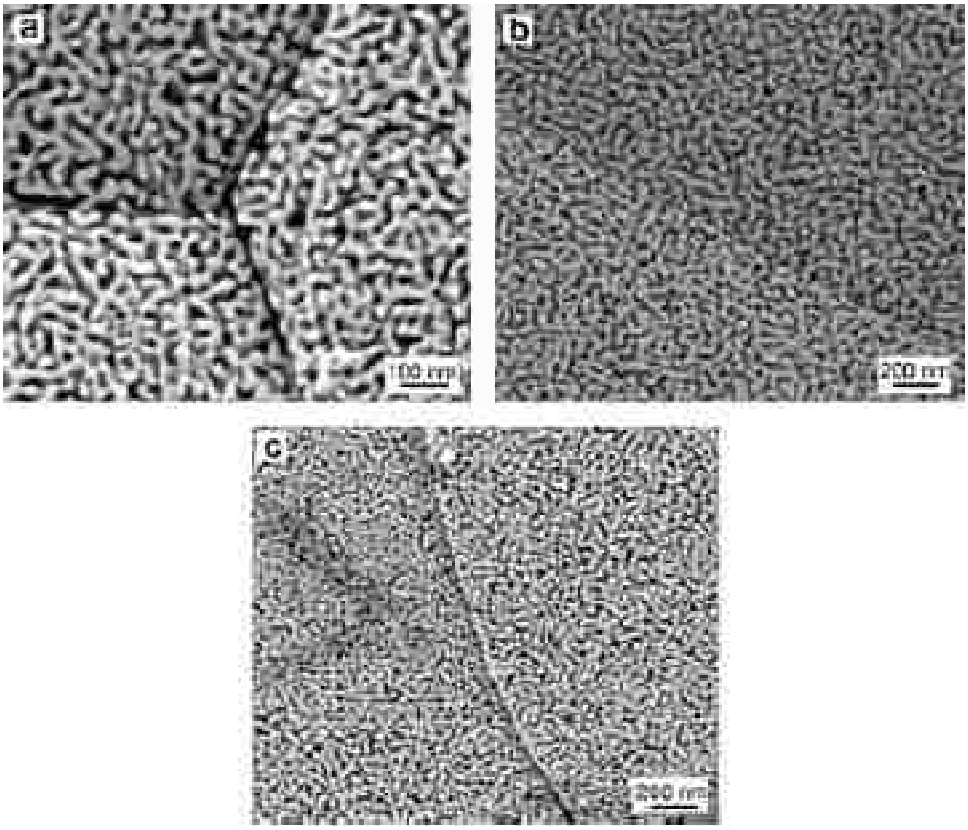

Figure 2.7. Three types of grain boundaries observed in nanoporous gold. a) open grain boundary (gap), b) continuous structure along the grain boundary and c) fused grain boundary. (Reprinted from [58] with permission from Elsevier)

A strong advantage that np metals offer is the ability to control the ligament and pore size. This is of particular interest because it allows one to study the mechanical properties of a np metal over a wide range of ligament sizes. Structure coarsening can be achieved by increasing the time spent in the dealloying solution, even after full removal of the sacrificial element, or by annealing of the sample. This coarsening occurs by diffusion of the MN atoms at the surface of the ligaments and is driven by surface energy reduction (capillarity) as explained by Erlebacher[65]. During this process, the relative density is conserved, as both ligaments and pores grow simultaneously, as shown in Figure 2.8.

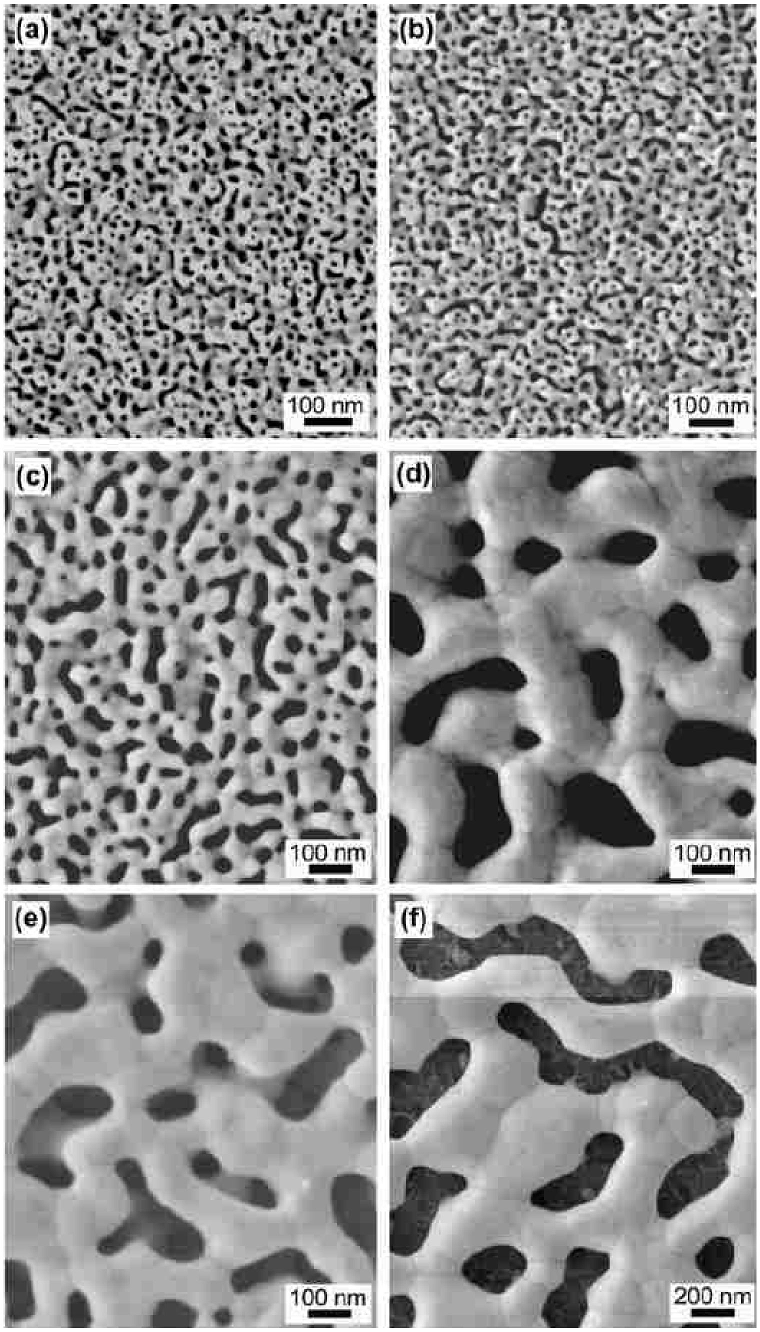

Figure 2.8. Coarsening of the ligaments in a nanoporous gold film annealed in nitrogen at different temperatures. a) as-dealloyed, b) 100ºC, c) 200ºC, d) 300ºC, e) 400ºC and f) 500ºC. (From[69], reproduced with permission from Taylor & Francis Group)

2.3. Applications of np-Au

Due mainly to their extremely large surface areas in minimal volumes (up to 7 $m^2.g^{-1}$[47]), np metals in general and np-Au in particular have been the subject of many investigations. As for any material presenting such specificity, the properties of np-Au have been studied for catalysis applications, as well as for sensing and actuating. Moreover, np-Au has been investigated for its potential applications in energy storage.

2.3.1. Catalysis

Although gold is normally regarded as inert, it has been the subject of research in the field of catalysis in the past two decades, mainly inspired by Haruta's work[70]–[75]. Among others, low temperature CO oxidation on supported gold particles has been the focus of extensive research[72], and naturally, in the last decade, the properties of np-Au have been investigated for the same application[19]–[21], [76] as well as for other catalytic reactions[22], [77].

2.3.2. Sensing and actuation

Np-Au has also shown some promising results in the fields of sensing and actuation. By controlling the charge distribution at the surface of the gold ligaments, the surface can be placed under a tensile or compressive stress. The material then reacts to this change of stress by expanding or contracting. Actuation in np-Au is therefore a surface driven mechanism and has been showed to demonstrate macroscopically detectable deformation[20], [31], [78]. Similarly, any chemical reaction or phenomenon modifying the surface stress in np-Au can be detected. This can be used for sensing applications, and as the surface-to-volume ratio is very large for np-metals, detection limits are potentially very low, meaning sensing capabilities with very low detection threshold[20], [32].

2.3.3. Energy storage

Energy storage has become one of the most investigated field of research due in part to the increasing reliance on portable electronics (batteries) and drive to clean and independent energy. Hydrogen storage capabilities have been reported for np-Pd[59], [79] and np-Au has shown potential in batteries[37] and supercapacitors[34], [35] applications.

2.3.4. Radioprotection

Recently, the resistance of np-metals, and np-Au in particular, to ion irradiation has been the subject of research[50], [80]–[82]. Because of the small size of the ligaments that constitute the np structure, accumulation of defects in such confined volumes have been found to be reduced, as defects migrate to the free surface and disappear before extensive damage can be done to the material.

2.4. Deformation behavior and mechanical properties of np-Au

Np-Au, at the macroscale, is extremely brittle and therefore is a challenging material to manipulate. This is a counter-intuitive observation as gold is a ductile material and one would expect this ductility to remain in the porous form. The macroscopic brittleness of np-Au has prompted researchers to study the deformation behavior at the microscopic scale to determine whether the gold ligaments themselves were becoming brittle at the dimensions and in the geometrical configuration of np-Au.

2.4.1. Deformation behavior at the microscopic scale

Suppression of dislocation nucleation and activity within the confined volumes of the ligaments could explain the brittleness of np-Au. Another cause could be the macroscopic morphology of the samples. Li and Sieradzki investigated the presence of a ductile-brittle transition based on the sample size in np-Au[83]. They observed fracture strains indicating ductile behavior for small sample size. As the size of the sample increased, the fracture behavior gradually became more brittle. Based on their data and microscopic observation of the fracture surface, they concluded that the ductile-brittle transition observed when increasing the sample size did not have an origin at the microscopic level. Biener *et al.*[84] fractured polycrystalline np-Au bulk samples using three-point bending as well as Vickers indentation, and they characterized the fracture surfaces with scanning electron microscopy. They observed extensive elongation and necking of the ligaments, as shown in Figure 2.9, meaning that individual ligaments are still deforming plastically before failure, and confirming Li and Sieradzki's determination that the macroscopic brittleness of np-Au is not of microscopic origin. Ductile behavior of the ligaments in np-Au has also been reported during nanoindentation by Hodge *et al.*[85] and in specimens tested in tension by Balk *et al.*[86].

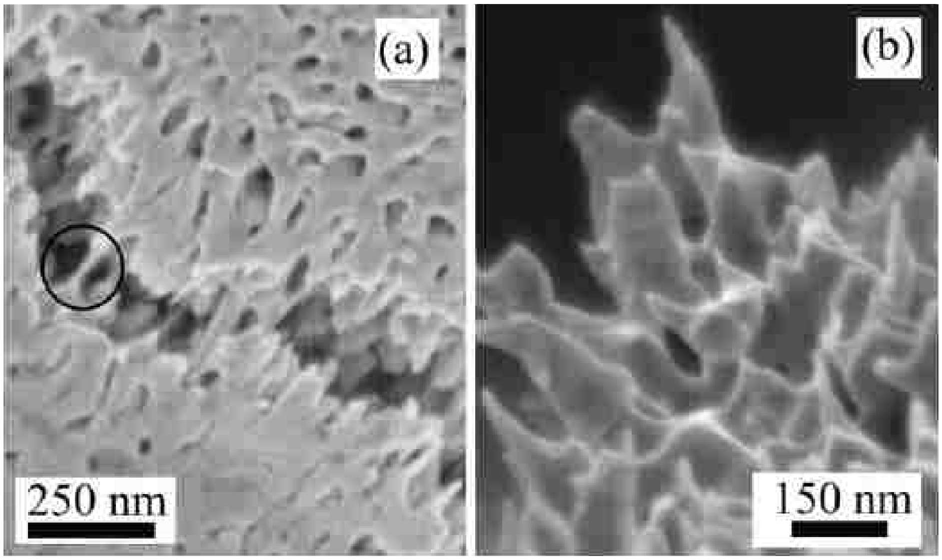

Figure 2.9. SEM images of np-Au fractured by Vickers indentation. a) highly strained ligaments bridging the sides of a crack, b) extensive elongation and necking of the ligament prior to failure. (Reprinted with permission from [75]. Copyright 2005, AIP Publishing LLC)

Direct observation of the plastic deformation of ligaments was made by Balk *et al.* who conducted *in situ* indentation of np-Au in the transmission electron microscope (TEM)[87]. They observed dislocation activity with nucleation followed by gliding of the dislocation along the length of the ligaments towards the nodes of the structure, as seen in Figure 2.10. They also observed the continuous, gradual collapse of a pore, discerning dislocation activity within the adjacent ligaments.

These observations at the microscopic scale indicate that the brittle behavior of np-Au is not due to suppression of dislocation activity within the ligaments. Dislocations can nucleate and move within the ligaments and therefore demonstrate dislocation mediated plasticity at the microscopic scale.

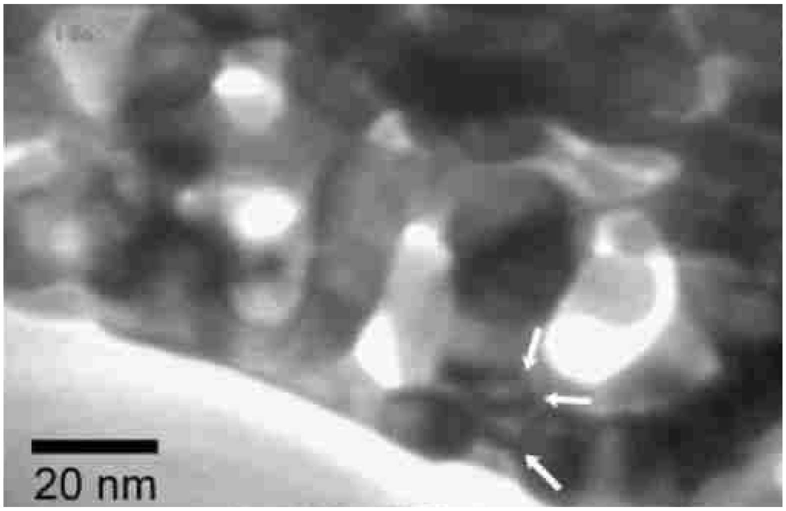

Figure 2.10. TEM still image of np-Au during *in situ* indentation, showing significant dislocation activity in the ligaments. Three dislocations are clearly observable (indicated by white arrows). (Reproduced with permission from Wiley, ©2009 [78])

2.4.2. Deformation behavior at the macroscopic scale

Observing the fracture surface following three-point bending fracture of bulk np-Au at a lower magnification in the SEM, Biener *et al.*[84] determined that the failure was partly inter- and transgranular in nature. Some grains presented strained ligaments throughout the whole surface, while the ligaments in others seem totally undeformed, as if the grain did not carry any load during mechanical testing (see Figure 2.11). It was concluded that rupture in polycrystalline np-Au initiates at the ends of a 2D defects such as an open grain boundary remnant of the original microstructure of the precursor alloy as describe in section 2.2. Crack nucleation is likely to occur on a site subject to larger stress concentration, such as the opposite ends of a grain boundary. Intergranular failure then occurs by propagation of the crack along the open grain boundary until the crack front reaches the surface of another grain at an angle, at which point failure can evolve to transgranular failure or not.

This determination is central in understanding the brittleness of np-Au at the macroscopic scale. Firstly, because the ligaments are microscopically ductile, the weakest part of the sample ruptures plastically, whether it be because of localized stress concentration or structural defect. In the case of a 2D defect, the crack rapidly propagates throughout the defect until it eventually reaches its end. At this time, because of the failure of the weakest regions of the sample, a reduced number of ligaments bear the load applied to the sample, which leads to localized stress increase and rapid plastic failure of the ligaments (transgranular failure). On a macroscopic standpoint, these localized plastic deformation cannot be observed nor detected, and as soon as the weakest part of the sample fails, rupture propagates catastrophically, in a brittle manner. This creates a challenge for macroscopic testing of np-Au, as experimental determination of yield and rupture strengths will be clouded by premature failure of the samples initiating not only within the samples on pre-existing defects, but also on surface defects, as is explained in Chapter 5.

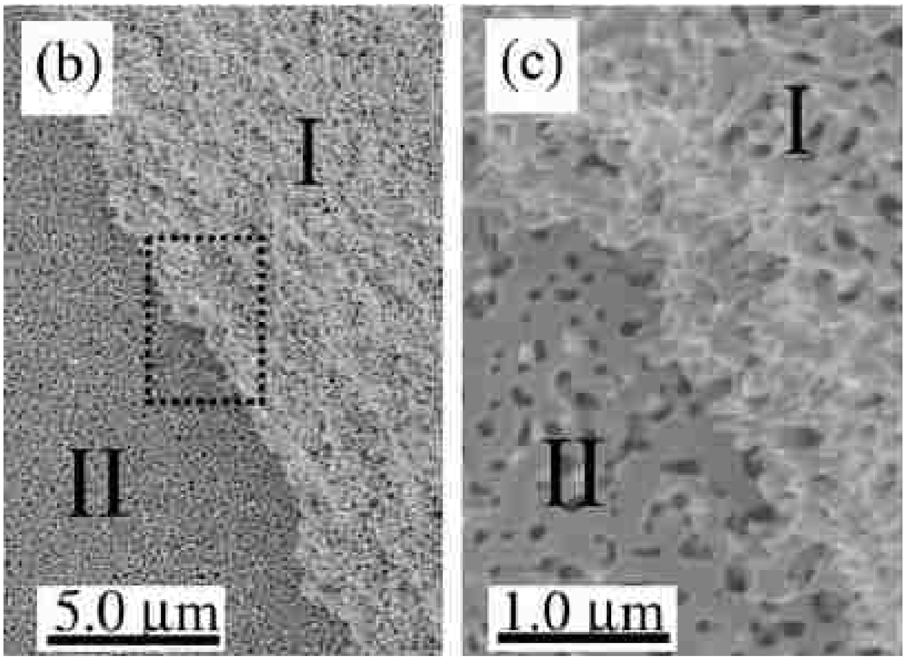

Figure 2.11. SEM image of the fracture surface of np-Au ruptured in three-point bending. Two grains, I and II can be observed. Rupture was transgranular in grain I as indicated by the highly strained ligaments, while rupture was intergranular along grain II, which shows non deformed ligaments. (Reprinted with permission from [75]. Copyright 2005, AIP Publishing LLC)

2.4.3. Mechanical properties of np-Au

As stated above, because of the brittle nature of np-Au, conducting experimental tests to determine its mechanical properties is challenging. Due to its relative ease of implementation, nanoindentation has been preferentially used, on the surface of np-Au samples which were polished beforehand (prior to dealloying). A strong advantage that nanoindentation and uniaxial compression of micropillar present is that testing can usually be conducted within a single grain of the microstructure, therefore preventing any interference of the original alloy microstructure on the test. This is not the case for millimeter-scale specimen tested in tension, compression or bending.

Biener *et al.* measured the hardness of a np-Au sample with relative densities ranging from 0.25 to 0.42 and ligament sizes from 10 to ~100 nm, using nanoindentation (Berkovich indenter tip)[88], [89]. Hodge *et al.* reported nanoindentation testing results from experiments on np-Au with relative densities between 0.20 and 0.42 and ligament sizes ranging from 5 to 900 nm[90]. All papers reported an indentation size effect during which the mean contact pressure exponentially decays with increasing depth, until it reaches a plateau, typical of a porous material for which the maximum applied stress normalized by the pores strength is related to the indenter size compared to the porous structure cell size[91]. Mean contact pressure p_c is generally used in nanoindentation and is a hardness value calculated with $p_c = P/A(h_c)$ where P is the load applied and A is the projected contact area at depth h_c determined from the tip calibration (diamond area function). Another way to calculate hardness is to use the area of the residual print left by the indenter after the test, i.e. $H = P_{max}/A_p$ with P_{max} and A_p the maximum load applied and the residual print area, respectively. For porous materials, the plateau value eventually reached by the mean contact pressure with increasing depth usually merges with the hardness values calculated using the area of the residual print. Therefore, the latter value is commonly used and reported for nanoindentation on np-Au. For low density polymeric and metallic foams, it has been observed that the hardness value is almost equivalent to the yield strength because of a lack of lateral expansion away from the indenter during testing[91]–[94]. Therefore, the hardness values obtained by nanoindentation are typically directly reported as the yield strength values for np-Au[88]–[90], [95]. Another method to calculate yield strength based on nanoindentation data was used by Lee *et al.*, where finite element techniques taking into account substrate effects and densification of porous material were used[96]. Experimentally determined elastic modulus, residual stress and sample thickness were used to feed the model, and a fixed work hardening coefficient was assumed to describe the deformation behavior. Using the Oliver-Pharr method, the Young's modulus can also be calculated from the nanoindentation curves, although it has not been explicitly reported in most papers testing np-Au by nanoindentation. Yield strengths and Young's modulus values determined by nanoindentation and reported in the literature are tabulated in Table 2.1. Vickers microhardness tests have also been conducted to measure the yield strength of np-Au. Jin *et al.* measured a Vickers Hardness of 27 MPa for a np-Au sample with a relative density of 0.26 and ligament size of 55 nm.

Other mechanical testing methods involving indenters have been used, mainly deflection tests. Lee *et al.* [73,74] fabricated dogbone shaped specimens from gold leaves ($Au_{37.4}Ag_{62.6}$ at%) glued on silicon wafers by electron beam lithography. They removed the silicon around and underneath the gage of the specimen by reactive ion etching to obtain freestanding np-Au specimens, as shown in Figure 2.12a. They conducted deflection tests using a nanoindenter with a Berkovich tip, by pushing the gage towards the substrate until rupture or contact between the specimen and the substrate. Elastic modulus values were determined by comparing measurements to an analytical model (bending of a double cantilever anchored at its ends and loaded at its center). They reported an average measured elastic modulus of 8.8 GPa.

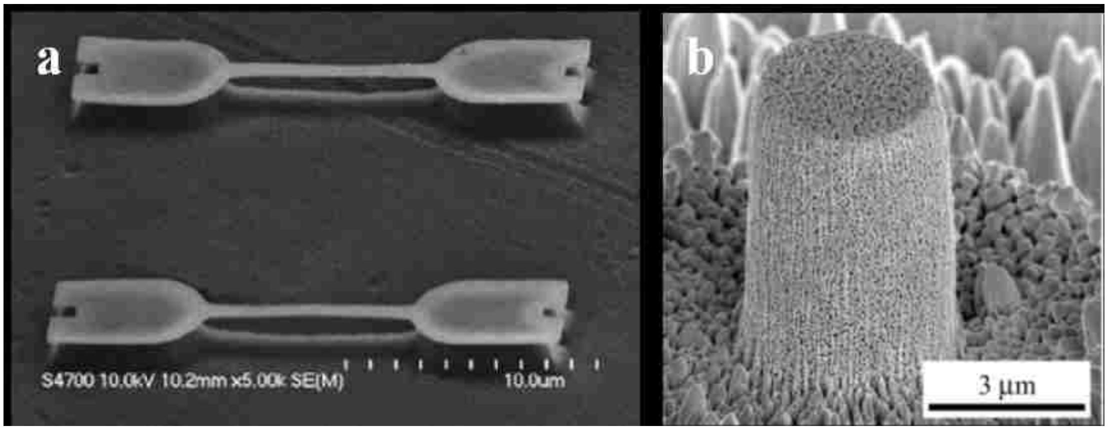

Figure 2.12. a) Freestanding np-Au specimens created from a gold leaf on silicon substrate by electron beam lithography and undercut by reactive ion etching (reprinted from[96] with permission from Elsevier); b) np-Au micropillar create using a focused ion beam, after dealloying (reprinted with permission from[89]. Copyright 2006 American Chemical Society).

Table 2.1. Nanoindentation results reported in the literature for np-Au

Relative density	**Ligament size [nm]**	**Loading rate [μN/s]**	**Load range [μN]**	**Yield strength [MPa]**	**Young's modulus [GPa]**	**Ref**
0.25	10	500	200-1800	171 ± 35	-	[89]
0.25	25			53 ± 9		
0.25	50			33 ± 2		
0.42	100	250	200-1800	145 ± 11	11.1 ± 0.9	[88]
0.42	100	500	200-4000	190[a]	-	[90]
0.42	40			247[a]		
0.35	50			196[a]		
0.30	50			71[a]		
0.30	40			83[a]		
0.30	60			70[a]		
0.30	60			58[a]		
0.30	160			44[a]		
0.30	480			27[a]		
0.30	900			16[a]		
0.25	50			54[a]		
0.25	10			176[a]		
0.25	200			36[a]		
0.20	20			69[a]		
0.35	162	500	2000-4000	-	2	[98]
0.30	5	up to 267	up to 800	990 ± 180	-	[95]
0.30	29			740 ± 120		
0.30	126			520 ± 140		
0.352	20-40	-	-	111 ± 35[b]	13.2 ± 3.4	[96]
0.305	30-40	-	~ 100	~ 400	-	[99]
0.30	54	500	2000-5000	~53[c]	1.83 ± 0.08	[100]

[a] values extracted from Fig.5 in[90]

[b] values determined from analysis of experimental nanoindentation data with finite element model, including assumption of a work hardening coefficient

[c] value extracted from Fig.3d in[100]

Uniaxial compression of np-Au micropillars is another technique that has been reported in the literature. Typically, a pillar with diameter between 1 and 5 µm and aspect ratio between 2 and 3 (height to diameter) is milled in a np-Au bulk sample using a focused ion beam (FIB), as seen in Figure 2.12b. Compression testing is conducted using a nanoindenter with a flat tip[89], [101]. Yield strength and Young's modulus values can be directly measured and Volkert *et al.*[101] reported a yield strength of 100 MPa and a modulus of 7 GPa for np-Au with a relative density of 0.33 and a ligament size of 15 nm. Biener *et al.*[89] reported a yield strength of 90 MPa for a np-Au micropillar of relative density 0.3 and ligament size of 40 nm.

Mathur and Erlebacher[102] used another technique to determine the Young's modulus of np-Au. Np-Au films were created from gold leaves and placed on a compliant substrate. Strain was induced in the np-Au leaf by deforming the substrate, and the morphology of the buckling of the film (wavelength of the buckles assuming a sinusoidal waveform) is related to the elastic modulus. The elastic modulus was found to rise rapidly for ligament sizes below 12 nm, from 6-12 GPa between 40 and 12 nm to 40 GPa for 3 nm wide ligaments. This surprising observation might have been caused by the testing method. Since determination of the modulus relies on buckling of the sample, hence bending of the structure, smaller ligaments not as stiff in bending might have led to higher modulus values determination.

More traditional mechanical testing has also been reported in the literature. Balk *et al.*[86] conducted tensile and compression test on millimeter-scale, polycrystalline np-Au dogbone shaped specimens. Elongation of the specimens was tracked by digital image correlation (DIC) based on images taken along the test. They reported an average yield strength of 11 ± 2 MPa in tension and 15 MPa in compression for np-Au samples with a relative density of 0.3 and ligament size between 20 and 35 nm. It is to be noted that yield and fracture strength were found to be equal for tension tests, as specimens are macroscopically brittle. Also, it was found that failure initiated at the radius between the ends ("ears") of the specimens, so that the reported fracture strengths probably represented a lower bound estimate. An average Young's modulus of 3 GPa was measured during tension and compression. Jin *et al.* also conducted compression tests of millimeter-scale np-Au samples[103], with rectangular cuboid shapes. They reported yield strengths of 7.5 and 27 MPa for sample with relative densities of 0.26 and 0.275 and with ligament size of 55 and 15 nm, respectively.

All reported yield strengths values are reported in Figure 2.13.

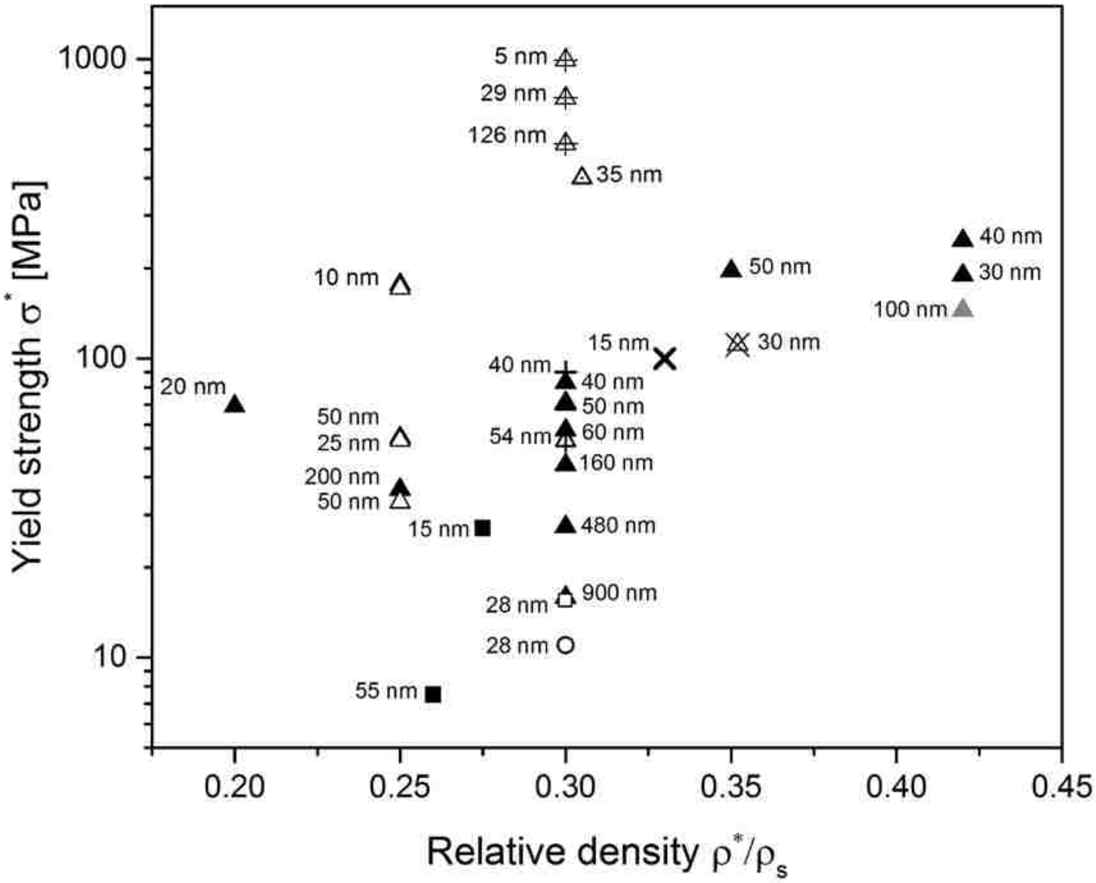

Figure 2.13. Yield strengths reported for np-Au in the literature, determined using different measurement techniques: nanoindentation (black filled triangles adapted from [90], grey filled triangle adapted from[88], white open triangles from[89], open triangles with vertical crosses from[95], open triangle with diagonal cross from[96], open triangle with dot from[99], open triangle with vertical line from[100]); compression testing of millimeter-size samples (filled squares from[103], open square from[86]); tensile testing of millimeter-size samples (open circle from[86]); micropillar compression (diagonal cross from[101], vertical cross from[90]).

2.4.4. Scaling relations for porous materials

Relations that relates the mechanical properties of a porous material to those of its bulk, dense counterpart have been proposed by Gibson and Ashby[94] and are widely used for all types of porous materials, including np metals and np-Au in particular. These relations, known as scaling relations, have been derived using simple beam bending theory on a simplified structure representing the cell of a porous material. This simplified structure assumes cubic pores delimited by straight, thin struts of length l with square cross-sections, as shown in Figure 2.14.

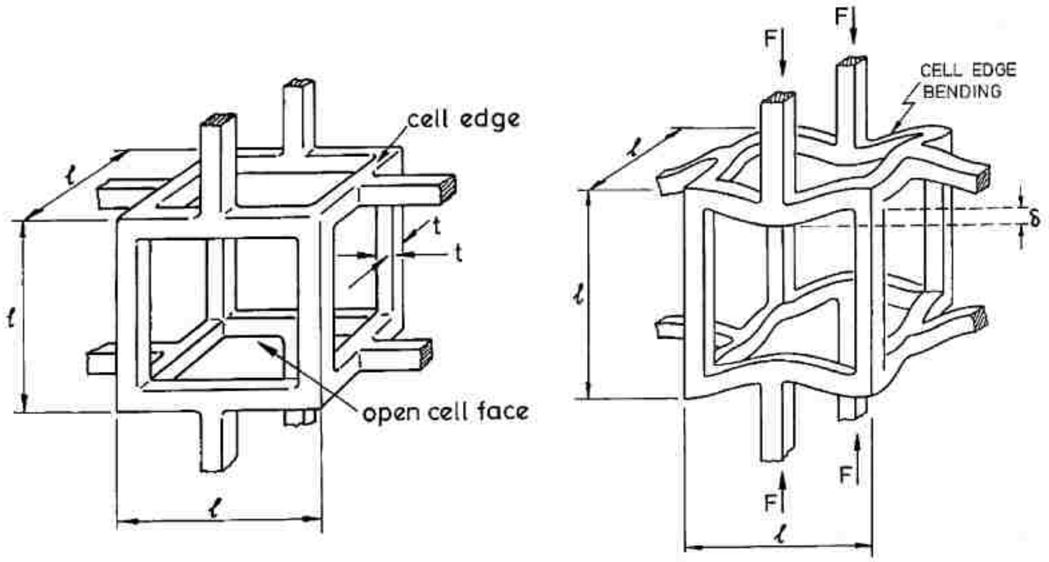

Figure 2.14. Schematic of a cell in Gibson and Ashby's model. The cell is cubic, with ligaments of length l and thickness t. (From[94], reprinted with the permission of Cambridge University Press)

For a beam with rectangular cross-section

$$I = \frac{bh^3}{12} \qquad \text{Equation 2.1}$$

where I is the area moment of inertia of the beam, b is the width of the beam and h is the height. In the case of a square cross-section, as it is in Gibson and Ashby's model, Equation 2.1 becomes

$$I = \frac{t^4}{12} \qquad \text{Equation 2.2}$$

where t is the strut thickness. For a beam loaded at its center with a force F, the deflection at midpoint is given by

$$\delta = \frac{Fl^3}{48EI} \qquad \text{Equation 2.3}$$

where l is the length and E is the Young's modulus of the beam, respectively. The force F being applied to the whole porous cell, stress is given by

$$\sigma^* = \frac{F}{l^2} \qquad \text{Equation 2.4}$$

where $\sigma^*$is the stress on the porous material. By re-arrangement of the previous equations, and with $\varepsilon \propto \delta/l$ it can be seen that

$$\varepsilon \propto \frac{\sigma^* l^2 l^3}{lEt^4} \qquad \text{Equation 2.5}$$

which leads to

$$E^* = \frac{\sigma^*}{\varepsilon} \propto E\,\frac{t^4}{l^4} \qquad \text{Equation 2.6}$$

where E^* and E are the Young's moduli of the porous material and of the corresponding dense material forming the structure. Also, because of the geometry of the cell used for this model, the relative density can be calculated by dividing the volume of solid by the total volume of the cell, so that

$$\frac{\rho^*}{\rho_s} = \frac{12lt^2}{4l^3} \propto \left(\frac{t}{l}\right)^2 \qquad \text{Equation 2.7}$$

Combining Equation 2.6 and Equation 2.7, Gibson and Ashby's scaling law for the Young's modulus of porous materials can obtained and written as

$$\frac{E^*}{E_s} = C_1 \left(\frac{\rho^*}{\rho_s}\right)^2 \qquad \text{Equation 2.8}$$

where C_1includes all the constant of proportionality. Using experimental data found in the literature for porous materials (mainly polymers) with relative densities between 0.01 and almost up 1, a value close to unity was determined for C_1. Consequently, it is commonly assumed that $C_1 = 1$.

In a similar way, still assuming bending as the primary mode of deformation, the yield strength of a porous structure can be determined by considering the plastic collapse of a cell. This happens when the moment exerted by the applied force at the center of the cell's edge becomes larger than the plastic moment. The plastic moment can be written as

$$M_p = \sigma_{ys} Z_p = \sigma_{ys} \frac{bh^2}{4} \qquad \text{Equation 2.9}$$

where Z_p is the plastic section modulus and σ_{ys} is the yield strength of the material of the cell edges, in dense form. For a square cross-section, Equation 2.9 becomes

$$M_p = \sigma_{ys} \frac{t^3}{4} \qquad \text{Equation 2.10}$$

The maximum bending moment can be written as

$$M_p \propto Fl = \sigma_{ys}^* l^3 \qquad \text{Equation 2.11}$$

where σ_{ys}^* is the yield strength of the porous material. Combing Equation 2.10 and Equation 2.11

$$\frac{\sigma_{ys}^*}{\sigma_{ys}} \propto \frac{t^3}{l^3} \qquad \text{Equation 2.12}$$

which becomes

$$\frac{\sigma_{ys}^{*}}{\sigma_{ys}} \propto \left(\frac{\rho^{*}}{\rho_{s}}\right)^{3/2} \qquad \text{Equation 2.13}$$

For simplification, Equation 2.13 can be re-written and Gibson and Ashby's scaling relation for porous materials' yield strength becomes

$$\frac{\sigma^{*}}{\sigma_{s}} = C_{2}\left(\frac{\rho^{*}}{\rho_{s}}\right)^{3/2} \qquad \text{Equation 2.14}$$

where σ^{*} and σ_{s} are the yield strength of the porous material and of the material in its dense form. The pre-factor C_2 contains all the constants of proportionality and was determined, based on fitting of experimental data, to have a value of 0.3. It is of importance that the scaling relations have been derived assuming deformation of porous materials dominated by bending of the edges of the cell. However, although the model was found experimentally to work relatively well with sample of higher relative densities, extension/compression of the edges aligned with the direction of the force start contributing in a non-negligible way to the overall behavior of the porous material for relative densities larger than 0.1 as described by Warren and Kraynik[104].

Nonetheless, the scaling relations have been widely used in the literature for np-Au. Biener *et al.*[88] measured a np-Au yield strength value of 145 MPa for a relative density of 0.42. At that relative density and assuming a yield strength value of 200 MPa for gold, the scaling relation predicts a porous structure's yield strength of 16 MPa, almost 10 times smaller than the experimentally determined value. However, if the experimental value is assumed to describe np-Au properly, then the same scaling relation predicts a ligament strength of nearly 1.8 GPa, approaching the theoretical value for the yield strength of gold[105]. Similarly, in another paper[89], ligament strength values between 880 MPa and 4.6 GPa were calculated for samples with decreasing ligament sizes (50 nm down to 10 nm). Results from micropillar compression led to a calculated ligament yield strength value of 1.5 GPa for 15 nm wide ligaments, based on a measured yield strength of 100 MPa[101]. However, using the scaling relation for this particular sample, the relative density of 0.36 would dictate a maximum yield strength of 13 MPa for np-Au. Similar observations have been made for the results obtained in tension and compression[86], [103]. These discrepancies arise from the fact that the scaling law for yield strength do not include a ligament size parameter. Therefore, the material constituting the edges of the pores in the structure is assumed to have identical mechanical properties whether its dimensions are at the nano-, micro- or macro- scale. Consequently, it is now generally accepted that the scaling relation for yield strength is not valid in the case of np-metals, and that a ligament size effect contribution has to be represented in a new, updated scaling relation. Hodge *et al.* have proposed a new relation that incorporates a Hall-Petch-type equation aimed to describe this ligament size effect[90]:

$$\sigma^* = C_s \left[\sigma_0 + k l^{-\frac{1}{2}}\right] \left(\frac{\rho^*}{\rho_s}\right)^{\frac{3}{2}} \qquad \text{Equation 2.15}$$

where C_s is a fitting coefficient, σ_0 is the yield strength of bulk, dense gold, k is the Hall-Petch-type coefficient for gold at the scale of interest (10 nm to 1 μm) and l is the ligament size.

Because of the few reported values for the Young's modulus, the corresponding scaling relation (Equation 2.8) as not been the focus of many comparisons with experimental data. Volkert and Lilleodden[101], as well as Biener *et al.*[88] reported results close to the predictions from the scaling relation, whereas Balk *et al.*[86] reported modulus values much lower than half the predicted value.

Chapter 3 : Materials and experimental methods

3.1. Film deposition by magnetron sputtering

Sputtering is a physical vapor deposition (PVD) technique widely used to produce thin films on substrates. In particular, magnetron sputtering is widely used as it allows higher deposition rates. A gaseous plasma, is created in an evacuated chamber and is accelerated towards the material to deposit, commonly referred to as the target. The target is set at a negative potential using either a DC or RF power supply configuration. This bombarding plasma erodes the target, and the ejected particles (atoms or clusters of atoms) travel to the surface substrate on which they progressively create a thin film.

For the present work, sputtering of AuAg films was performed using magnetron sputtering with a ATC Orion system from AJA International, Inc., using a DC power supply for silver and a RF power supply for gold deposition. Base pressure in the sputtering chamber (vacuum level before argon was introduce in the chamber) was below 10^{-6} torr. Substrates were rinsed with alcohol (either ethanol or iso-propy alcohol) and de-ionized water prior to their introduction in the vacuum chamber. Further cleaning of the substrate, usually called substrate biasing, was performed prior to deposition. During substrate biasing, the gaseous plasma bombards the substrate instead of the target, removing any surface contaminant. An interlayer of tantalum (~10 nm) was deposited directly on the substrate, enhancing adhesion of the films. More details about the various films used during this work will be given in the respective chapters.

3.2. Dealloying

Dealloying of the AuAg alloys thin films was performed by simple immersion with mild agitation (free dealloying), in solutions of nitric acid HNO_3 (Mallinckrodt Chemical – 70% stock solution) and de-ionized water. Dealloying of bulk AuAg sample was conducted by a combination of free and electrochemical dealloying steps in nitric acid, under mild agitation, to minimize volume contraction and prevent cracking[53]. Electrochemical dealloying was performed using the setup schematically drawn in Figure

3.1. The sample to be dealloyed, in this case the AuAg precursor alloy, was immersed in a solution of HNO_3 and connected to the positive end of a DC power supply (Extech Dual Tracking 382285) through a conductive mesh. A platinum wire in a coil shape acted as the counter-electrode and was connected to the negative end of the power supply. An analog, precision amperemeter (range 0 to 1 mA, 20 µA graduations) was attached in series and provided real-time display of the current flow in the circuit, thus allowing monitoring of the dealloying current.

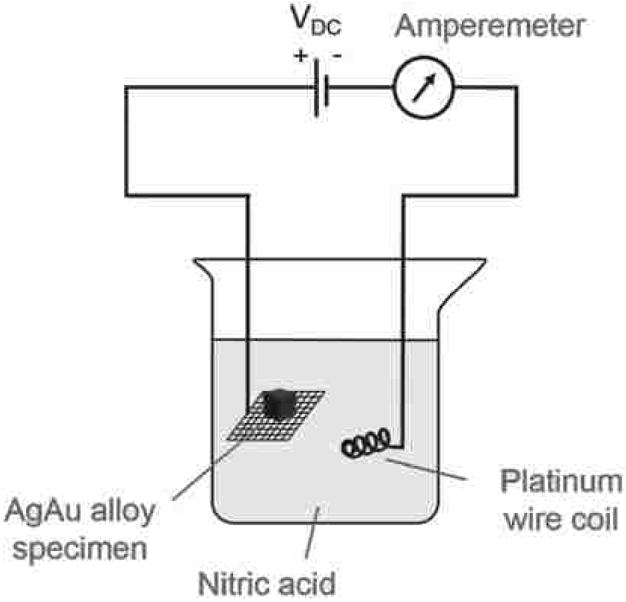

Figure 3.1. Schematic representing the electrochemical dealloying setup used for this work.

Removal of the sacrificial element (silver) during dealloying was tracked by measuring the sample's mass loss with a precision scale (Mettler AE 260 DeltaRange®). Care was taken to rinse and dry the sample before mass measurement to minimize false readings because of liquid trapped in the pores of the structure. Manipulation being difficult because of the high fragility of np-Au, samples were typically scooped using flat tweezers or were simply dropped in beakers containing solution, with a net to catch them during the slow fall. After dealloying, samples were carefully rinsed in de-ionized water then immersed in iso-propyl alcohol for a minimum of 24 hours. After rinsing, samples were left to dry at air and stored in petri dishes or membrane boxes, making sure not to have the surfaces in contact with any abrasive material. Np-Au being so fragile, regular wipers (Kimwipes, Kimtech Science) were found to be abrasive, so that membrane boxes or paraffin film (Parafilm® M) was generally used to protect the samples. Because of its natural resistance to oxidation, no further storage precautions were taken.

3.3. Characterization

3.3.1. Optical microscopy

Observation of the samples at the macroscale and down to the imaging of features of tens of micrometers was conducted using an Olympus BX 41 compound microscope equipped with objectives 5x, 10x, 20x and 50x. Acquisition of the images was possible using an Olympus CCD camera (Q-Color3™, 3.2 MP). A compound microscope is an optical microscope with lenses collecting lights reflected by the surface to observe and creating a virtual, enlarged image of it. Because visible light is used to carry information, the minimum dimensions of the features that can be observed in optical microscopy are in the hundreds of nanometers, at best. Although optical microscopy is a powerful tool to image microstructure, its resolving power is not high enough to image np structures. Consequently, np-Au structure at the nanoscale was observed using electron microscopy.

3.3.2. Electron microscopy

Unlike optical microscopy, electron microscopy relies on electrons instead of visible light to carry the information. This allows electron microscopy to image much smaller features, down to a few nanometers for scanning electron microscopy, and below 1 nm for transmission electron microscopy. A scanning electron microscope (SEM) uses a focused electron beam that scans the surface to observe. Different types of electrons are re-emitted from the sample: secondary electrons (SE) are attracted by a specific detector and the image is reconstituted based on the intensity detected at each point on the surface scanned by the beam; backscattered electrons (BSE) are collected by another specific detector, and are used to create an image with grayscale colors based on the atomic numbers of the elements constituting the sample (commonly called Z-contrast). Transmission electron microscopes (TEM) also use a beam of electrons, but the beam goes through the sample and is projected onto a phosphor screen (or a digital camera). For this technique, samples have to be very thin (electron transparent) and more preparation is usually required than for SEM observation. However, in the case of thin films, samples can be directly suitable for TEM observation as long as the substrate is locally thin enough. In addition to high magnification, TEM offer the possibility to observe the diffraction pattern created by diffraction of the electrons (from the beam) by the atoms of the sample, acting as a diffraction grating. This technique, called selected area diffraction (SAD) allows access to valuable information about the crystallinity of the sample.

High-resolution imaging of np-Au was performed on a Hitachi S-4300 SEM with field emission gun (electron source) and on a JEOL 2010F TEM with field emission gun (electron source), at the Electron Microscopy Center (EMC) of the College of Engineering at the University of Kentucky.

3.3.3. Elemental analysis

When a beam of electrons interact with a sample in a SEM, secondary and backscatter electrons are not the only entities emitted from the sample. When an incident electron has enough energy to eject one electron of an atom in the sample, the atom is in an excited state. To return to an unexcited state, another electron from the atom (from a higher energy, outer electron shell) fills the newly created hole in the inner shell. This electron migration releases some energy in the form of an x-ray, with energy characteristic of the atom. This x-ray is then collected by a specific detector, an x-ray energy-dispersive spectroscopy (EDS) detector which can discretize the energy of incoming x-rays. Consequently, the x-rays collected are characteristic of the sample and an elemental composition can be calculated.

During this work, a Princeton Gamma Tech SDH071-1045 EDS detector attached to a Hitachi S-4300, an Evex detector attached to a Hitachi S-3200, as well as a Bruker XFlash® 5010 EDS detector attached to a Zeiss EVO MA10 SEM, were used. Care was taken to use an appropriate acceleration voltage (minimum of 20 kV) for the electron beam, insuring sufficient energy of the incident electrons. Quantitative analysis to determine composition of the samples was performed using the L peaks for silver and the M peaks for gold as the L peaks for gold was found not to be sufficiently excited at 20 or 25 kV which was leading to error in quantification.

3.4. Anelastic relaxation: damping measurements

3.4.1. Internal friction

Under static or quasi-static load, metals are showing elastic properties, meaning that at low strains, deformation resulting from application of a load appear instantaneously. Upon removal of the load, the material immediately deforms back to its initial dimensions. This linear elastic behavior can be expressed mathematically by Hooke's law, for which there is no time dependency:

$$\sigma = \varepsilon E \qquad \text{Equation 3.1}$$

with σ the stress applied to the material, ε the resulting strain under that load and E the Young's modulus of the material. However, under dynamic load, a lag can appear between application of the load and the apparition of the corresponding strain. This behavior appears in the elastic regime, meaning that upon removal of the dynamic load, the sample comes back to its initial dimensions (no permanent deformation). This time-dependent behavior is named anelasticity and although it appears in metals, it is usually minimal and is neglected.

Under cyclic loading, such as a controlled vibration (used in the present work), the phase difference δ between stress and strain gives rise to a certain amount of energy dissipated, for each cycle. This energy can be written as

$$\Delta E = \oint \sigma . d\varepsilon \qquad \text{Equation 3.2}$$

with ΔE the energy dissipated per cycle, and σ and ε the stress and strain on the material. For every load cycle, some energy is stored and some is dissipated (lost). The ratio of the dissipated energy to the stored elastic energy can be written as

$$\frac{\Delta E}{E_{stored}} = 2\pi \frac{M_2}{M_1} = 2\pi \tan \delta \qquad \text{Equation 3.3}$$

with M_1 and M_2 the storage and loss moduli, respectively. For very small values, $\tan \delta \cong \delta$, and δ is typically used to characterize the damping capacity of the material, and is called the internal friction or the damping ratio. Because of the similarities with the quality factor Q used in electrical engineering, which is the reciprocal of the phase angle, δ is often written as Q^{-1} and sometimes referred to as the inverse quality factor. The behavior of anelastic materials can generally be described using the standard linear solid model. Using this model, it can be shown that, for small δ

$$Q^{-1} = \delta \cong \tan \delta = E_s \frac{\omega\tau}{1 + (\omega\tau)^2} \qquad \text{Equation 3.4}$$

with E_s the relaxation strength, ω the angular frequency of the cyclic load and τ the mean relaxation time. It can be deduced from Equation 3.4 that a maximum damping ratio is obtained for $\omega\tau = 1$. Therefore, for a particular combination of frequency and temperature, damping in the material will be maximized. Finding this maximum damping ratio can be done by either fixing the temperature and measuring the damping ratio for various frequencies, or fixing the frequency and varying the temperature. For both methods, a peak in damping ratio will be observed when the conditions for maximum damping are met, called a relaxation peak or sometimes a Debye peak.

If the internal friction mechanism from which damping of the vibration arises is thermally activated, its activation energy H is related to the relaxation time τ by

$$\omega\tau = \omega\tau_0 \exp\left(\frac{H}{kT}\right) \qquad \text{Equation 3.5}$$

with τ_0 the pre-exponential time factor and k the Boltzmann constant. Identifying the maximum damping ratio for multiple conditions (for different temperatures or for different frequencies) allows the construction of an Arrhenius plot, after which the internal friction mechanism can be identified from the calculated activation energy.

3.4.2. Measurement system

Measurements were conducted on a home-built system, originally donated by Prof. Nix from Stanford University, later modified to accommodate low temperature cooling. The system consists of a vacuum chamber, evacuated by a turbomolecular pump backed by a mechanical pump, a laser vibrometer and a heating/cooling copper stage. Pressure during testing was kept below 9x10^{-5} torr, insuring air in the chamber was not influencing the damping measurements. A controlled, cyclic load was applied in the form of a vibration, induced in cantilever-shaped samples (details of the samples fabrication will be given in Chapter 4). This vibration was induced by electrostatic forces: the samples stage is connected to the electrical ground, while the sample is connected to an AC power supply. The alternating sign of the potential created attractive or repulsive forces at the surface of the sample, leading to deflection. The damping ratio is determined from the free decay of the vibration after the excitation voltage is removed. Amplitude of the oscillations during this free decay is measured in real time by a laser Doppler vibrometer (Polytec OFV 353 with OFV 2200 controller). Fitting of the envelope of the signal is shown in Figure 3.2 and allows calculation of Q^{-1}. A schematic of the damping system and its components as well as a photograph of the system are shown in Figure 3.2 and Figure 3.3.

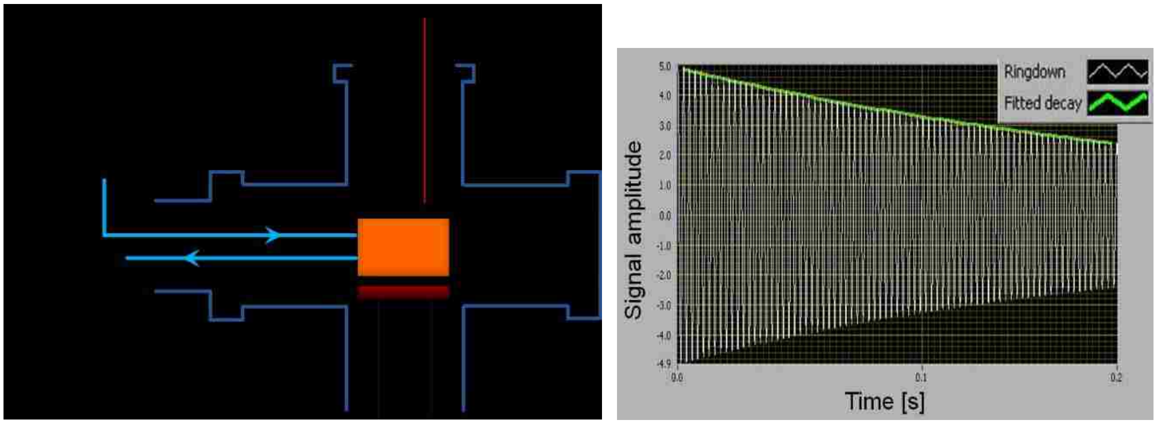

Figure 3.2. Damping system's configuration. (left) schematic of the system's elements (cross-section view), (right) schematic representing the free decay of the vibration induced by electrostatic forces in a cantilever shaped sample.

To maximize the magnitude of the sample's deflection, the applied AC signal frequency has to be close to the resonant frequency of the sample. Therefore, to cover a wide testing range of frequencies, multiple samples with different geometries and masses, hence resonant frequencies, were used. Consequently, out of the two methods described in section 3.4.1 to determine the maximum damping ratio, fixing the frequency and varying the temperature was used. Heating of the sample was made possible by placement of a ceramic heating element under the stage, controlled by feedback from a thermocouple placed in contact with the copper stage. Cooling of the stage, and therefore of the sample, was realized by flowing liquid nitrogen through the stage. Measurement of the sample's temperature was possible with a fine gage thermocouple glued with thermally conductive silver paint on a similar sample placed next to the sample being tested. Attaching the thermocouple directly onto the sample being tested was found to prevent proper testing, since it interferes with the vibration. Control of the system, as well as temperature and laser vibrometer data recording was made using a custom written Matlab® code, originally created by Dae-han Choi at Stanford University during his doctorate work, and later optimized by Jens Steiger from the Karlsruhe Institute of Technology (KIT) during his diploma thesis work at the University of Kentucky.

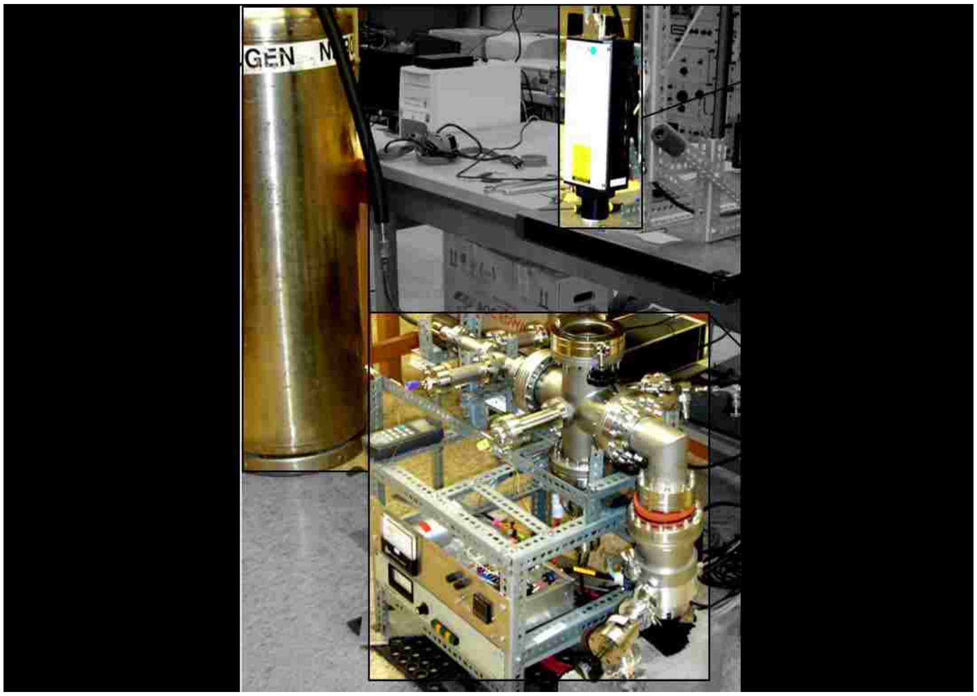

Figure 3.3. Photograph of the damping system, showing the main components of the setup.

3.5. Tension/compression testing of millimeter-scale specimens

Two systems were used for this work, both capable of quasi-static tensile and compression testing of small-scale specimens (millimeter-size). For tensile and compression testing of polycrystalline and single crystalline dogbone shaped np-Au specimens, the experiments were conducted on a pre-existing system at the Karlsruhe Institute of Technology (KIT, Germany) in collaboration with Dr. Chris Eberl and his doctorate student at the time, Tobias Kennerknecht. For compression testing of polycrystalline np-Au specimens with rectangular cuboid shape, experiments were conducted at the University of Kentucky on a custom-built system inspired by the one in KIT. As a result, both systems share the same type of design and components as will be describe in this section.

The specimen, dogbone shaped for tensile testing and cuboid for compression, sits on custom-made grip supports. Grip supports are made out of stainless steel to limit system compliance, or aluminum if the mass of the grip is a concern (moment induced in the piezoelectric actuator and on the load cell). For tension tests, the specimen is held by grips specifically designed for its geometry, as shown in Figure 3.4 on the UK system. The grips were extracted from hard stainless steel (17-4 PH is used on the UK system) by wire electro-discharge machining (EDM) to obtain the desired geometry and smooth edges, in a hard material. For compressions tests, grips were made out of stainless steel with a narrow ledge making a 90 degrees angle with the surface of contact. The latter surface was polished after machining to minimize surface roughness. To ensure that the specimen is making good contact with the wall and is not sitting on the fillet left by machining, two fine gage (AWG 25) plastic wires were placed in the fillet to elevate the specimen.

For both tension and compression testing, the deformation is solely applied by a piezoelectric actuator, with closed-loop displacement control (positioning controlled with real-time feedback from the actuator). Rough positioning of the specimen before testing is made by the use of a precision stepper linear actuator, also with closed-loop configuration. The stepper actuator pushes a plate on which the piezoelectric actuator sits, and there is no contact between the two actuators. Load measurements is carried out by using an in-line miniature load cell, attached on and aligned with the axis of the piezoelectric actuator and the center of the specimen’s gage. The amplitude of the signal generated by the load cell being low, a signal amplifier is used before data acquisition. The load cell excitation voltage is supplied by an external, dedicated DC power supply. The load cell calibration is verified periodically (typically between series of tests) with calibration standard weights attached to the load cell in a vertical configuration. A load cell calibration curve is determined, which shows the load cell output as a function of the load applied. The calibration factor is used after test during post-processing to calculate load values. Images of the specimen are taken along the test a fixed time interval (typically 1 sec or less) using a compound optical microscope equipped with a high resolution digital camera. Accurate determination of the strain is possible using digital image correlation (DIC). DIC allows non-contact strain measurement by tracking pixels shift from a reference region. The pixels position for each image is compared to the position on the previous image, therefore allowing direct determination of the true strain. DIC can also track the lateral displacement of the specimen’s gage, thus giving the possibility to determine Poisson’s ratio. A DIC code written for MATLAB®[106] was used to determine true strain values. The system is assembled on an optical table to minimize vibrations from the environment. Vibrations can have a negative effect by impacting load recording and imaging of the specimen.

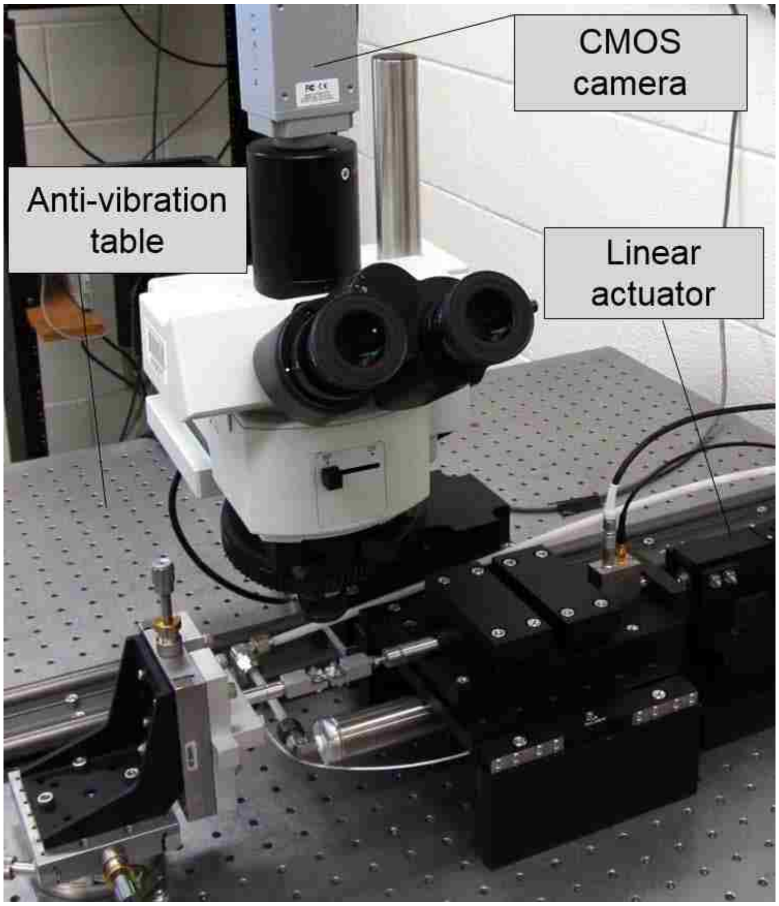

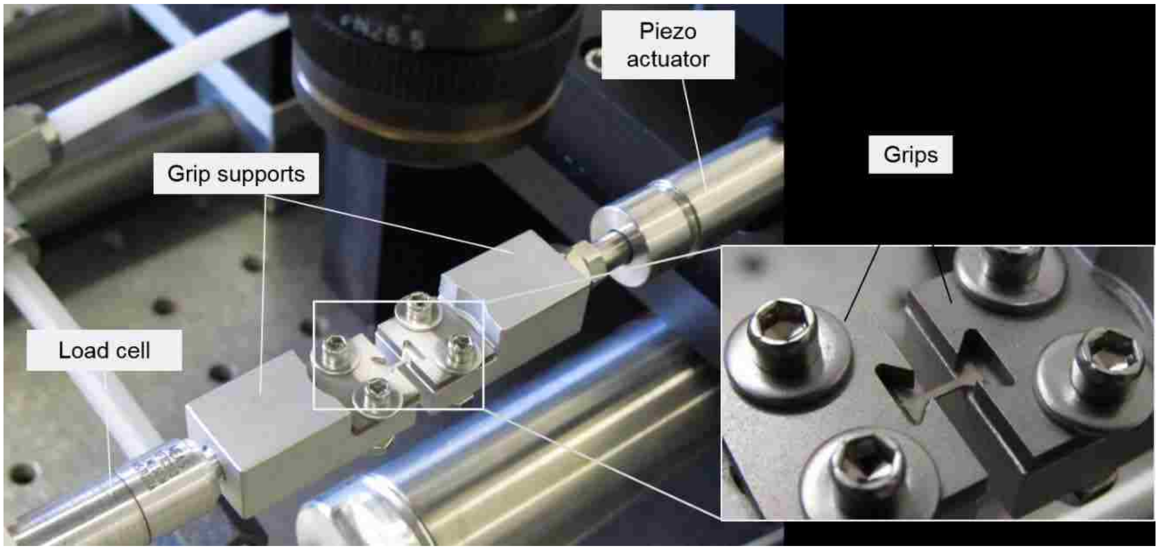

Figure 3.4. Photographs of the small-scale testing setup at UK, in tensile testing configuration. (top) overview of the system, (bottom) close-up showing the grips and the positioning of a tensile testing, dogbone shaped specimen.

For fast and reliable data acquisition, both systems rely on a dedicated programmable controller, controlled through a human-machine interface, here a graphical user interface (GUI). The KIT system uses LabVIEW™ on a Windows® OS to program and control an onboard field-programmable gate array (FPGA) chip board. The UK system uses a programmable logic controller (PLC) controlled by Unity Pro M on a Windows® OS computer. Both designs are similar in the sense that the configuration is intended to separate automation of the machine from the tasks of the computer's processor. Therefore, potential lag in the testing setup automation is greatly reduced, as a dedicated processor is in charge of machine control (whereas the computer's processor has to run tasks in the OS). In both design, testing parameters are entered by the operator in the GUI which is transferred to the programmable controller. During the test, even though parameters (such as actuators velocity or datapoint per sec) and signals (load cell value) can be modified or monitored in real time, the architecture of the programming is fixed, and acquisition is performed by the controller, not the computer. Details of the GUI, programming and electronics schematics for the UK system are given in Appendix B through D.

The model of the components used on each system, as well as some of their specifications, can be found in Table 3.1 and Table 3.2. It can be seen that absolute positioning resolutions for the linear actuators are better for the KIT system and that the cameras and load cells are identical. Because real displacements applied by the piezoelectric actuator are tracked by DIC during post-processing, the absolute value of the real-time positioning is not critical. Rough positioning of the specimen in the grips prior to testing also does not necessitate extreme absolute precision. Therefore the choice was made to select a piezoelectric actuator model with reduced absolute precision, but with greater range of motion (100 vs 60 µm) to accommodate long, but still accurate, displacements. The load cell and the camera being the devices directly used to acquire information about the test, choice was made to select high precision devices identical to the components on the KIT system.

The machine controllers on the two systems both have their advantages and drawbacks. The FPGA card is capable of more operations per second than the PLC (operations at 40 MHz vs 8.3 MHz), although speed limitations for the tests of interest are in the process and acquisition of signals, not in computation. The FPGA provides much higher speed in digital output and analog input (1 MHz and 200 kHz) than the PLC modules (~1 kHz both for digital and analog) although for quasi-static tests, operation and acquisition at rates higher than 100 Hz are generally not necessary. On both systems, the piezoelectric actuator is controlled by DC voltage supplied from the controller analog output. The FPGA on the KIT system has a resolution of 16 bit whereas the PLC analog output on the UK system has a 12 bit resolution. This leads to a minimum voltage output signal resolution of 0.3 mV for the KIT system and of 4.9 mV for the UK system (or minimal displacement of 1.83 nm and 49 nm). For a 1.5 mm long gage typically used for tensile test specimens in this work, this means a minimum strain resolution of 1.2×10^{-6} for the KIT system and 3.3×10^{-5} for the UK system. Although this resolution difference is important, the minimal deformation that can be applied by the UK system is still over an order of magnitude smaller than what is necessary to conduct mechanical testing on np-Au, for which the strain at rupture usually lies between 5×10^{-3} and 8×10^{-3} (meaning that a minimum of ~150 data points describe the whole stress-strain curve).

Even though the FPGA is much faster than the PLC configuration, it also has its drawbacks. The FPGA is generally integrated on a PCI board that is physically inserted in a computer (although recently, external models have been offered by some manufacturers). Therefore, only one computer can control it, whereas a PLC configuration allows control by several computers. Another advantage the PLC configuration offers is full customization, at any time along the life of the PLC. Data acquisition modules can be added as needed and communicate with the PLC. Therefore, if the UK system needed higher resolution for voltage signal generation to take the example detailed above (16 bit resolution instead of 12 bit), a specific module with higher resolution could be purchased independently. This advantage is critical during cost comparison.

Table 3.1. List of components for the KIT small-scale mechanical testing system.

Component	Manufacturer	Model	Range	Resolution
Linear stepper	Physik Instrumente	M-230.25	25 mm	0.1 µm
Piezoelectric actuator	Physik Instrumente	P-843.40	60 µm	1.2 nm
Load Cell	Disynet/Measurement Specialties	XFTC-310	+/- 50 N	≤0.5% F.S.
Signal amplifier	FGP Sensors	XAM-BV	+/- 100 mV	not specified
DC power supply	Voltcraft	unknown	40 V/ 2.5 A	not specified
Compound microscope	Nikon	LV series	N/A	N/A
Digital camera	Pixelink	B782-F	up to 25 fps at 1280x1024	up to 2208x3000
Automation / Acquisition	National Instrument	SCB68	+/- 10V (AI/ AO)	16 bit analog
Programmation software	National Instrument	Labview	N/A	N/A

Table 3.2. List of components for the UK small-scale mechanical testing system.

Component	Manufacturer	Model	Range	Resolution
Linear stepper	Thorlabs	DRV013	25 mm	< 1 μm
Piezoelectric actuator	Thorlabs	PAZ015	100 μm	25 nm
Load Cell	Disynet/Measurement Specialties	XFTC-310	+/- 50 N	≤ 0.5% F.S.
Signal amplifier	Phoenix Conatact	MACX MCR-UI-UI-SP-NC	+/- 100 mV	not specified
DC power supply	Mastech	HY3005D	30 V / 5 A	≤ 0.5 mV
Compound microscope	Olympus	BXFM	N/A	N/A
Digital camera	Pixelink	B782-F	up to 25 fps at 1280x1024	up to 2208x3000
Automation / Acquisition	Schneider Electric	Modicon M-340	+/- 10V (AI/ AO)	12 bit analog
Programmation software	Schneider Electric	Unity Pro M	N/A	N/A

3.6. Nanoindentation

Nanoindentation is a particular variety of hardness measurement techniques used for the determination of mechanical properties of small volumes. Whereas classic indentation methods, such as Vickers, Brinell and Rockwell, use loads in the hundreds of newtons, nanoindentation rarely uses loads higher than a couple tens of millinewtons. Therefore, very shallow penetration of the material is occurring and the properties of very confined volumes of materials can be determined. Nanoindentation usually uses a Berkovich indenter tip, which has the shape of a three-sided pyramid and has the property of geometrical similarity. Geometrical similarity refers to an indentation where there is a constant ratio between the length of the pyramid diagonal and the penetration depth in the sample. This feature implies that the value measured for hardness with a geometrically similar tip will be the same independently of the load applied.

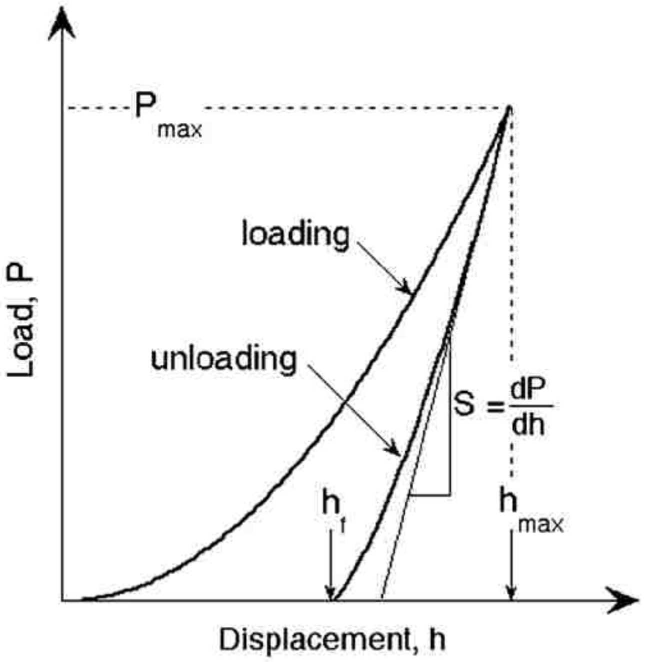

Figure 3.5. Shape of a typical nanoindentation curve. (From[107], reproduced with permission)

Several definitions are used to define hardness for nanoindentation tests, but all use a ratio of load to surface, so that

$$H = \frac{P_{max}}{A} \qquad \text{Equation 3.6}$$

with H the hardness value, P_{max} the full load applied and A the surface of indentation. As described in section 2.4.3, different values can be used in Equation 3.6. The mean contact pressure uses the maximum load applied divided by the projected contact area obtained from the indenter's tip geometry. Another method commonly used is to replace the value of the projected contact area by the area of indentation left by the indenter at the surface of the sample, measured by microscopy techniques. As detailed in section 2.4.3, both definitions have been used in the literature concerning the mechanical properties of np-Au.

Hardness is not the only property than can be determined from a nanoindentation test. If it is assumed that the deformation during the unloading portion of the test is purely elastic, the elastic unloading stiffness $S = dP/dh$ can be determined (see Figure 3.5), from which the reduced modulus can be determined and the Young's modulus calculated (Oliver-Pharr method [108]). The reduced modulus E_r is related to the Young's modulus by

$$\frac{1}{E_r} = \frac{(1-\nu^2)}{E} + \frac{(1-\nu_i^2)}{E_i} \qquad \text{Equation 3.7}$$

with E and ν the Young's modulus and Poisson's ratio of the indented material and E_i and ν_i of the indenter. For the present work, a NanoTest™ Vantage nanoindenter (Micro Materials Ltd) with Berkovich indenter tip was used.

Chapter 4 : Identification of microstructural defects by anelastic relaxation

One challenge faced in the determination of the deformation mechanisms in nanoscale samples is specimen preparation. In order to observe individual ligaments of np-Au by electron microscopy techniques, preparation techniques have to be employed that are generally invasive and might modify the specimen to be characterized. In addition to the difficulty of preparation, a danger of such methods is the possible alteration of the specimen or of its properties without realizing it. This can lead to mis-observations and erroneous conclusions. For example, Sun and Balk[53] observed the influence of focused ion beam (FIB) exposure on the np-Au structure, and found that significant damage was created at the surface of the sample. Short FIB exposure created cracks at the grain boundaries as well as in the structure, and initiated ligament coarsening. Therefore, preparation steps conducted after dealloying of the precursor alloy can have a significant impact on the presence of defects in the final sample and on its properties.

In contrast, anelastic relaxation studies can provide useful insights on the presence of internal defects in the structure, without relying on potentially damaging preparation techniques. The presence of defects such as dislocations and point defects can be detected, without applying any permanent deformation to the material. Also, sample preparation for this technique is minimal and allows characterization of the structure in its pristine state. Studying the damping properties of np-Au can consequently allow identification of the presence of dislocations and internal defects in the ligaments and nodes, after dealloying and without any mechanical or chemical alteration.

The measurement setup described in section 3.4.2, originally built at Stanford, did not allow measurements below room temperature. Because some of the relaxation peaks of interest for gold were expected to appear below room temperature for the range of frequencies used in this work, the original measurement setup was modified. Verification of the range of temperature accessible by the new design was performed while studying the damping properties of nanocrystalline nickel (nc-Ni). Previous studies on nc-Ni[109] above room temperature allowed identification of two Hasiguti relaxation peaks P_β and P_γ, involving the interaction of dislocations and points defects (see Figure 4.1). However, the activation energy calculated for the P_β peak (0.7 eV in Figure 4.1d) did not match the value reported in the literature, and was closer to the value reported for P_γ. Because Hasiguti peaks are commonly observed by set of three, and because the first peak P_α was expected to appear below room temperature, detection of this latter relaxation peak was the initial motivation for the system's modification. To clarify the observations and determine if the peaks observed did match the Hasiguti peaks reported in the literature, testing below room temperature was imperative. A literature review of the relaxation peaks commonly observed in nickel is shown in Table 4.1, where the internal friction mechanisms and their respective activation energies are listed.

Table 4.1. Summary and details of the internal friction peaks observed in nickel, after[109]

H [eV]	Peak temperature [K]	Frequency [Hz]	Peak type	Mechanism	Ref
0.31 ± 0.04	155	~1,000	Hasiguti P_α	Interaction of dislocations and point defects	[110]
0.53 ± 0.05	350	~1,000	Hasiguti P_β		
0.72 ± 0.06	397	~1,000	Hasiguti P_γ		
0.14	131-145	~30,000	Niblett-Wilks	Dislocations: kink/anti-kink pair nucleation	[111], [112]
0.40	208-288	~30,000	Bordoni		
1.1 0.1	~650	10-10,000	GB		[113]
1.25 ± 0.15	475 at 0.2Hz	0.01-10	GB	grain boundary diffusion	[114]
1.25 ± 0.15	475-660	0.01-10,000	GB		[115]

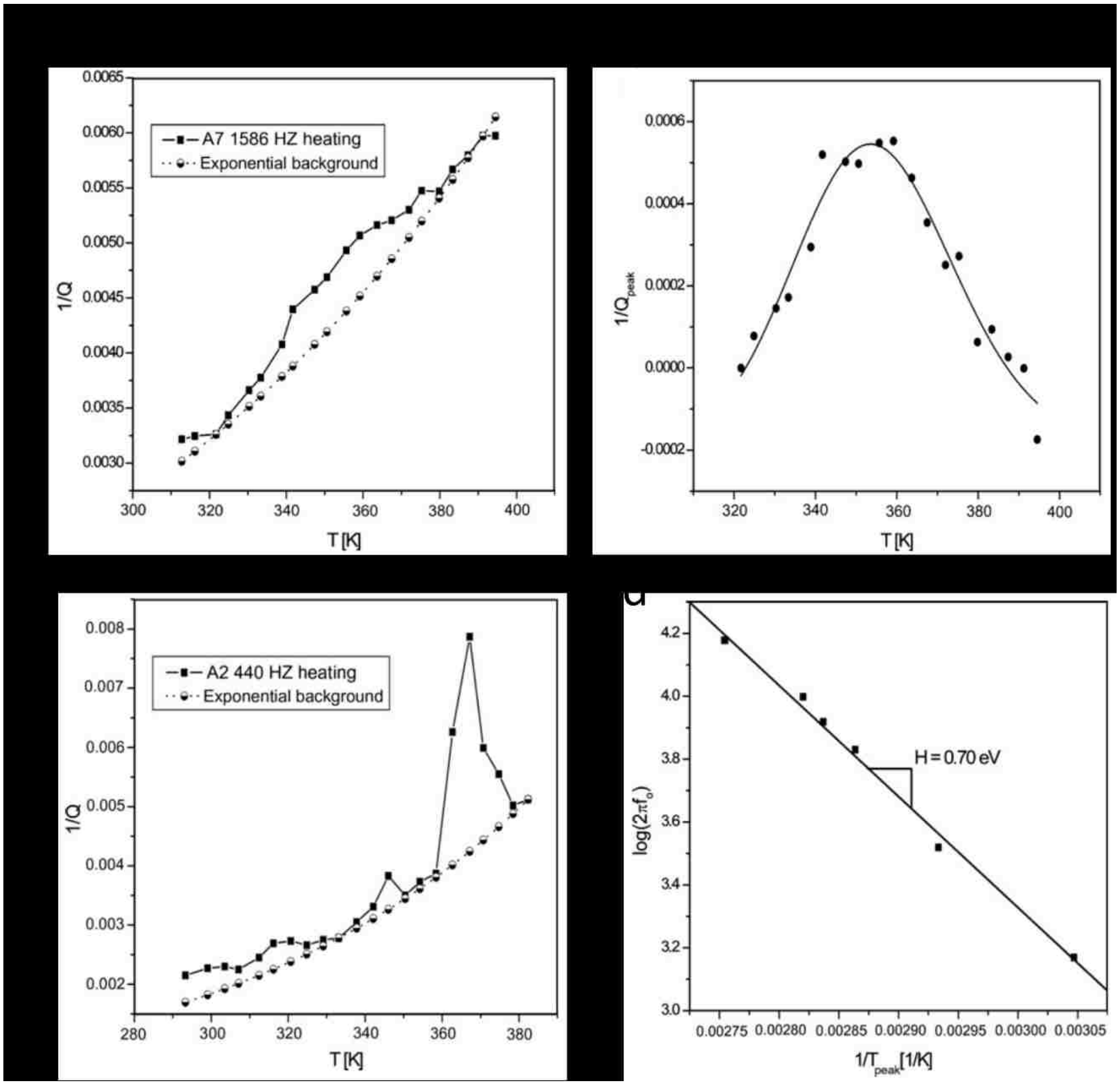

Figure 4.1. Damping ratio as a function of temperature for nc-Ni, measured using the Stanford system, before modifications. Experiments were conducted by Jochen Lohmiller and reported in[109]. a) damping ratio vs. temperature for an induced vibration at 1586 Hz; b) relaxation peak after subtraction of the background from plot in a). The peak was identified as the Hasiguti peak P_β; c) damping ratio vs temperature for a test with initial vibration at 440 Hz. The peak detected is identified as the Hasiguti P_γ; d) Arrhenius plot allowing determination of the activation energy associated with the peak observed in a) and b). (All figures reprinted from[109] with permission from Elsevier)

4.1. Specimen fabrication and experimental details

4.1.1. Nc-Ni specimens

The samples for nc-Ni damping studies were extracted by wire electro-discharge machining (EDM) at the Karlsruhe Institute of Technology, from a nc-Ni sheet (Integran Technologies Inc., Toronto, Canada). The original sheet, produced by electrodeposition, was 110 µm thick with average grain size of 20 nm. As described in section 3.4, the method chosen to determine the maximum damping ratio was to fix the frequency and vary the temperature. This choice arises from the nature of the imposed vibration control: because the cyclic load is induced by electrostatic forces at the resonant frequency of the sample, the frequency used cannot be changed for a single specimen. Consequently, several specimens were made to be able to determine the maximum damping ratio for various frequencies. Changing the resonant frequency was achieved by changing the mass of the sample. The design chosen for the damping samples was similar to a cantilever beam with a paddle at the end, and is shown in Figure 4.2. The size of the paddle was changed between samples to create the range of different resonant frequencies. Paddle sizes between 2 mm x 2 mm and 8 mm x 8 mm were used, leading to usable frequencies between 200 and 3000 Hz. For testing, the samples were clamped on the base and the cantilever and paddle part were standing free over the electrode, able to deflect under the applied cyclic voltage.

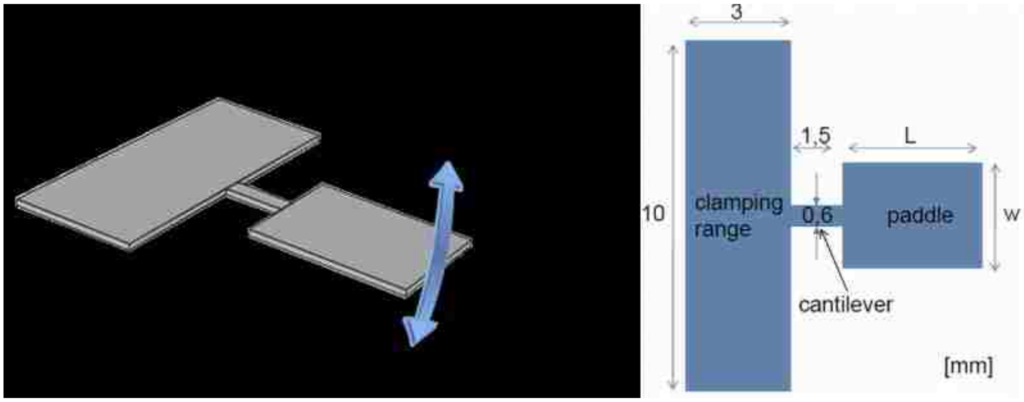

Figure 4.2. Geometry of the nc-Ni damping samples. The samples were cut by wire EDM with various paddle sizes but constant clamping area and cantilever beam dimensions. (left) representation of a damping sample, the arrow demonstrating the direction of the cyclic deformation (vibration); (right) Typical dimensions of a sample. The base and cantilever portion were identical for all samples.

Grain size within the sample was determined by XRD after several temperature cycles, and it was determined that grain growth was limited. For instance, after 5 thermal cycles up to 386 K, one of the sample exhibited a change in grain size from 19.5 to 20.4 nm.

4.1.2. Np-Au specimens

To make sure that the np-Au structure was not altered during sample preparation, it was important to perform all the steps to create the sample in its final dimensions before even creating the np structure. In his doctoral dissertation[116], Dae-Han Choi was able, using the same system, to study the damping properties of thin films deposited on silicon substrates. It was therefore decided to deposit thin films of the precursor alloy, AuAg onto silicon substrate, by magnetron sputtering (a description of this technique is given in section 3.1). To minimize the influence of the substrate on the overall damping properties of the sample, silicon wafers (4 inch diameter) from Wafer Works Corp (Taiwan) were used, with a thickness of 230 ± 15 µm.

To prevent any alteration of the np-Au structure, the silicon substrates were first brought to the geometry and dimensions described in the previous section for nc-Ni samples. Fabrication steps are schematically detailed in Figure 4.3. To achieve this goal, the silicon was chemically etched through patterned open regions at the surface of the silicon wafer, created by photolithographic techniques. First the photoresist AZ5214 was spin coated on the silicon substrate, and exposed to UV (Karl Suss MJB-3 Mask Aligner) through a mask (chrome on glass) containing the sample’s geometry. Although this photoresist is a positive photoresist, meaning that the region exposed to UV light are soluble, it can be used in image reversal mode. An inverse image of the mask is then obtained, suitable for lift-off as described below. The photoresist opens a window over the bare silicon substrate, in the shape of the damping sample, as shown in Figure 4.3b.

The next preparation step is to deposit the precursor alloy onto the photoresist patterned substrate. Before sputtering the alloy, a tantalum layer is deposited first, followed by a second interlayer of gold to enhance adhesion. Both interlayers had a thickness of ~ 10 nm. The gold interlayer provides increased adhesion of the dealloyed film, creating a gold-to-gold bonding between the gold ligaments and the interlayer. It was found that sputtering the alloy directly on the tantalum interlayer often led to delamination of the film during dealloying, as the gold ligaments to tantalum adhesion was not as strong. Sputtering of the precursor alloy was conducted by co-deposition with two targets (gold and silver), that could independently be covered with a mechanical shutter. The gold target shutter was always opened first and also closed first. This way, the first layer deposited was always gold, preventing the deposition of a monolayer of pure silver that could lead to delamination of the film during dealloying. The silver shutter was closed last, to make sure that the surface of the film was not made a pure monolayer of gold that could potentially passivate the surface and prevent dealloying of the film. Details of the sputtering conditions and parameters are given in Table 4.2. Composition of the sputtered films were verified by EDX in the SEM (Hitachi S-4300). The composition of the precursor alloy was found to be $Ag_{65}Au_{35}$.

Table 4.2. Sputtering details for the deposition of the gold-silver films on silicon, for the preparation of damping samples.

Material deposited	Chamber pressure [torr]	Target power [W]	Time	Target thickness [nm]
tantalum	2.5 x 10^{-3}	75W RF	3 min	10
gold	2.5 x 10^{-3}	70W RF	43 s	10
gold silver	2.5 x 10^{-3}	76W RF 66W DC	14 min 18 s	500

This precursor alloy deposition coated the exposed silicon at the surface of the sample as well as the regions covered by the photoresist (see Figure 4.3c). The photoresist used here being soluble in acetone, the sample was then immersed in acetone. Dissolution of the photoresist lifted-off the sputtered AuAg alloy, except in the regions where no photoresists was present. In the end, the damping sample shape was created in AuAg at the surface of the silicon wafer, as represented in Figure 4.3d.

Separation of the specimen from the rest of the silicon wafer was done by chemical etching. Etching of the silicon in potassium hydroxide (KOH) solutions was used at first, but the repeatability of this process was challenging. Another chemical etching technique was then used, successfully. The samples were immersed in a mix of hydrofluoric (HF), nitric (HNO_3) and acetic (HAc) acids, commonly referred to as HNA. This mix of acid is generally used during the final step of TEM sample preparation, to etch the silicon until it becomes electron transparent. The proper ratio of acids was empirically determined, and the final mix used had the following ratio, by volume: 12% HF - 44% HNO_3 - 44% HAc. With this solution, the silicon wafer was etched through in less than 20 minutes. During both etching methods (KOH and HNA), it can be seen that the gold-silver film is actually used as an etch mask, protecting the silicon underneath the surface to be exposed to the solution (but not the back-side). Therefore, because nitric acid is present in HNA, it had to be determined if dealloying during etching of the silicon took place in the gold-silver, and if so, verify that the np-structure did not contain cracks. The surface of the film was then observed in the SEM (Hitachi s-900) after the silicon etching step, and is shown in Figure 4.3e. It was found that although dealloying started in the film, it was not complete and no sign of cracking of the structure was found. It is interesting to notice that because the backside of the sample was not protected during wet etching, the overall thickness of the silicon substrate was divided by two before the damping sample was fully released. The final sample thickness was measured at ~ 107 µm, by a precision dial indicator (Mitutoyo).

The final step was to further dealloy the AuAg film until the fully dealloyed np-Au film was obtained on the silicon substrate, in the shape of a damping sample. This was done by free dealloying of the sample in concentrated HNO_3 for 20 minutes, with mild agitation. The structure was then characterized in the SEM (Hitachi s-900), and is shown in Figure 4.3f. It can be seen that the structure is nanoporous and does not present any cracks. Removal of the sacrificial element (silver) was further verified by EDS in the SEM (Hitachi S-3200) and showed a residual content of silver below 4% at.

Because annealing cycles were conducted on the samples during testing, the np structure was characterized by SEM before and after, to evaluate the degree of ligament coarsening. Figure 4.4 shows the np-Au ligaments before testing and after three runs below room temperature. No ligament coarsening can be observed. Figure 4.5 shows another sample before and after conduction of several experiments, both below and above room temperature (up to ~ 450 K). It can be seen that although the structure appears to coarsen, the structure still stays nanoporous.

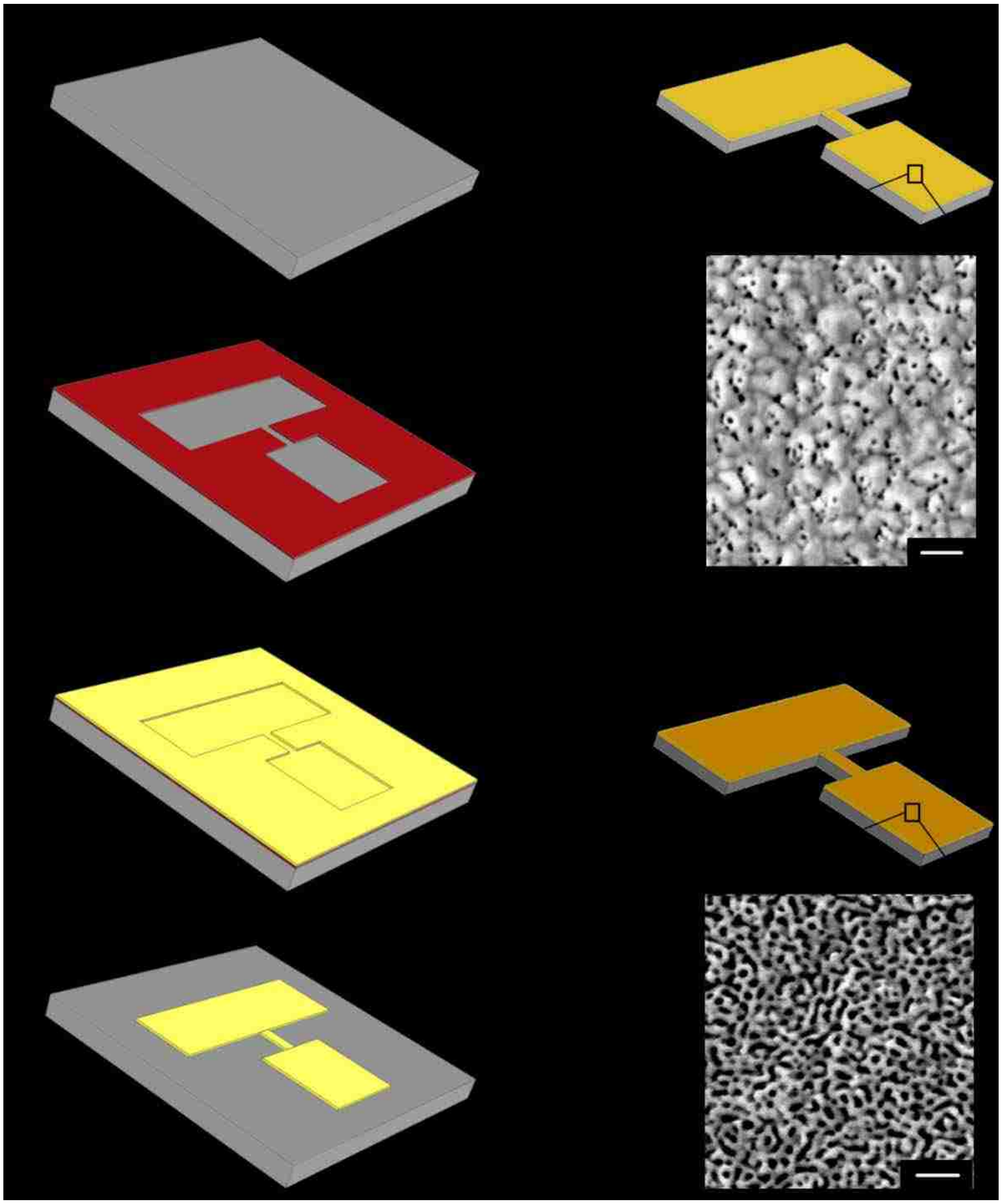

Figure 4.3. Details of the fabrication process for the np-Au damping specimens. a) bare silicon wafer, b) patterned photoresist on silicon, c) gold-silver sputtering, d) lift-off of the photoresist and the gold-silver film away from the damping sample geometry, e) wet etching of the silicon in HNA. The film is partly dealloyed after this step, f) complete dealloying of the gold-silver film. In e) and f), scale bars are 100 nm.

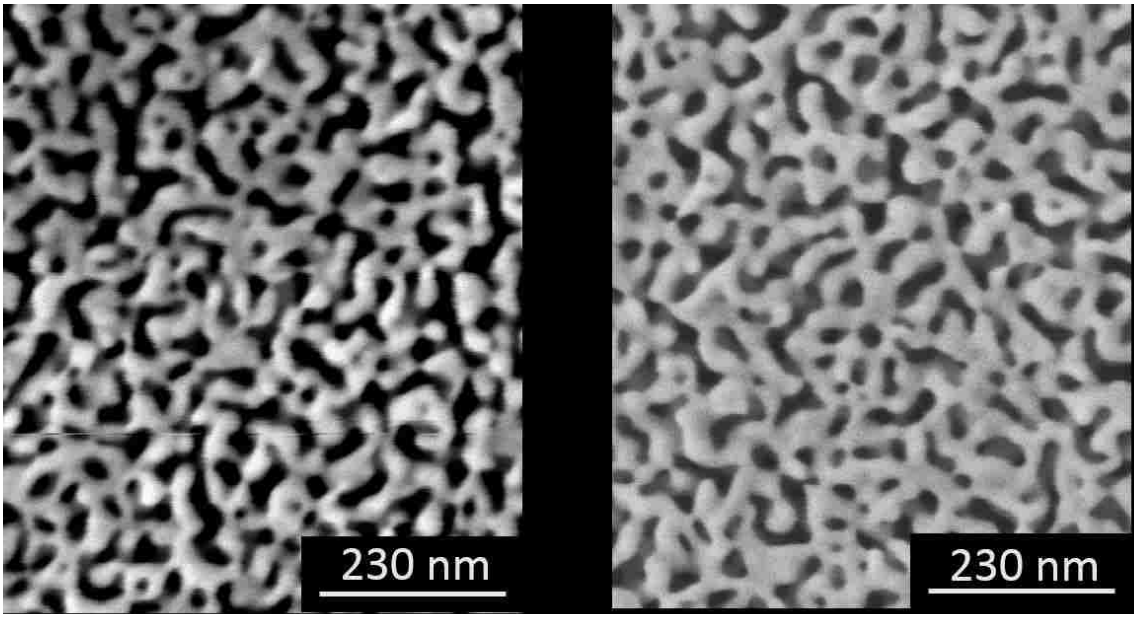

Figure 4.4. SEM micrographs of the np-Au film on top of silicon for the same damping sample (left) before testing (as-dealloyed state), (right) after 3 cycles below room temperature.

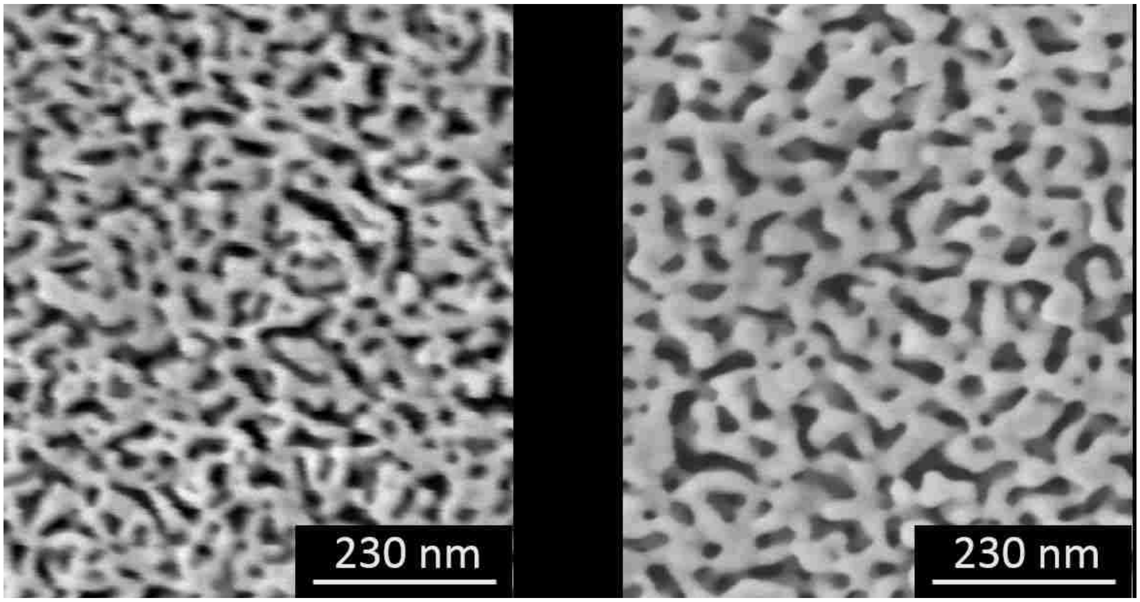

Figure 4.5. SEM micrographs of the np-Au film on top of silicon for the same damping sample (left) before testing (as-dealloyed state), (right) after 2 cycles below room temperature and 2 cycles above temperature (up to 450 K).

4.2. Experimental details

The samples were clamped at their base on the stage, the chamber was evacuated to prevent air friction influence on the damping of the vibration. All tests were conducted with a chamber pressure below 9x10^{-5} torr. The laser vibrometer used to monitor the deflection was focused on the center of the paddle. The AC voltage can then be controlled through a Labview™ program, and the vibration at the resonant frequency is then impose in the sample. The amplitude of the vibration can be monitored in real-time on the computer. Once the excitation voltage is stopped, the free decay of vibration is recorded, and the envelope of the signal is fitted with an exponential function:

$$A(n) = a\exp(bn) \qquad \text{Equation 4.1}$$

with $A(n)$ the amplitude of the signal at the n^{th} cycle, and a and b being constants. The damping ratio is then calculated by

$$Q^{-1} = -\frac{1}{N\pi}\ln\frac{A(n+N)}{A(n)} \qquad \text{Equation 4.2}$$

To cover the widest range of temperature possible, liquid nitrogen was flown through an internal circuit dug into the copper stage until no further drop in temperature was detected. The flow of liquid nitrogen was then stopped and the free decay of the vibration was recorded as the specimen was slowly heating up towards room temperature. Damping ratio values were continuously measured every 3 K along the whole range of temperature, typically between ~100 and 450 K. The damping background was estimated by fitting an exponential curve to the data, not taking the peaks into account. After subtraction of this background, the evolution of the damping ratio with temperature allowed identification of the relaxation peaks, associated with internal friction mechanisms activated for particular sets of frequency and temperature. Once activated, these mechanisms consume some of the applied energy from the mechanical cyclic deformation, hence accelerating the vibration decay process. This leads to the calculation of higher damping ratios for these particular conditions.

4.3. Results and discussion

4.3.1. Nc-Ni specimens

Between 100 and 400 K, three internal friction relaxation peaks were observed in the nc-Ni samples: two below and one above room temperature, as seen in Figure 4.6. The temperatures at which the peaks were observed are in good agreement with the values reported in the literature and listed in Table 4.1. Based on the measured temperatures, the first and third peaks observed in nc-Ni, at ~170 K and ~355 K, appear to correspond to the first and second Hasiguti peaks (P_α andP_γ). An activation energy of 0.70 eV was previously calculated for this third peak[109] (see Figure 4.1d), which although corresponded to the Hasiguti peak P_γ, was originally identified as the P_β peak because of the temperature at which it was detected.

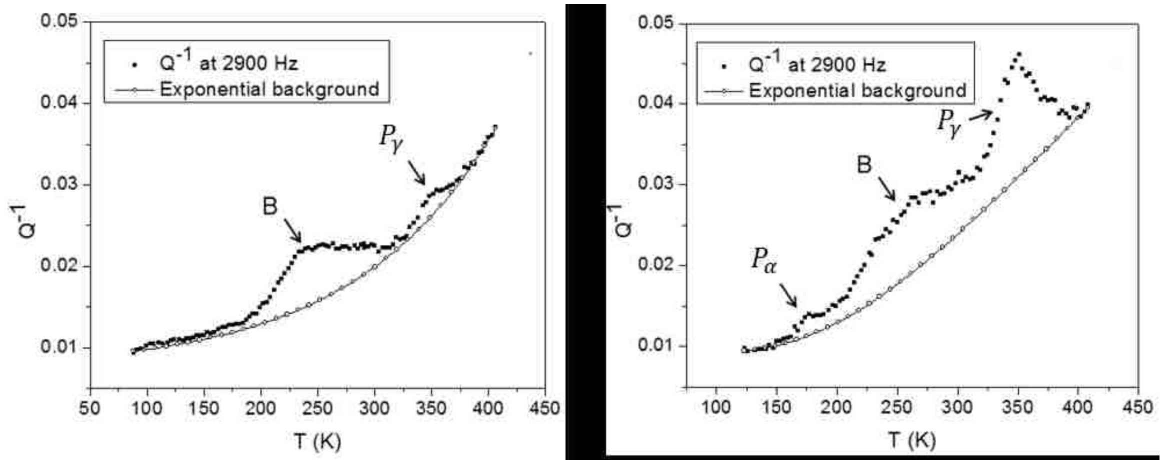

Figure 4.6. Damping ratio as a function of temperature for the same nc-Ni sample, at a resonant frequency of 2900 Hz. The tests were performed on two consecutive days, under the same conditions. The Bordoni peak's intensity was found to decrease while the Hasiguti P_α and P_γ grew.

It has also been reported in the literature that all three Hasiguti peaks are not commonly observed in the same experiment, as described by Benoit *et al.* [117] and Okuda *et al.*[118]. The second Hasiguti peak (P_β) is typically observed in the first damping experiment, immediately after cold working, but P_α and P_γ are not observed at this point. After further testing, after the sample has been annealed above room temperature, the P_β peak disappears, while P_α and P_γ appear and then remain the only observable peaks. This reinforces the belief that the relaxation peak observed in this study around 355 K is, in fact, the P_γ peak. Although the activation energy for the first peak observed in this study has not been reliably calculated, its temperature and the fact that it appears in the same experiments as P_γ supports the hypothesis that it is, in fact, P_α.

The second (broad) peak observed between 200 and ~320 K appears to correspond to a Bordoni peak, also reported in that temperature range for Ni in the literature. The overall shape of the relaxation peak agrees well with reports in the literature, describing Bordoni peaks in face-centered cubic (f.c.c.) metals to be often accompanied by another peak, known as the Niblett-Wilks peak. This peak is usually detected at a temperature just below the Bordoni peak and is often characterized as a “left shoulder” to the Bordoni peak. This typical shape was observed in this study for nc-Ni samples, as shown Figure 4.7.

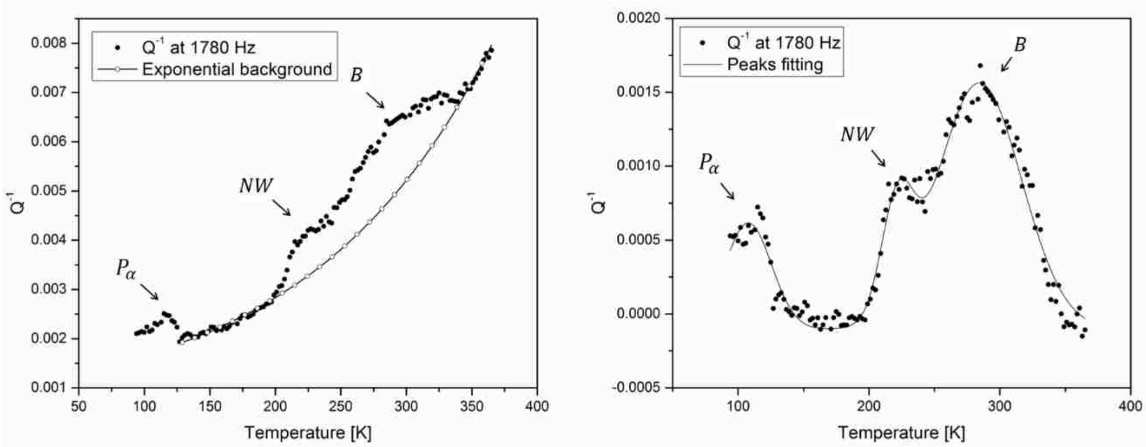

Figure 4.7. Damping ratio as a function of temperature for a nc-Ni sample with resonant frequency of 1780 Hz. (left) raw data with fitting of the exponential background; (right) after subtraction of the background, the Niblett-Wilks NW can be distinguished as the left shoulder to the Bordoni peak B.

Hasiguti peaks have been reported to arise from the interaction between pinning points and dislocations, and more specifically from the “unpinning from pinning points (assisted by mechanical vibrational stress)” as described by Hasiguti[119].

Bordoni relaxation peaks in f.c.c. metals have been well described by Seeger[120]. The Bordoni peak arising below room temperature is due to the thermally activated (assisted by mechanical stress) creation of kink/antikink pairs on the (111) slip planes. Dislocation lines oriented along different directions on the slip plane can lead to separate peaks at different temperatures, and with different activation energies[121]. The broad peak observed in this study of the damping behavior of nc-Ni is generally associated with dislocations aligned along [110] directions and the left-shoulder Niblett-Wilks peak is believed to originate from dislocations aligned along [112] directions.

During this study, an interesting correlation between the Bordoni and Hasiguti peaks was observed. While conducting several tests on the same sample, with maximum temperature approaching 400 K, the intensity of the Bordoni peak was found to gradually decreased, while the intensities of the Hasiguti peaks increased, from one test to the next. This observation can clearly be seen in Figure 4.6, where the damping ratio as a function of temperature is plotted for two consecutive experiments, which were conducted on the same sample, under the same conditions, two days in row. It is apparent that, in the first experiment, the Bordoni peak is clearly visible but P_γ's intensity is much lower above the background while P_α is hardly detectable. The next day, both Hasiguti peaks are clearly observable and P_γ's intensity is much higher than that of the Bordoni peak. On another sample, several experiments were conducted, and the evolution of the Bordoni and Hasiguti P_γ can be seen in Figure 4.8. Again, for this sample, the Bordoni peak gradually disappears and the P_γ peak slowly grows. Unfortunately for this sample, the first Hasiguti P_α was not observed. It is possible that the latter peak is detectable at a temperature lower than the measurement system's capabilities. In fact, in one of the experiments (on 10/22/2010), the damping ratio at very low temperature is seen to decrease at the beginning of the test, indicating that a peak could be detected below 100 K.

This evolution of damping behavior can be attributed to the different causes of internal friction, and has been reported in the literature[119]. During annealing of the sample, point defects such as interstitials can migrate towards the dislocations and pin them down. The result is that the Bordoni peak intensity decreases, since it arises from free (unpinned) dislocations, while the intensities of Hasiguti peaks increase, since they arise from the bowing-out and unpinning of dislocations. It was also reported by several authors[122], [123] that irradiation of the sample, to introduce point defects, would make the Bordoni peak disappear. Pinning of dislocations by defects strongly reduces the Bordoni relaxation peak.

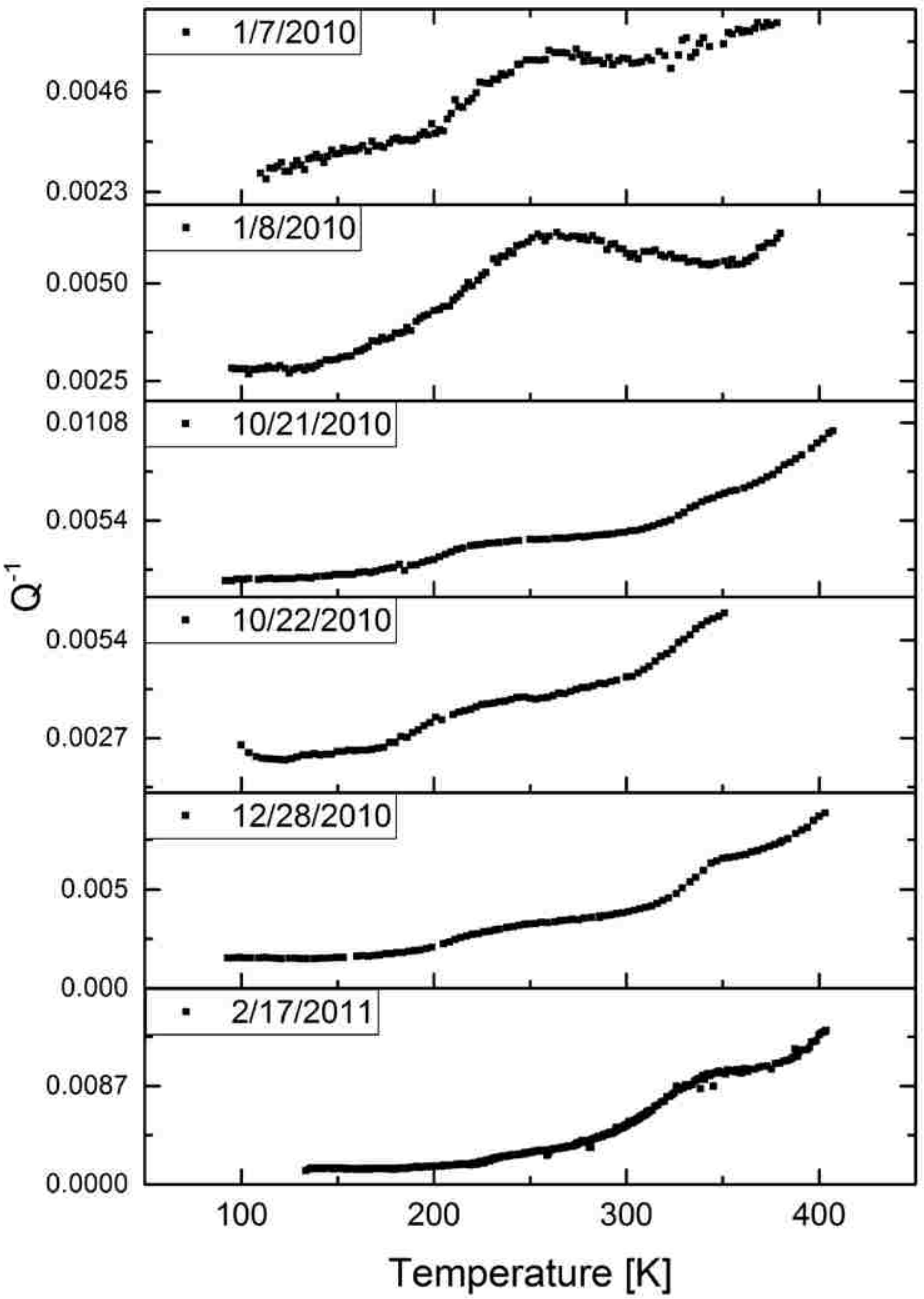

Figure 4.8. Evolution of the damping ratio vs. temperature plots, for the sample nc-Ni sample tested several times, at different times. During the first tests, only the Bordoni peak was observed. This peak gradually disappeared while the Hasiguti P_γ peak's intensity gradually increased.

During early experiments, dislocations in the nc-Ni samples were most likely not pinned and therefore the generation of kink pairs in free dislocations led to the Bordoni peak. However, after several experiments conducted to temperatures up to 400 K, many dislocations may have become pinned, not necessarily due to the migration of point defects, but perhaps due to interaction with the grain boundaries. The complete disappearance of the Bordoni peak after several experiments in Figure 4.8, could then be explained by the very limited volumes of the nanocrystalline structure (the grains dimensions are very small, ~20 nm). Once the dislocations are pinned at the grain boundaries, the peak cannot be observed anymore. Additionally for nc-Ni, a peak at high temperature arising from grain boundary diffusion should be much larger for nanocrystalline structures. This peak was observed by Lohmiller *et al.*[109] and shown in Figure 4.1c. Unfortunately, this peak was not observed in experiments conducted with the upgraded measurement system.

Answers to these hypotheses will be discussed in future work, after annealing of the nc-Ni samples to initiate grain growth. It is possible that a larger grain size would reduce the number of dislocations pinned by grain boundaries and therefore strongly decrease the intensities of the Hasiguti relaxation peaks, while the Bordoni peak would remain visible. At the same time, the amplitude of a large peak related to grain boundary diffusion should gradually decrease, as the grains grow larger.

Determination of the internal friction mechanisms' activation energies from the observed relaxation peaks was not possible, mainly due to inaccuracies in the temperature measurements. Although the general shape and position of the peaks on the damping ratio vs. temperature plots was repeatable, the error in temperature reading evolved during the test, based on different reasons. Because the sample is placed in vibration for the test, the thermocouple cannot be directly attached to it. Consequently, all temperature measurements are calculated from calibration tests during which thermocouples are placed on the sample. Factors such as vacuum level, liquid nitrogen flowrate, positioning of the sample relative to the thermocouple, were also found to influence the readings by a few degrees, enough to prevent the construction of reliable Arrhenius plots. Improvements in temperature determination will be primordial to the calculation of activation energies, which will allow confirmation of the nature of the internal friction mechanisms.

4.3.2. Np-Au specimens

A limited number of experiments were conducted on np-Au samples. Several challenges not present during the testing of nc-Ni samples. First, the np-Au films were deposited on silicon substrates, which were very fragile and consequently challenging to clamp in position without breaking them. Second, the np-Au films did not allow a good reflection of the laser from the vibrometer. Np structures have been shown to act as a light sink, which in this case can prevent acquisition of a good signal from the sample’s vibration. In addition, wet etching of the silicon to release the sample led to surface texturization of the silicon, especially for KOH etching. This texturization, while very good for light trapping, also led to low signal strength and noise issues during acquisition. It was then chosen to clamp the samples with the film facing down, as it was found to give the strongest, most reliable signal during testing.

Because of these issues, only noisy damping ratio vs. temperature curves could be obtained at first, as shown in Figure 4.9. The second set of np-Au samples were created by wet etching in HNA and the film was thicker (500 nm). The signal was improved significantly, and the damping ratio vs. temperature plots were considerably better and repeatable as seen in Figure 4.10. Best results were obtained during natural cooling and heating of the specimen. Therefore, samples were initially cooled down with liquid nitrogen flow in the copper stage, and acquisition of the data was conducted during the natural heating of the sample. Similarly, the stage and sample were then heated to high temperature (~ 450 K), and data were recorded during the cooling down towards room temperature.

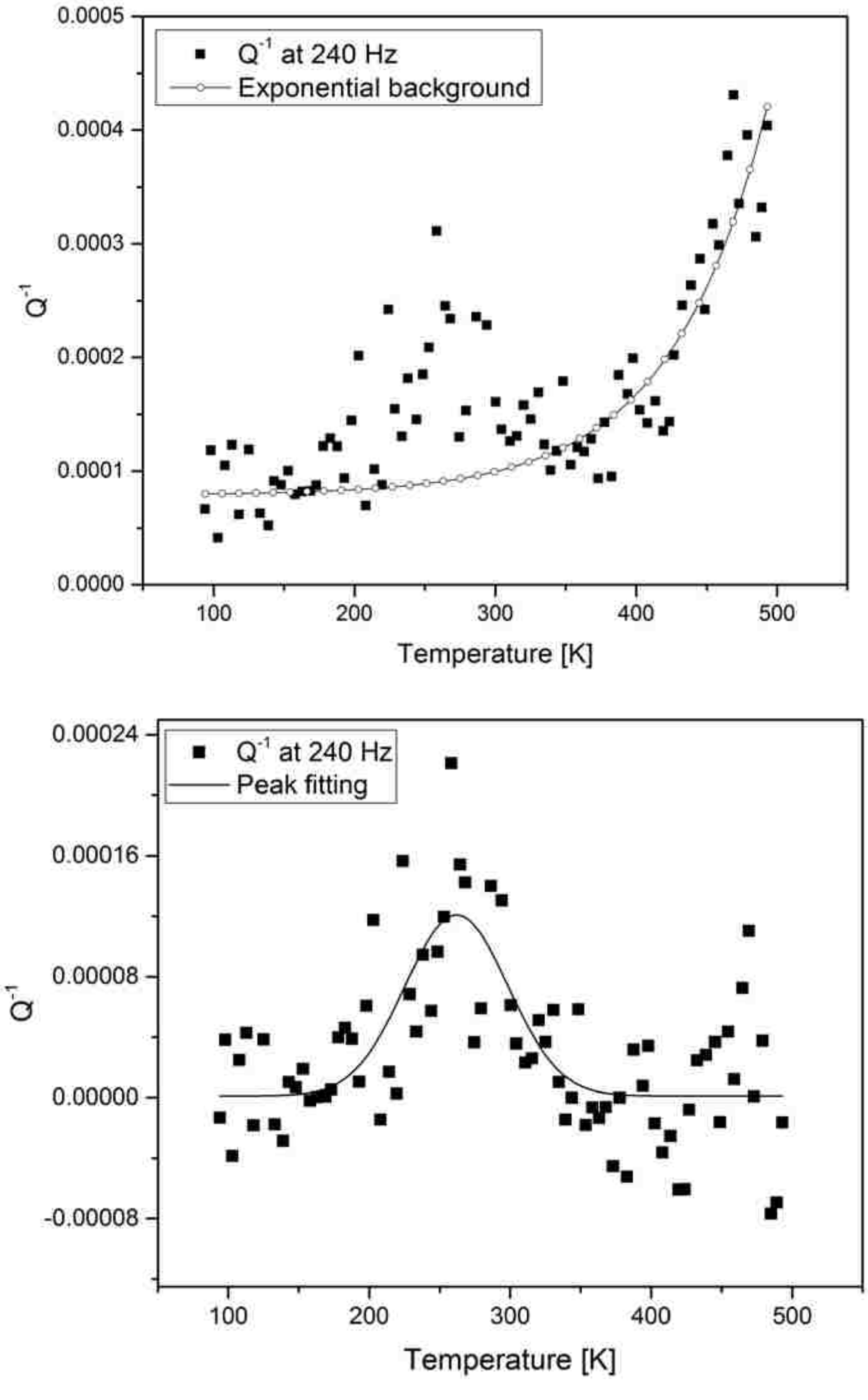

Figure 4.9. Damping ratio vs. temperature for the first set of np-Au films on silicon, created by KOH wet etching. Poor signal led to noisy data, but a damping peak can be identified at ~ 260 K. (top) Raw data obtained with an excitation frequency of 240 Hz; (bottom) data after subtraction of the exponential background. The damping peak can be fitted as a Gaussian peak.

Based on these experiments, three different peaks can be clearly observed. The first one is located at ~ 150 K, the second at ~ 230 K and the third at ~ 350 K. Several experiments were conducted on the samples, with temperatures up to ~ 450 K. It can be seen on Figure 4.10 that even after repeated annealing cycles, all three peaks are still observable, and there is no clear change in their amplitude. The np-Au film being deposited on a silicon substrate with interlayers of tantalum and pure gold for adhesion, some or all the peaks can potentially arise not from np-Au but from the other parts of the sample. The np-Au film and the gold interlayer were then removed using *aqua regia*, and the silicon substrate with tantalum interlayer was tested. In addition, a sample only made of silicon was also tested. It can be seen that the relaxation peak above room temperature is present in all plots in Figure 4.11, and this peak therefore comes from the substrate and not the np-Au film. The second peak around ~ 230 K clearly disappears when np-Au is removed, and can therefore be attributed to the structure of interest. The lower temperature peak is more difficult to identify after removal of the np-Au film, but the disappearance is not obvious.

Okuda and Hasiguti[118] observed a set of three damping peaks below room temperature in gold, at ~ 150 K, ~ 190 K and ~ 225 K. Interestingly, they observed the second peak (~ 190 K) after cold rolling at low temperature while the other two peaks were not detectable. After annealing at room temperature, the peak disappeared and the other became apparent. They attributed all these peaks to interaction between dislocation lines and point defects, respectively single vacancies, interstitial and di-vacancies for the first, second and third peak. Their tests were conducted down to a minimal temperature of ~ 100 K and they observed an increase of the damping ratio cooling from ~ 125 K to ~ 100 K. They tentatively attributed this observation to the higher temperature side of a Bordoni peak, which arises from free dislocation lines forming kink pairs.

Tanimoto *et al.*[124] studied the damping behavior of np-Au below room temperature and also observed two relaxation peaks, centered at ~ 130 K and ~ 260 K. These peaks were attributed to grain boundaries and the ligaments free surface.

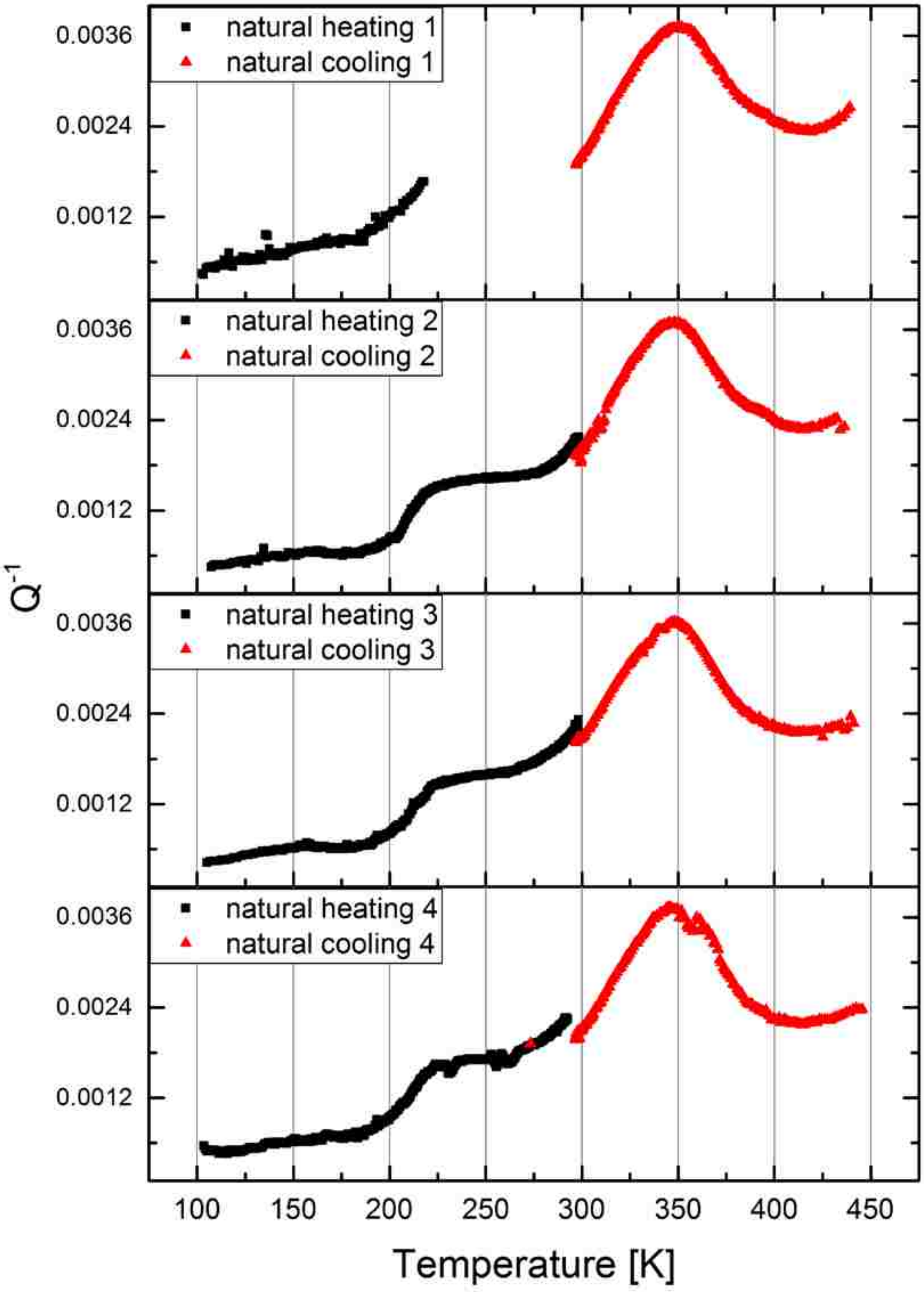

Figure 4.10. Evolution of the damping ratio vs. temperature curves through several cycles from low to high temperatures. Data points were recorded during natural heating and cooling. The amplitude of the relaxation peaks stays constant and no obvious difference is determined after several cycles. For the first natural heating, hardware issues prevented recording of the data up to room temperature.

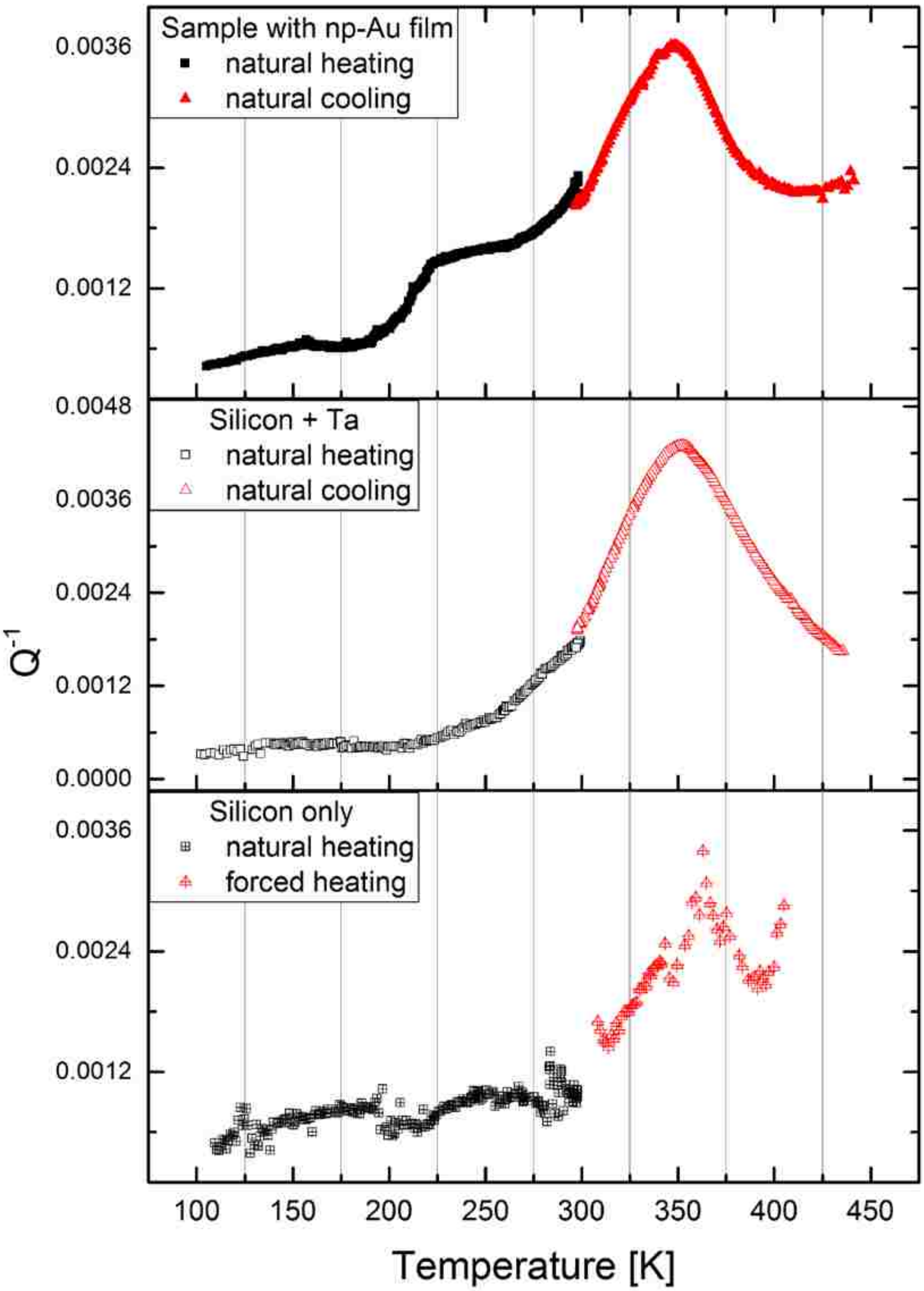

Figure 4.11. Comparison of damping ratio vs. temperatures curves for the sample with the np-Au film, the sample with only the Ta and Au interlayers, and bare silicon. The relaxation above room temperature is clearly not associated with the np-Au film.

The two damping peaks observed below room temperature for np-Au are in good agreement with the peaks observed by Tanimoto *et al.*, as well as with the first and third peaks described by Okuda and Hasiguti. Similarly to Tanimoto *et al.*, the second peak reported by Okuda and Hasiguti was never observed in np-Au. Because the samples were at room temperature for a significant amount of time before cooling and testing, it is possible that the defects potentially at the origin of this particular damping peak migrated to the free surface. It could also signify that few interstitials are present in the np structure. However, the existence of well-defined peaks below room temperature indicates the presence of pinned dislocations in the ligaments and nodes of np-Au. In addition, the damping ratio increase reported by Okuda and Hasiguti in gold at very low temperature was not observed for np-Au. They attributed this rise to the side of a Bordoni peak. The fact that no Bordoni peak appears in np-Au could mean that there are no or few free dislocation lines in the ligaments or nodes of the np-structure. Because the ligaments in np-Au represent a very small volume, it is possible that dislocations are pinned by defects at the free surface. This could explained the peaks observed, which seem to be arising from pinned dislocations.

4.4. Conclusion and future work

Unfortunately, because of the same temperature measurement issues reported in the previous section for nc-Ni, the activation energies of the mechanisms related to the relaxation peaks in np-Au could not be determined. Improvement of the system to be able to accurately determine the temperature of the samples will be needed to identify the mechanisms involved in internal friction in np-Au.

More investigations are needed, but it appears that the relaxation peak detected below room temperature shows the presence of dislocations in the ligaments of as-dealloyed np-Au. This is interesting, as it would demonstrate that dislocations are already in the ligaments and nodes of the np-structure, and were not caused by sample preparation or interaction with an ion or electron beam (FIB machining or TEM observation). Precise calculations of the activation energies could allow identification of different origins of dislocation pinning between np-Au and dense, polycrystalline gold. Annealing of the np-Au samples to coarsen the structure could allow observation of an evolution in the relaxation peak’s mechanism, transitioning from dislocations pinned at the surface of the ligaments, to dislocations pinned by defects inside the bulk.

This work has shown that detection of the “signatures” from internal defects is possible in np-Au, by identifying their contribution to the damping of a mechanical vibration. This rapid, non-invasive technique will be used on other projects, such as irradiation studies on np-metals. The defects that are usually created and accumulate in metals under ion irradiation have been observed to migrate to the free surfaces of the ligament in np-Au. Therefore, below a ligament size threshold, np-Au appears to be radiation resistant. Investigations of the damping properties of np-metals with different ligament sizes could allow precise determination of this threshold size, as the apparition and accumulation of defects will be accompanied by relaxation peaks.

Chapter 5 : Mechanical testing of pseudo-single crystalline np-Au in tension

Tensile testing is one of the most commonly used technique to determine the mechanical properties of a material. In general, it is fast, reliable and easy to implement. Important properties can be readily obtained, such as the Young's modulus, the yield strength, the ultimate tensile strength (UTS), the rupture strength, as well as the strain and Poisson's ratio the sample undergoes during testing. However, in the case of np-Au, implementing such a classic test presents many challenges.

First, because the material of focus is made out of gold, working on specimens as small as possible is obviously preferred. A standard specimen has a 50 mm long gage with a 12.5 mm diameter. At the time of writing, such as gage would cost close to $5,000 while not accounting for the specimen's ends by which it is attached during testing. Therefore, experiments are usually conducted on millimeter-size samples. Second, dealloying of thick samples is more challenging and requires more time and attention than samples in a thin film configuration or with at least one small dimension. Because tensile testing probes the entire gage section of the specimen, it is required that the np structure be consistent throughout the sample. Last, after dealloying, gold in its np form is brittle and very challenging to manipulate. Consequently, extreme care has to be taken when positioning the specimen in the testing equipment. Also because of its brittleness, the ends of the specimen cannot be clamped or firmly fastened in the grips, as any applied force would break them. Therefore, custom testing systems and specimen geometries have to be used, as described in the experimental section of this dissertation (section 3.5).

Another issue that was observed during previous tests on millimeter-size specimens [86] is stress concentration on microstructural defects such as grain boundaries and on specific regions of the specimen, due to its geometry. Localized stress concentration was found to invariably lead to premature rupture of the sample. Consequently, measured yield and fracture strengths values are underestimates of the real value. To remedy this issue, tensile testing of specimens without grain boundaries was investigated.

5.1. Specimen fabrication and characterization

As described above, measurement of the yield and fracture strength of np-Au through tensile testing of small-scale specimens can only be achieved on a structure that does not contain grain boundaries. These defects have been identified to act as stress concentration spots leading to premature failure and consequently to underestimations of the yield strength of np-Au. In order to test millimeter-scale single crystalline samples, the formation of AuAg monocrystals large enough to extract dogbone specimens was explored.

Annealing of metallic samples following deformation is a classic method to increase grain size within a sample, by grain growth. Upon annealing of a plastically deformed sample, recovery and recrystallization occur first. The dislocations created during deformation can move and cancel each other if they have opposite signs (dislocation annihilation). They can also migrate and re-arrange to form subgrain walls, lowering the overall stored energy, a process known as polygonization. Simultaneously, nuclei appear at points of high lattice-strain energy and grow into new, strain-free grains (recrystallization). These grains will grow until their boundaries meet other new grains' boundaries, stopping their expansion. After recovery and recrystallization is over, the internal energy can only be further lowered by reduction of the total grain boundary surface. This phenomenon through which some grain continue to grow larger to the expense of neighboring grains is called grain growth.

A metastable equilibrium can be reached when the grain boundaries energies balance each other's. Grains usually meet at a triple junction as shown in Figure 5.1. Symmetrical consideration dictates that the angles between the boundaries have to be 120°. If grains have 6 sides, perfect 120° angles will be made by the boundaries. If a grain has more or less than 6 sides, keeping a 120° angles between the boundaries will create curved grain boundaries. Because of theses curvatures, there will be a force acting on the grain boundary and, for a radius of curvature r, a force proportional to γ/r will pull the boundary towards its center of curvature, with γ the boundary tension. Therefore, if a grain has less than 6 sides, it will tend to shrink, whereas a grain with more than 6 sides will have its boundaries pulled away from the center of the grain, leading to growth.

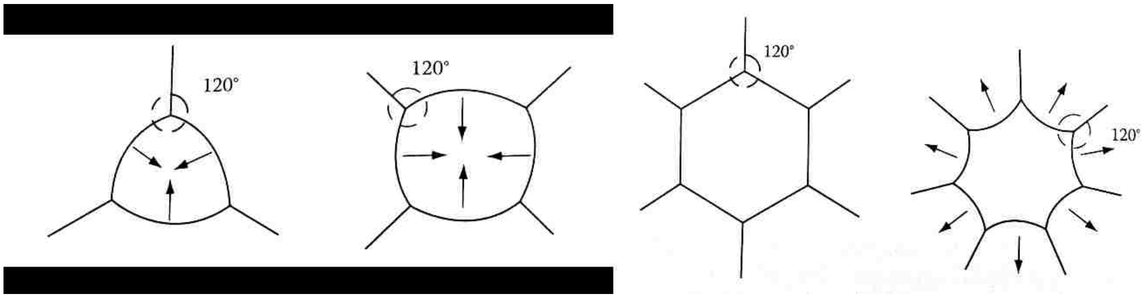

Figure 5.1. Grain growth based on number of grain sides (2D). With less than 6 sides, grains will shrink and disappear; with more, grains will grow. (Republished with permission of Taylor and Francis Group LLC from[125]; permission conveyed through Copyright Clearance Center, Inc.)

Shrinking or growth of a grain happens by grain boundary migration, during which atoms attached to one grain will detach themselves, cross the boundary and attach to the neighboring grain. Because of the boundary curvature, there will be a difference in free energy ΔG between the two grains. For a pure metal, free energy is equal to chemical potential. The driving force for atoms to cross the boundary is therefore the lowering of their chemical potential. However, a certain amount of energy has to be provided for the atoms to overcome their binding energy and cross. In the case of annealing, temperature will provide this energy, and in general, temperature has to be above half the melting temperature to initiate grain growth.

The 2D microstructural evolution during grain growth based on the number of sides is based on von Neumann[126] and Mullins work and makes some assumptions. Among others, it considers all grain boundaries to have identical mobilities, even though high angle grain boundaries (HAGBs) have higher mobilities than low angle grain boundaries (LAGBs). The latter can be used as an advantage for abnormal grain growth (AGG). During AGG, one or a few grains grow much larger than the other grains. This is different than normal grain growth during which all grains grow at relatively similar rates and reach similar sizes. Just as for normal grain growth, AGG is driven by internal energy minimization by reduction of the grain boundaries total area. However, certain grains will have an advantage on others for growth. This can happen in different conditions such as particles pinned boundaries or samples with limited thickness. Another particular condition is for samples presenting a strong texture component. For certain conditions of deformation and recrystallization, most of the recrystallized grains will have the same orientation, leading to low misorientation between boundaries, i.e. LAGBs. If one particular grain has an orientation which is very different than the others, it is likely to make HAGBs with these neighboring grains. Because HAGBs have higher mobility, this grain will grow much faster than others surrounding it. This phenomenon has been observed by Beck[127] in copper and by Kim[128] in aluminum, where strong cube textures were observed after deformation and recrystallization. Using electron backscattered diffraction (EBSD), it was observed that growth was inhibited for grains presenting the cube texture, whereas grains with different orientations quickly and easily grew, consuming the rather immobile cube oriented grains. In contrast, in samples where grains were randomly oriented, no AGG was observed.

Based on the previous observations, a similar approach was used to initiate abnormal grain growth in the precursor AuAg alloy, to form grains large enough to extract tensile test specimens. Different conditions of deformation and annealing were explored in order to determine the ideal parameters for which AGG was occuring.

AuAg pellets (99.99% purity, purchased from Kurt J. Lesker Co.) with composition $Au_{35}Ag_{65}$ and dimension approximately 5 x 5 x 10 mm^3 were cut at low speed using a precision saw (Buehler IsoMet® 1000). Slices of various thickness ranging from 1.1 to 1.7 mm were cut from the pellets. AGG was initiated by a combination of deformation and annealing steps. Deformation by cold-rolling was applied at room temperature using a jewelry rolling mill with flat rolls (purchased from Ottofrei). Thickness of the sample was measured using an electronic caliper, before and after rolling. The desired thickness was achieved with several passes, and the mill's rolls was lubricated with general purpose oil (3-in-One oil). Samples were then rinsed in alcohol and dried at air before annealing. Because of the AuAg alloy natural resistance to oxidation, annealing was conducted in air in a regulated furnace. Grain size was observed after annealing steps by optical microscopy. Best parameters to initiate AGG were found empirically, and the following steps led to AGG:

(1) Thickness reduction 20%.

(2) Annealing at 700 °C for 20 h.

(3) Thickness reduction 25%.

(4) Annealing at 850 °C for 20 h.

(5) Thickness reduction 30%.

(6) Annealing at 955 °C for 20 h.

After these steps, the samples presented final thicknesses between 450 and 700 µm and large grains (millimeter scale), in a matrix of much smaller grains, were observed with optical microscopy as shown in Figure 5.2. In f.c.c. metals with low stacking-fault energy, rolling has been shown to give a preferential orientation to grains. Consequently, smaller grains forming the matrix in AuAg were re-oriented during cold-rolling while a few grains were not. The latter ones were able to grow abnormally, as their orientations gave them an advantage for growth at the expense of the other grains, as described above.

The small grains are mostly located at the ends of the sample, because of the method used to apply deformation. Samples were cold-rolled along the longitudinal axis, so that the ends do not experience the same deformation as the middle region, which is constrained during thickness reduction. Therefore, the strain induced by rolling is different between the ends and the middle of the sample. The amount of strain being critical for grain growth, this strain difference leads to different final microstructures. Many annealing twins are also observed in the final microstructure, which is common in low stacking fault energy f.c.c. metals. Their formation is based on growth accidents and has been described by Cahn and Haasen[129] based on the work from Burke and Turnbull[130] and Smith[131].

Millimeter-scale specimen for tensile testing were extracted from the sample by wire EDM (Integrity Too & Engineering Inc., Ramsey MN) to obtain dogbone shaped specimens, as shown in Figure 5.3. Although grains presented millimeter dimensions after AGG, some grain boundaries from former, consumed grains remained in the samples and were unfortunately still present in the gage section of the tensile testing specimens, as can be seen in Figure 5.4. Because of these remaining grain boundaries, the specimens cannot be considered as fully single crystalline even though the gage section is mostly made out of a single grain. The specimen are then referred to as pseudo-single crystalline. Specimens were all cut with a gage length of 1.5 mm and width of 260 or 500 µm.

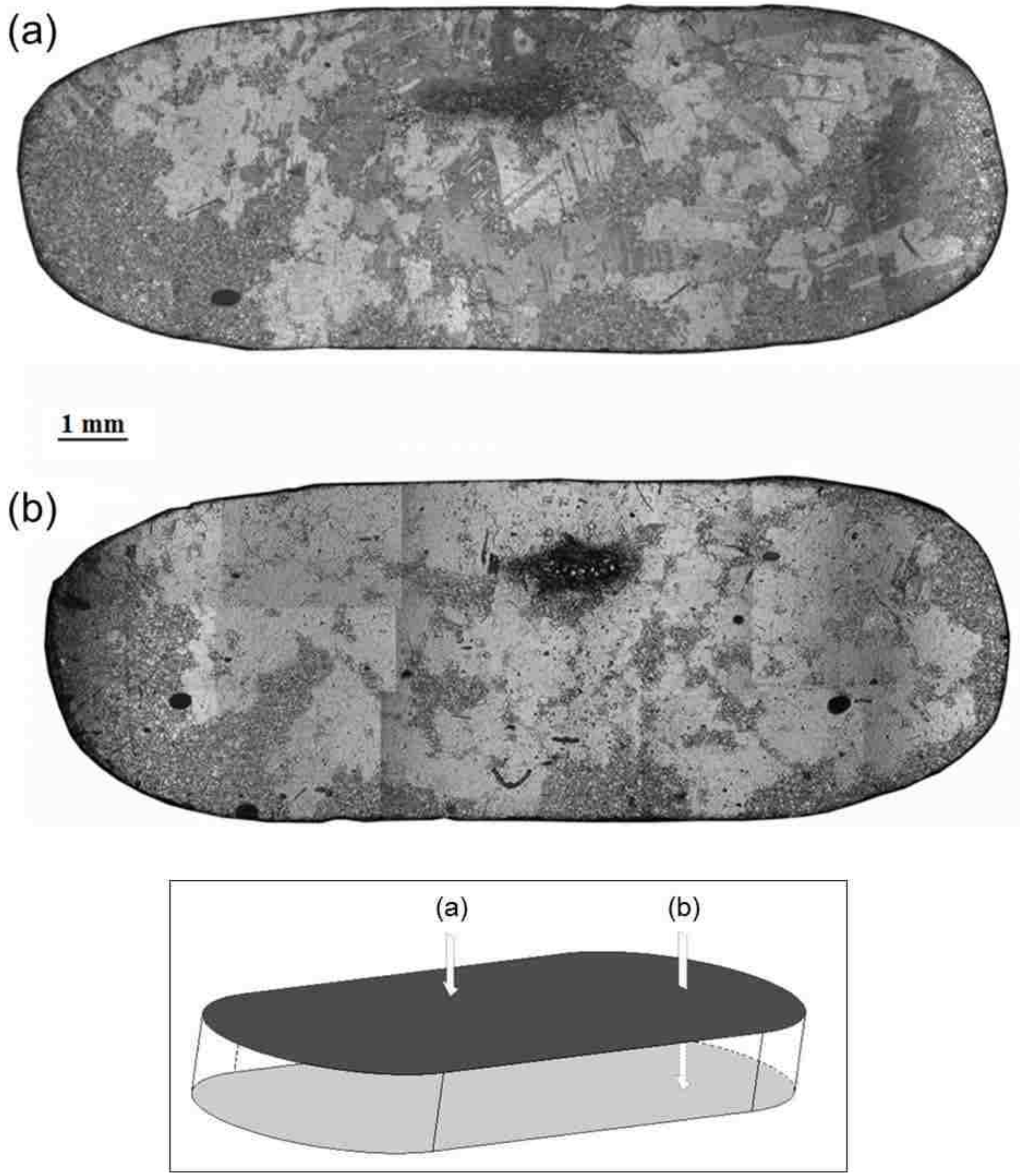

Figure 5.2. Sample ($Au_{35}Ag_{65}$) after cold-rolling and annealing steps, showing large grains obtained by AGG. The front (a) and back side (b) of the sample can be seen, with the backside oriented to allow direct comparison of the microstructure, as schematically represented below the micrographs. (From[132], reprinted with permission from Taylor & Francis Group)

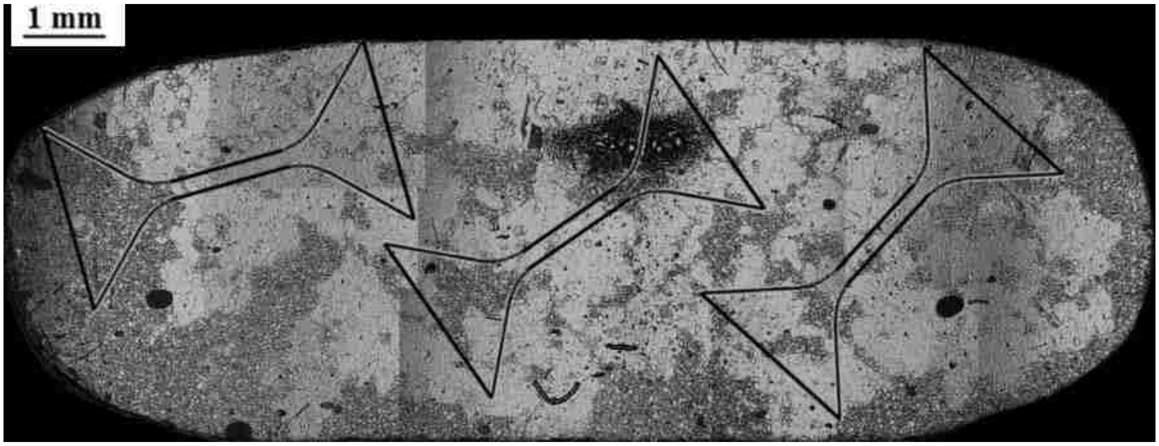

Figure 5.3. Optical micrograph of a sample after AGG, showing regions chosen to extract tensile testing specimens by wire EDM.

Because wire EDM cuts by locally melting the sample, the chemical composition of the region near the path of the wire can potentially be affected. Also, wire EDM usually leaves a surface roughness with peaks and valleys separated by 10 to 15 µm. To minimize these potential problems, the specimens were annealed at 950ºC for 24h following EDM and prior to dealloying. Composition homogeneity throughout the specimen was verified by EDS.

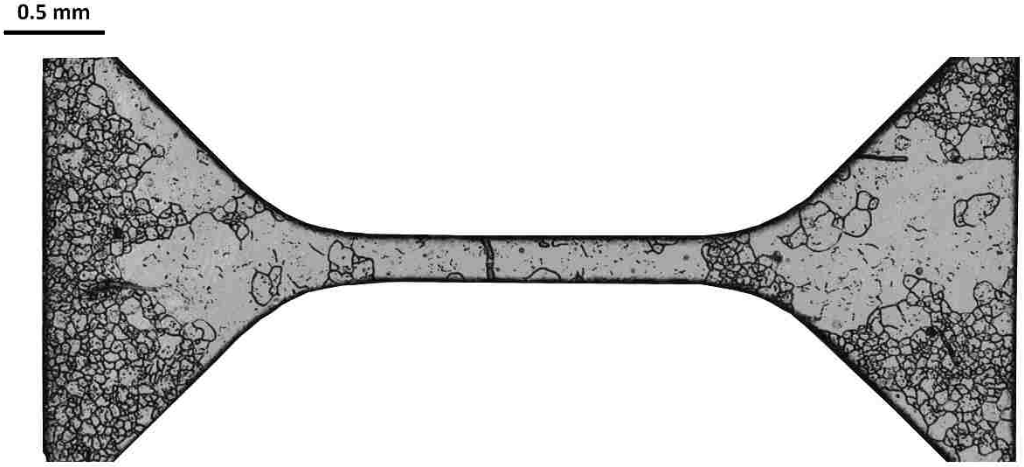

Figure 5.4. Optical micrograph of a tensile testing specimen with dogbone shape, after extraction by wire EDM. Some grain boundaries can be seen to still be present in the gage section, despite the grain size reached by AGG.

Dealloying of the specimens was performed by a combination of free and electrochemical dealloying, in diluted and concentrated nitric acid solution. Details of the apparatus used for the creation of the np-Au structure can be found in section 3.2. During dealloying, the current flow was maintained below 70 $A.m^{-2}$ to prevent cracking of the structure, following observation by Okman *et al.*[133], [134]. This technique also minimized volume contraction as reported by Sun and Balk[53], so that the relative density of the specimen after dealloying can be directly determined from the atomic composition in the precursor alloy. Removal of the sacrificial element, silver, was monitored by measuring the mass loss throughout dealloying. The following process was used:

(1) Free dealloying in diluted HNO_3 (1 part acid, 2 parts distilled water), for 1 h.

(2) Electrochemical dealloying in diluted HNO_3 (1 part acid, 2 parts distilled water), for 72–96 h, depending on specimen thickness, geometry and mass loss.

(3) Electrochemical dealloying in diluted HNO_3 (1 part acid, 1 part distilled water) or in concentrated HNO_3, for 10–72 h depending on specimen thickness, geometry and mass loss.

Following this process, between 94 and 98% of the mass of silver was lost during dealloying. Final chemical composition was also verified by EDS and confirmed that only traces of silver could be detected. The np-Au structure morphology and the absence of cracks were observed in the SEM on the rupture surfaces, after mechanical testing. A typical np structure obtained by this technique can be seen in Figure 6.2.

An important morphological information that can be obtained during SEM observation is the diameter of the ligaments, commonly referred to as the ligament size in the literature. The ligament size does not represent the length of the ligament, but the diameter, and is an important feature to determine as will be seen in the subsequent sections. Measurement of the ligament size was performed on SEM micrographs, using ImageJ software. In np-Au, ligaments become larger as they approach the nodes at which they are connected. Measurement was taken at the narrowest region, as shown in Figure 5.5 and Figure 6.3. Because measurements of the ligament size are performed on a two-dimensional image, there is an error associated with this technique. Care was taken to image the sample with proper contrast and with the surface normal to the electron beam, to minimize the error inherent to this measurement method. Ideally, better determination of the ligament size can be attained using transmission electron tomography, so that the dimensions can be measured in a three-dimensional space[135], [136]. However, transmission electron microscopy necessitates the preparation of thin, electron transparent specimens, which would be challenging to prepare from a bulk, dealloyed specimen.

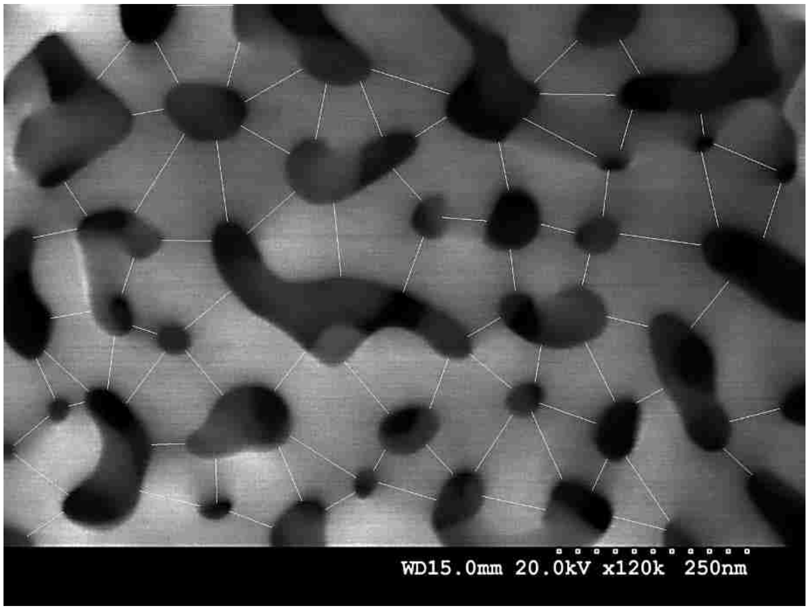

Figure 5.5. Typical np-Au structure obtained after dealloying of a bulk AuAg specimen. Determination of the ligament size is based on the measurement of the narrowest diameter along individual ligaments (micrograph adapted from[132], reprinted with permission from Taylor & Francis Group)

Not all ligaments within the structure have the same size, and the ligament size distribution can typically be described by a lognormal fit, as shown in Figure 6.3. Throughout this work, the ligament size used and reported was determined from the maximum of the lognormal fit of the size distribution. Therefore, although the ligament size is reported with a precision to the angstrom, the value is mathematically calculated, not measured. Such a measurement precision is obviously not possible using a SEM micrograph.

5.2. Experimental details and results

Tensile testing was performed using the KIT system, at strain rates ranging from 10^{-5} to 10^{-3} s^{-1}. Care was taken to align the specimen in the grips and to have the axis of the gage aligned with one axis of the camera, so that the deformation of the gage is aligned in the camera's field of view. If the camera is placed at an angle, the deformation will have horizontal and vertical components on the optical micrographs taken along the test, complicating the strain determination. Tensile tests were conducted until the specimens ruptured. The sample failed in a brittle manner and no plastic deformation was detected macroscopically, as can be seen on a typical stress-strain curve, with multiple load-unload cycles, in Figure 5.6a. Stress was calculated from the load data, and DIC was used to determine strain values in the longitudinal and transversal direction. Consequently, Young's modulus and Poisson's ratio were determined from the optical micrographs recorded along the tests.

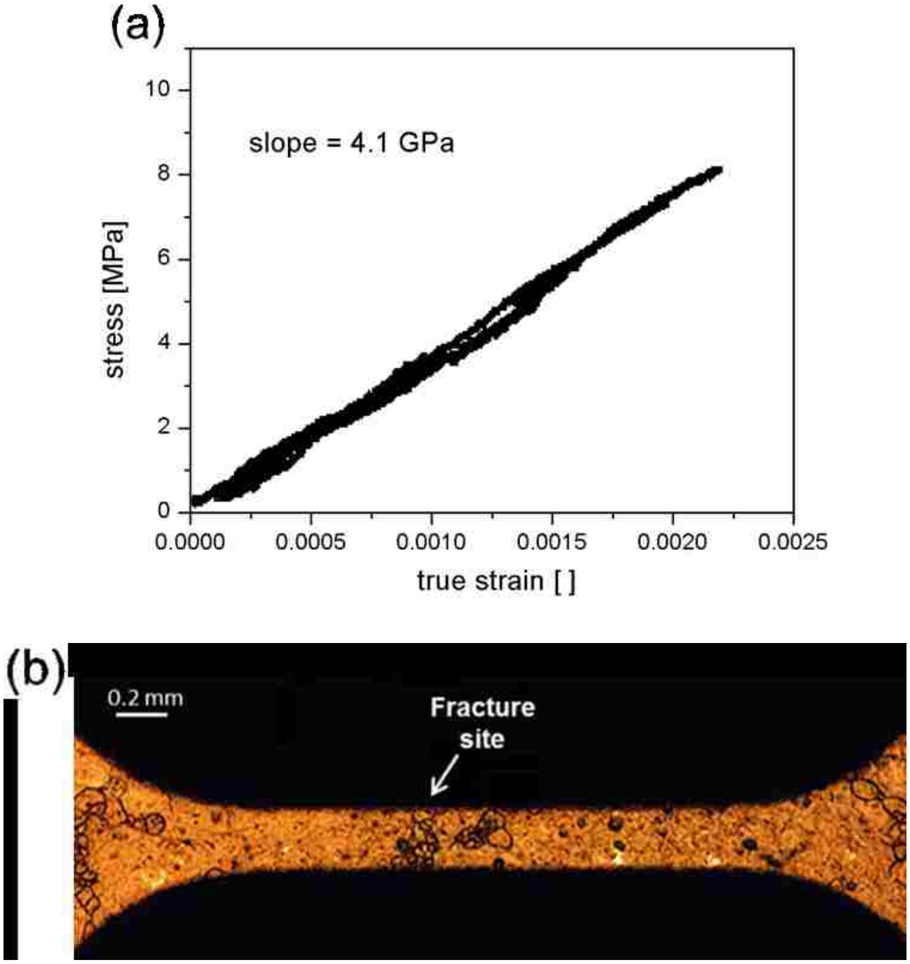

Figure 5.6. (a) Stress-strain curve calculated from the data recorded during the tensile test of a pseudo-single crystalline np-Au specimen. (b) The sample fracture initiated on grain boundaries remaining in the precursor alloy after AGG, and retained during dealloying. (from[132], reprinted with permission from Taylor & Francis Group)

For this set of np-Au pseudo-single crystalline specimens, an average yield/fracture strength value of 7.9 MPa was measured, with values ranging from 5.2 to 12.1 MPa. The average calculated Young's modulus and Poisson's ratio were 6.25 GPa (values ranging from 4.1 to 7.3 GPa) and 0.225 (values from 0.22 to 0.23), respectively.

It was clearly observed that the brittle fracture initiated on the grain boundaries still present in the specimen despite AGG and dealloying, as shown in Figure 5.6b. Therefore, rupture occurred at a random position along the gage section for each sample, where stress concentration on existing defects, grain boundaries in this case, led to premature failure. Rupture on remaining grain boundaries was confirmed by observation of the fracture surfaces in the SEM. Different grains can clearly be seen on the images and indications of both intergranular and transgranular fracture regions can be observed. Regions where intergranular rupture occurred does not show any traces of ligament deformation and appear to be totally unchanged. These regions do not appear to have been carrying any load during tensile testing and ligaments are smooth and identical to the freshly dealloyed np structure. In contrast, other regions show extensive plastic deformation and necking of the individual ligaments. The latter observation confirms that although the specimen fractured in a brittle manner at the macroscopic scale, gold ligaments plastically deforms under load before rupture. The different regions can be clearly noticed in the SEM as, at low magnification, transgranular rupture regions present a rough surface (indicated by a white arrow on Figure 5.7) whereas regions where intergranular rupture occurred are smooth. Another SEM micrograph is shown in Figure 5.8, at lower magnification.

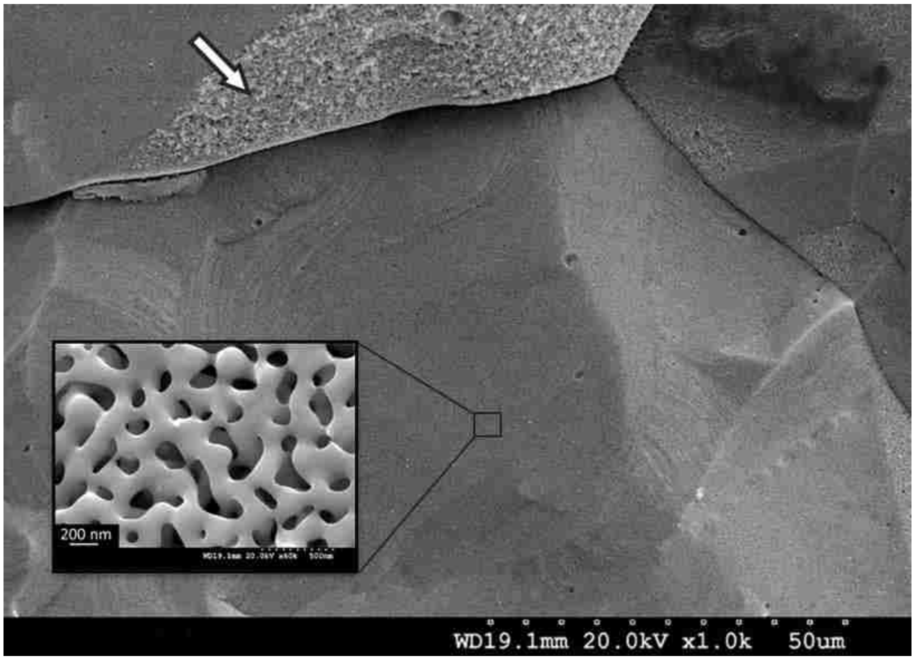

Figure 5.7. SEM micrograph of the fracture surface of a pseudo-single crystalline np-Au specimen after rupture in tension. Regions where transgranular rupture occurred appear rough with extensive ligament deformation (indicated by the white arrow). In contrast, regions where intergranular rupture took place appear smooth. (from[132], reprinted with permission from Taylor & Francis Group)

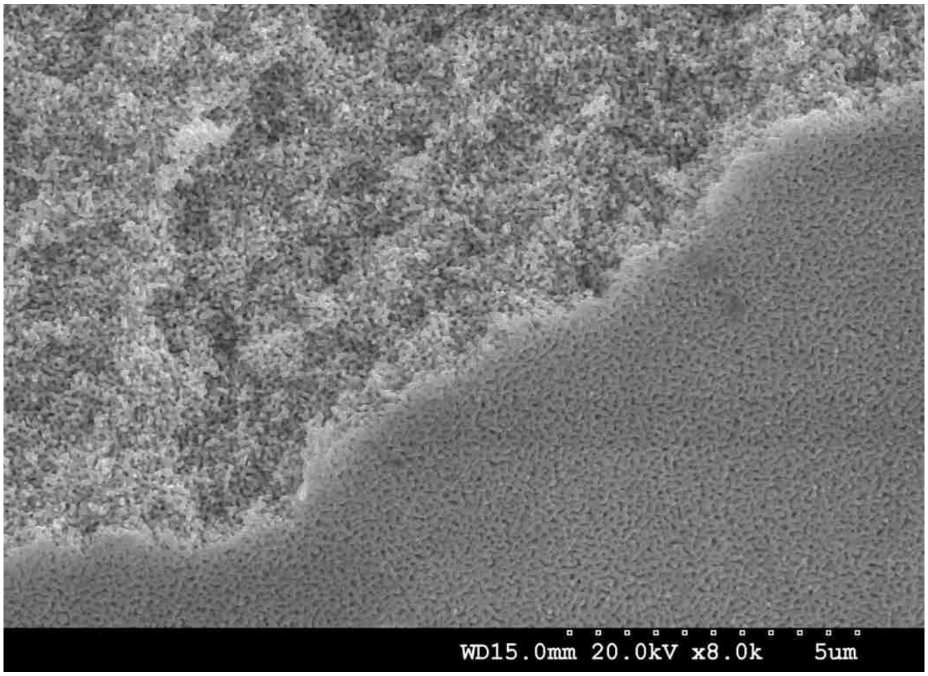

Figure 5.8. SEM micrograph of a specimen ruptured in tension, illustrating the difference between regions that underwent deformation and others that did not bear load.

5.3. Discussion

The objective of this work was to determine the mechanical properties of np-Au, mainly the Young's modulus, yield strength and Poisson's ratio, in tension. Determination of the Young's modulus and the Poisson's ratio was successful, and are in line with previous results reported by Balk *et al.*[86] for polycrystalline np-Au made from $Au_{30}Ag_{70}$. They reported an average elastic modulus of 3.15 GPa in tension and a Poisson's ratio of 0.15. Unfortunately, yield/rupture strength values were also comparable to those measured on polycrystalline np-Au with grain dimensions ranging from 20 to 250 µm. Balk *et al.* reported an average yield/ruptured strength of 10.7 MPa in tension, but observed that rupture was initiating on region where stress was concentrating, such as the fillet at the end of the gage section, near the portion of the specimen that is supported in the grip. Also, after premature failure of a specimen in the fillet, they re-loaded the specimen and rupture then occurred in the gage section, at a 30% higher stress. This indicates that rupture of np-Au takes place on the weakest portion of the sample, whether that weak spot is created by specimen geometry or by microstructural defects (for instance grain boundaries). These observations are consistent with those made during the testing of pseudo single crystalline specimen in this work.

Premature failure occurs in np-Au in localized regions where stress is concentrated. The observations in the SEM confirmed that rupture occurred along the grain boundaries, as the failure was determined to be partly intergranular. Although most of the gage section in AGG grown specimens was single crystalline, stress during testing was concentrated on the remaining grain boundaries. After dealloying, some of the initial grain boundaries were found to be unfused, creating 2D gaps between np-Au grains and acting as cracks within the specimen's gage section. Such open grain boundaries can be seen in Figure 5.9. Because these cracks are regions where stress can locally be concentrated, these open grain boundaries likely were at the origin of the failure. Also, since the structure appear to not have been cohesive at the grain boundaries after dealloying, these regions did not appear to carry any load during the test, meaning that a reduced cross-sectional area was carrying it.

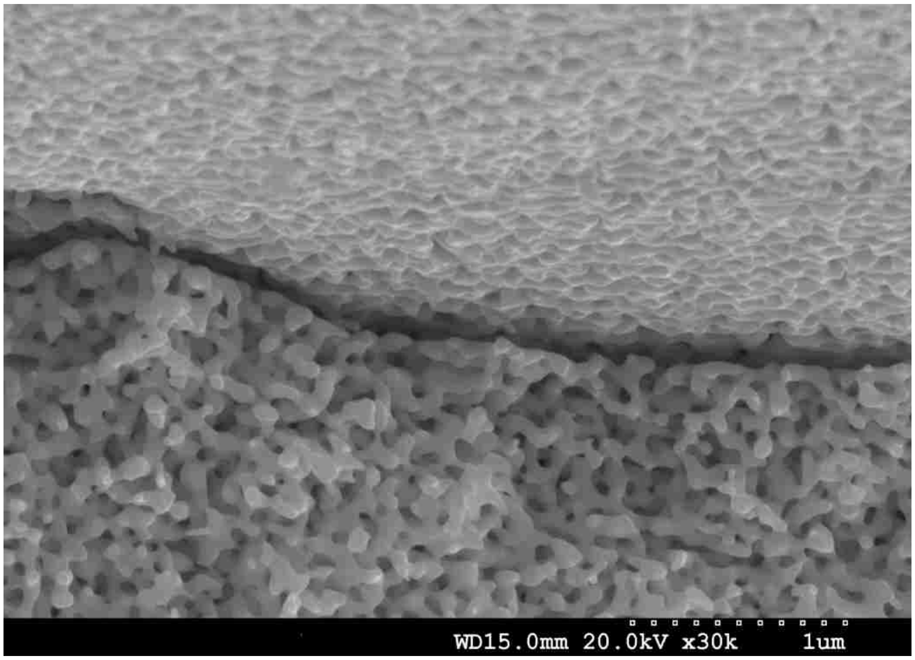

Figure 5.9. SEM micrograph of an unfused grain boundary, after dealloying, observed at the rupture surface of a pseudo-single crystalline specimen tested in tension.

Consequently, fracture strengths values determined on pseudo-single crystalline specimens are underestimations of the true strength of np-Au. The real stress at rupture at that position in the specimen was higher than calculated based on the specimen geometry. Figure 5.10 shows the fracture surface of one of the pseudo-single crystalline np-Au specimen after rupture in tension. For clarity, the regions that did not seem to bear any load and remain seemingly unaffected after the test are colored in red. Regions that exhibits extensive ligament plasticity and that most likely carried the load in tension are colored in blue. Using ImageJ software, the surface of the blue regions can be found to account for ~35% of the cross-section area in this field of view. Using the average yield/fracture strength value of 7.9 MPa, and using only the blue region as the surface on which the tensile force was applied, an equivalent stress of nearly 23 MPa can be calculated. This value, while closer, is still lower than the values determined by other techniques and reported in the literature, by a factor of ~ 5.

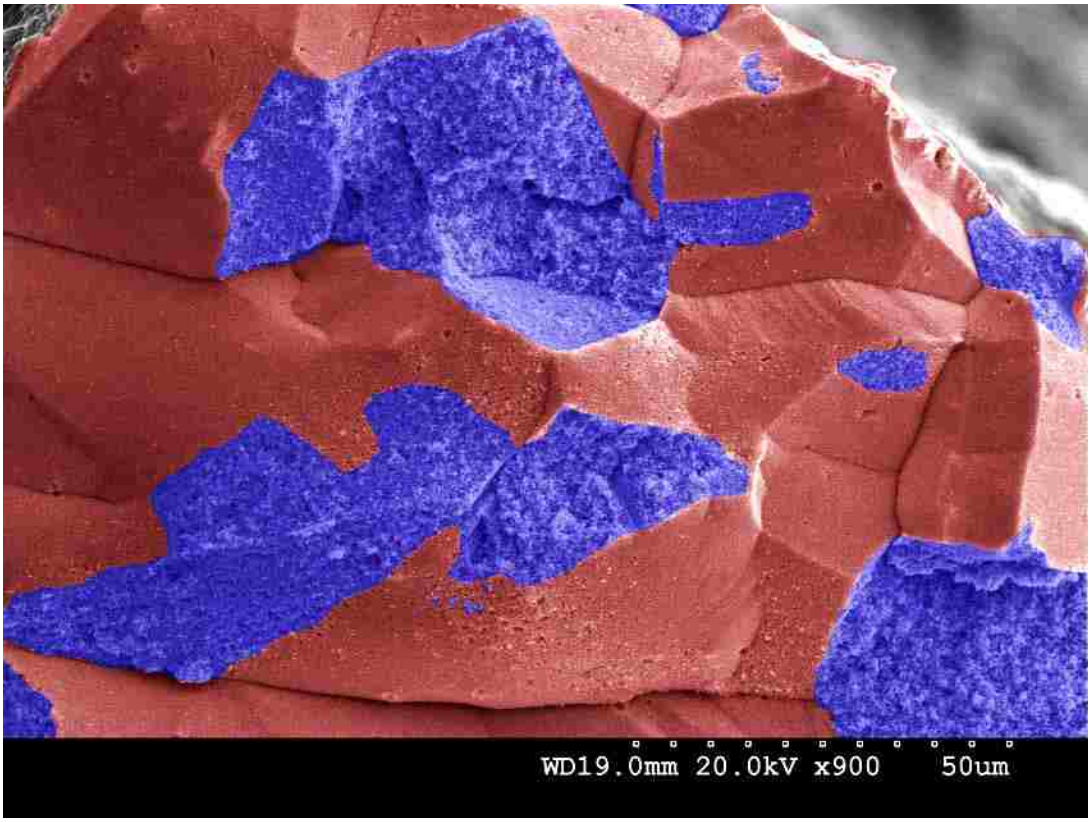

Figure 5.10. SEM micrograph of the fractured surface of a pseudo-single crystalline np-Au specimen tested in tension. Regions exhibiting ligament plasticity are colored in blue, while regions seemingly unloaded during the test are colored in red.

To be able to experimentally measure the real yield strength of np-Au in tension, and because creating a fully single crystalline gage section by AGG was eventually unsuccessful, specimens extracted from grown single crystals were tested. The specifics of specimen fabrication, experimental conditions and results are detailed in section Chapter 6.

Chapter 6 : Mechanical testing of single crystalline np-Au

As described in Chapter 5, rupture in np-Au initiates on the weakest portion of the sample, then catastrophically propagates to the rest of the structure. Macroscopically, this catastrophic failure appears brittle even though microscopically, np-Au ligaments demonstrate some plasticity up to failure. Consequently, because the structure will only be as strong as its weakest region, any defect in the material on which stress will be able to concentrate will lead to premature failure. Thus, measuring yield/fracture strengths on a polycrystalline specimen will always lead to underestimated values of the real strength of np-Au. It is however important to point here that the strength values measured on polycrystalline or pseudo-single crystalline are relevant, if one needs to know the strength of np-Au as a structural material. Because the prospect of using single crystalline np-Au for applications that necessitate more than a few grams of material is low, the mechanical properties of polycrystalline np-Au are of significant importance. However, full understanding of np-Au behavior or of the relations between morphology and mechanical properties can only be attained by measuring the intrinsic properties of np-Au.

Those properties can only be determined when suppressing the sources of stress concentrations such as defects and grain boundaries. Therefore, tensile tests detailed in this chapter were performed on single-crystalline np-Au specimens. The values measured during these tests show the real strength of np-Au and have been used to determine new scaling equations that relate the yield strength of np-Au to the yield strength of bulk, dense gold, as detailed in Chapter 7.

6.1. Specimen fabrication and characterization

Because the creation through AGG of grains large enough to extract dogbone shaped tensile testing specimens was unsuccessful, a single crystal (20mm long, 6mm diameter) with composition $Au_{33}Ag_{67}$ was purchased from Metal Crystals and Oxides Ltd. (Harston, Cambridgeshire, United Kingdom). The single crystalline rod was grown with random orientation but one end was machined to indicate the (110) orientation (see back-reflection Laue diffraction pattern in Figure 6.1). Specimens were extracted from the single crystal by wire EDM at the Karlsruhe Institute of Technology. The shape of the specimen was first extracted through the rod, with the length of the gage aligned with the longitudinal axis of the single crystalline rod. The precise crystal orientation of the gage was not taken into account during extraction of the specimen, as the orientation is believed not to influence the mechanical properties for np-metals (the ligaments are spatially randomly oriented relative to the load axis). After that first step, a specimen was obtained with a thickness close to the diameter of the single crystal. This thick specimen was then sliced through the thickness to create several identical specimens. Final specimens' thickness of 220 µm was obtained with gage length of 1.9 mm and gage width of 475 µm, as can be seen in Figure 6.2.

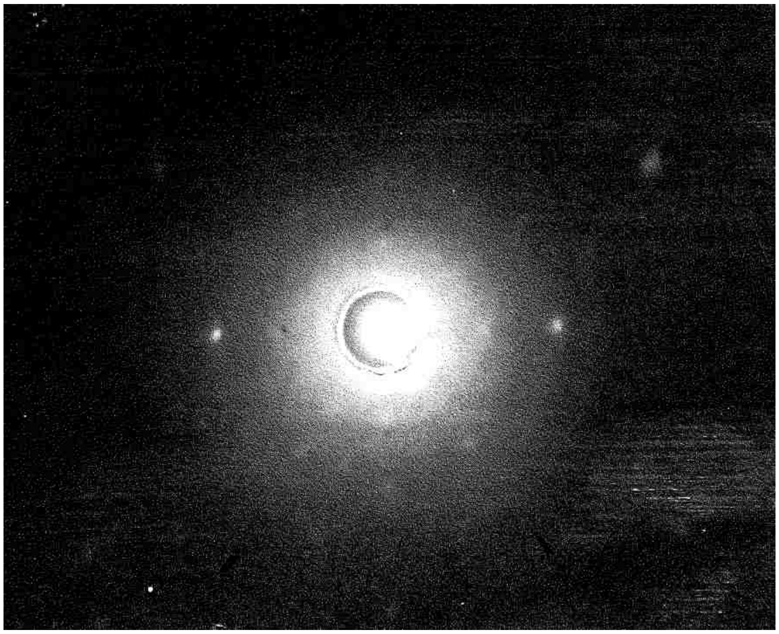

Figure 6.1. Back-reflection Laue diffraction pattern of (110) from the AuAg single crystal used to extract tensile testing specimens (photograph provided by Metal Crystals and Oxides Ltd.)

Because wire EDM was used to cut the specimens, they presented a rough surface with sharp peaks. Using an optical compound microscope and focusing at the top of the peak then at the bottom, a surface roughness of ~12 µm (peak-to-valley) was estimated. Also, because EDM was used to not only cut the shape of the specimen but also to slice this shape into individual specimens, the surface roughness left by EDM was not only present on the contour of the specimens but also on its main surfaces (all sides). This is different than for the pseudo-single crystalline specimen where the samples were extracted from slices created by rolling, and for which only the contour presented EDM roughness. The roughness can be seen in Figure 6.2 where the some regions appear as white spots due to difference in light reflection. The appearance of the surface is not an issue for DIC tracking of the deformation, and is actually beneficial, as the roughness creates features that can be easily tracked from one optical micrograph to the next.

Specimens were dealloyed following an identical setup and a similar process as the one described in Chapter 5, with some minor modifications in step duration and acid dilution. During dealloying, the current density was kept below 70 $A.cm^2$ to minimize cracking and volume contraction as described in Chapter 5. Based on the specimen mass loss after dealloying, nearly all the silver was removed (97 to 100% of the silver mass was lost) with the following process:

(1) Free dealloying in diluted HNO_3 (1 part acid, 2 parts distilled water), for 2 h.

(2) Electrochemical dealloying in diluted HNO_3 (1 part acid, 2 parts distilled water), for 72h.

(3) Free dealloying in concentrated $HNO_3$for 2 h.

(4) Electrochemical dealloying in concentrated $HNO_3$for 24h.

Complete dealloying of the specimen was further verified by EDS on the fracture surface of the specimen after testing, and no silver was detected. An SEM micrograph showing the crack-free nanoporous structure of a dealloyed specimen is shown in Figure 6.2.

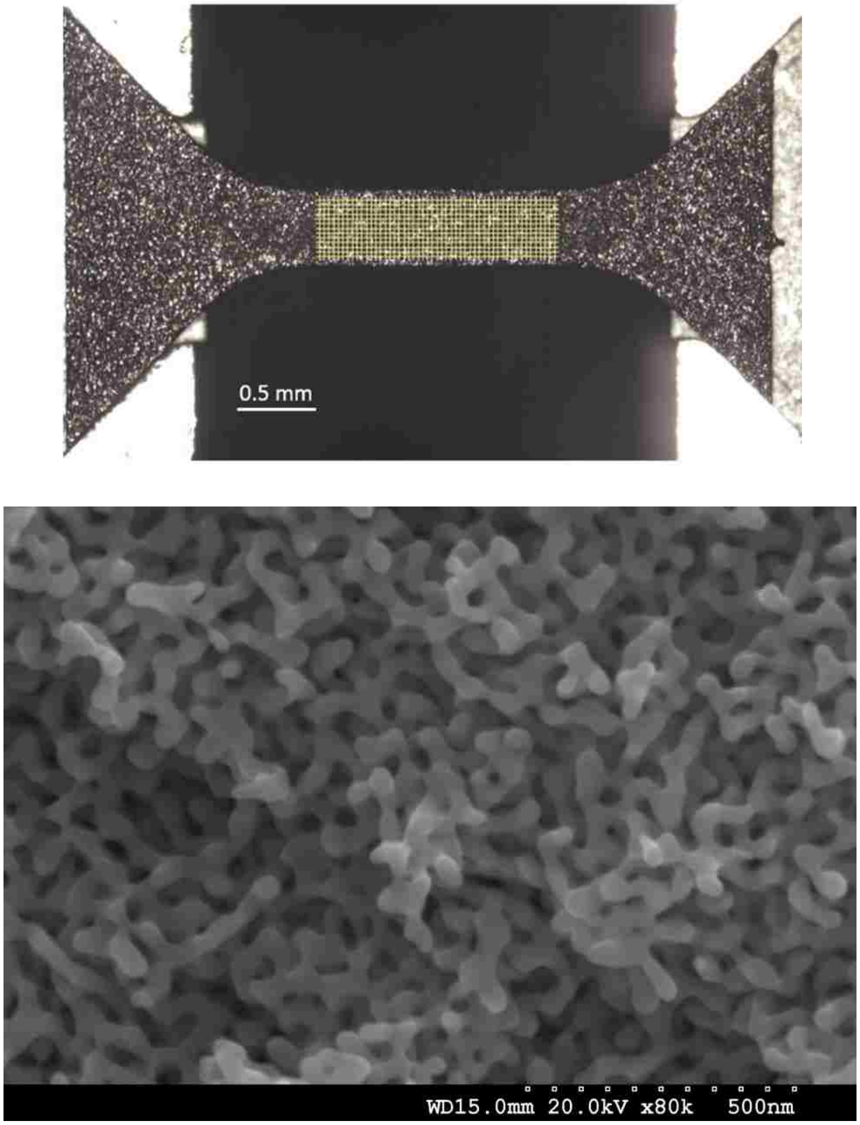

Figure 6.2. (top) Optical micrograph of a single crystalline np-Au small-scale tensile specimen in the grips, before testing. The grid used to track deformation through DIC can be seen superimposed on the gage section of the specimen (hatched region) (from[132], reprinted with permission from Taylor & Francis Group); (bottom) SEM micrograph of the typical np-Au structure obtained after dealloying of a AuAg specimen.

As detailed in Chapter 5, the ligament size was measured using ImageJ, taking the narrowest portion of the ligament. The value used to represent the ligament size is taken as the maximum of the lognormal fit of the ligament size distribution, as shown in Figure 6.3. Specimens were found to have ligaments sizes ranging from 32 to 65 nm, and a relative density of 0.33 was used since no volume contraction was detected after dealloying. Details for each specimen can be found in Table 6.1.

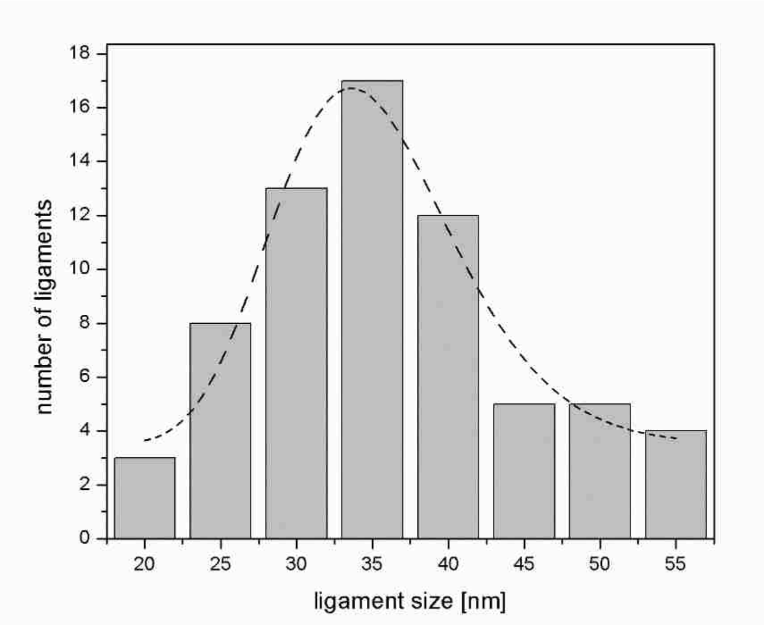

Figure 6.3. Typical ligament distribution within a np-Au specimen. Ligament size is determined from the maximum of the lognormal fit of the size distribution. (from[132], reprinted with permission from Taylor & Francis Group)

6.2. Experimental details and results

Testing was conducted on the small-scale testing setup at the Karlsruhe Institute of Technology already used for tensile testing of the pseudo-single crystalline specimens, at different strain rates ranging from 10^{-3} to 10^{-6} s^{-1}. Strain was determined from the optical micrographs recorded during the test and stress was calculated from the force recorded with the load cell and the dimension of the specimen's cross-section.

The first single crystalline specimen was tested with a strain rate of 10^{-5} s^{-1} and ruptured without showing any macroscopic plastic deformation. This agrees with observations from previous tests on polycrystalline and pseudo-single crystalline specimens. A Young's modulus of 4.4 GPa and an average Poisson's ratio of 0.24 were determined from the linear portion of the stress-strain and transverse vs. axial strain curves shown in Figure 6.4. Young's modulus and Poisson's ratio were found to vary along the test, as the stress-strain curve was initially non-linear at the beginning of the test. Failure occurred at 18.6 MPa, more than twice as high as the average yield/fracture strength calculated for pseudo-single crystalline specimens.

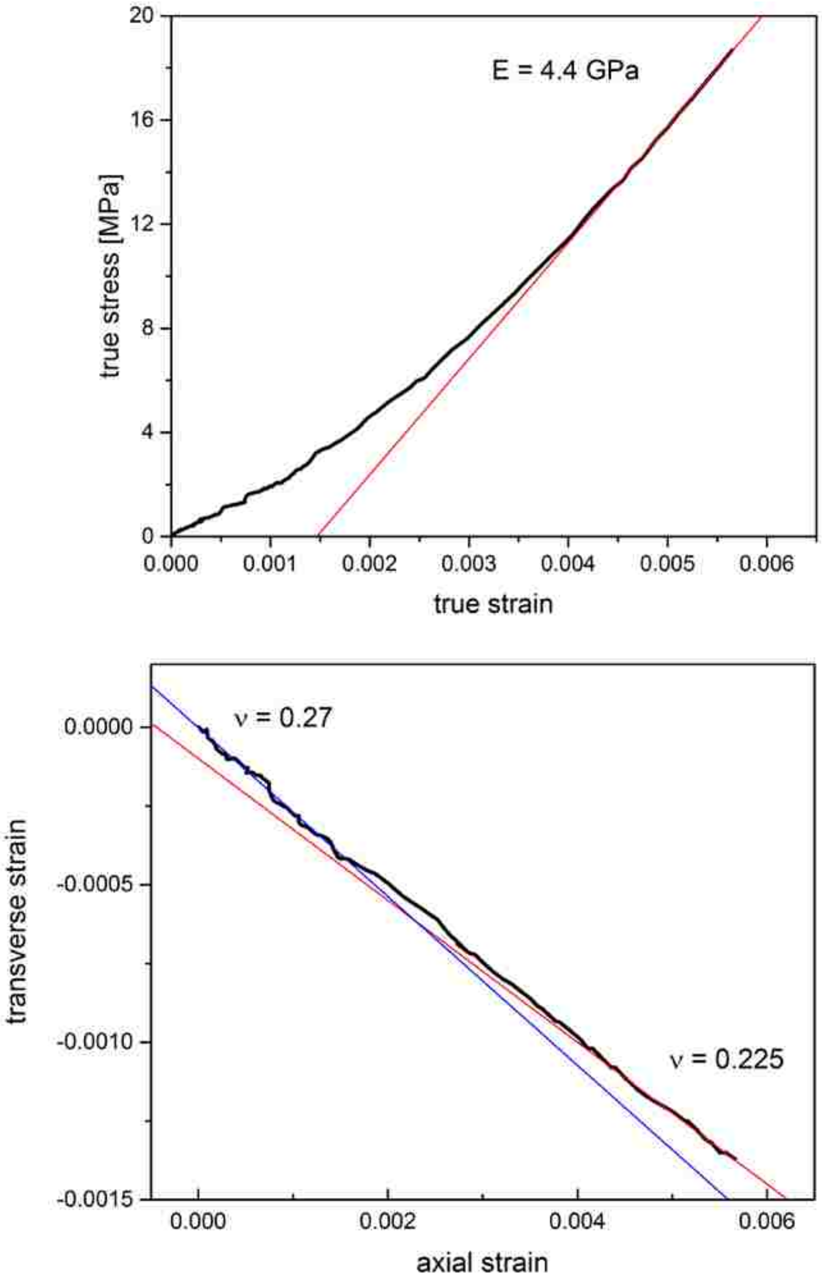

Figure 6.4. (top) Stress-strain curve calculated from data recorded during tensile testing of a non-annealed single crystalline np-Au specimen. Young's modulus is calculated from the linear portion of the curve, just before failure; (bottom) Transverse vs axial strain curve from which Poisson's ratio can be extracted. The value is found to decrease as the stress-strain curve becomes linear.

The fracture surface was observed in the SEM and it appeared that fracture initiated at the surface of the specimen, probably because of the sharp features (surface roughness) still present after dealloying. The fracture initiation site can be seen at the bottom right corner of the fracture surface shown in Figure 6.5.

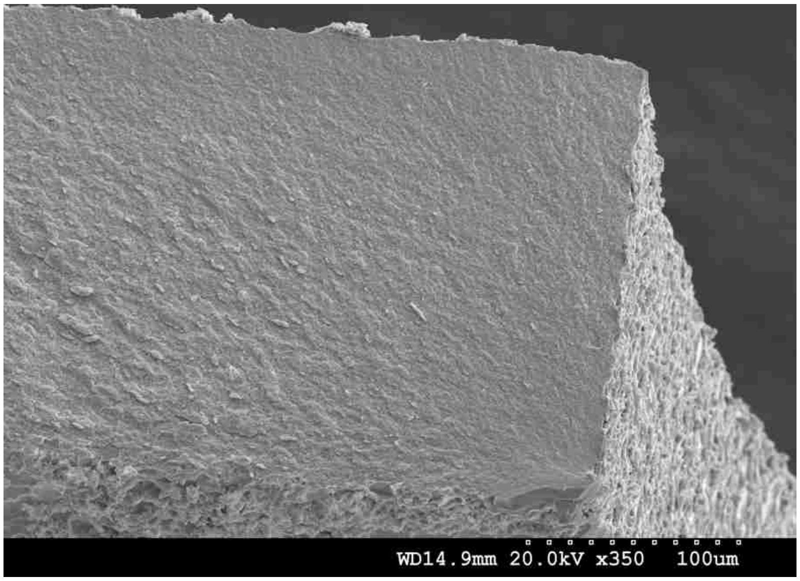

Figure 6.5. SEM micrograph from the fracture surface of the first single crystalline np-Au specimen, not annealed prior to dealloying.

Consequently, to minimize the sharpness of the features at the surface and also to make sure that precursor alloy composition was homogeneous throughout the whole specimen before dealloying, all the other specimens were annealed at 950ºC for 20 h prior to dealloying. The sharpness of the features at the specimen surface decreased and the peaks appeared to be more rounded. Using the same method as described above, a roughness of 8 µm was estimated (peak-to-valley).

A typical stress-strain curve calculated from the data recorded during tensile testing of one of the specimens annealed prior to dealloying is shown in Figure 6.6. This curve is similar to the stress-strain curve calculated from the tensile testing of the non-annealed single crystalline specimen. At the onset of the test, the curve is non-linear but slowly becomes linear as the specimen approaches rupture. For all specimens, rupture was sudden and catastrophic, with no macroscopic plastic deformation. Young's modulus values were determined from the linear region of the stress-strain curves and Poisson's ratio was determined from the corresponding region, from the transverse vs. axial strain curves. Strain rate was found to have no significant effect on the mechanical properties, in the range tested (10^{-3} to 10^{-6} s^{-1}), as can be seen from values in Table 6.1. Young's modulus values ranging from 3.8 to 5.4 GPa were calculated, with an average value of 4.5 GPa. Poisson's ratio values between 0.17 and 0.28 were calculated, with an average of 0.22.

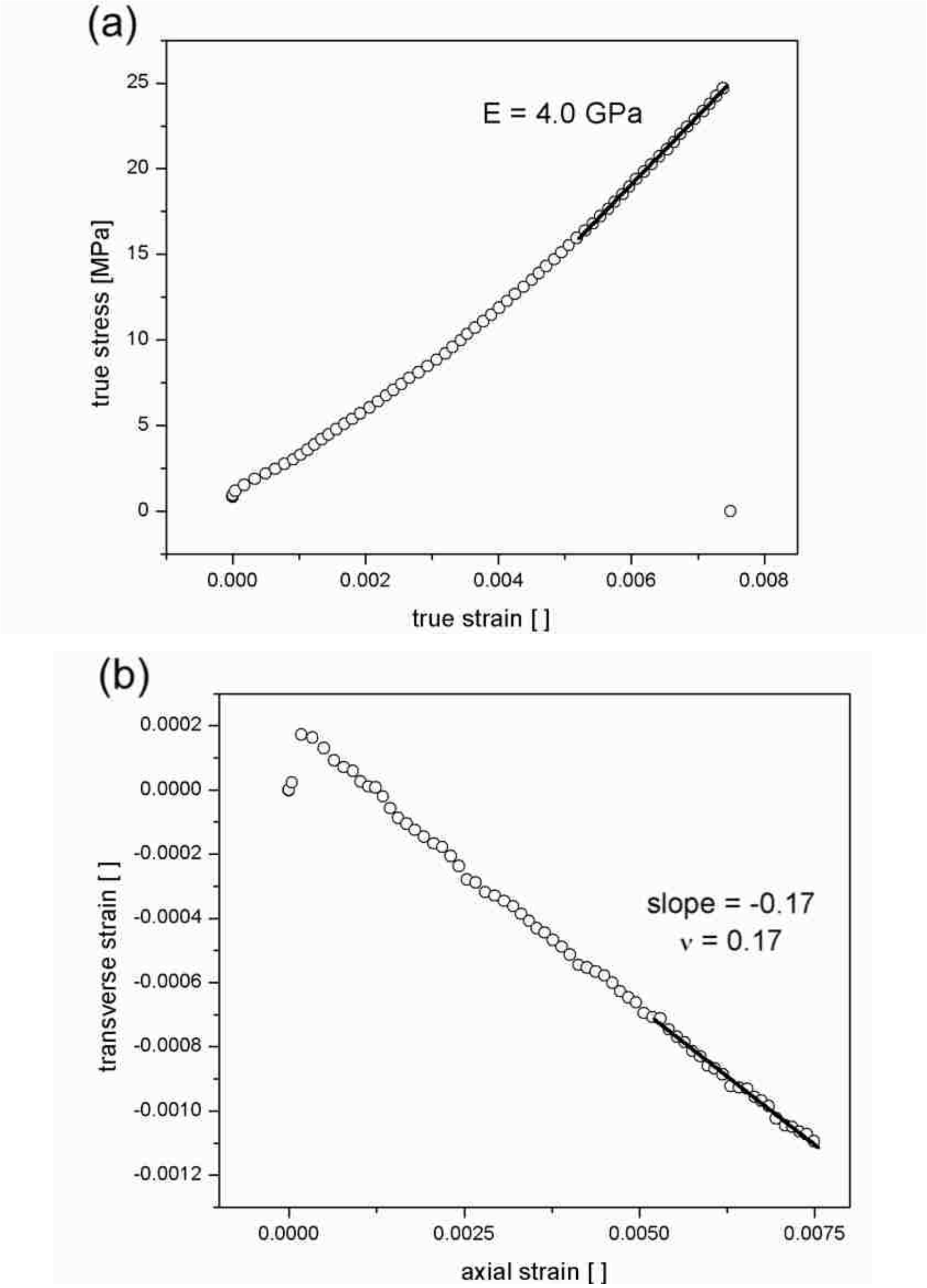

Figure 6.6. (a) Stress-strain curve calculated from data recorded during tensile testing of specimen 1-5; (b) corresponding transverse vs axial strain curve. Young's modulus and Poisson's ratio are calculated from the linear region of the curves. For both plots, only one every four datapoint is shown to improve clarity. (from[132], reprinted with permission from Taylor & Francis Group)

Observation of the fracture surface in the SEM revealed that load was carried by the whole cross-section during the test and up to failure. It can clearly be seen (Figure 6.8) that plastic deformation of individual ligaments before rupture took place throughout the whole gage cross-section. The contrast with Figure 5.10 is clear and shows that rupture was not intergranular, on grain boundaries left in the specimen after dealloying. Similarly to the observations made on fracture surfaces of pseudo-single crystalline specimens, individual ligaments exhibited plastic deformation and necking before failure. Most ruptured, elongated ligaments were found to be aligned with the loading axis of the tensile test. However, for the ruptured ligaments that were found not to be aligned with the load axis, limited plasticity and no necking were observed, with appearance of a shearing induced rupture, as seen in Figure 6.9. Also, it can be seen in Figure 6.7 that below the heavily deformed surface, the ligaments only a couple cells away from the fracture surface appear to be intact. This demonstrates how localized rupture is in np-Au, and failure is concentrated only on the weakest region of the specimen, while the rest of the sample remains undamaged.

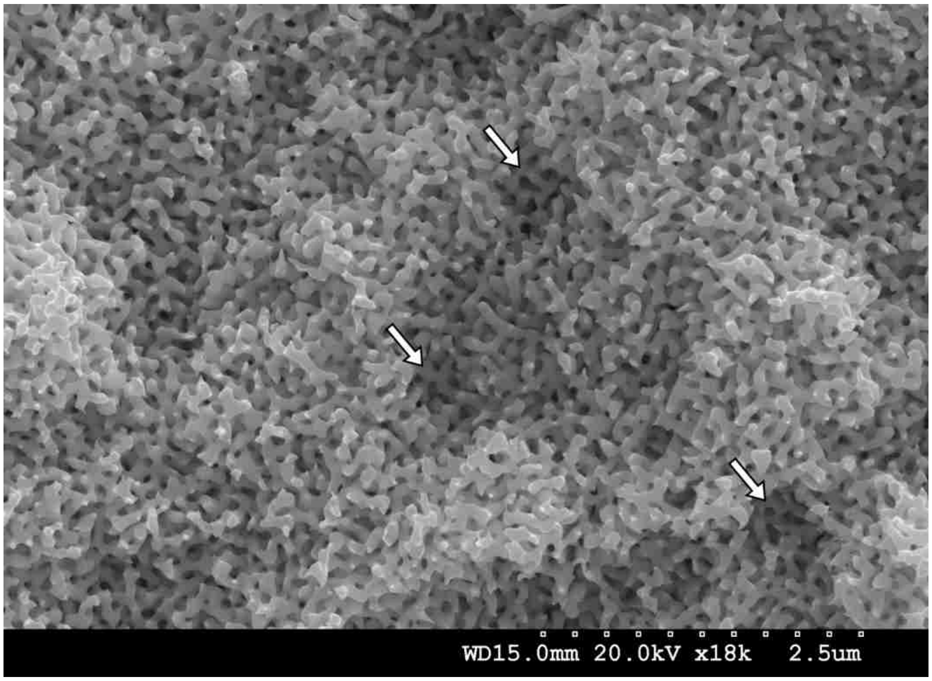

Figure 6.7. SEM micrograph from the rupture surface of a np-Au specimen ruptured in tension. Regions only a couple cells below the rupture surface are found to be intact (indicated by white arrows).

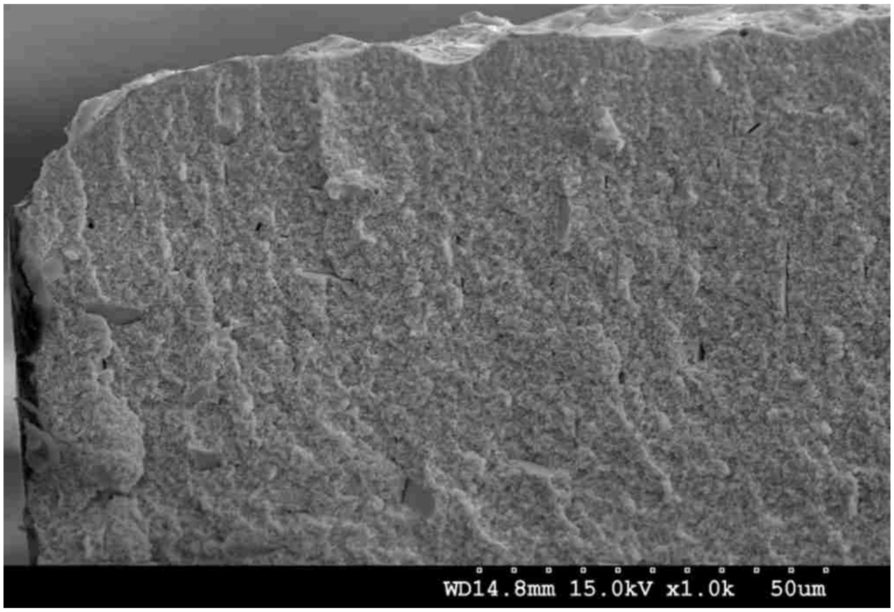

Figure 6.8. SEM micrograph of the fracture surface of a single crystalline np-Au specimen that was annealed prior to dealloying. The whole cross-section shows deformed ligaments, indicating that the load was carried by the whole gage during testing and up to rupture. Some empty regions can be seen, which were likely impurities or silver rich pockets before dealloying.

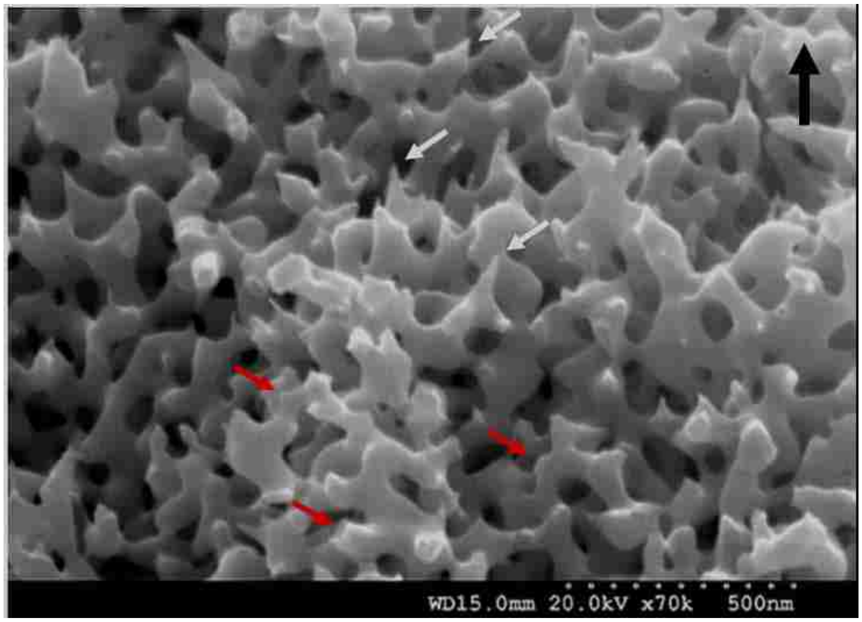

Figure 6.9. SEM micrograph of the fracture surface after tensile testing of a single crystalline np-Au specimen. The loading axis is indicated by the black arrow in the top right corner. Most ligaments show extensive plastic deformation and necking in the direction of the load (typical regions indicated by a white arrow) while others, not aligned with the load axis do not (red arrows). (adapted from[132], reprinted with permission from Taylor & Francis Group)

Some empty, localized regions can be seen in the SEM micrograph in Figure 6.8 (and with higher magnification in Figure 6.10), which were likely some impurities or silver rich pockets present in the single crystal that were not eliminated by the annealing step. These regions account for a very small part of the specimen and were not likely to influence rupture of the specimen, as it was found that failure primarily occurred in the curved transition region between the gage and the ear of the specimen. For some specimens (1-3 and 1-4), premature rupture took place inside the grip and the test did not run to completion. For the other specimens, rupture was found to occur at strengths ranging from 21.2 to 28.4 MPa, with an average value of 25.2 MPa. Results details are reported in Table 6.1. A stress concentration of ~ 11% was estimated in the region of rupture, using finite element simulations performed with Ansys®, not accounting for surface roughness. Therefore, although the measured values are much higher than values measured on polycrystalline and pseudo-single crystalline specimens previously tested, the yield/fracture strength reported for single crystalline np-Au are probably still slightly underestimating the real value.

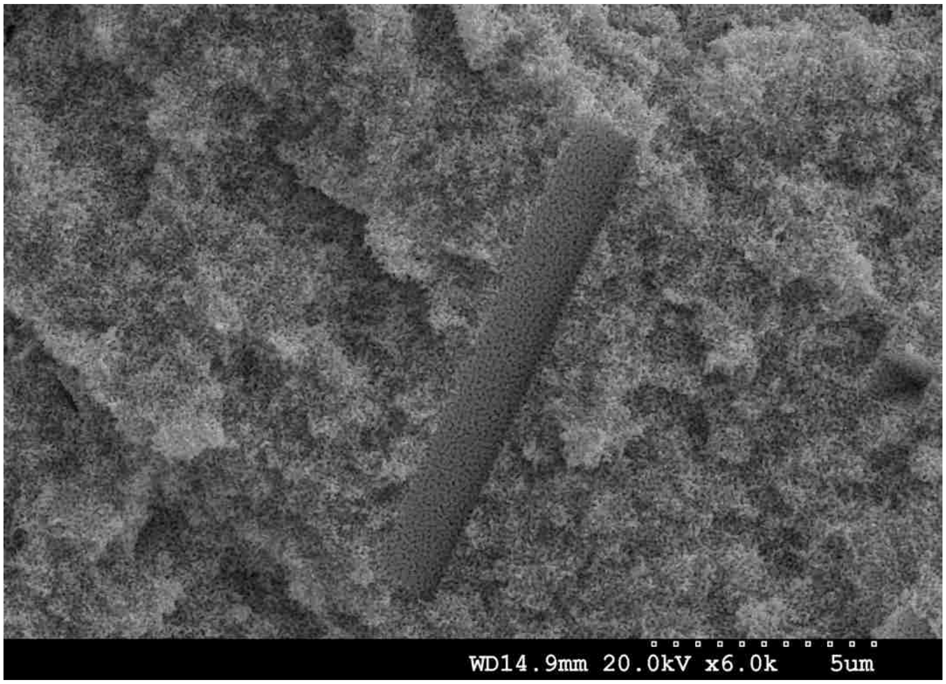

Figure 6.10. SEM micrograph of an empty pocket found at the fracture surface of a specimen tested in tension.

Table 6.1. Summary of tensile test results for single crystalline nanoporous gold specimens.

Sample ID	Ligament size [nm]	Yield strength [MPa]	Young's modulus [GPa]	Poisson's ratio	Strain rate [s^{-1}]
1-2	32.2	28.4	4.9	0.18	10^{-5}
1-3	58.5	15.8	3.9	0.22	10^{-4}
1-4	58.8	18.6	5.0	0.27	10^{-5}
1-5	65.3	24.9	4.0	0.17	10^{-4}
1-6	58.7	25.8	*	0.23	10^{-5}
1-7	33.4	25.3	4.5	0.18	10^{-3}
1-8	55.9	25.3	3.8	0.28	10^{-3}
1-10	59.5	21.2	5.4	0.24	10^{-6}

* Young's modulus could not be determined from the experimental dataset for this specimen.

6.3. Compression testing of single crystalline np-Au

A compression test was conducted on one of the tensile specimens that broke in the transition region between the gage and the ear (sample 1-8). The specimen's end that was broken was placed against the flat part of the opposing grip and the sample was pushed against this flat wall. The test was conducted until the specimen buckled and rotated out of axis, which corresponds to the sudden decrease in stress at the end of the plot in Figure 6.11, for a stress above ~ 32 MPa.

A Young's modulus of 18 GPa was calculated which is almost 5 times higher than the modulus measured during the tension test and seems incompatible with the results obtained during previous compression tests on polycrystalline specimens, where the elastic modulus determined in tension and compression were comparable[86]. Moreover, a Poisson's ratio of 0.46 was calculated which is even higher than the Poisson's ratio of dense gold (0.42). However, inspection of the linear portion of the stress-strain plot reveals sudden spike of the stress (or strain) at regular strain intervals, which are incompatible with the continuous deformation applied by the piezoelectric actuator. It is therefore clear that the strain was not properly determined for that particular test, in contrast with the results from the other tests where this curve shape during the elastic regime was not observed. Several sources of error have been considered including light reflection on the specimen's surface or table vibration, but no clear cause was determined to explain the shape of the plot.

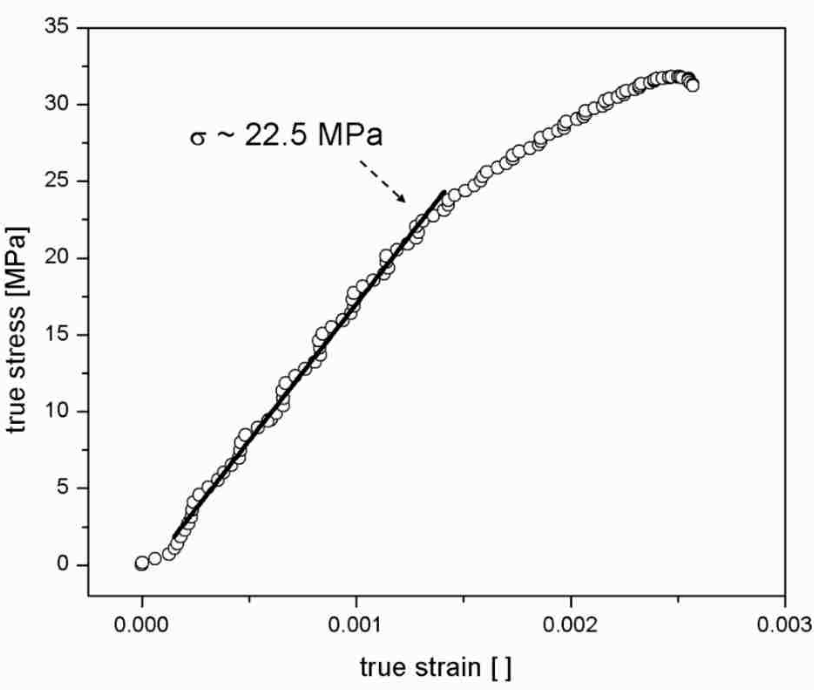

Figure 6.11. Stress-strain plot obtained during compression testing of a np-Au specimen previously tested in tension up to rupture. Although strain values were not properly determined and the specimen buckled at ~32 MPa, the load values are still valid. (from[132], reprinted with permission from Taylor & Francis Group)

Although calculation of the Young's modulus and Poisson's ratio were ultimately not possible based on this test, the yield strength value determined from this test is still valid. Since the specimen was properly aligned and did not rotate nor buckled until after yielding, the load measured was not influenced by the error in strain measurement. A yield strength of 22.5 MPa was determined, ~ 11% lower than value determined from the tensile test.

6.4. Fracture toughness

As previously mentioned, rupture of the specimens during tension tests preferentially initiated at the transition region between the gage and the ear of the specimen. For some specimens, it was possible to correlate the fracture location and a specific spot at the surface where the roughness formed a “notch”. Considering this notch caused by the surface roughness as a pre-crack from which fracture initiated, it was possible to estimate the fracture toughness of np-Au. Because of the size of the pre-cracks, error in the determination of the notch dimensions using optical microscopy was admittedly above average. Besides, because the specimen’s surface images were recorded with a top 2D view, it was not possible to verify the perpendicularity between the notch and the gage axis. Nevertheless, estimations of the fracture toughness K_{Ic} was made based on the yield/fracture strength measured experimentally σ^*, assuming a plate with edge crack of length a, with $K_{Ic} = 1.1\sigma^*\sqrt{\pi a}$, and using this method, an average fracture toughness of 0.24 MPa.m$^{1/2}$ was calculated. It is important to note that if the notch observed at the specimen surface was not continuous through the whole thickness of the gage, the pre-crack could be considered as a semicircular corner crack. In this case, the fracture toughness can be calculated with $K_{Ic} = (1.12)^2\frac{2}{\pi}\sigma^*\sqrt{\pi a}$, and the calculated value would decrease by ~27%.

Based on Irwin’s relation, a critical value of the crack extension force G can be calculated, at which fracture will occur. Because G corresponds to the rate of change of energy with crack depth, it is also commonly called the strain energy release rate. In plane strain condition, fracture occurs when $G = G_c$ and is related to the critical stress by

$$\sigma_c = \sqrt{\frac{EG_c}{\pi a(1-\nu^2)}} \qquad \text{Equation 6.1}$$

Taking $\sigma_c = \sigma^*$ at rupture, we obtain

$$K_{Ic} = 1.1\sqrt{\frac{EG_c}{1-\nu^2}} \quad \text{Equation 6.2}$$

Using the average values determined for np-Au Young's modulus (4.5 GPa) and Poisson's ratio (0.22), a G_c value of 10 J.m^{-2} can be calculated.

6.5. Discussion

6.5.1. Deformation behavior

Tensile tests of single crystalline np-Au were successful, although residual surface roughness may have led to slight underestimations of the yield/fracture strength values. The typical shape of the stress-strain curves determined from experimental measurements present a non-linear region at the beginning of the tests. Part of this behavior can be attributed to proper positioning and aligning of the specimen within the grips, as the pre-load applied to the specimen before the test is generally not enough to guarantee proper seating in the grips. This region typically extends to strain of 0.4%, at which the stress-strain curve become linear and the Young's modulus can be extracted.

However, this transient re-alignment of the specimen in the testing apparatus does not solely explain the non-linear behavior. This upward curvature at the beginning of tensile testing of porous materials has been observed and reported before in the literature [104], and has been attributed to the progressive re-orientation of the cell-edges (ligaments) towards the applied load axis. At the beginning of the test, rotation of the ligaments which are not aligned with the tensile axis represents the main contribution to the overall elongation of the specimen. As the applied load increases, recruitment of non-aligned ligaments becomes more difficult, and deformation based on ligament re-orientation decreases, increasing the macroscopic stiffness of the sample. Once all possible re-alignments have occurred, elongation is mostly carried out by stretching of the aligned ligaments, with some limited bending contribution from the ligaments with strong mis-orientation with the load axis. Therefore, the stress-strain curve becomes gradually linear with the progressive re-alignment of ligaments and their contribution to stiffness. Warren and Kraynik studied this non-linear behavior and, for uniaxial tension, described it with a third-order polynomial[104]:

$$\frac{\sigma^*}{E_s} = A\left(\frac{\rho^*}{\rho_s}\right)^2 \varepsilon + B\left(\frac{\rho^*}{\rho_s}\right)^2 \varepsilon^2 + C\left(\frac{\rho^*}{\rho_s}\right)\varepsilon^3 \qquad \text{Equation 6.3}$$

with E_s the Young's modulus of the dense material, ε the strain, $\left(\frac{\rho^*}{\rho_s}\right)$ the relative density of the porous material and A, B and C fitting parameters.

This realignment of the ligaments under uniaxial load is illustrated by the change in Young's modulus that was measured during loading cycle applied to one of the specimen (sample 1-5), as shown in Figure 6.12. The specimen was loaded to a value at which the stress-strain curve became linear, after gradual increase of the Young's modulus at the beginning of the test. Just before failure, the ligaments realigned with the load axis contribute to the overall stiffness and a value of 4 GPa can be calculated. Hence, this value represents the stiffness composed by ligament realignment and elongation of ligaments (stretching).

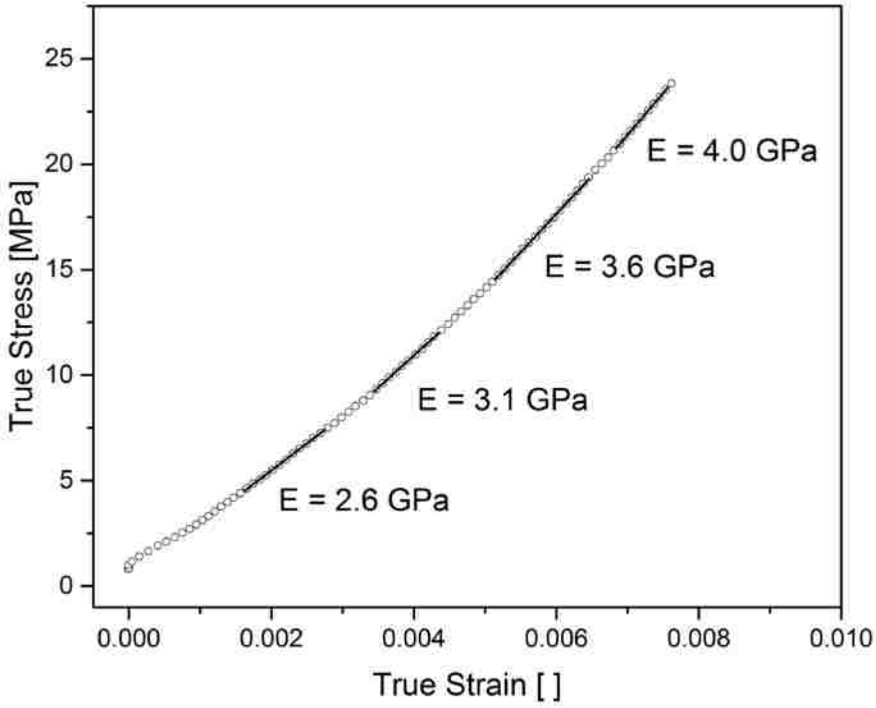

Figure 6.12. Stress-strain curve from tensile testing of sample 1-5. The evolution of the Young's modulus is shown, gradually increasing and becoming linear before rupture.

No plastic deformation of the specimen was observable during tensile testing, and the samples catastrophically fractured in a brittle manner. However and as reported in the literature before [84], plastic deformation and necking of individual ligaments was observed in the SEM on the fracture surface, after testing. This confirms that even though np-Au is macroscopically brittle, the gold ligaments still exhibit ductile behavior at the nanoscale. The np-Au structure below the plane of rupture was observed to be rather undeformed, leading to the conclusion that failure in np-Au is highly localized. It is likely that an internal defect can locally weaken the specimen and initiate a crack that rapidly extends to the sides of the specimen upon further loading, leading to macroscopic brittleness. In the present case and for most specimens, geometrical defects at the surface (roughness), combined with stress concentration at the transition region between the gage section and the ear of the specimen (sample design), led to catastrophic failure.

Most ruptured ligaments presenting a plastically elongated and necked region were found to be aligned with the load axis. The large number of aligned ligaments at the fracture surface, in addition to the shape of the determined stress-strain curves, indicate that re-alignment along the tensile axis took place before rupture. However, not all ligaments can rotate and accommodate the stress by aligning with the tensile axis. Some ligaments present an orientation much different than the tensile axis. The latter ligaments were also found on the sample fracture surface, but did not exhibit large deformation or necking before failure, and appear to have rupture in a brittle manner. Interestingly, Lu *et al.*[137] observed two modes of failure in gold nanowires under uniaxial tensile testing. For nanowires aligned with the load axis, a ductile mode where the nanowires extends in the loading direction and exhibits necking was observed. However, for nanowires that were mis-aligned during the test, i.e. when the load axis and the nanowire axis made an angle larger than 10º, a brittle-like failure was observed, with a flat fracture surface perpendicular to the loading axis. These observations could explain the two types of ligament rupture observed after tensile testing of np-Au, shown in Figure 6.9. The ligaments that could not re-aligned during loading exhibit this flat rupture surface while the aligned ligaments show signs of extensive axial deformation. It is therefore important to realize that fracture of np-Au is not purely based on stretching of aligned ligaments, but also involves a significant portion of mis-aligned ligaments that deforms differently, which can be compared as bending and brittle rupture of cell-walls, as described by Gibson and Ashby. Consequently, not only Young's modulus but also yield and fracture strength values of np-Au will be dependent on this mixed deformation behavior.

Deformation behavior of individual ligaments in np-Au can be compared with the behavior of gold nanowires reported in the literature. It has been shown that deformation of np-Au, just like in gold nanowires, is dislocation mediated[87], [105], [138]–[141]. As the size of the sample decreases, nucleation and multiplication of dislocations within the materials becomes increasingly restricted, potentially leading to dislocation starvation and an increase in strength[142]. However, because apparent signs of plasticity have been observed, it is clear that dislocations are the source of deformation in nanowires and ligaments. It has been found that surface nucleation of dislocations governs deformation in nanowires of diameters up to tens of nanometers. The high stresses required to nucleate these dislocations explains the high yield strength values reported for nanowires in the literature and has been found to be strongly influenced by temperature and strain rate[143], [144]. Upon loading, dislocations nucleating at different locations on the nanowires' surface glide along different {111} planes and intersect within the material. This process gradually creates a necked region within the nanowire that rapidly evolves and is followed by rupture[145].

Because np-Au ligaments aligned with the load axis can be assimilated to nanowires loaded axially, and because they present elongation and necking in the loading direction, a deformation mechanism similar to the one described previously can be expected to take place. However, for mis-aligned ligaments that presented a flat rupture surface, Lu *et al.*[137] reported the formation of twins under load, perpendicular to the axis of the nanowire. Under increasing load, brittle failure invariably occurred at the region separating the twin from the f.c.c. structure. Creation of twinning or non-twinning partial dislocations is based on the mis-alignment with the loading axis, and lead to the two different modes of deformation observed in gold nanowires. Because in np-Au, many ligaments have not rotated and are not aligned with the load axis, the deformation mechanism described by Lu *et al.* can be expected, and corresponds to the SEM observations at the fracture surface.

6.5.2. Yield Strength

Testing on specimens that do not include grain boundaries prevented crack initiation and intergranular propagation that led to the low strength values determined from polycrystalline and pseudo-single crystalline specimens. However, crack initiation was found to have taken place at the surface of the specimens, on sharp features of surface roughness created by the sample preparation process, in this case wire EDM. Additionally, because of the specimen geometry, rupture in tension preferentially occurred at the transition region between gage and ear of the dogbone shaped specimens, leading to premature rupture. In the case of np-Au, this localization of stress due to specimen geometry is particularly important, as early crack initiation leads invariably to sudden, catastrophic failure. In that sense, it was found that np-Au is not forgiving and the slightest mis-alignement of the specimen in the testing setup or the smallest surface defect will always lead to premature failure. For comparison, aluminum specimen with the same geometry were used for system alignment and calibration, and only in rare cases did fracture not occurred in the middle of the gage section.

The average yield strength value of 25 MPa which was measured during tensile testing of single crystalline np-Au, while twice as high as previous measurements on polycrystalline np-Au, are still much lower than values reported in the literature, even taking the stress concentration into account. For similar relative densities and ligament size, nanoindentation experiments led to the determination of yield strengths values roughly three times higher than tensile testing[90]. Micropillar compression testing also led to much higher yield strength values, about four times as high[101], although for higher relative density samples with smaller ligament size in that particular case.

The widely used scaling relations from Gibson and Ashby, introduced in section 2.4.4, linking the mechanical properties of porous materials to their fully, dense counterpart materials, have been found to agree very well with experimental measurements of polymeric and metallic foams with ligaments of micrometer scale dimensions. They have been widely used on np-Au in the literature to estimate the mechanical properties of individual ligaments of the np structure. The yield strength $\sigma^*$of np-Au can be used to determine the yield strength σ_s of the individual ligaments using

$$\sigma^{*} = 0.3\sigma_{s}\left(\frac{\rho^{*}}{\rho_{s}}\right)^{1.5} \qquad \text{Equation 6.4}$$

with ρ^{*}/ρ_{s} the relative density of np-Au. Using Equation 6.4 with the average value determined in this work in tension, i.e. 25.2 MPa, a ligament yield strength of just above 440 MPa can be calculated. This value is well below the values estimated and reported in the literature, based on nanoindentation measurements (1.5 GPa and above depending on the ligament size). Additionally, a yield strength value of 440 MPa is much lower than values experimentally determined for gold nanowires. During tensile testing of nanowires[137], Lou's group observed typical engineering yield strength values above 800 MPa for gold nanowires of diameter ~10 nm. For single crystalline gold nanowhiskers with diameters between 44 and 126 nm, Sedlmayr *et al.*[146] measured yield strength between 600 MPa and 1.6 GPa. Based on these reported experimental values, it becomes clear that using the classic yield strength scaling relation with values experimentally determined in tension for np-Au does not allow an accurate estimation of the yield strength of gold nanowires.

Using Equation 6.4 to predict the yield strength of np-Au based on relative density and yield strength of dense gold (up to 205 MPa for polycrystalline gold, rolled to 60% thickness reduction), a σ^{*} value of nearly 12 MPa is calculated. This value is less than half the value experimentally determined.

These calculations illustrate the need to derive a new scaling relation for the yield strength of np-Au and np materials in general. As described in section 2.4.4, the classic scaling relation for yield strength does not include a ligament size parameter, meaning that the yield strength σ_{s} of the material in its ligament form (nanometer scale dimensions) is assumed to be the same as for a macroscopic sample. More details on this size effect parameter and a new relation will be discussed in Chapter 7.

6.5.3. Young's modulus

As previously described in section 2.4.4, another widely used scaling relation allows prediction of the Young's modulus of a porous material based on its relative density ρ^{*}/ρ_{s} and the Young's modulus E_{s} of the material in its dense form:

$$E^{*} = E_{s}\left(\frac{\rho^{*}}{\rho_{s}}\right)^{2} \qquad \text{Equation 6.5}$$

Using this relation with the Young's modulus of gold, i.e. E_s of 78 GPa, a np-Au Young's modulus of 8.5 GPa is predicted. This value nearly twice as high as the modulus determined during tensile testing. Using the E^* value measured experimentally (4.5 GPa), a Young's modulus of 41 GPa would be calculated for gold, almost 50% lower than what should be determined. This observation demonstrates that the classic scaling relation, valid for porous materials with features dimensions in the micrometer and millimeter scale, do not accurately describe the behavior and properties of np-Au. Interestingly, although a ligament size effect is missing from the scaling relation for yield strength, no such ligament size effect should influence the Young's modulus. Because the modulus scaling relation does not agree for np-Au, it appears that deformation behaviors at the nanoscale, such as ligaments re-alignment, cell-walls bending and ligament axial stretching also need to be accurately described by the relation. More details on the effect of the np structure deformation behavior on the scaling relations will be given in Chapter 7 and Chapter 8.

6.5.4. Fracture toughness

The average fracture toughness value of 0.24 MPa.m$^{1/2}$ determined during testing of single crystalline np-Au is typical of brittle materials. For comparison, glass or concrete have fracture toughness values below 1 MPa.m$^{1/2}$ while ductile materials like metals record fracture toughness values in the tens of MPa.m$^{1/2}$. Moreover, the calculated strain energy release rate G_c^* value of 10 J.m^{-2} illustrates the typical brittleness of np-Au. For metals, G_c is usually measured above 1000 J.m^{-2} and values below 10 J. m^{-2} are more typical of glasses. Interestingly, it can be seen that even if the error in crack dimensions measurements was very high (one order of magnitude), a G_c^* value of ~ 100 J.m^{-2} would be calculated for np-Au, still characteristic of a brittle material.

Gibson and Ashby [94] also proposed a relation linking the fracture toughness K_{Ic}^* of a porous material to the fracture strength σ_{fs} of the dense material, based on the relative density and the cell size l :

$$K_{Ic}^{*} = W\sigma_{fs}\sqrt{\pi l}\left(\frac{\rho^{*}}{\rho_{s}}\right)^{1.5} \qquad \text{Equation 6.6}$$

with W=0.65. Based on the engineering fracture strength of gold nanowires determined by Lou's group (~800 MPa), a fracture toughness value of 0.043 MPa.m$^{1/2}$ should be measured for a np-Au structure with 60 nm wide ligaments, well below the experimentally determined value. Using the same equation, this time using the K_{Ic}^{*} value calculated in this work (0.24 MPa.m$^{1/2}$), a value of 3.6 can be found for W, about 5 times as high as in Equation 6.6. Another use of this relation, this time based on the calculated K_{Ic}^{*} value (0.24 MPa.m$^{1/2}$) and taking W=0.65 would lead to an estimation of ligament fracture strength of 4.5 GPa, much higher than the fracture strength value of ~ 800 MPa reported by Lou's group, and similar to the theoretical shear strength for gold (4.3 GPa)

The constant inability for classic scaling relations to properly describe the mechanical properties of np-Au confirms the idea that new relations need to be established to fully and accurately estimate the properties of np-Au. This will be the aim of Chapter 7, where a new scaling relation for the yield strength of np-Au will be proposed.

Chapter 7 : New scaling relation for the yield strength of np-Au

Based on np-Au yield strengths values reported in the literature and on the experimental results obtained from tensile testing of single crystalline np-Au specimens, it has been shown that the classic scaling relations are not properly estimating the mechanical properties of np-Au. As it has been described in the past in the literature[90], the Gibson and Ashby scaling relation for yield strength does not include a size effect component. If this parameter can be neglected for ligament size in the micron scale and beyond, it is expected to be of significant importance at the nanoscale. This ligament size effect on the yield strength of np-Au has been investigated through nanoindentation experiments and reported by Biener[89] and Hodge[90] and can be seen on Figure 2.13.

On another hand, yield strength values have been reported for np-Au of similar relative density and ligament size, but determined by different techniques. The largest discrepancies are found between nanoindentation results and the values determined by the tensile testing experiments conducted during the present work and detailed in Chapter 6. Yield strengths values determined by tensile testing were found to be significantly lower than results from nanoindentation experiments. Because most data reported in the literature are based on nanoindentation experiments, these discrepancies need to be addressed to be able to propose a new scaling relation for np-Au.

Both of the issues described above need to be taken into account. First, nanoindentation results, both from the literature and from new experiments, will have to be reconciled with tensile testing data. This harmonization of the yield strengths values reported for np-Au is required before any scaling relation can be studied. In a second time, a ligament size effect will be included into the derivation of a new scaling relation.

7.1. Specimen fabrication and characterization

To ensure that nanoindentation and tensile testing were conducted on comparable structures, care was taken to fabricate samples for nanoindentation following a similar process as the one used to prepare the tensile testing specimens. Therefore, the same AuAg pellets used in Chapter 5 with precursor alloy compositions $Ag_{65}Au_{35}$ and $Ag_{70}Au_{30}$ were used, as well as the single crystal with composition $Ag_{67}Au_{33}$ used in Chapter 6. Three samples were then prepared with three relative densities to cover a range as wide as possible.

Samples with initial composition $Ag_{65}Au_{35}$ and $Ag_{70}Au_{30}$ and large grains were originally prepared during the abnormal grain growth studies described in Chapter 5. Some of these samples were not used to extract tensile testing specimens but still presented large grains and flat, parallel sides from the cold-rolling steps. They were therefore used to prepare nanoindentation samples. Specimens with ~ 20 mm^2 of usable surface were cut from these samples. In parallel, a third specimen was cut from the single crystal used in Chapter 6 with a precision saw (Buehler IsoMet® 1000). It was then cold-rolled to proper shape (roughly parallel sides) and dimensions (~ 20 mm^2), then annealed at 800ºC for stress relief and composition homogenization.

All samples were then mounted on polishing stubs with Crystalbond™ 509 and polished on one side with 1200 grit polishing paper on a Buehler MetaServ® 250 polishing station. This way, a flat surface of reference was created. The samples were then flipped and re-mounted onto the polishing stubs with polished faced down. The new exposed face was mirror polished using different grit papers followed by diamond pastes (down to 0.1 µm) on polishing cloths. Parallelism of the two polished faces was ensured by the use of a manual polisher/grinder (Gatan Inc. disc grinder 623) to hold the stubs on which the samples were mounted. Flatness and parallelism of the surfaces are of high importance for the quality of the nanoindentation results. After polishing, all samples had a thickness of at least 100 µm, preventing any influence of the holder during testing. No annealing steps were conducted prior to dealloying, as previous experience showed that surface roughness significantly increased during annealing of the polished samples and the non-flat surface was interfering with nanoindentation.

Dealloying of the samples was then conducted in nitric acid solutions, following a similar process described in Chapter 6. The four-step process guaranteed a non-cracked np structure and no volume contraction. After dealloying, samples were rinsed in water and immersed in iso-propyl alcohol for at least 24 hours. Full removal of the sacrificial element (silver) was verified by mass loss and EDS in the SEM. Ligament size was determined by taking the maximum of the lognormal fit of the ligament size distribution, as described in Chapter 6 and illustrated in Figure 6.3.

7.2. Experimental details and results

Indentations were conducted on all three samples at room temperature, with maximum loads ranging from 0.5 to 20 mN, in load-controlled mode, using a NanoTest™ Vantage nanoindenter (Micro Materials Ltd., United Kingdom). Loading and unloading rate was maintained constant at 0.025 mN.s^{-1} for all indentations. A minimum of 25 indents were performed for each load, on each sample.

Different loading/unloading rates have been used and reported in the literature. Therefore, in parallel and only for one of the samples (np-Au with relative density of 0.30), additional indentations (12 indents per load) were performed with fixed loading/unloading times of 20 seconds and maximum loads ranging from 0.25 to 20 mN. This allowed measurements with loading/unloading rates between 0.0125 mN.s^{-1} and 1 mN.s^{-1} effectively covering all loading/unloading rates used in the literature.

As described in section 3.6, hardness values were determined both by the mean contact pressure (dividing the maximum load applied by the projected area of contact based on the indenter depth and the tip geometry calibration) and by measuring the area of the residual indentation print left at the surface of the sample after testing (in the SEM).

Figure 7.1 shows nanoindentation curves obtained using different maximum loads on the sample with relative density of 0.30, with constant loading and unloading rates of 0.025 mN.s^{-1}. A typical indentation print is left at the surface of the np-Au sample, as can be seen in an SEM micrograph in the same figure, and its area is used for hardness determination. A change in the loading curves slope can be seen around a depth of 1500 nm, and was consistently observed at different loads and different locations (hence different grains) on the sample. However, it was not found to influence the hardness measurements, as can be seen in Figure 7.2, where a comparison of the hardness values obtained by the two different calculations methods are shown. In addition, values determined both with constant loading/unloading rate and with constant loading/unloading time are plotted. As can be readily observed, the hardness values determined using the diamond tip geometry calibration (open markers) are found to gradually decrease with total indentation depth, eventually reaching a steady-state plateau, indicated by a dashed line in the figure. This has previously been observed and reported in the literature by Biener[88] and Hodge[90] and was attributed to the indentation size effect (porous material cell size relative to the indenter size). These values are found to merge with values determined from area measurements of the residual print left at the surface of the material, for indentation depth approaching 1500 nm. The latter values are found to be constant, independently of the indentation depth. The depth at which hardness values are not further influenced by the calculation method, and at which values merge with data determined from residual area measurements is consistent with observations reported in the literature for np-Au.

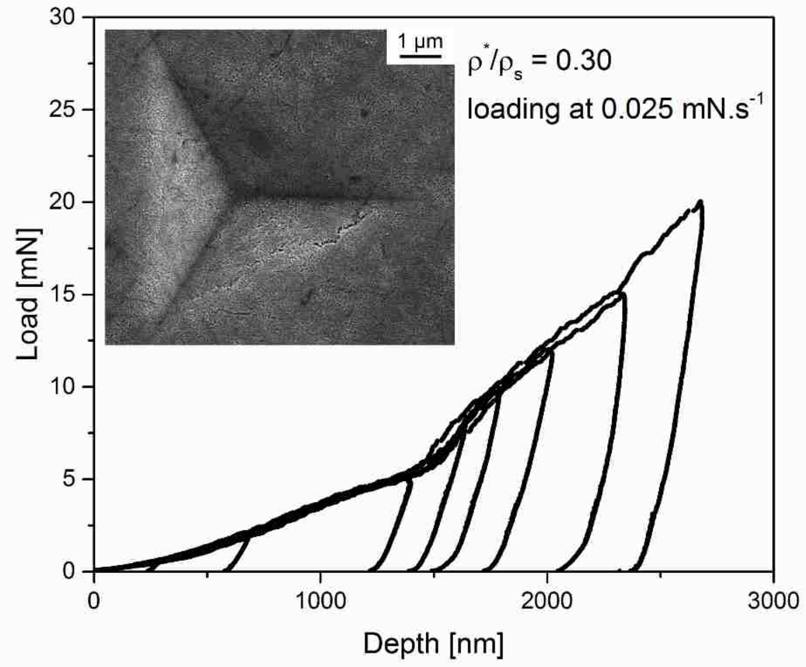

Figure 7.1. Load vs. depth nanoindentation curves obtained at different maximum loads during testing of np-Au with relative density of 0.30, with loading and unloading rates of 0.025 mN.s^{-1}. A typical indentation image is shown in the top left corner, obtained by SEM.

From Figure 7.2, it can also been seen that there was no influence of the loading/unloading rates on the hardness values calculated, in the range studied (0.0125 to

1 mN.s^{-1}). Theses hardness values are represented by black markers in Figure 7.2 are in good agreement with all the other values calculated. This is an important observation, because it allows direct comparison between values reported in the literature by different authors and those measured during this work. On a related note, it was also found during tensile testing of single crystalline specimens that strain rate did not have a noticeable effect on the yield/fracture strength, in the range studied (10^{-6} to 10^{-3} s^{-1}).

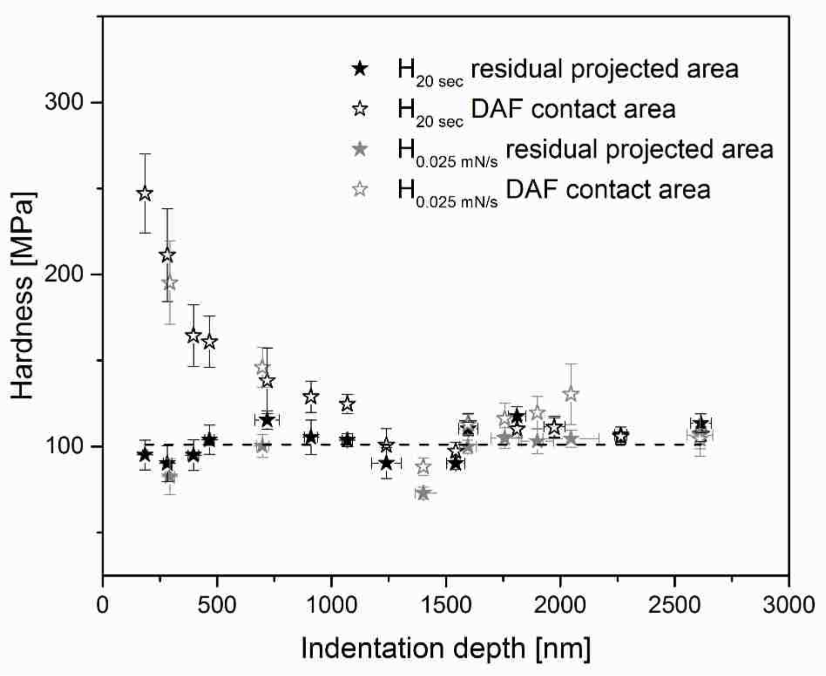

Figure 7.2. Hardness values as a function of indentation total depth determined from experiments on np-Au with relative density of 0.30. Open markers represent values obtained by calculating hardness based on the indenter tip geometry, while values represented by filled markers were determined using the area of residual print measured on SEM images after testing. Grey markers show data obtained with constant loading/unloading rate of 0.025 mN.s^{-1} while black markers show hardness values determined with constant loading/unloading time of 20 seconds.

For this study, hardness values determined both from the residual indent print dimensions and from the tip geometry calibration (plateau values) were ultimately similar. The hardness values used for the rest of this study will be taken as the average value from all indentations at different loads, with constant loading/unloading rate of 0.025 mN.s^{-1}, determined from the dimensions of the residual indent, as measured on SEM micrographs. This method was used by others in the literature, and is consequently preferable for comparison purposes. Hardness values as well as sample details are shown in Table 7.1. It can be immediately seen that these results do not agree with those from tensile tests, although ligament sizes for the nanoindentation samples were lower than for the tensile testing specimens. However, they match values reported in the literature for nanoindentation on np-Au and confirms that for the same np-Au material, nanoindentation and tensile testing lead to two distinct results for yield strength. These values need to be reconciled, as described in section 7.3.

Table 7.1. Sample details and nanoindentation results for np-Au with different relative densities. Ligament size was determined from the maximum of the lognormal fit of the ligament size distribution, as measured on SEM images. Hardness values are the average values calculated from indentations with different maximum loads and constant loading/unloading rate. Hardness was calculated from the maximum load applied and the residual indent area left at the surface of the sample, measured on SEM images.

Relative density ρ^*/ρ_s	Ligament size [nm]	Hardness [MPa]
0.30	19.3	97 ± 13
0.33	19.1	170 ± 22
0.35	18.9	230 ± 56

7.3. New scaling relation

As described in previous sections in this work, scaling relations from Gibson and Ashby relate the mechanical properties of a porous material and those of the material in its dense, bulk form. For yield strength, as described before in this work, the following relation can be used:

$$\sigma^* = C\sigma_s\left(\frac{\rho^*}{\rho_s}\right)^n \qquad \text{Equation 7.1}$$

with n = 3/2 and C = 0.3. The scaling coefficient C contains all the geometrical proportionality constants and was experimentally determined[94]. The scaling exponent n is dependent on the deformation behavior of the porous structure under load. For porous materials with very low density (ρ^*/ρ_s < 0.1), deformation up to failure is typically assumed to be dominated by bending of the thin, long cell edges (ligaments). In this particular configuration, a value of 1.5 can be calculated for n which describes this deformation behavior (see section 2.4.4). These parameters have been found to agree very well with experimental measurements of the yield strength of many porous materials with cell size of micrometer dimensions and low relative densities. However, for np-Au, ligaments are found to be shorter, bulkier and interconnected at nodes of substantial size, all creating the typical higher relative densities found in np-metals (0.2 to 0.5). Because of this significant difference in morphology, deformation behavior of np-Au can be expected to be different than the one considered during derivation of the classic scaling relations. Therefore, in this chapter, not only the value of C but also of n will not be assumed but experimentally determined.

As seen in Chapter 6, the scaling relation for yield strength does not include a ligament size effect, and therefore cannot be properly used. For a sample with ligaments of micrometer dimensions, the equation can be used reversibly, because the yield strength of the ligaments and of the dense material in its bulk form are identical. As the ligament size decreases to the nanoscale, this does not hold anymore. Therefore, as described and reported before by others[90], a ligament size effect will be included in the new scaling relation.

7.3.1. Nanoindentation vs. tensile testing

As shown in the previous section, results from nanoindentation and tensile testing on similar samples do not lead to the same yield strength values. This difference of results between mechanical testing on a millimeter-scale specimens and indentation has also been observed by the Weiβmüller group, which conducted compression testing followed by microhardness indentations. They found that the hardness values were higher than the compression values by a factor of roughly 3.

These discrepancies originate from the assumption made when extracting data from nanoindentation (and indentation techniques in general). Whereas tensile or compression testing provides direct observation and measurement of the yield strength, nanoindentation leads to the determination of a hardness value. These hardness values can be converted into yield strength values but only after making assumptions on the behavior of the material under the indenter during the indentation test. Following nanoindentation tests on np-Au, the assumption typically made is that hardness is equal to yield strength. Therefore, all nanoindentation yield strength data reported in the literature are in fact hardness values.

Generally, for dense metals, it has been found that yield strength and hardness are related according to the Tabor's relation[147]:

$$H \cong 3\sigma_s \qquad \text{Equation 7.2}$$

The previous relation assumes that the material is isotropic, fully work-hardened with a constant yield strength and that the ratio between Young's modulus and yield strength is larger than 100. It is therefore assumed that the material in the vicinity of the indenter is being plastically deformed. For porous materials with relative density below 0.3, it has been reported (Wilsea *et al.*[148]) that there is no lateral expansion as the indenter penetrates the sample, and that all pores in the indenter collapse before the neighboring cells are deformed, accommodating the displacement of the indenter without causing deformation of the surroundings. This observation leads to the assumption that the plastic Poisson's ratio (lateral strain divided by axial strain in the plastic regime) is null, which would characterize np-Au as a fully compressible material until all ligaments were collapsed and densification of the structure occurred.

The general assumption that porous materials are not constrained by the surrounding structure during indentation means that indentation of porous materials is equivalent to uniaxial compression. Consequently, for porous materials and in the present case for np-Au, it is assumed that hardness and yield strength are equal. This was observed by Shaw and Sata[149], who measured hardness to yield strength ratio close to 1 for porous polystyrene (i.e. a plastic Poisson's ratio ~ 0). However, the relative density of that material is very low, typically bellow 0.05[150]. They also measured this ratio for other porous materials and reported rapid rise from unity to three as the relative density of the porous material increased from ~ 0 to 0.5. For instance, they reported a hardness to yield strength ratio of ~ 2.5 for foamed aluminum with a plastic Poisson's ratio of 0.15. Therefore, while several studies have reported plastic Poisson's ratio values close to 0, the materials studied in these cases presented relative densities below 0.1[151], [152].

An estimation of the constraints acting on a porous material during compression can be obtained based on the computational work by Brydon *et al.*[153] in which the forces acting on the boundaries of a finite volume of low-density porous material are determined. Although the plastic Poisson's ratio does fall to zero for engineering strain of nearly 0.5, the value stays well above zero and interestingly close to the elastic Poisson's ratio value up to a strain of ~ 0.3. Furthermore, *in-situ* indentation of np-Au in the TEM, performed by Sun *et al.*[87], showed that although collapse of the pores under the indenter progressively took place, the underlying np-structure deformed, with this deformation extending to several cells ahead of the collapsed region. It can then be concluded that a gradient of deformation exists during the penetration of the indenter, with most of the np structure experiencing strain below 0.5.

If the plastic Poisson's ratio for np-Au was zero and nanoindentation were equivalent to traditional compression testing, uniaxial compression test conducted on micropillars by Volkert and Lilleodden[101] up to significant strain values should also reveal that the specimen does not expand laterally. However, this was not the case, and based on measurement of the dimensions of the micropillar before and after compression, they determined an average Poisson's ratio value of 0.20. Interestingly, this value is in very good agreement with the Poisson's ratio measured, during the elastic regime, for tensile testing of millimeter-scale specimens and reported in Chapter 5 and Chapter 6, as well as previous experiments on polycrystalline specimens[86]. Unfortunately, because no plastic region could be measured before rupture of specimens in tension, no plastic Poisson's ratio values could be determined. Results of compression testing on millimeter-scale specimens are presented in Chapter 8 and give some insights on Poisson's ratio evolution before and after the yield point.

Using results from Shaw and Sata[149] and the average Poisson's ratio value of 0.22 calculated from the single crystalline tensile tests of np-Au, a hardness-to-yield strength ratio of 2.65 can be determined, in a similar approach to that used by Volkert and Lilleodden[101]. Consequently, and for the rest of this chapter as well as during the derivation of the new scaling relation for yield strength of np-Au, all nanoindentation hardness values will be adjusted, dividing them by 2.65 to allow direct comparison with yield strength values obtained by tensile testing.

7.3.2. Ligament size effect

As previously described, a ligament size effect influencing the yield strength of np-Au is to be expected and has been proposed in the literature by Hodge *et al.*[90]. The size effect on yield strength usually has a similar form as the Hall-Petch relation describing the increase in yield strength with decreasing grain size commonly observed in metals. However in the case of np-Au, the increase in strength is not due to dislocation pile-ups on grain boundaries but on the limitation the confined volumes impose on dislocation nucleation and multiplication, as described in section 6.5. Nevertheless, a ligament size related effect can be expected to be well described by a relation in the form of

$$\sigma_s = \sigma_0 + kl^{-m} \qquad \text{Equation 7.3}$$

Because the tensile tests were conducted on single crystalline specimens, all ligaments are single crystalline. In a similar observation, because nanoindentation tests are performed within a single grain to prevent any grain boundary effect, the ligaments probed during nanoindentation are also single crystalline. Therefore, in Equation 7.3, σ_0 should be taken as the yield strength of single crystalline gold, not polycrystalline gold (used in the literature). This value has been reported to be lower than 2 MPa for AuAg alloys with silver content up to 3.5 at.%[154]. Consequently, because the yield strength of nanowires is much larger than the latter value (at least two orders of magnitude), σ_0 can be neglected and Equation 7.3 becomes

$$\sigma_s \cong kl^{-m} \qquad \text{Equation 7.4}$$

with l the ligament size, k the size effect coefficient and m the size effect exponent. These parameters will be determined and will describe the ligament size effect in the updated scaling relation.

7.3.3. New scaling relation derivation

Incorporating the ligament size effect described above in Equation 7.1, we obtain the general form of the updated scaling relation:

$$\sigma^* = Ckl^{-m}\left(\frac{\rho^*}{\rho_s}\right)^n \qquad \text{Equation 7.5}$$

This relation looks similar to Equation 2.15 proposed by Hodge *et al.*[90] but significant differences can be seen. First, the ligament size effect in Equation 7.5 does not assume a size effect exponent m of 0.5, value used in the Hall-Petch relation. Because grain boundaries are not at the origin of the size effect in the ligaments, the exponent should reflect the effect of confined volume on deformation. In the present study, the value of the size effect exponent will be determined based on experimental values. Second, because, as previously explained, σ_0 can be neglected, the yield strength of polycrystalline, dense gold does not appear in the relation. Third, the value of the scaling exponent n is not fixed and will also be determined. As described before, the value of 3/2 used in the Gibson and Ashby yield strength scaling relation originates from a derivation assuming that deformation up to the point of yielding is solely based on cell edges bending. However, as observed in Chapter 6, both ligament bending and stretching contribute to the deformation of np-Au. Therefore, the original scaling exponent of 3/2 should be re-evaluated, and the new value should be determined by the particular deformation behavior of np-Au.

For reliability, experimental values used to obtain the new scaling relation need to cover a wide range of relative densities and ligament sizes. Therefore, it was decided to use the nanoindentation results reported by Hodge[90] and Biener[88] as they covered a range of relative densities between 0.25 and 0.42 and ligament sizes from 10 to 900 nm. In addition, the results from the nanoindentation experiments conducted in the present study as well as the yield strength values measured by tensile testing on single crystalline np-Au specimens were used. As described before, all nanoindentation hardness values have been divided by 2.65. Also, because finite element modeling with Ansys® found a stress concentration of 11% in the region of the specimen on which rupture occurred during tensile testing (see section 6.2), all yield strength values reported in Table 6.1 have been adjusted (increased by 11%).

All the yield strength values (raw nanoindentation values) can be plotted based on their relative densities as shown in Figure 7.3. It is clear that in that form, no clear relation between the data is visible. After adjusting nanoindentation values according to findings detailed in section 7.3.1, the scatter in the values decreases but no clear trend is observed in Figure 7.4.

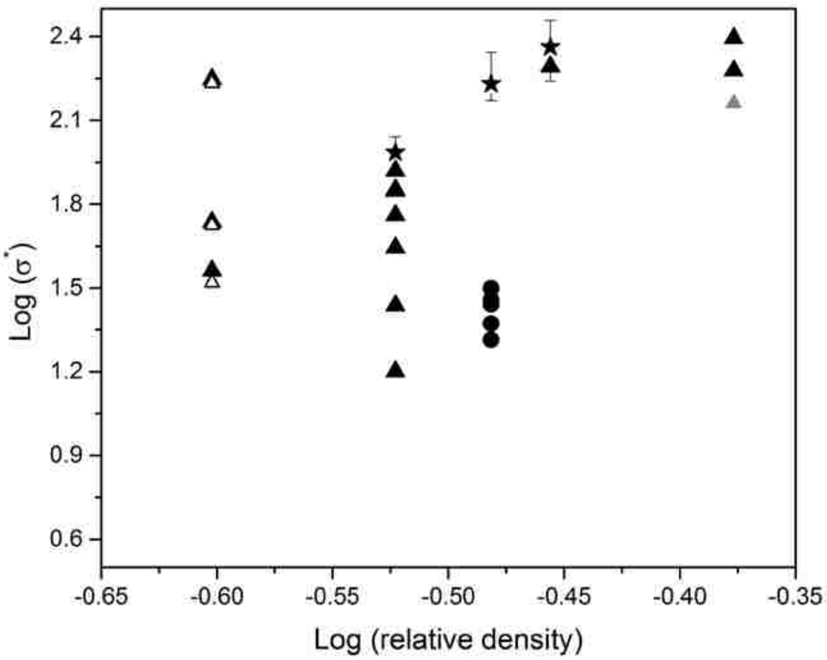

Figure 7.3. Values reported for yield strength in the literature (obtained by nanoindentation) and obtained in the present study from nanoindentation experiments and tensile testing of single crystalline specimens. The nanoindentation values are the raw measurements, assuming the hardness and yield strengths are equal. The tensile testing values have been adjusted (11% increase) to correct the stress concentration caused by sample geometry and surface roughness. Black filled triangles adapted from[90], grey triangle from[88], white open triangles from[89], filled stars from present work's nanoindentation and filled circles from tensile testing of single crystalline specimens[132].

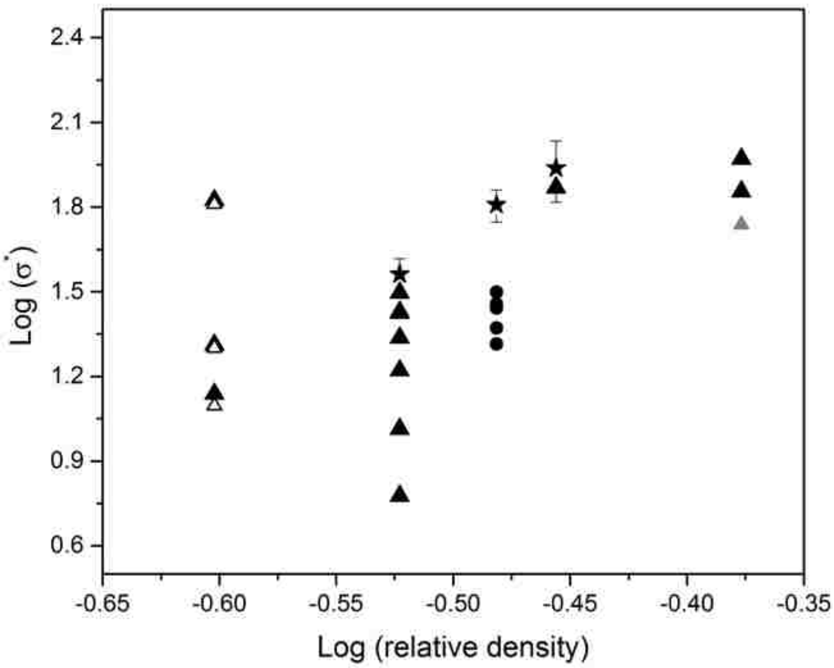

Figure 7.4. Similar plot to the one showed in Figure 7.3, after all nanoindentation hardness values have been divided by a factor of 2.65. Markers identical to those listed in Figure 7.3.

Because of the ligament size effect, values reported in the literature can only be compared once normalized to a fixed ligament size. A general ligament size of 50 nm can be chosen, as it lies in the middle of the range typically obtained by classic dealloying of AuAg alloys. Using Equation 7.5, we can write

$$\begin{cases} \sigma^*_{l=L} = CkL^{-m}\left(\frac{\rho^*}{\rho_s}\right)^n \\ \sigma^*_{l=50nm} = Ck50^{-m}\left(\frac{\rho^*}{\rho_s}\right)^n \end{cases} \qquad \text{Equation 7.6}$$

from which we can obtain

$$\frac{\sigma^*_{l=L}}{\sigma^*_{l=50nm}} = \left(\frac{L}{50}\right)^{-m} \qquad \text{Equation 7.7}$$

with $\sigma^*_{l=L}$ the yield strength of np-Au with a ligament size of equal to L and $\sigma^*_{l=50nm}$ the yield strength of the same np-Au sample after normalization to a ligament size of 50 nm. At this point, the size effect exponent m is not known and consequently the values reported in the literature and measured in tension cannot be normalized. However, after normalization to a single ligament size, Equation 7.5 essentially comes back Equation 7.1 with the size effect exponent m included into the ligament yield strength σ_s. Therefore, the exponent m can be used as the fitting parameter to empirically determine the best fit of all yield strength data on the plot created in Figure 7.5. With this method, best fit of the values is found for m = 0.551, and it can be seen that the scatter that was caused by ligament size is significantly reduced and the trend becomes obvious.

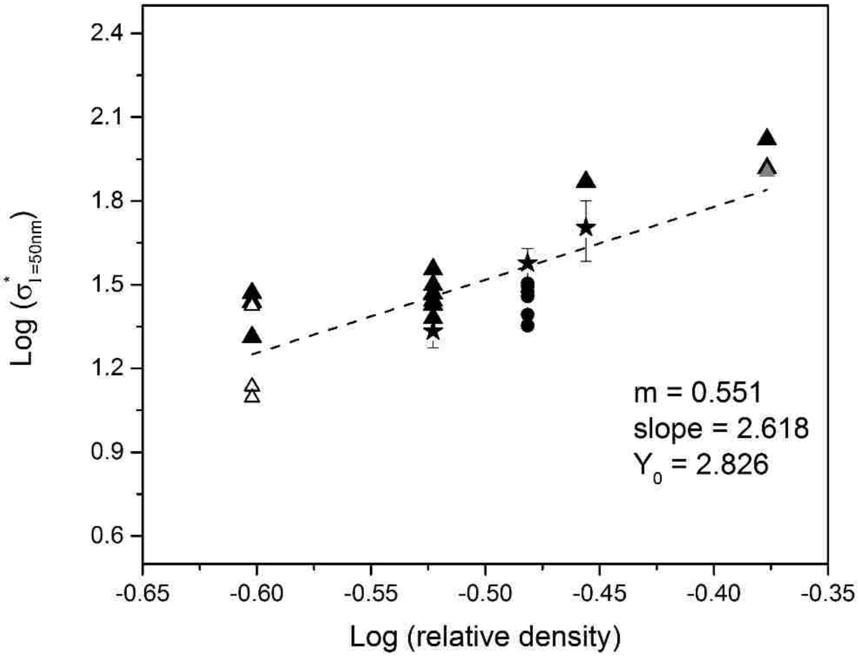

Figure 7.5. Similar plot to the one showed in Figure 7.4, after all yield strength values have been normalized a similar ligament size of 50 nm. Markers identical to those listed in Figure 7.3. Using the size effect exponent m as the fiiting parameter, best fit of the values is obtained for m = 0.551.

To confirm the value obtained for m, it is possible to only focus on a single relative density and observed the influence of the ligament size on the reported yield strength. This way, the porous scaling effect caused by changes in relative density is removed. Such a range of data has been reported by Hodge[90], for a relative density of 0.30 and np-Au samples with ligament size ranging from 40 to 900 nm. The reported hardness values obtained by nanoindentation can be divided by the factor of 2.65 and are plotted in Figure 7.6. Fitting of the data leads to a size effect exponent m value of 0.485, in relatively good agreement with the value determined earlier and based on all yield strengths values.

Therefore, the value m = 0.551 will be taken as the size effect exponent for the remainder of the new scaling relation determination.

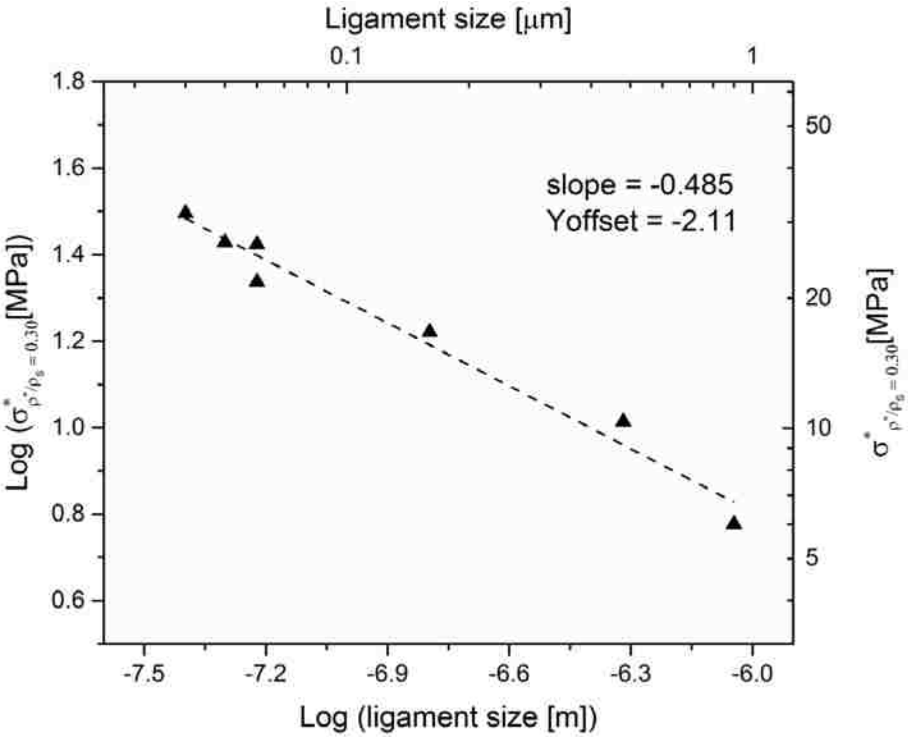

Figure 7.6. Ligament size effect on yield strength, based on data reported by Hodge[90], for a relative density of 0.30. The nanoindentation hardness values have been divided by a factor of 2.65.

The plot shown in Figure 7.5 is described, from Equation 7.5, by

$$\log(\sigma^*_{l=50nm}) = [\log(Ck) - m\log(l)] + n\log\left(\frac{\rho^*}{\rho_s}\right) \qquad \text{Equation 7.8}$$

Therefore, the slope of the linear fit of the yield strength values in Figure 7.5 directly gives the value of the scaling exponent n. In this case, n = 2.618. Also, because the y-intercept is equal to $\log(Ck) - mlog(l)$ and l was taken to be 50 nm, Ck can be calculated and is equal to 0.0636 MPa.m$^{0.551}$.

Determination of C or k is necessary to obtain all the parameters of the new scaling relation. However, measurements of the yield strength of individual ligaments of different sizes would need to be conducted to have an experimental value of k, which is beyond the scope of this study. Nevertheless, a value for k can be determined from the literature, as gold has been the subject of extensive research focused on the size effects on the mechanical properties. Tension and compression of gold micro- and nanowires, micropillar testing have been used to study the evolution of mechanical behavior as sample size decreases from micrometer dimensions to nanometer ones. Yield strength values were extracted from the relevant literature [89], [103], [142], [155], [156] are plotted in Figure 7.7. Because mechanical testing on these samples have been conducted with different crystal orientations relative to the load axis, all values have been normalized using the highest Schmid factor on the (111) <110> slip system. Best fitting of the values, which cover a range of size between ~ 40 nm and 10 µm, leads to m and k values of 0.623 and 0.0116 MPa.m$^{0.623}$, respectively. It is to be noted that other values of yield strength reported in the literature[156], [157] agree well with the trend shown in Figure 7.7 but were not used because the loading orientation could not be identified. This value of m is in good agreement with the value determined before. However, because m is taken to be equal to 0.551, the unit of k should be MPa.m$^{0.551}$. To obtain the value in the proper unit, linear fitting of the yield strength values plotted in Figure 7.7 with a fixed slope of -0.551 is possible and is shown in Figure 7.8. A new value of k = 0.0328 MPa.m$^{0.551}$ is then obtained.

The units for k match the exponent m value and consequently caution should be taken when comparing the value of k calculated here. However, as mentioned by Hodge, values for k reported for gold range between 1900 and 7900 MPa.nm$^{0.5}$[90] while the k value calculated in the present study is equal to 0.0328 MPa.m$^{0.551}$ or 2985 MPa.nm$^{0.551}$.

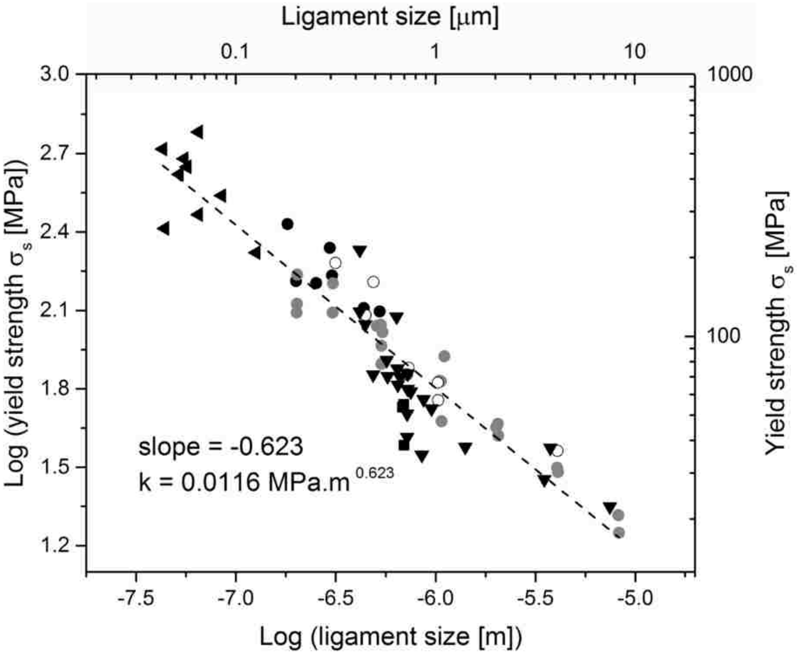

Figure 7.7. Yield strength values reported in the literature for gold micro- and nanowhiskers, and for micropillars. Values have been normalized the highest Schmid factor on the (111) <110> slip system. Data adapted from[158] (square markers),[155] (open and closed circles),[142] (triangles pointing down) and[146] (triangles pointing left). Linear fitting of the data allows determination of the size effect exponent m and of k.

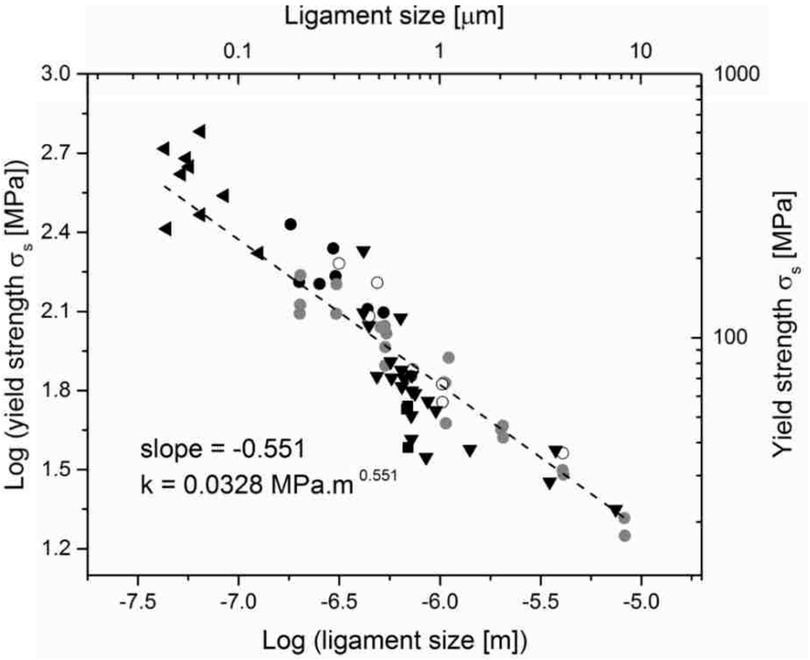

Figure 7.8. Identical plot as shown in Figure 7.7 but a fixed slope of -0.551 was used for the linear fit in order to obtain k in units of MPa.m$^{0.551}$, in agreement with the size effect exponent m value.

Based on the calculated value for k, it is possible to determine C and the updated scaling relation proposed to describe the yield strength of np-Au as a function of ligament size and relative density is written as:

$$\sigma^* = 1.939\,\sigma_s \left(\frac{\rho^*}{\rho_s}\right)^{2.618} \qquad \text{Equation 7.9}$$

with

$$\sigma_s = 0.0328 l^{-0.551} \qquad \text{Equation 7.10}$$

Parameters in Equation 7.9 and Equation 7.10 are reported with three significant figures to prevent rounding imprecisions, even though obviously one or two figures would be sufficient. Interestingly, if m was taken to be equal to 0.623 as determined from yield strength values of gold wires and pillars testing, k would then be equal to 0.0116 MPa.m$^{0.623}$, while C and n would be equal to 1.769 and 2.68, respectively. These values are very close to the one proposed in the new scaling relation. Moreover, if m was chosen to be equal to 0.50, as proposed by Hodge *et al.*[90], calculations would lead to k = 0.0683 MPa.m$^{0.50}$, C = 2.075 and n = 2.573, also very close to the parameters in Equation 7.9 and Equation 7.10.

7.4. Discussion and applicability of the new scaling relation

Apart from the addition of a ligament size effect in the scaling relation of yield strength, it can be seen that the values of the new parameters are significantly different than those in Gibson and Ashby's initial relation. In particular, the scaling exponent n originally equal to 1.5 now has a value of 2.618. The original value of n was obtained assuming that deformation and yielding of the porous structure is dominated by bending of the pore cells' edges. As shown in section 2.4.4, the value of the scaling exponent in Gibson and Ashby's relation is 3/2, where the numerator 3 originates from maximum bending moments and the denominator 2 arises from Equation 2.7. While the latter assumption - that relative density is proportional to $(t/l)^2$ – is valid for long, thin ligaments with low thickness to length ratio typically present in porous materials with very low relative densities (~ 0.01), it is not applicable to np-Au. Np metals and np-Au in particular have thicker, shorter ligaments with low aspect ratios that interconnect at bulky nodes in the structure. They also have much higher relative densities (0.25 and higher for np-Au).

The influence of relative density and nodes on the mechanical properties of np metals have been investigated by Liu and Antoniou[159]. They found that variations in the ligament aspect ratio t/l have significant impact on the mechanical properties. Also, based on np-Au, np-Cu and np-Pt structures, they reported the dependence of relative density on the ligaments aspect ratio to be almost linear.

Based on the scaling exponent n value of 2.618 determined in the present study, and assuming ligament bending as the main mode of deformation and yielding (numerator equal to 3 in the scaling exponent), the relative density can be calculated to be proportional to $(t/l)^{1.15}$. This dependence is close to the linear relationship reported by Liu and Antoniou. Given the morphology of the np-Au structure, it is however expected that both ligament bending and stretching contribute to the deformation and yielding. Proper estimation of the contributions of each behavior to the overall deformation of the structure is beyond the scope of this study. Nonetheless, the empirically determined parameters, and the scaling exponent n in particular does describe the deformation behavior of np-Au and includes the influence of ligament morphology on the mechanical properties.

The new scaling relation can be applied to the np-Au yield strength values σ^* reported in the literature in order to estimate the individual ligament yield strength σ_S. Taking nanoindentation values reported in the literature and determined during this study (divided by a factor of 2.65) as well as the values calculated from tensile testing of single crystalline specimens, it is possible to determine σ_S from Equation 7.9. Estimated values are plotted in Figure 7.9 (blue, half-filled markers) and super-imposed on reported values of yield strengths for gold micro- and nanowires as well as micropillars, already plotted in Figure 7.7 and Figure 7.8. From Figure 7.9, it can be concluded that the new scaling relation accurately captures the ligament size effect, and that estimations of ligament strengths σ_S for ligament sizes of 10 nm and higher are in good agreement with experimental measurement of gold wires and pillars. For instance, for a ligament size of 10 nm, a yield strength of ~ 1.3 GPa is calculated, which is about a third of the theoretical shear strength for gold ($G/2\pi$ = 4.3 GPa with G the shear modulus of gold). This yield strength agrees well with experimental values measured by Lu *et al.*[137] during tensile test of single gold nanowires. Although they did not specifically reported the yield strengths, it can be determined from their stress-strain plots that nanowires with diameters of ~ 10 nm yielded in tension at values up to ~ 1 GPa.

Other values of ligament yield strength σ_S have been calculated from values of σ^* measured by mechanical testing of np-Au. These values were similar of higher[88], [101] (approaching theoretical yield strength[89]) than the values calculated by the new scaling relation. However, all these calculated values used the original Gibson and Ashby scaling relation that did not account for ligament size effect nor contribution of stretching to the overall deformation of the np-Au structure.

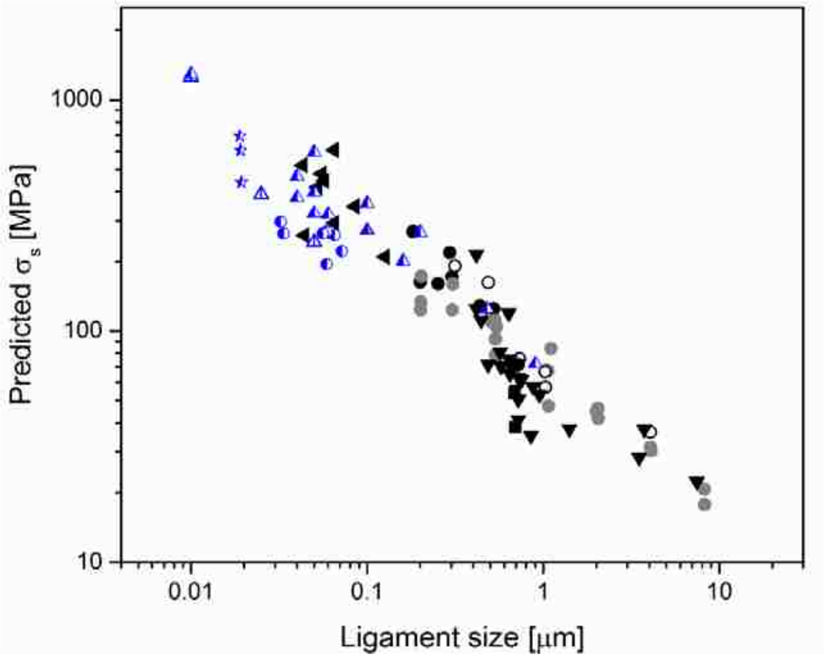

Figure 7.9. Calculated yield strength values of individual np-Au ligaments (blue, half-filled markers) based on np-Au yield strength values reported in the literature and obtained during this work. Values have been estimated using Equation 7.9. Calculated values are in good agreement with values found in the literature for gold wires and pillars (open and filled markers, similar to Figure 7.7 and Figure 7.8.

It is important to note that in Figure 7.9, the calculated yield strength values are compared to results of tests conducted on single wires or pillars under uniaxial loading. Therefore, it is assumed that ligaments strengths is directly comparable to aligned nanowires and whiskers. The good agreement between the two trends means that although there is some contribution of bending in the deformation of np-Au, stretching of the ligaments is the predominant factor during yielding and final rupture of the ligaments in the porous structure. This observation corresponds to the observations made during SEM imaging of the fracture surfaces after tensile testing, where it was found that most ligaments were aligned with the load axis, after undergoing some degree of re-alignment along the test, and exhibited strong signs of plasticity and necking.

The new scaling relation can also be used to estimate the yield strength of np-Au σ^* knowing the ligament size and the relative density of the structure. For all the values used to obtain the new scaling relation, comparison of the estimated value (blue, half-filled markers) and the experimentally measured value (black markers) is shown in Figure 7.10. The different yield strengths for single relative densities come from the different ligament sizes in the specimens. It is found that the new scaling relation leads to relatively accurate estimations of the final np-Au samples yield strength σ^*.

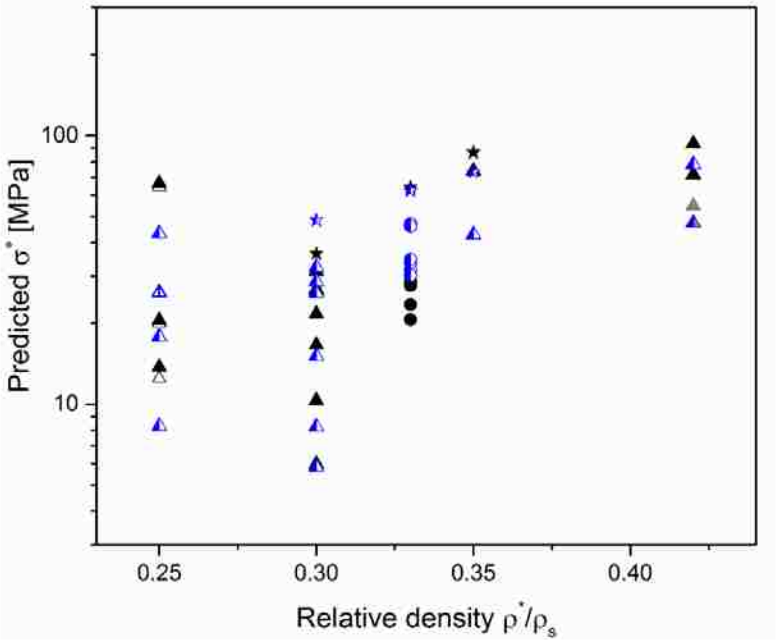

Figure 7.10. Calculated values of np-Au yield strengths (blue, half-filled markers) for different relative densities. Values have been estimated using Equation 7.9 and Equation 7.10, based on the reported ligament size and relative density of the sample. Black markers show the value experimentally measured, which agrees very well with estimations from the new scaling relation.

The size effect that was incorporated into the new scaling relation for yield strength of np-Au leads to a decrease of the estimated σ^* values as the ligament size increases. However, above a size threshold commonly referred to as the critical diameter, the dependence of np-Au yield strength on the ligament size should disappear. Consequently, above this threshold ligament size value, estimations made using the new scaling relation should be comparable with those made using the initial Gibson and Ashby relation. For a fixed relative density of 0.35, Figure 7.11 shows the estimated value of σ^* based on ligament size. Because the original scaling relation does not have a size effect parameter, the estimated value does not change in the range of ligament sizes displayed here. Also, depending on the value σ_s taken as the yield strength of gold, a range of values can be calculated by the Gibson and Ashby relation, and is represented by the grey area in the plot shown in Figure 7.11. It is important to note that the different scaling exponents n in the two scaling relations contribute to differences with a factor of ~ 3 on the calculated values, which does not have an important influence on the curves for ligament sizes larger than 1 µm, which is found to be the critical ligament size. This value agrees well with the critical diameter reported for gold in the literature[142].

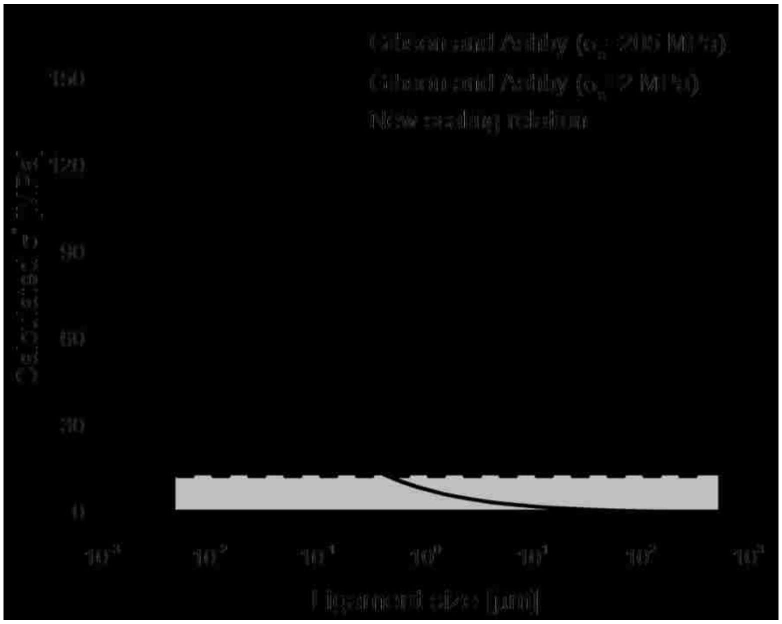

Figure 7.11. Calculated yield strength values for np-Au with various ligament sizes, based on calculations using both Gibson and Ashby scaling relation and the new scaling relation. The gray region represent all the possible values calculated by the original scaling relation, depending on the value chosen for σ_s (between 2 and 205 MPa).

Chapter 8 : Mechanical testing of polycrystalline specimens in compression

The mechanical properties of np-Au have been successfully determined in tension on single crystalline specimens. An average Young’s modulus of 4.5 GPa has been calculated as well as a Poisson’s ratio of 0.22 for np-Au with relative density of 0.33. An average yield strength of 25.2 MPa was experimentally determined, although specimen ruptured catastrophically at the location of stress concentration (~ 11%). As previously described, premature rupture occurred at the transition region between the gage and the ear of the specimen in contact with the grips. Therefore, the average yield strength value is probably a slight underestimate of the real yield strength of np-Au.

Compression testing can allow accurate determination of the yield strength of np-Au, because samples are expected to densify and not catastrophically rupture. Also, even in the eventuality of an internal defect (non-fused grain boundary, foreign particle, crack), the region concerned could be crushed and present no further contribute to the deformation process. If this collapsed region is confined to only a few layers of pores, the overall deformation would remain unaffected at the macroscale.

Therefore, compression of millimeter-scale specimens were performed, and results for yield strength have been compared to those obtained in tension. Moreover, accurate determination of the Young’s modulus is possible, and the applicability of the Gibson and Ashby scaling relation for modulus is discussed in this chapter.

The work presented in this chapter has been conducted in collaboration with Michael Bürckert, student at the Karlsruhe Institute of Technology at the time of the study. The experimental work from this chapter have been performed at the University of Kentucky and was the subject of focus for his Master’s thesis.

8.1. Specimen fabrication and characterization

Specimens were extracted from a AuAg alloy pellet, with initial composition $Ag_{65}Au_{35}$, already used for abnormal grain growth and nanoindentation experiments, and for which details can be found in Chapter 5 and Chapter 7. First, slices of thickness ~ 1.5 mm were cut from the pellet using a precision saw (Buehler IsoMet® 1000). In a similar way to the preparation of the nanoindentation sample described in Chapter 7, samples were mounted onto polishing stubs with Crystalbond™ 509 and both sides were polished on 800 and 1200-grit paper using a grinder/polisher holder (Gatan Inc. disc grinder 623) to obtain parallel, flat and polished faces. Then, several rectangular rods were cut from the polished samples, with width of ~ 1.2 mm and length of ~ 3 mm. These rods are the specimens that were tested in compression, after final shaping and polishing. Each specimen was then mounted on the polishing stub and all four faces were grinded and polished, making sure that opposite faces were parallel and forming 90º angles with the two other faces. This method allowed fabrication of specimens with square cross-section and with ~ 800 µm side.

To ensure that the two ends of the specimens were parallel while being perpendicular to the long axis of the specimen, a special holder was made. In this holder, a specimen can be clamped and, using a granite stand and an angle plate with a reference 90º angle, the specimen can be perfectly aligned. After grinding and polishing of one end of the specimen, verification of the alignment is conducted with a height comparator. The holder, angle plate and comparator are shown in Figure 8.1. Polishing of the specimen ends in the holder was performed on a flat glass surface, with two different pastes made of aluminum oxide powder and de-ionized water. The first grinding step was conducted using a powder with 600-grit particles, and, for the second and final polishing step, a powder with 5 µm particles was used. The final specimens were then inspected under the microscope and all burrs were removed using a single edge blade and 1200-grit paper.

Figure 8.1. (left) custom made specimen holder used to clamp the specimen in proper position to ensure perpendicularity of the ends with the long axis, (middle) holder in position against angle plate and granite stand to position the specimen and (right) verification of the final polished end face using a comparator. (images reproduced from Michael Bürckert Master thesis)

8.2. Experimental details and results

The specimens were dealloyed in nitric solution using a similar four step dealloying process as was used for preparing the tensile testing and the nanoindentation specimens. This method is described in details in sections 3.2, 5.1 and 6.1. After dealloying, specimens were rinsed in de-ionized water and immersed for a minimum of 15 hours in iso-propyl alcohol. Removal of the sacrificial element, silver, was tracked by mass loss and final dealloying was verified by EDS in the SEM. It was found that all specimens had a remaining silver content below 3.5 %at. For each specimen, the ligament size was determined in a similar way as previously described in sections 5.1 and 6.1. Ligament sizes are listed in Table 8.1.

Compression tests were conducted using the system built at the University of Kentucky, and described in section 3.5. The specimens were placed between grips with flat, polished surfaces that provided good contact with the specimen's ends. Displacement was applied by control of the deformation of the piezoelectric actuator. Tests were conducted at applied strain rates ranging from 10^{-5} s^{-1} to 5 x 10^{-3} s^{-1}. However, due to system compliance, the actual strain rates were slightly lower, between 0.7 x 10^{-5} s^{-1} and

2.5×10^{-3} s^{-1}. Because digital image correlation allows determination of the true strain, system compliance does not impact the values and therefore the system compliance was not evaluated. Compression tests were performed until rupture of the specimen or reach of the measurement system limitations (~ 40 N maximum load or ~ 100 µm piezoelectric actuator displacement). During each tests, several loading and unloading cycles were performed before loading to the specimen rupture, in order to properly determine the mechanical properties and observe their potential evolution. For each specimen, Young's modulus values were determined from the linear portion of the stress-strain curves during the loading and unloading cycles. Poisson's ratio values were determined from the same portions of the tests, based on the true axial and true transverse strain values determined by digital image correlation. Yield strengths were taken as the first deviation from the linear portion of the stress strain curve, during the first loading segment. The offset yield strength at 0.2% was also determined. All results are detailed in Table 8.1. For some isolated specimens, it was found that dealloying led to cracks in the structure, and therefore the results were not taken into account during calculations.

The average yield strength was calculated at 22.7 MPa with values ranging from 18.1 to 26.4, not taking in to account the values for the specimens that presented cracked structure after dealloying. The average modulus value of 5.34 GPa was taken from the averages of the measurements during the unloading segments of the tests. The average Poisson's ratio value of 0.268 also comes from the average values determined from the unloading portions of the tests, for each specimen.

Table 8.1. Polycrystalline np-Au compression specimen details and results from mechanical testing. The yield strength is taken as the first deviation from the linear region of the stress strain curve, during loading. For each specimen, the Young's modulus values and the Poisson's ratio values are averages of the values determined during the unloading portion of the test.

Sample ID	Ligament size [nm]	Yield strength [MPa]	Yield strength 0.2% offset [MPa]	Young's modulus [GPa]	Poisson's ratio [ ]
1-1	59.3	26	39.9	5.75	0.241
1-2	55.5	19.8	41.0	4.77	0.280
1-3	74.7	18.1	33.9	4.89	0.241
1-4	57.6	23.7	46.5	5.80	0.312
1-5	54.6	22.2	47.1	5.42	0.289
1-6*	94.8	12.2	29.9	4.13	0.239
1-7	60	26.4	50.3	5.39	0.248
1-8*	60.1	16.8	25.5	4.02	0.235
1-9*	197.6	11	18.5	3.18	0.229
Average	-	22.7	39.0	5.34	0.268

* not considered for average values calculations

Typical stress strain curves are shown in Figure 8.2, for some of the loading/unloading cycles performed on specimen 1-5. The Young's modulus values determined during the unloading segment of the tests are shown in the figure. For tests where the maximum load applied was beyond the yield strength of the specimen, a permanent deformation remained in the specimen after full removal of the load. For clarity, the strain values have been adjusted so that the initial strain on all stress strain plots is null at the beginning of all tests, in Figure 8.2. For all tests, a non-linear region at the onset of the experiment was observed. Upon loading, the curves became progressively linear, until the yield point was reach if the load applied was sufficient. The unloading segment was found to be linear immediately after the displacement direction was reversed, and only when approaching full removal of the load was a non-linear region observed. The extent of the latter region gradually decreased with several loading cycles beyond the yield strength. For the first loading/unloading cycle, the transverse vs. axial strain plot is shown in Figure 8.3 and the Poisson’s ratio values determined during loading and unloading are reported.

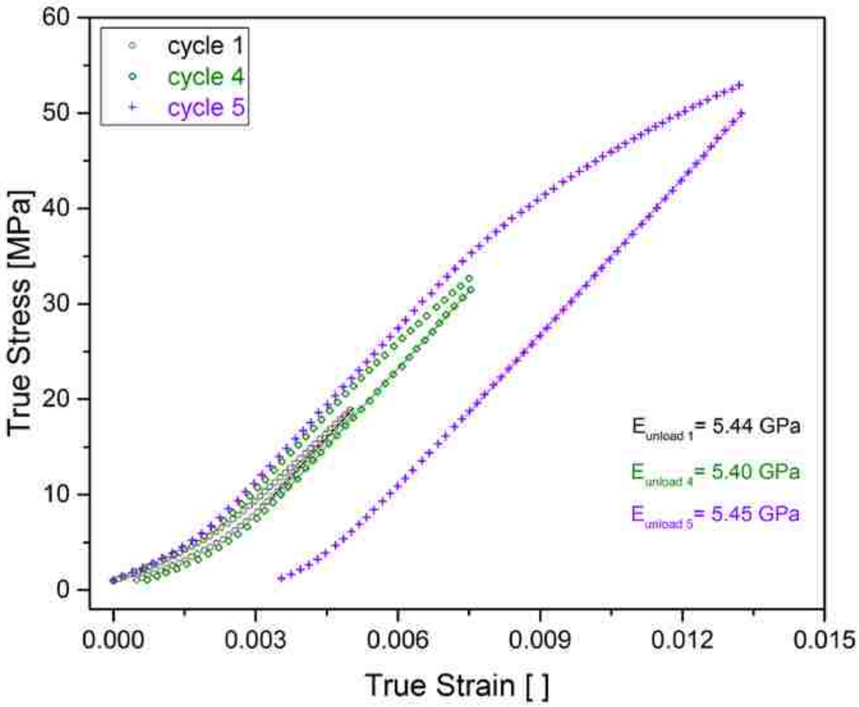

Figure 8.2. Stress strain curves for three of the six loading/unloading cycles conducted on specimen 1-5, in compression. For all plots except the first one, the strain values have been adjusted so as to start all plots with a strain value of ~ 0.

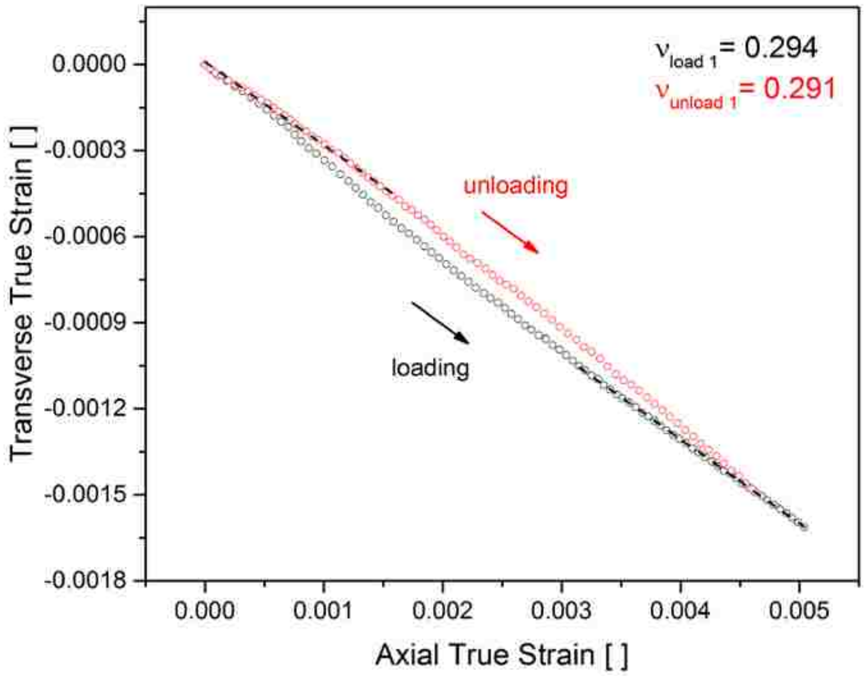

Figure 8.3. Transverse strain vs. axial strain for the first loading/unloading cycle conducted on specimen 1-5. For clarity and direct comparison, the unloading plot has been adjusted so that the strain at the start of the unloading portion is set to ~ 0.

8.3. Discussion

8.3.1. Stress strain curves

The compression tests conducted on millimeter-scale polycrystalline specimens allowed determination of the mechanical properties of np-Au in compression. The stress strain curves recorded during testing are typical of compression testing of porous materials which is commonly separated in three regions. First, the sample is loaded elastically and a linear dependence between stress and strain can be measured. Then, once the yield strength σ^* is reached, pores in the weakest regions of the porous structure start collapsing. This region is commonly called the plastic collapse region, during which the slope of the stress strain curve is much lower than during the linear elastic region. Once most pores have collapsed, densification of the structure takes place and the stiffness rises rapidly to eventually approach the value of the dense material. These three regions are shown in Figure 8.4.

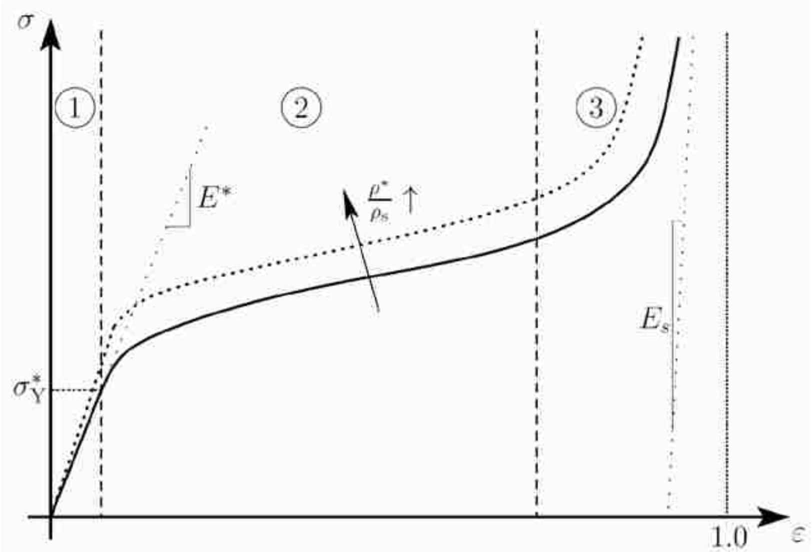

Figure 8.4. Ideal stress-strain curve for a porous material, showing the three separated regions: elastic loading, plastic collapse and densification. (figure reprinted from Michael Bürckert Master thesis)

Because of system limitations, only the first and second regions of this ideal stress strain curve was experimentally observed for np-Au. Np-Au has been shown to be highly compressive, and Jin *et al.*[103] reported strains of up to 0.70 in compression. For the specimen geometry used in the present study (~ 3 mm long specimen), this strain would mean a deformation of ~ 2 mm which is far beyond the measurement system capabilities. During the present study, maximum strains of ~ 0.025 were applied, corresponding to specimen deformation of 75 µm (not accounting for system compliance).

The stress strain curves presented a non-linear region at the beginning of the test, which seemed to gradually disappear after several cycles conducted beyond the yield point, as can be seen in Figure 8.5 for specimen 1-5. This non-linearity is caused by the imperfection of the specimen. Although efforts were made to create specimens with parallel ends, perfect parallelism was not achieved. Therefore, at the beginning of the test and in spite of the application of a pre-load of 0.7 N, part of the end surface of the specimens was not making good contact with the grip's wall at the beginning of the test. Upon loading, the stress concentrates in the small region of contact between the grip and the end of the specimen. This region of the specimen rapidly deforms under the stress and the end of the specimen progressively makes contact with the grip, increasing the surface of contact at the interface between the grip and np-Au. Once the whole surface of both the specimen ends are in contact with the grip, the stress strain curve becomes linear. Upon removal of the compressive load, the stress strain curve is linear until the ends of the specimen start not making proper contact with the grips anymore. At this point, the curve becomes non-linear once again.

In addition, it can be seen in Figure 8.5 that during the first loading cycle, the unloading portion of the stress strain curve does not follow the loading one, and that the strain value at the end of the tests does not match the initial one before tests. This indicates that some permanent deformation has been applied to the specimen, even though the stress applied to the specimen did not seem to reach the yield strength. Moreover, it can be observed by comparing loading cycles 1 through 3 that this difference between loading and unloading decreases and disappears after several cycles. The remnant strain after the first loading was determined to be 4.3×10^{-4} while it was null for cycle 2 and 1×10^{-4} for cycle 3. Therefore, this phenomenon is attributed, to the plastic, permanent deformation of the ends of the specimens which are collapsing first during loading. After several cycles with the same maximum load applied (in this case ~19 MPa for cycles 1 through 3) all the permanent deformation that can occur already occurred, and further loading below 19 MPa will present overlapping loading and unloading stress strain curves.

Another indication that the ends of the specimens initially contribute to the deformation is the Young’s modulus values determined during the loading cycle. For all specimens, the modulus measured during the first load was always significantly lower than during the subsequent cycles, when the values where close to the ones determined during unloading (which were stable). All values for specimen 1-5 are listed in Table 8.2. During the first loading, because the ends of the specimen are not yet permanently deformed, their deformation contributes to the overall specimen deformation and, therefore, a lower Young’s modulus is measured.

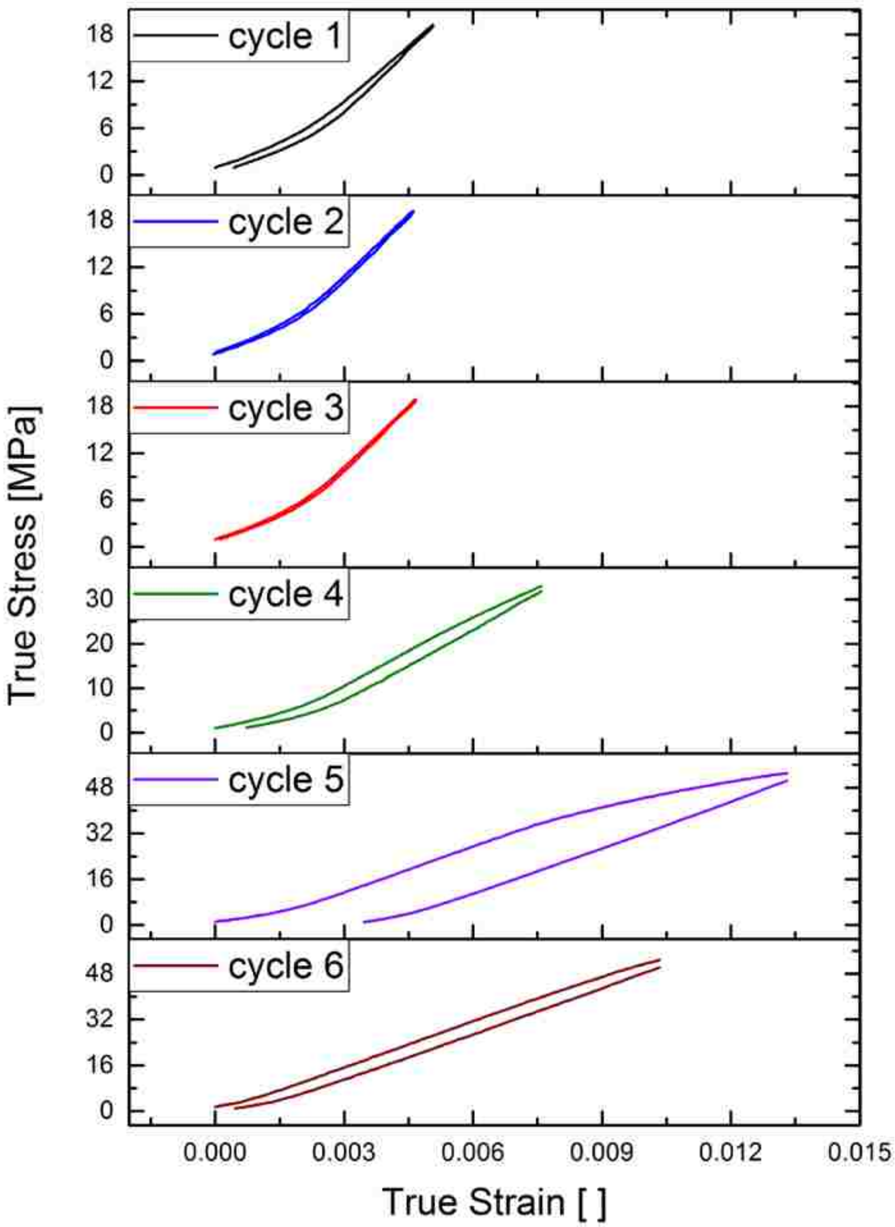

Figure 8.5. Stress strain curves for all loading/unloading cycles conducted on specimen 1-5, in compression. For all plots except the first one, the strain values have been adjusted so as to start all plots with a strain value of ~ 0.

It can also be seen in Figure 8.5 that the stress strain curve becomes linear just beyond a strain of 0.003 for the first loading while the curves for cycles 2 and 3 become linear just below this strain value. The fourth loading then goes beyond the specimen's yield strength, and consequently some permanent deformation is applied to the specimen, by collapse of some regions. Therefore, the unloading portion of the test does not follow the loading portion anymore and a permanent remnant strain can be determined. After several loading cycles beyond the yield point of the structure (cycles 4 and 5), the amount of permanent deformation at the ends of the specimens has increased, leading to shorter periods of non-proper contact with the grips. Essentially, the ends of the specimens re-adjusted themselves in the grips of the measurement system. For cycle 6, the non-linear region at the onset of the curve attributed to the ends of the specimens finishes at an approximate strain of 0.001.

Table 8.2. Detailed results from compression testing cycles conducted on specimen 1-5. The Young’s modulus values determined during loading progressively match the value determined during unloading.

Sample ID	Loading			Unloading	
	E^* [GPa]	ν^* [ ]	σ^* [MPa]	E^* [GPa]	ν^* [ ]
1-1	4.78	0.294	-	5.44	0.291
1-2	5.26	0.299	-	5.45	0.286
1-3	5.23	0.291	-	5.43	0.288
1-4	5.28	0.290	22.2	5.4	0.299
1-5	5.35	0.276	32	5.45	0.285
1-6	5.38	0.272	39.9	5.37	0.282

Interestingly, the yield strength values determined in compression from the first deviation from the linear portion of the stress strain curve agree very well with the values measured in tension and compression of single crystalline np-Au. During the compression tests, an elastic-plastic transition can be seen on the stress strain curves, during which the slope of the curve gradually changes over a relatively long deformation. The stress continues to increase past the yield point, despite assumption that no strain hardening can occur in np-Au, as dislocations created in the ligament, which are mediating plastic deformation in the cells, are escaping at the ligaments' surface. Consequently, the continuous rise in stress in the plastic region of the stress strain curve is attributed to a distribution of yield strength in the np structure.

In tension, as soon as the weakest region of the specimen fails, catastrophic rupture occurs. Therefore, the yield strength measured in tension characterizes the strength of the weakest part of the specimen. However, in compression, the test can continue past that point. Once the weakest region fails, i.e. collapses, under a stress similar as the one determined to cause rupture in tension, this localized volume in the specimen collapses but the specimen overall does not rupture. Upon increase of the load, the second weakest region fails but the tests still continues. Consequently, as the load needed to rupture the weakest part of the specimen gradually increases, the corresponding region of the stress strain curve shows a gradual increase in stress. After re-loading of a specimen that was previously loaded beyond its yield strength, it can be seen that the yield strength is now identical to the previous maximum stress applied before unload. This is readily observed in Figure 8.5 with load cycles 4 through 6. In cycle 4, yielding of the structure occurs at 23.7 MPa and the specimen is loaded up to ~ 33 MPa. After unloading and reloading in cycle 5, it can be seen that the new yield occurs at ~ 33 MPa. During cycle 6, the specimen is not loaded to a value higher than the one used in cycle 5, and therefore little permanent deformation can be observed.

During the loading portion of cycle 6 for specimen 1-6 (see Figure 8.6), it can be seen that the stress strain curve becomes almost flat. This approaches the ideal stress strain curve shown in Figure 8.4. This means that the applied stress to specimen 1-6 was almost sufficient to collapse any region in the specimen. When this happens, the whole structure collapses and the strain increases because the sample is being compacted, but the stress does not. It can also be seen that during the first 5 cycles, the permanent deformation applied to the end of the specimen led to the reduction of the difference between loading and unloading curves. For this specimen, the initial non-linear region is not pronounced as the ends of the specimens did not show much parallelism error.

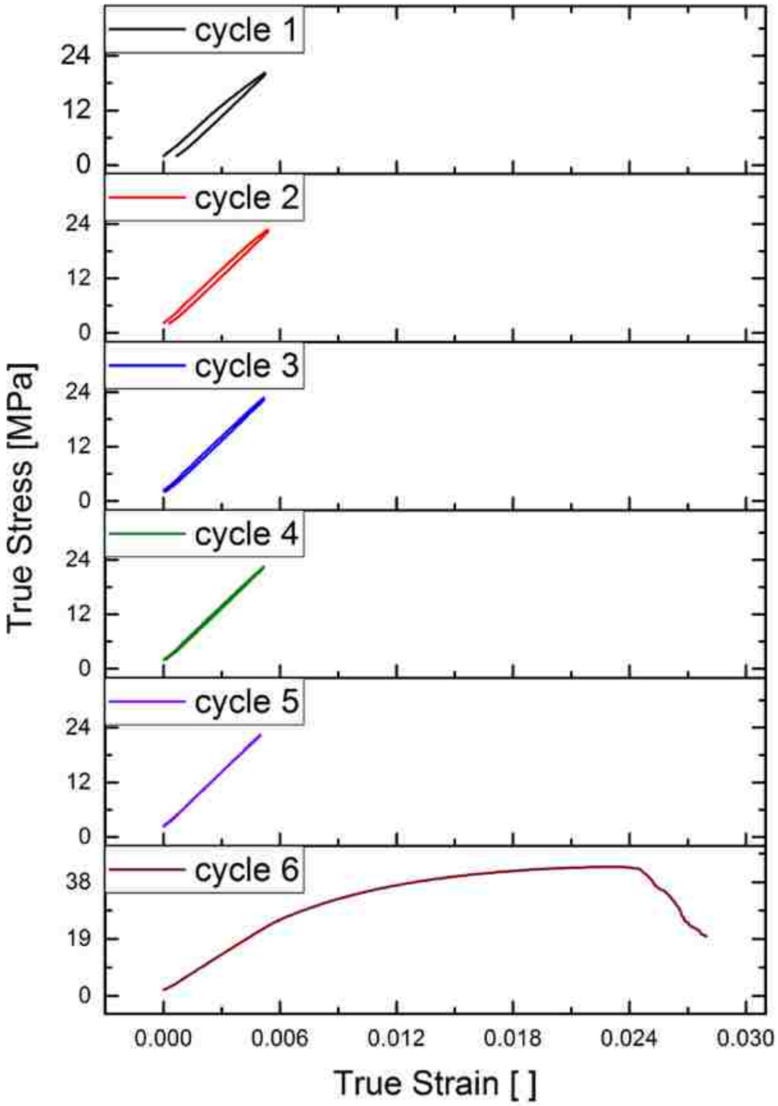

Figure 8.6. Stress vs. strain curves for compression testing on specimen 1-6.

8.3.2. Plastic Poisson's ratio

Direct measurement of the plastic Poisson's ratio was not possible during tensile testing of np-Au, since no plastic deformation was macroscopically observed. However, in compression, because the test can still be conducted beyond the yield point as described previously, values can be calculated from this region during which cells are gradually collapsing. The evolution of the Poisson's ratio during loading cycles that were conducted past the yield point are shown in Figure 8.7 and Figure 8.8, corresponding to the fourth and fifth loading performed on specimen 1-5. It can be seen that after the applied stress passed the yield strength of the specimen, the Poisson's ratio, or plastic Poisson's ratio in this case, decreases but its value stays significantly larger than zero.

This observation confirms that the Poisson's ratio is not null when cells collapse in compression. Therefore, this conclusion in addition to the observation by Sun *et al.*[87] that the np-Au structure is being deformed several cells ahead of the indenter during nanoindentation, indicates that np-Au definitely does not behave like a very low relative density foam, and consequently, valid assumptions for the latter structure cannot be applied to np-Au.

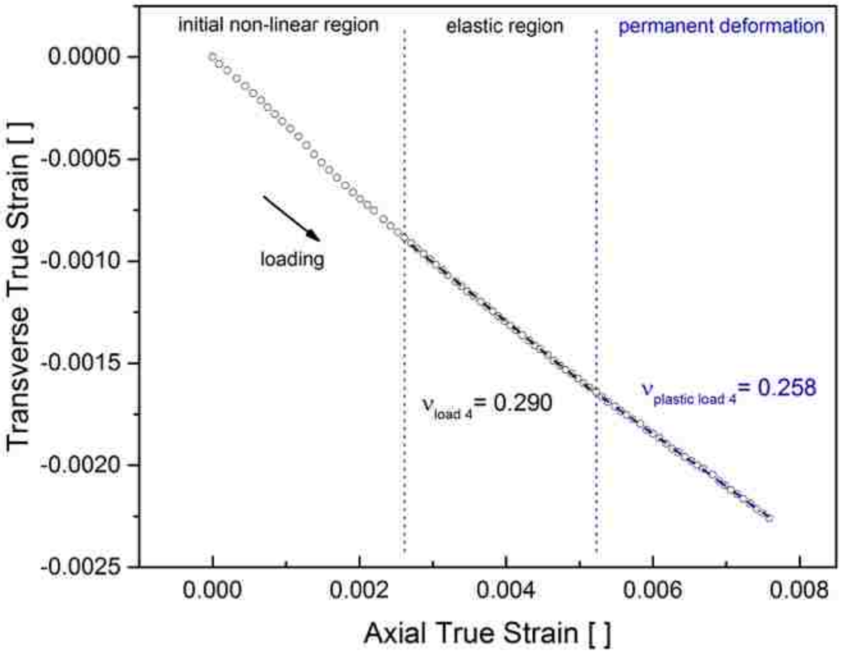

Figure 8.7. Transverse vs axial strain for the fourth loading cycle conducted on specimen 1-5. The Poisson's ratio is determined in the region that corresponds to the elastic region in the stress strain curve and in the region past the yield point.

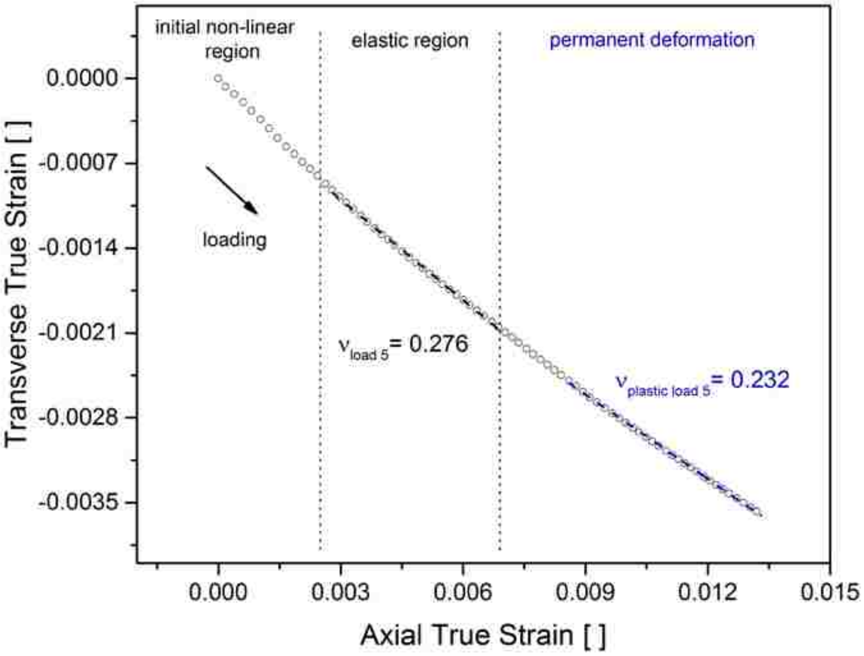

Figure 8.8. Transverse vs axial strain for the fifth loading cycle conducted on specimen 1-5. The Poisson's ratio is determined in the region that corresponds to the elastic region in the stress strain curve and in the region past the yield point.

8.3.3. Comparison with new yield strength scaling relation

The yield strength of np-Au determined by compression can be compared to the values calculated using the new scaling relation proposed in Chapter 7, based on the ligament size. Figure 8.9 shows the yield strength values determined from the compression tests. Both values determined after the first deviation from the stress strain curves during first loading (square markers) and with a 0.2% offset (circle markers) are plotted in the graph. The open markers represent the yield strength values for the specimens in which cracks were found after dealloying. In addition, np-Au yield strength predictions using the original Gibson and Ashby scaling relation is represented by a straight line (red color). Similarly to Figure 7.11, the predicted value in this case stays identical for all ligament sizes, as no size effect parameter is included in the original scaling relation. The second line in this figure (black line), represents the calculations from the new scaling relation (Equation 7.9 and Equation 7.10), for which the calculated yield strength varies as the ligament size changes.

It can be seen that yield strength at a 0.2% offset values determined from the stress strain curves agree well with the calculated values from the new scaling relation, while the values measured from the first deviation from the linear portion of the stress strain curve are lower than the predictions. This seems to confirm that the values measured in tension are probably lower estimates of the yield strength of np-Au, as they approach the lower strengths values reported in compression. In fact, the yield strength values measured in tension are intermediate values between the two different set of yield strengths plotted in Figure 8.9. It is also important to remember that during tension tests, the major contributor to yielding was found to be stretching of the ligaments. In compression, ligaments buckle under the load and bending should be the predominant contributor. The lower yield strength reported in compression also illustrate the difficulty to extract data from the stress strain curves, as the yield point extends through a significant region, for which different values can be taken as yield strength. Different methods have been reported to determined yield strength from stress strain curves for np-Au, using either the first deviation, a 0.2% offset[160] or a 1% offset[103].

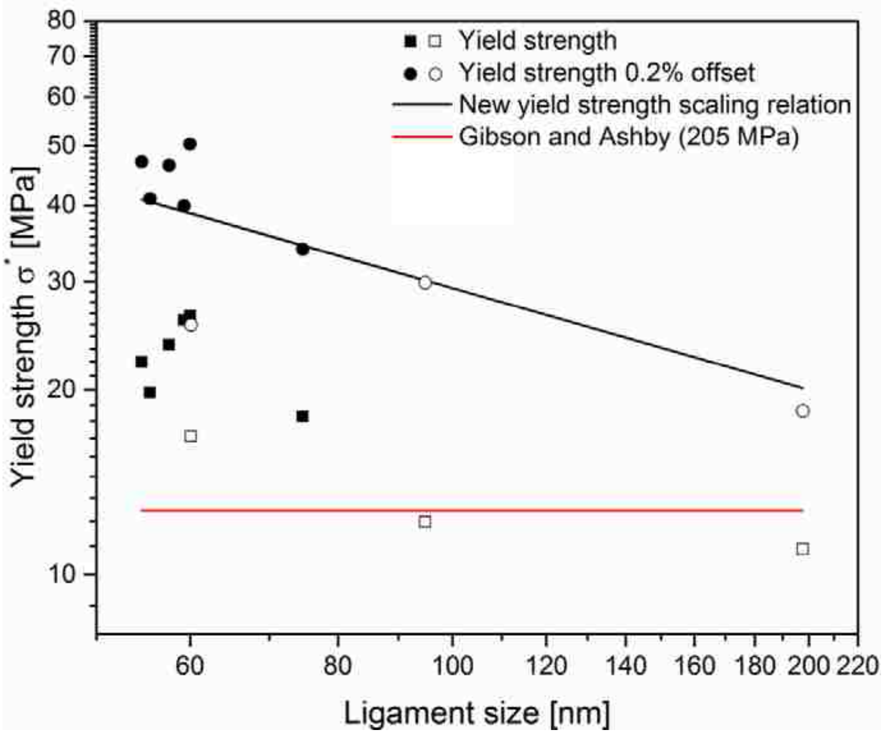

Figure 8.9. Comparison of the yield strength values determined during compression testing and estimations based on the new scaling relation presented in Chapter 7 and the Gibson and Ashby relation. Values of yield strength at 0.2% offset are found to agree well with the new scaling relation.

Another important point is that the new scaling relation for yield strength that was developed and reported in Chapter 7 was created based on data originating from tension and nanoindentation testing. The results in the present chapter originate from uniaxial compression testing. Therefore, using and comparing all the values assumes that a similar deformation behavior is at the origin of yielding of np-Au. The fact that the data measured in compression agree with those measured in tension suggests the behaviors have similarities. In tension, it is supposed that stretching of the load-axis aligned ligaments in the np-structure is the predominant mode of deformation before rupture. Nevertheless, a non-negligible amount of ligaments were found to have been rupture by bending, on the fracture surface. However, no indication was found on whether one type of rupture had taken place before the other. In compression, re-alignment of ligaments with the load axis is not expected the axial compression of individual ligaments is minimal. Therefore, the portion of ligament failing in bending can be expected to be contribute more to the overall deformation than in tension.

8.3.4. Young's modulus scaling relation

The Young's modulus values obtained from the tensile and compression tests can be used to evaluate if the original Gibson and Ashby scaling relation properly describes the mechanical behavior of np-Au. As described in section 2.4.4, the Young's modulus of the porous material E^* is related to the Young's modulus of the corresponding dense material E_s by

$$E^* = CE_s \left(\frac{\rho^*}{\rho_s}\right)^n \qquad \text{Equation 8.1}$$

with C = 1 and n = 2. This relation was derived considering that elastic bending of the cell walls of the porous structure is the contributor to the deformation of the sample under uniaxial load. The exponent n originates from this assumption, the value of 2 coming from the fact that E^* is proportional to $(t/l)^4$ while the relative density is proportional to $(t/l)^2$ in that model. The value of the pre-factor C, as in the scaling relation for yield strength, contains all the geometrical constants. For np-Au, the size of the ligaments are not expected to directly influence the Young's modulus of the structure, as the modulus of gold nanowires should be identical to a macroscopic sample of gold. However, the np structure presenting relative densities much higher than the porous materials that generally agree well with the original scaling relation, its applicability to np-Au is in question. If the ligaments themselves do not impact directly the structure because of their diameter, it is possible that their aspect ratio t/l modifies the deformation behavior significantly. The ligaments in np-metals and in np-Au in particular are found to be shorter and wider than for lower density foams, and are also connected to each other at bulky nodes.

Figure 8.10 shows the log of the Young's modulus values obtained in tension for pseudo-single crystalline np-Au (relative density of 0.35) and single crystalline np-Au (relative density of 0.33), as well as polycrystalline compression [86] (relative density of 0.30). Linear fitting of these values coming from different testing conditions (material and/or technique), leads to the determination of a scaling exponent n value of 3.30. From the plot shown in Figure 8.10, it can be seen that the y-axis intercept Y_o corresponds to $\log C + \log E_s$. Taking the modulus of gold E_s as 78 GPa, the pre-factor C is calculated to be equal to 2.15. Therefore, based on the data used in Figure 8.10 an updated scaling relation for the Young's modulus of np-Au would be

$$E^* = 2.17\, E_s \left(\frac{\rho^*}{\rho_s}\right)^{3.3} \qquad \text{Equation 8.2}$$

This relation shows indicates that the change in relative density of the porous materials has a higher influence on the Young's modulus than what was predicted by the original equation. Because the relative density is ultimately linked to the ligaments' morphology, it is clear that the particular shape of the np-Au ligaments influences the deformation behavior. If the deformation behavior during elastic loading of the np-Au structure is assumed to be controlled by bending of the ligaments, then the scaling exponent n value of 3.3 means that $\rho^*/\rho_s \propto (t/l)^{1.21}$. This observation is very close to the one reported in section 7.4, where the yield strength scaling relation led to the observation that for np-Au the relative density was proportional to $(t/l)^{1.15}$. Equation 8.2 agrees well with calculations from Roberts and Garboczi[161], who found an exponent n of 3.15 for an open-cell Gaussian random field model with curved ligaments of variable thickness, similar to those typically observed in np-Au. However, this exponent was determined to be valid for porous structure with low density, below 0.20.

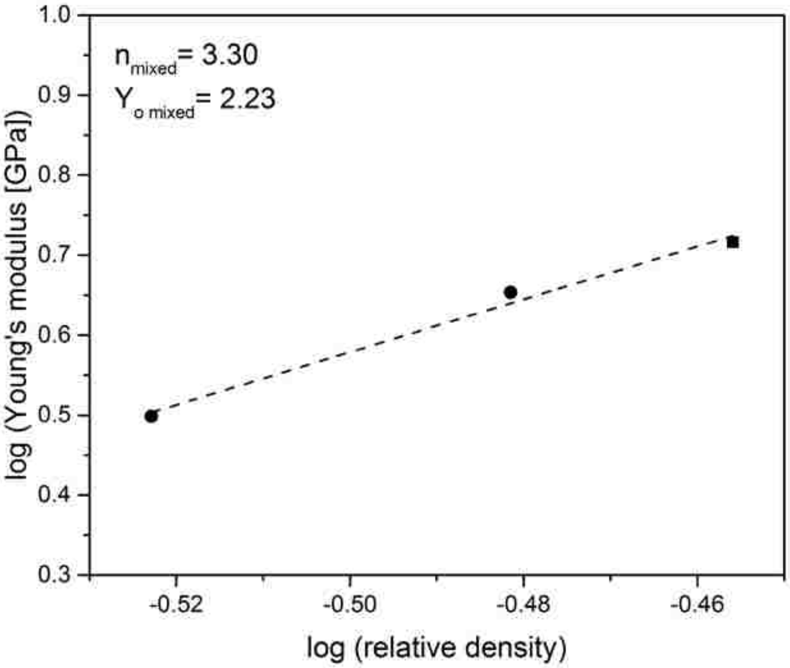

Figure 8.10. Determination of the scaling relation for the Young's modulus of np-Au based on results from mixed experimental techniques and structure. Filled circle markers indicate results obtained in tension while the square marker indicates results from the compression tests.

Because the deformation behavior in compression and in tension are not necessarily similar, it is also important to observe the values that were determined by the same technique. Figure 8.11 shows a similar plot to the one shown in Figure 8.10, although separating Young's modulus values obtained in tension (filled circle markers) from those obtained in compression (square markers). Fitting of the tensile tests results, all obtained during this work, leads to a different scaling exponent n equal to 4.38. Unfortunately, few modulus values have been reported in the literature, and only two points can be used for the compression results' plot. Fitting of the latter data leads to a similar scaling exponent that was determined from the tensile testing data, with a value of 4.25.

As stated above, because compression and tension create different deformation behavior in np-Au, the Young's modulus values should not be similar. Usually, for porous materials, the modulus in compression is lower than in tension: in tension, after rea-alignment, stretching of the ligaments dominates, while in compression, the ligaments buckle under the load. This was observed during this study and is visible in Figure 8.11. However, it becomes clear that more data are needed to determine how pronounced the difference of deformation behavior is in the elastic regime, and how the scaling exponent reflects this difference.

More compression tests on specimen with various relative densities need to be conducted, as well as new tension tests on single crystalline np-Au with different relative densities, in order to propose a new scaling relation for the Young's modulus of np-Au.

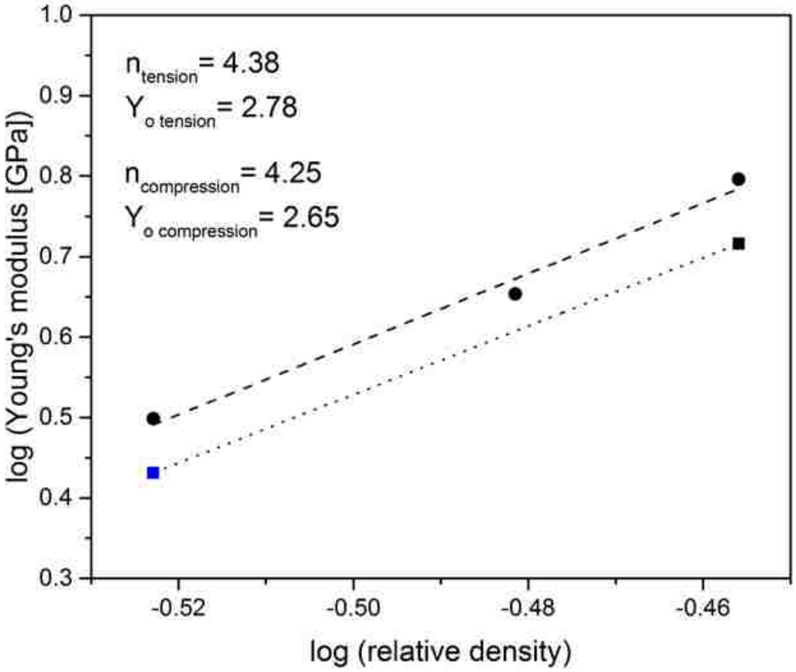

Figure 8.11. Determination of the scaling relation for the Young's modulus of np-Au based on results from similar experimental techniques. Filled circle markers indicates results from tensile tests while square markers indicate results from compression testing. The blue square marker comes from compression testing of polycrystalline np-Au with relative density of 0.30, reported by[86].

Chapter 9 : Conclusions and future work

The mechanical properties and behavior of np-Au were investigated by several techniques, both destructive and non-destructive. This work presented the first tensile testing experiments conducted on single crystalline np-Au, which allowed reliable measurements of the Young's modulus, Poisson's ratio and yield strength in tension. The Young's modulus of np-Au was also reported for the first from compression testing on millimeter-scale specimens.

A custom-designed measurement system was built, allowing testing of millimeter-scale specimen in tension and compression. Thanks to its versatility (every component can be individually changed), this system will also be capable to perform 3 and 4 point bending experiments, not only for np-Au but for other materials of interest (nanoporous or not). In addition, a second custom-built measurement system originally donated by Stanford University was modified to allow testing below room temperature.

This work on np-Au was conducted with three major areas to explore: what is the deformation behavior of np-Au? What are the mechanical properties of np-Au, determined from macroscopic samples? Are these mechanical properties in agreement with existing scaling relations and if not, how should they be modified?

The mechanical testing performed during this study not only verified that although np-Au is a very brittle material, with fracture toughness values more typical of ceramics than metals, the interconnected gold ligaments that form the structure deform plastically and exhibiting significant elongation and necking before rupture. It was also found during inspection of the fracture surfaces of specimens ruptured in tension that individual ligaments likely re-aligned with the load axis before failure of the sample. This re-alignment of ligaments under tension led to non-linear stress-strain curves a low strains, which became progressively and eventually fully linear before rupture. Although many ligaments were found to be aligned and plastically deformed in the load axis direction, some ligaments that kept a strong mis-alignment with the load direction were found to have ruptured without any plastic deformation. This observation was linked to the two modes of fracture in gold described proposed by Lou's group, during which nanowires were found to rupture in a brittle-like manner over a certain degree of mis-alignment between the load direction and the wire long axis.

Tensile testing on pseudo-single crystalline np-Au specimens demonstrated the importance of having fully single crystalline specimens to properly determine the yield strength of np-Au. Because original defects in the precursor gold-silver alloy, and in particular grain boundaries, remain in the sample after dealloying, premature rupture was always observed in tension for non-fully single crystalline specimens. It was found that for polycrystalline samples under tension, some regions will fail in a trans-granular manner, but rupture also propagates on these remaining grain boundaries, in an inter-granular fashion. Therefore, determination of the yield strength in tension from polycrystalline sample is not possible, as the whole specimen's cross-section does not carry the load.

It is important to re-iterate here that one goal of this work was to determine the yield strength of the np-Au structure. Therefore, preventing premature rupture caused by grain boundaries was primordial. However, np-Au is broadly and almost exclusively used in its polycrystalline form, meaning that the yield strength values measured in tension and compression on polycrystalline specimens are still particularly relevant.

Compression testing on np-Au, in combination with tensile testing observations, confirmed that np-Au ruptures on a "weakest link" basis. Under tension, this leads to a brittle, sudden and catastrophic failure: as soon as the weakest region in the sample fails, the rest of the specimen cannot carry the applied load and the rupture propagates rapidly. In compression, as soon as the weakest region fails, this region collapses and the sample as a whole does not fail. Increase of the load then selects another region which effectively became the weakest link after rupture of the first one. This process continues and leads to the gradual transition from the elastic behavior observed under compressive load.

The yield strengths values determined in tension and compression were much lower than values reported in the literature, mostly determined from nanoindentation techniques. Only previous experiments conducted on millimeter-scale specimens led to similar low values. In addition, it was found that applying the classic Gibson and Ashby scaling relation for yield strength, which has been shown to describe the properties of porous materials with micron and millimeter scale cells, did not accurately predict the properties of np-Au. Using the original scaling relation to estimate the properties of np-Au was not accurate, while using np-Au measured properties to estimate the individual ligaments yield strength was not consistent. As mentioned by others in the literature, the Gibson and Ashby relation, while still broadly used for np-Au related studies, cannot fully grasp the dependence on yield strength on the size of the ligaments, as there is no size effect parameter in the relation.

A new scaling relation for the yield strength of np-Au was proposed, that incorporates the ligament size effect, and which was found to properly estimate the yield strength of np-Au based on the ligament size and relative density. In addition, the new relation allowed estimation of the individual ligaments' yield strength, which were in agreement with reported values obtained from mechanical testing of gold nanowires and micropillars.

The determination of a new scaling relation of the yield strength of np-Au was only possible after reconciliation of the values obtained in tension and nanoindentation, both from the literature and new experiments. The assumption that for np-Au, hardness and yield strength are equal was at the basis of the discrepancies between the results of the two measurements techniques. After adjustment of the indentation values, all data were used together to obtain the new scaling relation for yield strength.

The Young's modulus values were the first values reported from mechanical testing on millimeter-scale samples, and did not agree with estimation from the original Gibson and Ashby scaling relation. Although more data are still needed to clearly evaluate the relation between modulus and the np-Au structure, it is apparent that there is a stronger dependency on the relative density that for low density porous materials.

Although mechanical properties values determined on millimeter-scale specimens were found to be reliable, many challenges were faced to create the samples and the proper testing conditions. These issues being solved, more tests are needed to access a better version of the new scaling relation for yield strength. Extending the range of relative densities and ligament sizes by selecting different precursor alloy compositions and various dealloying conditions and annealing processes will allow better determination of the relation parameters' values.

Other materials should also be explored to investigate the applicability of the new scaling relation for yield strength. Several other metals have been created in a nanoporous form, such as copper, silver, nickel or palladium. However, many of these other nanoporous metals have not been made from millimeter-size samples, large enough for tension or compression testing. As the derivation of the new scaling relation for yield strength was dependent on mechanical testing results from nanowires, np metals for which the mechanical properties at the nanoscale are already known should be prioritized.

More compression and tension testing on identical samples will also be important, to identify the differences in deformation behavior and possibly in modulus and strength. The data obtained during the present study were unfortunately not sufficient to conclude on this matter, although different response to load should be expected between compression and tension. In parallel, the deformation behavior of individual ligaments and cells under load should be investigated, probably by *in-situ* electron microscopy techniques. This would allow better understanding of the re-alignment, stretching and bending of the ligaments before rupture.

Other interesting investigations were conducted on np-Au during this study, which are not reported in this dissertation. Deflection control of flexible substrate coated with np-Au has been demonstrated, in a repeatable way. These tests were conducted using the system used for tensile/compression testing, showing the versatility of the setup. Recently, *in-situ* irradiation experiments were conducted on np-Au films in the TEM, in collaboration with the Ion Beam Laboratory (Sandia National Laboratories, Albuquerque, NM). The small volumes of the ligaments were found to not allow defect accumulation under irradiation, as they were found to be annihilated at the free surface. The mechanical properties of severely irradiated np-Au should be investigated. In addition, the damping properties of irradiated np-Au with the custom build system presented in this work could be of interest, as the accumulation of defects in the ligaments should be identifiable by apparition of specific relaxation peaks.

Appendix A

Operator Interface for Damping Properties Measurement System (Labview™)

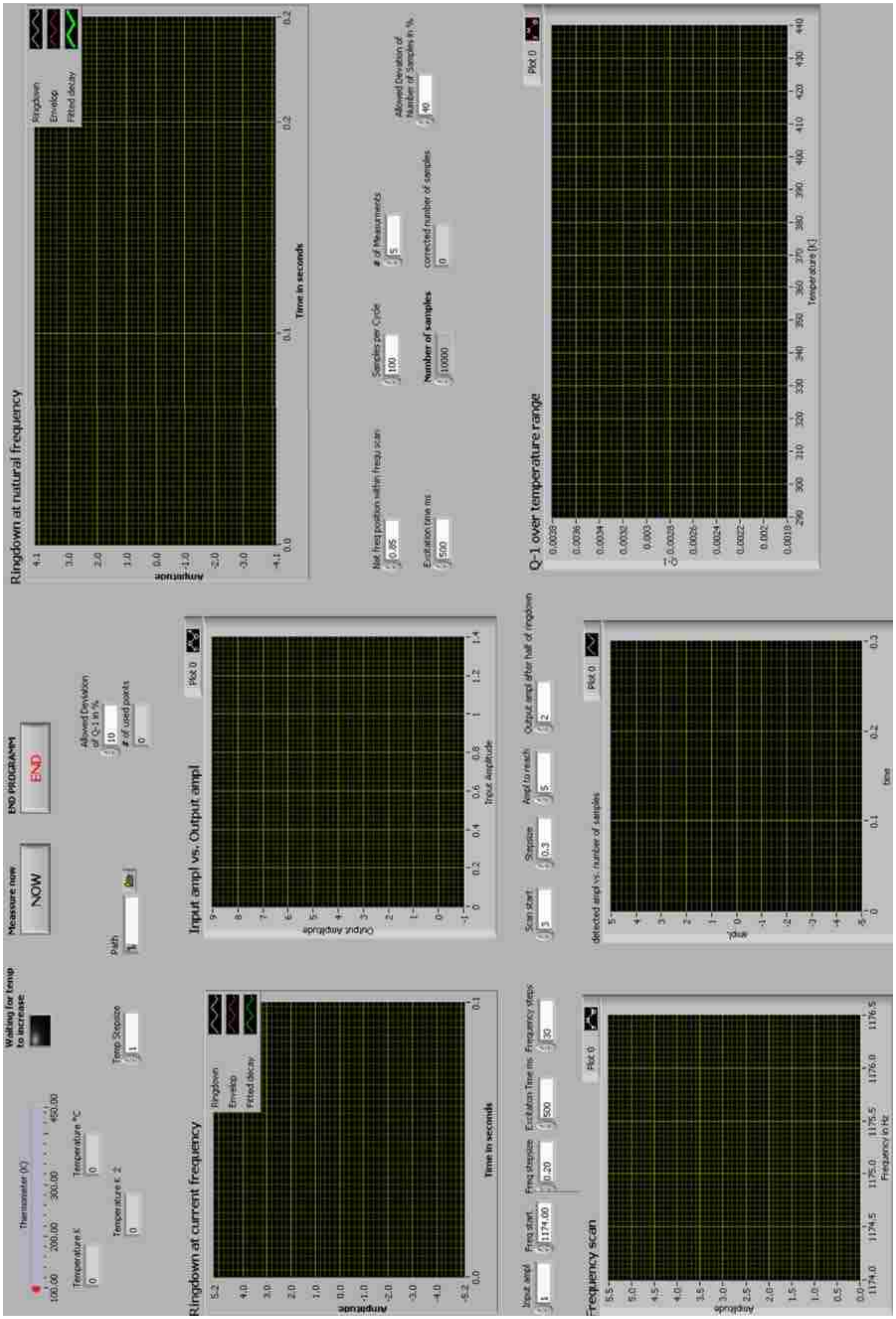

Nat. freq position within frequ scan: 0.85

Excitation time ms: 500

Samples per Cycle: 100

Number of samples: 10000

# of Measurements: 5

corrected number of samples: 0

Allowed Deviation of Number of Samples in %: 40

Temperature K: 0

Temperature °C: 0

Temperature K 2: 0

Temp Stepsize: 1

Allowed Deviation of Q-1 in %: 10

# of used points: 0

Input ampl: 1

Freq start: 1174.00

Freq stepsize: 0.20

Excitation Time ms: 500

Frequency steps: 30

Scan start: 3

Stepsize: 0.3

Ampl to reach: 5

Output ampl after half of ringdown: 2

Appendix B

Operator Interface for Small-Scale Testing Measurement System (Unity Pro M)

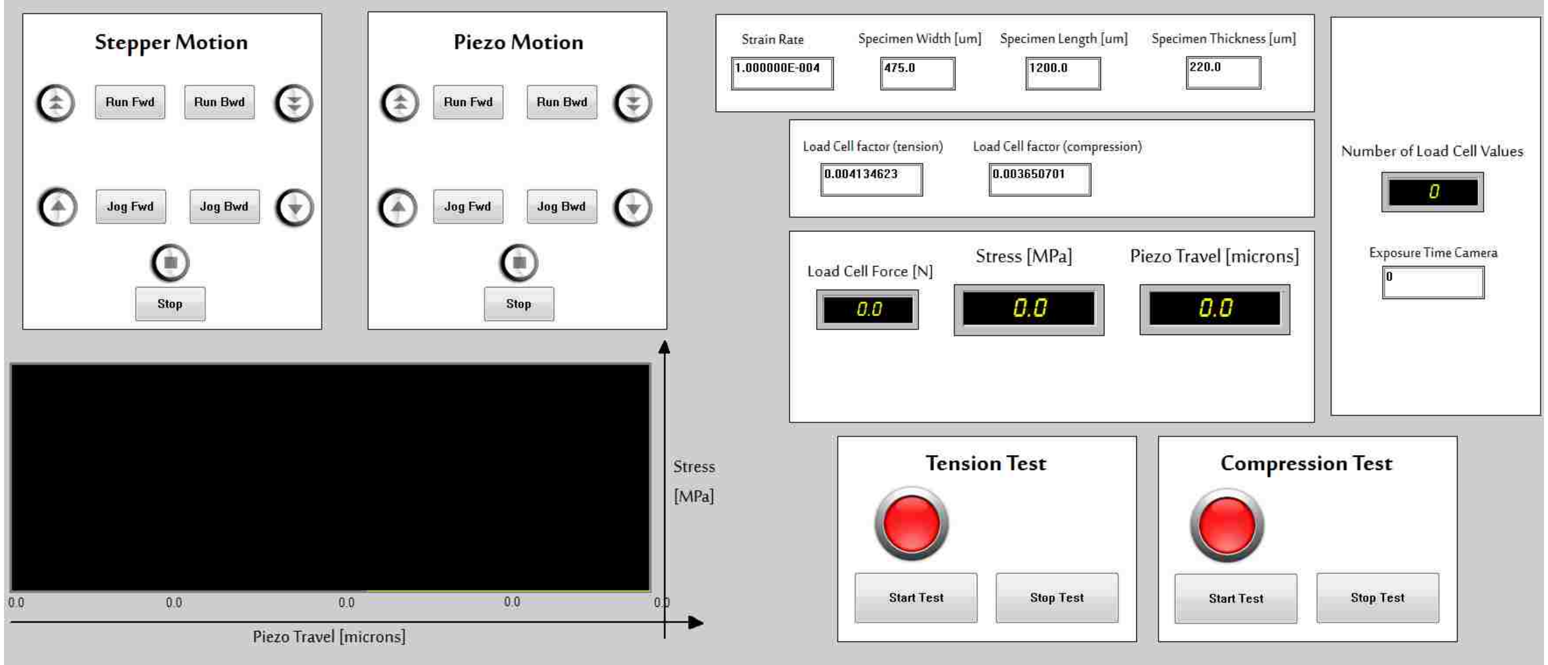

Strain Rate: 1.000000E-004

Specimen Width [um]: 475.0

Specimen Length [um]: 1200.0

Specimen Thickness [um]: 220.0

Load Cell factor (tension): 0.004134623

Load Cell factor (compression): 0.003650701

Load Cell Force [N]: 0.0

Stress [MPa]: 0.0

Piezo Travel [microns]: 0.0

Number of Load Cell Values: 0

Exposure Time Camera: 0

Appendix C

Function Block Diagrams and Ladder Programming Details for Small-Scale Testing Measurement System (Unity Pro M)

Piezo Motion Control

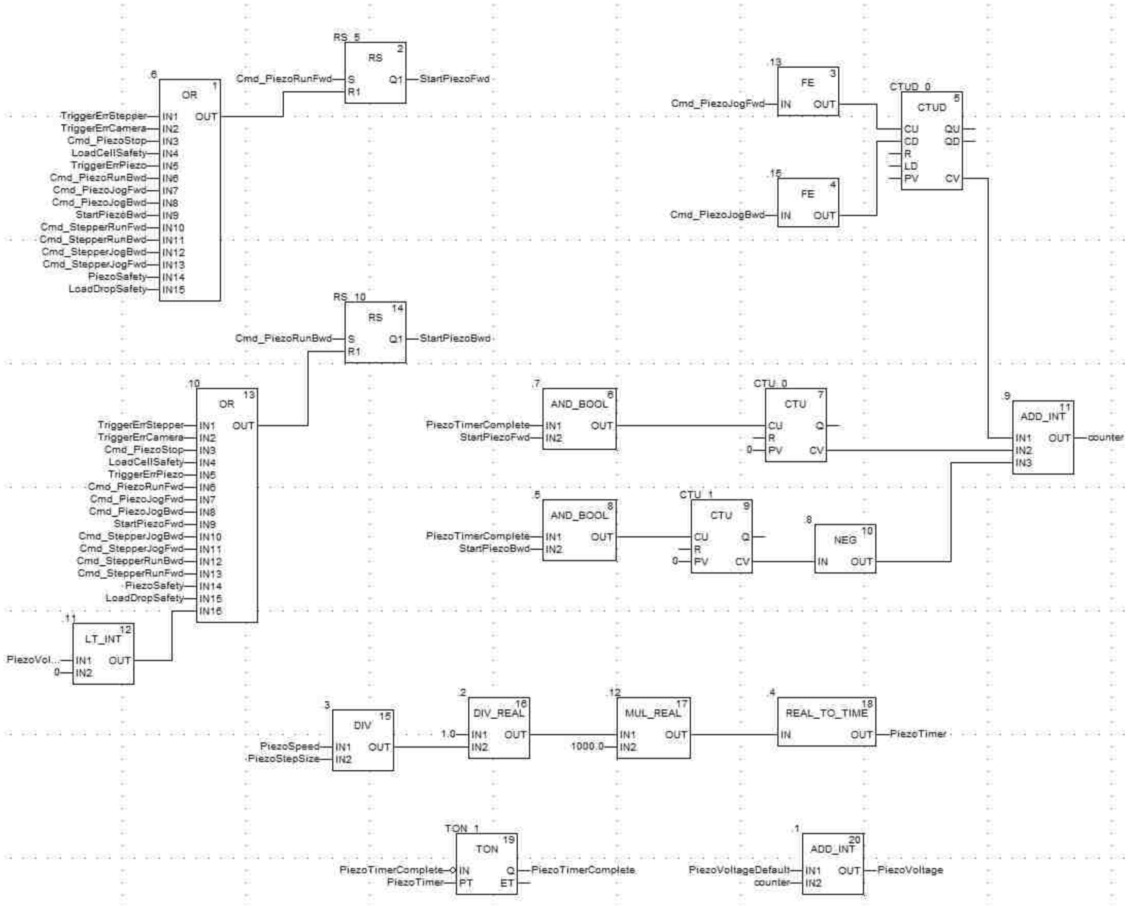

Stepper Motion Control

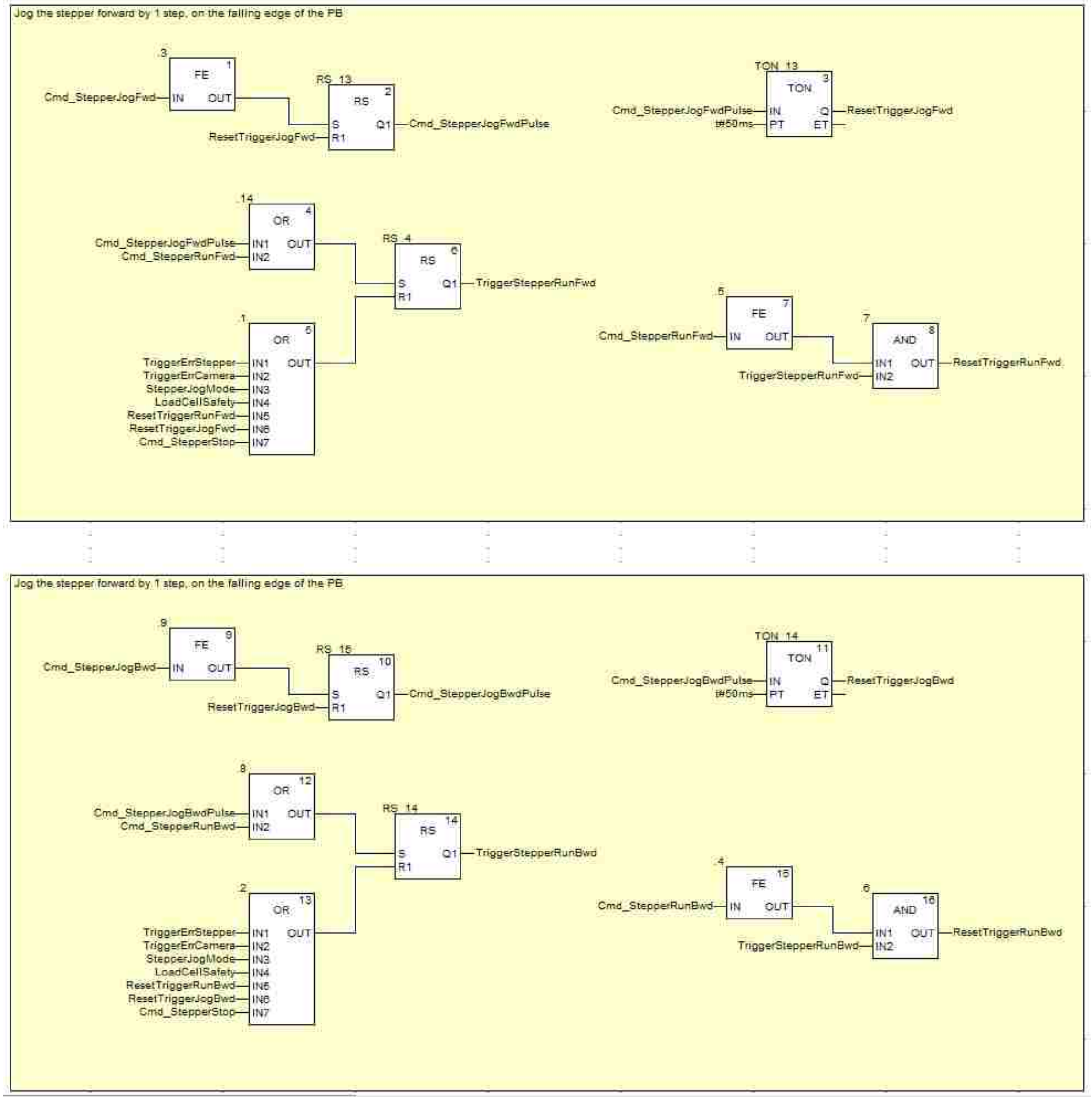

Stepper Interface Control

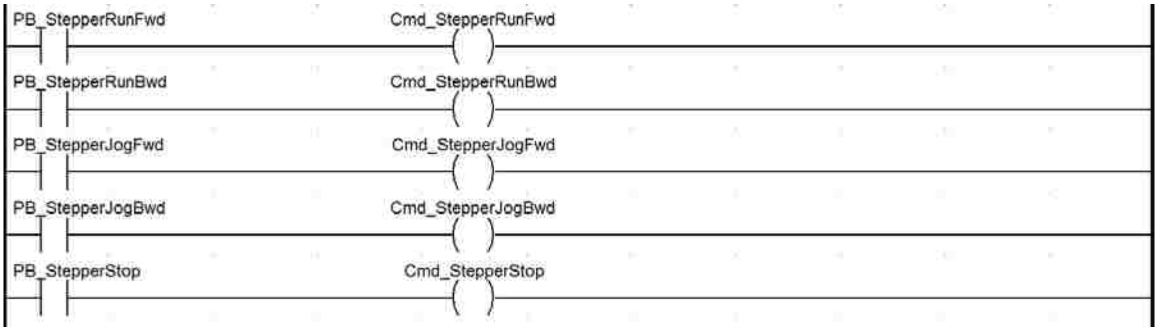

Piezo Interface Control

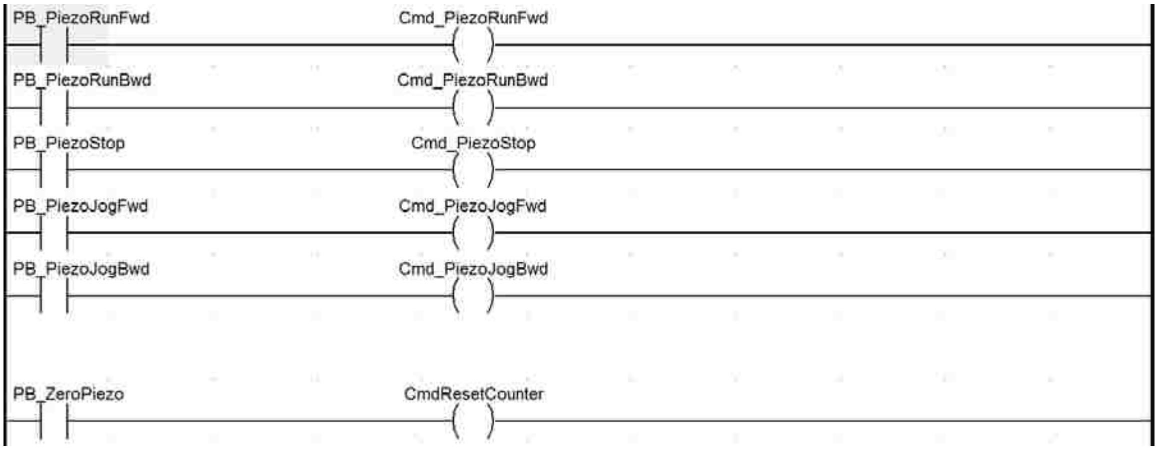

Testing Interface Control

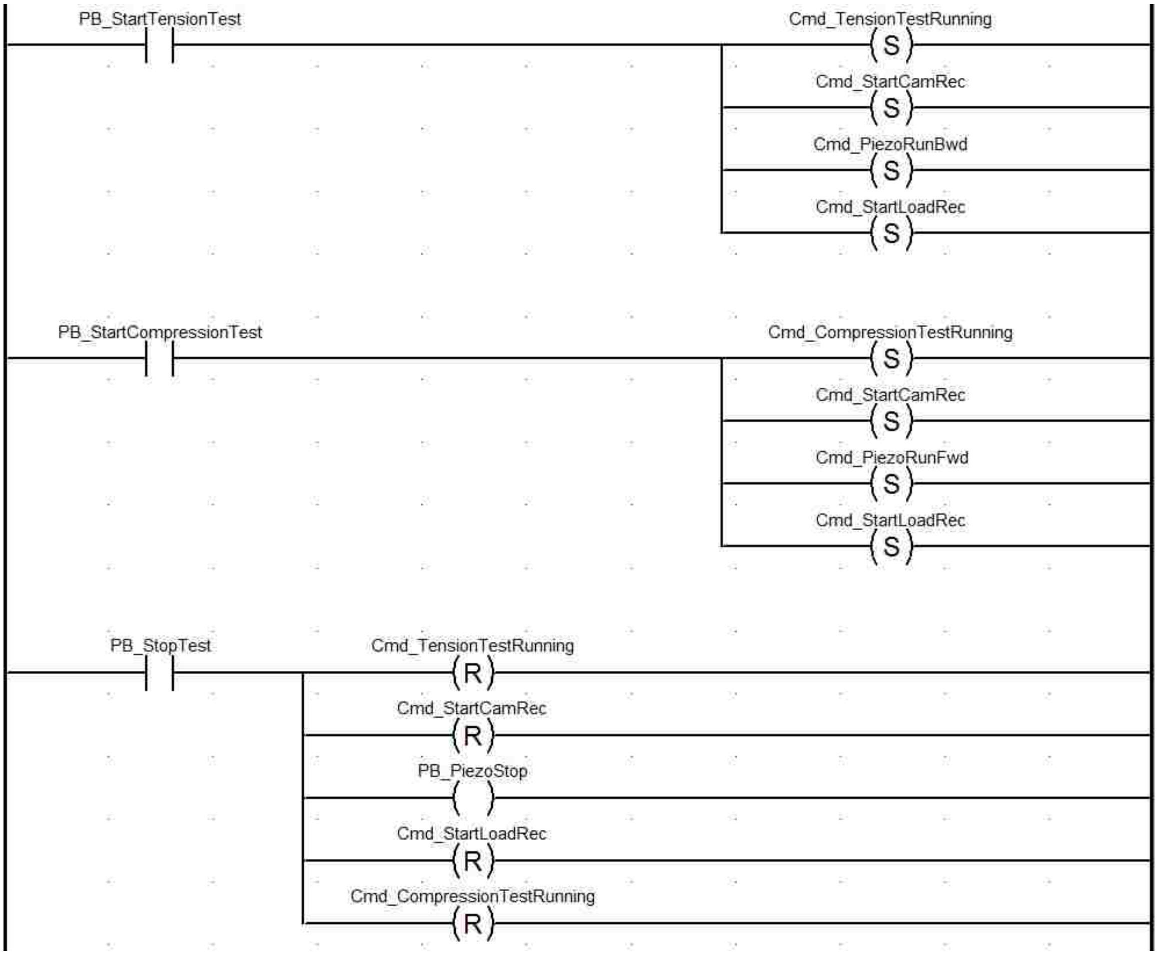

Data Recording Control

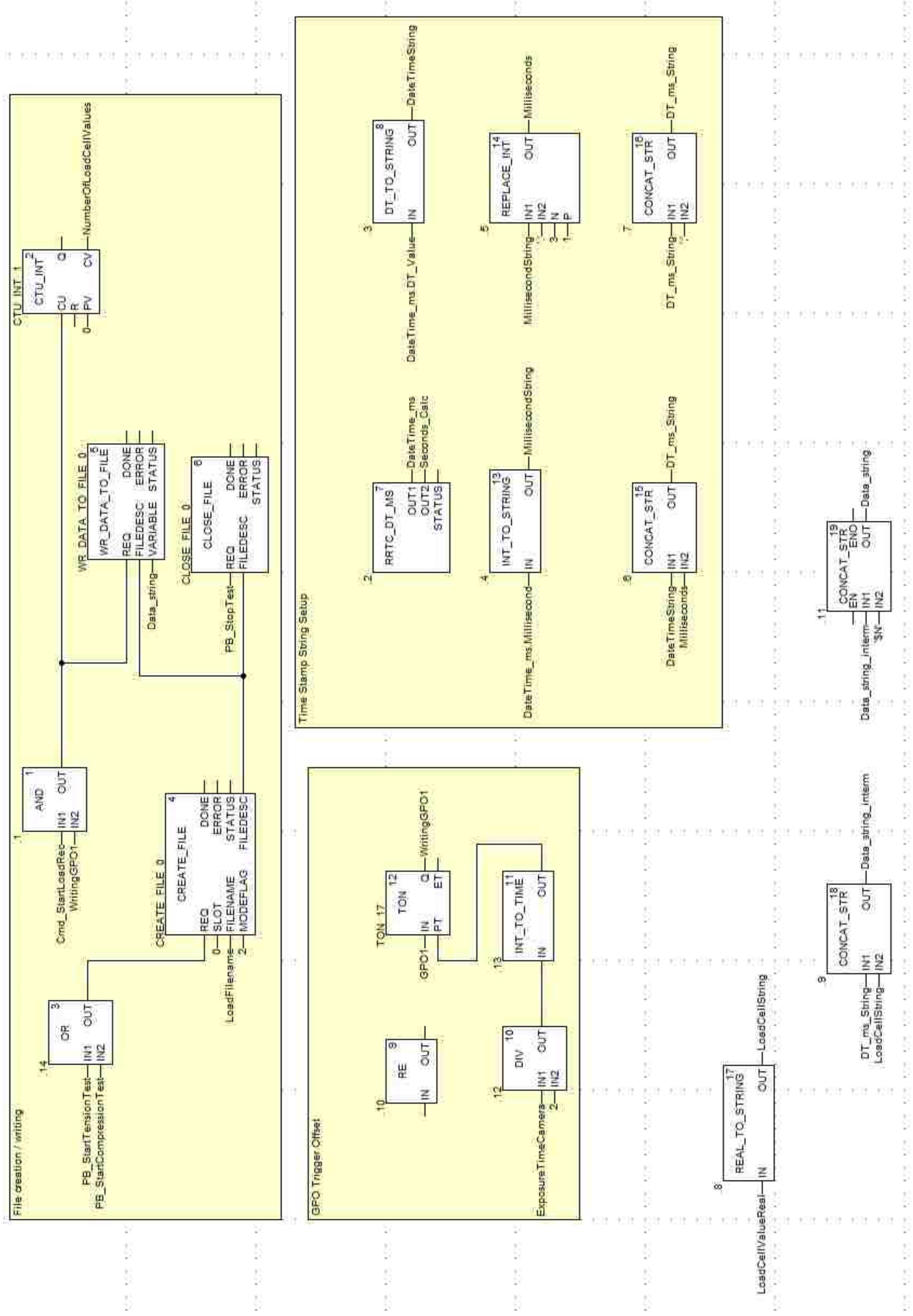

Parameters Calculations

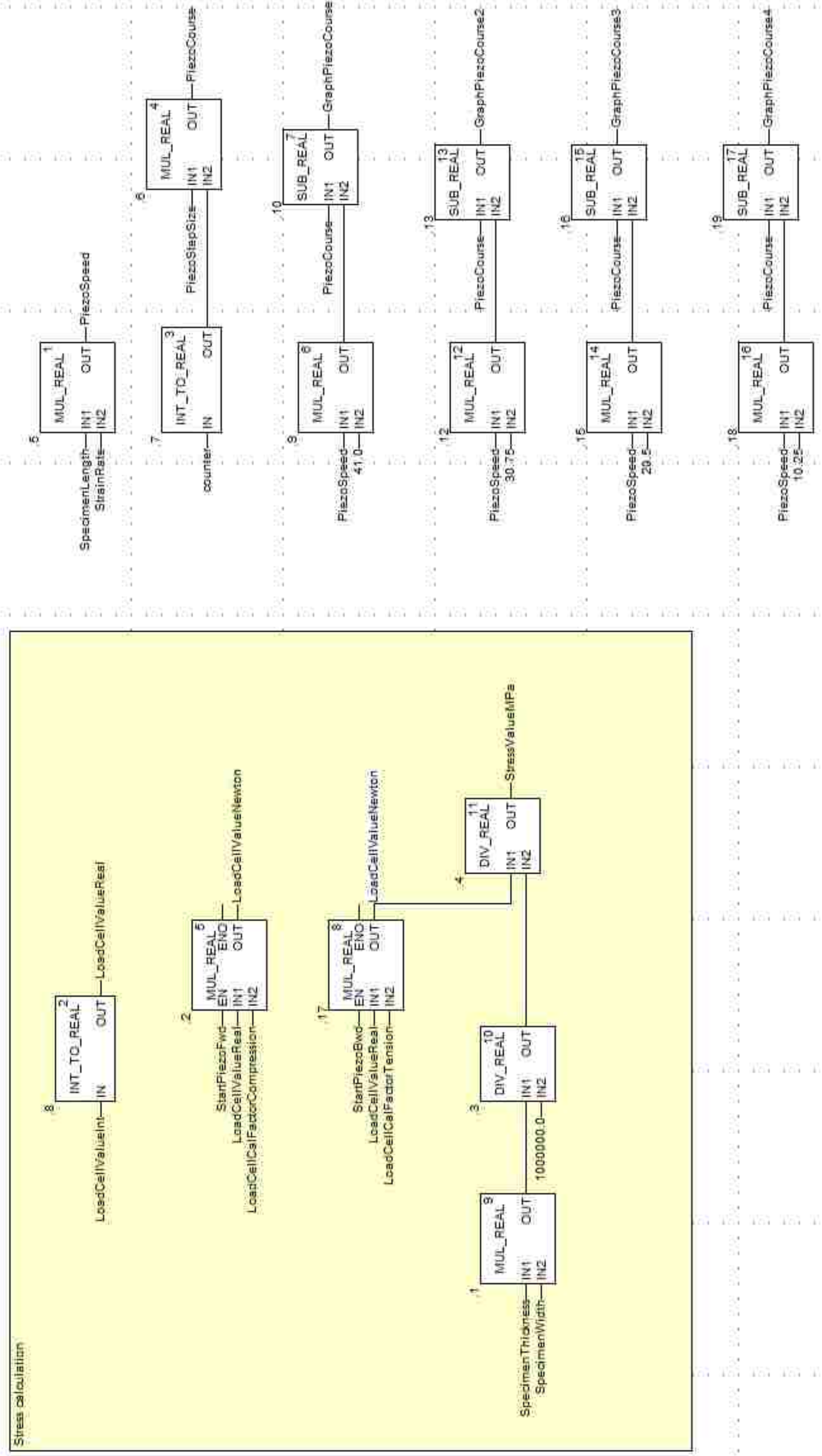

Safety Calculations

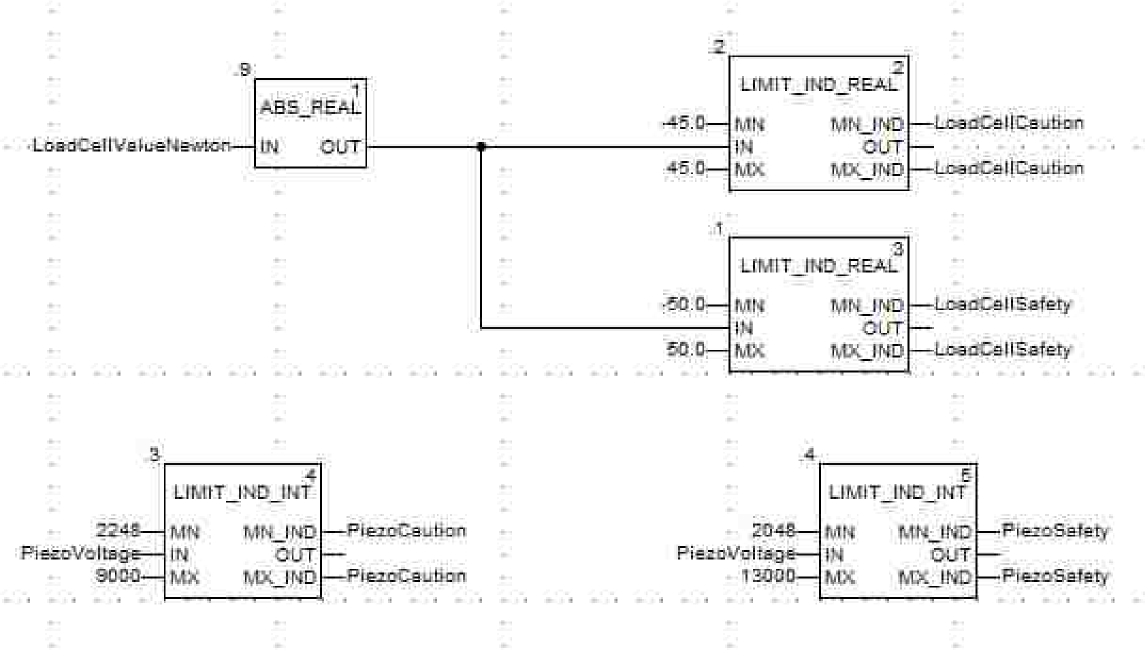

Appendix D

Cabling Schematic for Small-Scale Testing Measurement System

BSC101 (stepper controller) Cabling

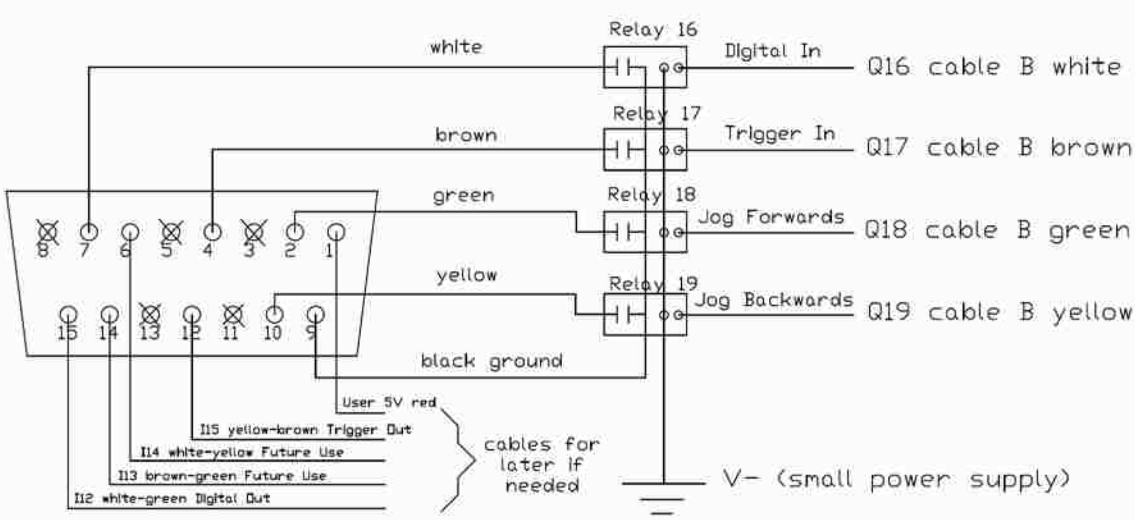

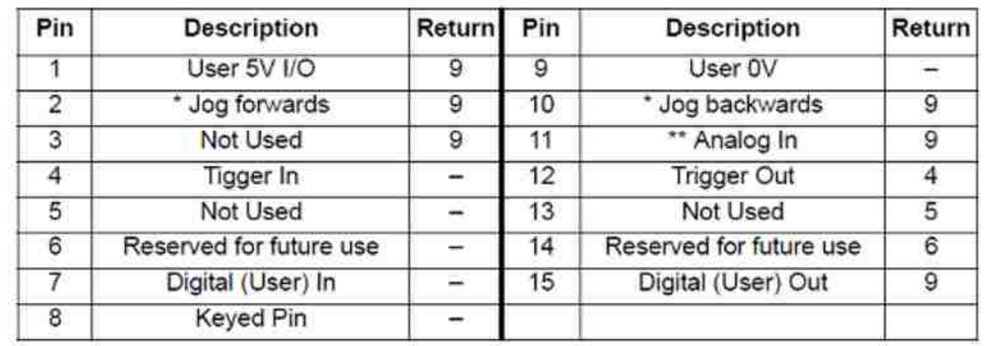

Pin	Description	Return	Pin	Description	Return
1	User 5V I/O	9	9	User 0V	–
2	* Jog forwards	9	10	* Jog backwards	9
3	Not Used	9	11	** Analog In	9
4	Tigger In	–	12	Trigger Out	4
5	Not Used	–	13	Not Used	5
6	Reserved for future use	–	14	Reserved for future use	6
7	Digital (User) In	–	15	Digital (User) Out	9
8	Keyed Pin	–			

Digital Interface Cabling (PLC)

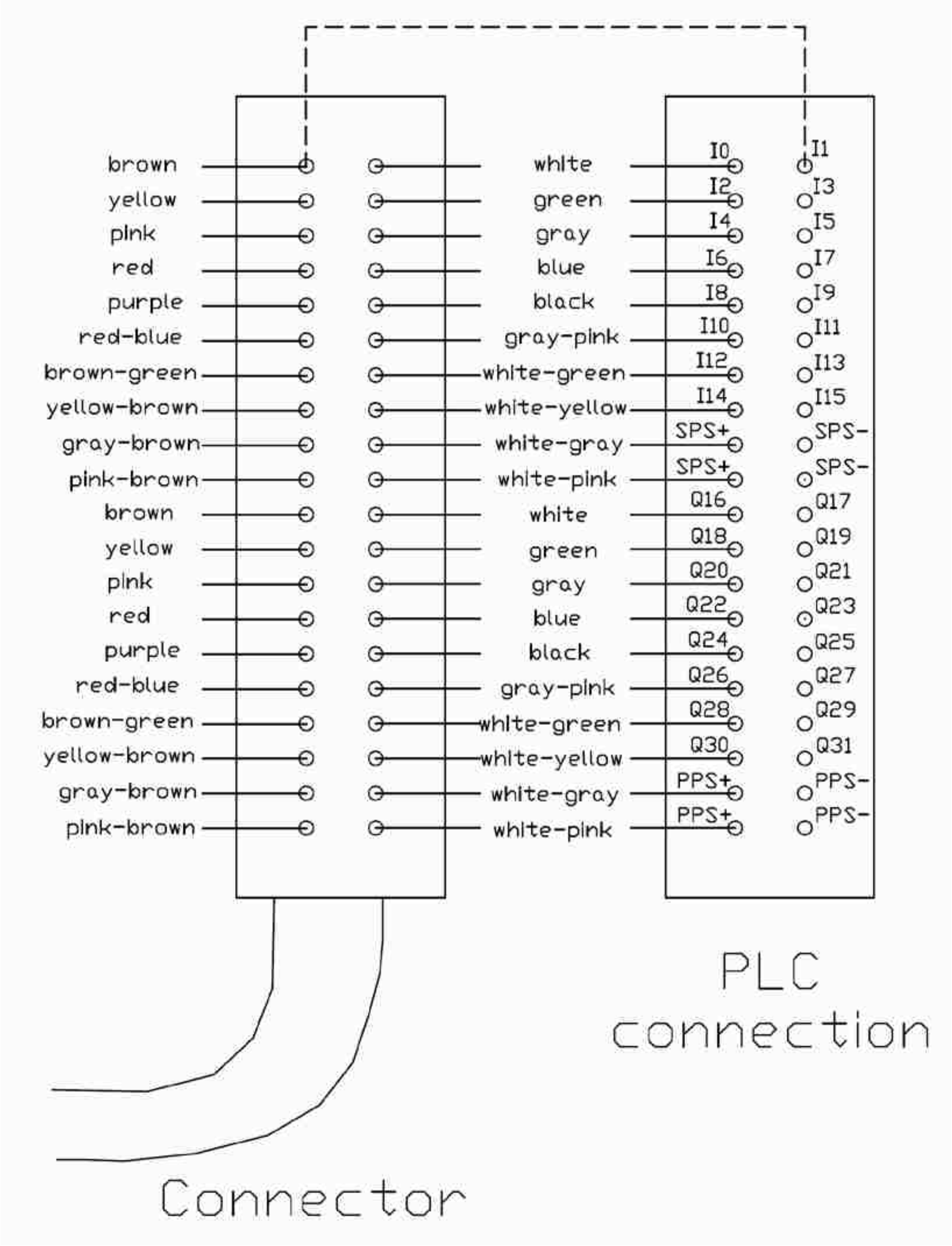

Camera (PL-B782F) Cabling

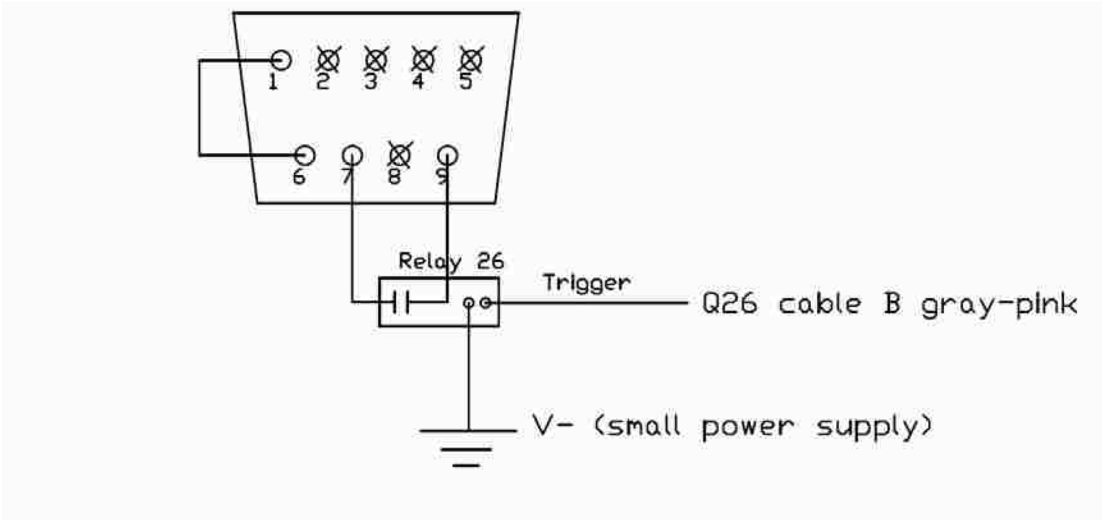

Pin	Pin Name	Function	Comments
1	POWER (Firewire camera only)	Firewire cable power, 8-30 VDC (typically 12 V)	Maximum current available from this pin is 250 mA
1	POWER (USB2 camera only)	+5.5 VDC (internally generated by camera)	Maximum current available from this pin is 50 mA
2	GP2+	Positive terminal of optically isolated General Purpose Output 2	Optical isolator open collector output. Provides current sink to pin 3 when GP2 is active. Also see GPO notes below chart.
3	GP2–	Negative terminal of optically isolated General Purpose Output 2	Optical isolator emitter output. Typically connected externally to pin 9 (Ground)
4	GP1+	Positive terminal of optically isolated General Purpose Output 1	Optical isolator open collector output. Provides current sink to pin 5 when GP1 is active. Also see GPO notes below chart.
5	GP1–	Negative terminal of optically isolated General Purpose Output 1	Optical isolator emitter output. Typically connected externally to pin 9 (Ground)
6	TRIGGER+	Positive terminal of optically isolated trigger input	See Trigger Notes below chart
7	TRIGGER–	Negative terminal of optically isolated trigger input	See Trigger Notes below chart
8		(no connection)	(not used)
9	GROUND	Logic and chassis ground	

References

[1] J. W. Patrick, *Porosity in carbons: characterization and applications*. New York: Halsted Press, 1995.

[2] J. H. Turney, “Dialysis: History, Development and Promise Todd S. Ing, Mohamed A. Rahman, Carl M. Kjellstrand, editors Singapore: World Scientific,” *Hemodial. Int.*, vol. 18, no. 1, pp. 218–219, 2014.

[3] D. Nicholson, “Using computer simulation to study the properties of molecules in micropores,” *J. Chem. Soc., Faraday Trans.*, vol. 92, no. 1, p. 1, 1996.

[4] E. Robens, *Characterization of Porous Solids III*, vol. 87. Elsevier, 1994.

[5] W. L. MacDonald, *The Architecture of the Roman Empire, Volume 1: An Introductory Study*, Revised ed. New Haven and London: Yale University Press, 1982.

[6] A. F. Cronstedt and H. Akad, “Ron och beskriting om en obekant b ä rg ant, som kallas zeolites,” *Akad. Handl. Stock.*, vol. 18, pp. 120–130, 1756.

[7] P. Chemistry and J. Yu, “Chapter 3 Synthesis of zeolites,” in *Introduction to Zeolite Science and Practice*, vol. 168, A. C. Jiří Čejka Herman van Bekkum and F. Schüth, Eds. Elsevier, 2007, pp. 39–103.

[8] R. Barrer, “435. Syntheses and reactions of mordenite,” *J. Chem. Soc.*, no. 2158, 1948.

[9] E. Flanigen, “Zeolites and molecular sieves an historical perspective,” *Stud. Surf. Sci. Catal.*, pp. 11–35, 1991.

[10] F. Di Renzo and F. Fajula, “Introduction to molecular sieves: trends of evolution of the zeolite community,” *Stud. Surf. Sci. Catal*, pp. 1–12, 2005.

[11] S. Davis and Y. Inoguchi, “CEH Marketing Research Report: Zeolites,” 2009.

[12] J. Rouquerol, D. Avnir, C. W. Fairbridge, D. H. Everett, J. M. Haynes, N. Pernicone, J. D. F. Ramsay, K. S. W. Sing, and K. K. Unger, “Recommendations for the characterization of porous solids (Technical Report),” *Pure Appl. Chem.*, vol. 66, no. 8, pp. 1739–1758, 1994.

[13] Á. Berenguer Murcia and Á. B. Murcia, “Ordered Porous Nanomaterials: The Merit of Small,” *ISRN Nanotechnol.*, vol. 2013, pp. 1–29, 2013.

[14] T. J. Maysl and T. Mays, “A new classification of pore sizes,” *Stud. Surf. Sci. Catal.*, vol. 44, no. 0, pp. 57–62, 2007.

[15] T. Xu, J. Stevens, J. A. Villa, J. T. Goldbach, K. W. Guarini, C. T. Black, C. J. Hawker, and T. P. Russell, “Block Copolymer Surface Reconstuction: A Reversible Route to Nanoporous Films,” *Adv. Funct. Mater.*, vol. 13, no. 9, pp. 698–702, 2003.

[16] C. R. Martin, “Nanomaterials: a membrane-based synthetic approach.,” *Science*, vol. 266, no. 5193, pp. 1961–6, Dec. 1994.

[17] J. C. Hulteen and C. R. Martin, “A general template-based method for the preparation of nanomaterials,” *J. Mater. Chem.*, vol. 7, no. 7, pp. 1075–1087, 1997.

[18] A. S. Poyraz, C.-H. Kuo, S. Biswas, C. K. King’ondu, and S. L. Suib, “A general approach to crystalline and monomodal pore size mesoporous materials,” *Nat Commun*, vol. 4, Dec. 2013.

[19] B. Jürgens, C. Kübel, C. Schulz, T. Nowitzki, V. Zielasek, J. Biener, M. M. Biener, A. V Hamza, and M. Bäumer, “New gold and silver-gold catalysts in the shape of sponges and sieves,” *Gold Bull.*, vol. 40, no. 2, pp. 142–149, Jun. 2007.

[20] A. Wittstock, J. Biener, and M. Bäumer, “Nanoporous gold: a new material for catalytic and sensor applications.,” *Phys. Chem. Chem. Phys.*, vol. 12, no. 40, pp. 12919–30, Oct. 2010.

[21] C. Xu, J. Su, X. Xu, P. Liu, H. Zhao, F. Tian, and Y. Ding, “Low temperature CO oxidation over unsupported nanoporous gold,” *J. Am. Chem. Soc.*, vol. 129, pp. 42–43, 2007.

[22] R. Zeis, T. Lei, K. Sieradzki, J. Snyder, and J. Erlebacher, “Catalytic reduction of oxygen and hydrogen peroxide by nanoporous gold,” *J. Catal.*, vol. 253, no. 1, pp. 132–138, Jan. 2008.

[23] D. a McCurry, M. Kamundi, M. Fayette, F. Wafula, and N. Dimitrov, “All electrochemical fabrication of a platinized nanoporous Au thin-film catalyst.,” *ACS Appl. Mater. Interfaces*, vol. 3, no. 11, pp. 4459–68, Nov. 2011.

[24] R. Zeis, A. Mathur, G. Fritz, J. Lee, and J. Erlebacher, “Platinum-plated nanoporous gold: An efficient, low Pt loading electrocatalyst for PEM fuel cells,” *J. Power Sources*, vol. 165, pp. 65–72, 2007.

[25] L. C. Nagle and J. F. Rohan, “Nanoporous Gold Catalyst for Direct Ammonia Borane Fuel Cells,” *J. Electrochem. Soc.*, vol. 158, no. 7, p. B772, 2011.

[26] J. Snyder, T. Fujita, M. W. Chen, and J. Erlebacher, “Oxygen reduction in nanoporous metal-ionic liquid composite electrocatalysts.,” *Nat. Mater.*, vol. 9, no. 11, pp. 904–7, Nov. 2010.

[27] H.-J. Jin, X.-L. Wang, S. Parida, K. Wang, M. Seo, and J. Weissmüller, “Nanoporous Au-Pt alloys as large strain electrochemical actuators.,” *Nano Lett.*, vol. 10, no. 1, pp. 187–94, Jan. 2010.

[28] J. Biener, a Wittstock, L. a Zepeda-Ruiz, M. M. Biener, V. Zielasek, D. Kramer, R. N. Viswanath, J. Weissmüller, M. Bäumer, and a V Hamza, “Surface-chemistry-driven actuation in nanoporous gold.,” *Nat. Mater.*, vol. 8, no. 1, pp. 47–51, Jan. 2009.

[29] M. Hakamada, S. Matsumura, and M. Mabuchi, “Electrochemical actuation of nanoporous Ni in NaOH solution,” *Mater. Lett.*, 2012.

[30] J. Weissmüller, R. N. Viswanath, D. Kramer, P. Zimmer, R. Würschum, and H. Gleiter, “Charge-induced reversible strain in a metal.,” *Science*, vol. 300, no. 5617, pp. 312–5, Apr. 2003.

[31] H.-J. Jin and J. Weissmüller, “Bulk Nanoporous Metal for Actuation,” *Adv. Eng. Mater.*, vol. 12, no. 8, pp. 714–723, Aug. 2010.

[32] Z. Liu and P. Searson, “Single nanoporous gold nanowire sensors,” *J. Phys. Chem. B*, vol. 360, pp. 4318–4322, 2006.

[33] K. Hu, D. Lan, X. Li, and S. Zhang, “Electrochemical DNA biosensor based on nanoporous gold electrode and multifunctional encoded DNA-Au bio bar codes,” *Anal. Chem.*, vol. 80, no. 23, pp. 9124–9130, Dec. 2008.

[34] X. Lang, A. Hirata, T. Fujita, and M. Chen, “Nanoporous metal/oxide hybrid electrodes for electrochemical supercapacitors.,” *Nat. Nanotechnol.*, vol. 6, no. 4, pp. 232–6, Apr. 2011.

[35] X. Y. Lang, H. T. Yuan, Y. Iwasa, and M. W. Chen, “Three-dimensional nanoporous gold for electrochemical supercapacitors,” *Scr. Mater.*, vol. 64, no. 9, pp. 923–926, May 2011.

[36] C. Hou, X.-Y. Lang, G.-F. Han, Y.-Q. Li, L. Zhao, Z. Wen, Y.-F. Zhu, M. Zhao, J.-C. Li, J.-S. Lian, and Q. Jiang, “Integrated solid/nanoporous copper/oxide hybrid bulk electrodes for high-performance lithium-ion batteries.,” *Sci. Rep.*, vol. 3, p. 2878, Jan. 2013.

[37] S. R. Gowda, A. L. M. Reddy, X. Zhan, H. R. Jafry, and P. M. Ajayan, “3D nanoporous nanowire current collectors for thin film microbatteries.,” *Nano Lett.*, vol. 12, no. 3, pp. 1198–202, Mar. 2012.

[38] S. D. Gittard, B. E. Pierson, C. M. Ha, C.-A. M. Wu, R. J. Narayan, and D. B. Robinson, “Supercapacitive transport of pharmacologic agents using nanoporous gold electrodes.,” *Biotechnol. J.*, vol. 5, pp. 192–200, 2010.

[39] S. P. Adiga, C. Jin, L. A. Curtiss, N. A. Monteiro-Riviere, and R. J. Narayan, “Nanoporous membranes for medical and biological applications,” *Wiley Interdisciplinary Reviews: Nanomedicine and Nanobiotechnology*, vol. 1. pp. 568–581, 2009.

[40] M. P. Klein, B. W. Jacobs, M. D. Ong, S. J. Fares, D. B. Robinson, V. Stavila, G. J. Wagner, and I. Arslan, “Three-dimensional pore evolution of nanoporous metal particles for energy storage.,” *J. Am. Chem. Soc.*, vol. 133, no. 24, pp. 9144–7, Jun. 2011.

[41] M. Bosman, G. R. Anstis, V. J. Keast, J. D. Clarke, and M. B. Cortie, “Light splitting in nanoporous gold and silver.,” *ACS Nano*, vol. 6, no. 1, pp. 319–26, Jan. 2012.

[42] T. V Teperik, V. V Popov, F. J. García de Abajo, T. a Kelf, Y. Sugawara, J. J. Baumberg, M. Abdelsalem, and P. N. Bartlett, “Mie plasmon enhanced diffraction of light from nanoporous metal surfaces.,” *Opt. Express*, vol. 14, no. 25, pp. 11964–71, Dec. 2006.

[43] T. Teperik, V. Popov, and F. García de Abajo, “Void plasmons and total absorption of light in nanoporous metallic films,” *Phys. Rev. B*, vol. 71, no. 8, p. 085408, Feb. 2005.

[44] M. Dixon, T. Daniel, and M. Hieda, “Preparation, structure, and optical properties of nanoporous gold thin films,” *Langmuir*, no. 19, pp. 2414–2422, 2007.

[45] F. Yu, S. Ahl, and A. Caminade, “Simultaneous excitation of propagating and localized surface plasmon resonance in nanoporous gold membranes,” *Anal. Chem.*, vol. 78, no. 20, pp. 7346–7350, 2006.

[46] J. Biener, G. W. Nyce, A. M. Hodge, M. M. Biener, A. V. Hamza, and S. A. Maier, “Nanoporous plasmonic metamaterials,” *Adv. Mater.*, vol. 20, pp. 1211–1217, 2008.

[47] C. Ji and P. Searson, “Synthesis and characterization of nanoporous gold nanowires,” *J. Phys. Chem. B*, vol. 3, no. pH 13, pp. 4494–4499, 2003.

[48] I.-C. Cheng and A. M. Hodge, “Strength scale behavior of nanoporous Ag, Pd and Cu foams,” *Scr. Mater.*, vol. 69, no. 4, pp. 295–298, Aug. 2013.

[49] C. Zhang, J. Sun, J. Xu, X. Wang, H. Ji, C. Zhao, and Z. Zhang, “Formation and microstructure of nanoporous silver by dealloying rapidly solidified Zn–Ag alloys,” *Electrochim. Acta*, vol. 63, pp. 302–311, Feb. 2012.

[50] C. Sun, D. Bufford, Y. Chen, M. a Kirk, Y. Q. Wang, M. Li, H. Wang, S. a Maloy, and X. Zhang, “In situ study of defect migration kinetics in nanoporous Ag with enhanced radiation tolerance.,” *Sci. Rep.*, vol. 4, p. 3737, Jan. 2014.

[51] Y. Ding, Y. Kim, and J. Erlebacher, “Nanoporous gold leaf:‘Ancient technology’/advanced material,” *Adv. Mater.*, no. 21, pp. 1897–1900, 2004.

[52] J. Weissmüller, R. C. Newman, H. Jin, A. M. Hodge, and J. W. Kysar, “N anoporous Metals by Alloy Corrosion : Formation and Mechanical Properties,” vol. 34, no. August, pp. 577–586, 2009.

[53] Y. Sun and T. Balk, “A multi-step dealloying method to produce nanoporous gold with no volume change and minimal cracking,” *Scr. Mater.*, vol. c, pp. 727–730, 2008.

[54] L. Wang, N. J. Briot, P. D. Swartzentruber, and T. J. Balk, “Magnesium Alloy Precursor Thin Films for Efficient, Practical Fabrication of Nanoporous Metals,” *Metall. Mater. Trans. A*, vol. 45, no. 1, pp. 1–5, Nov. 2013.

[55] L. Wang and T. J. Balk, “Using Multilayer Precursors to Create Nanoporous Gold and Nanoporous Iridium Thin Films with Layered Architecture,” *Metall. Mater. Trans. A*, vol. 45, no. 3, pp. 1096–1100, Jan. 2014.

[56] M. Hakamada and M. Mabuchi, “Preparation of nanoporous Ni and Ni–Cu by dealloying of rolled Ni–Mn and Ni–Cu–Mn alloys,” *J. Alloys Compd.*, vol. 485, no. 1–2, pp. 583–587, Oct. 2009.

[57] L. Wang and T. J. Balk, “Synthesis of nanoporous nickel thin films from various precursors,” *Philos. Mag. Lett.*, vol. 94, no. 9, pp. 573–581, 2014.

[58] X. Wang, W. Wang, Z. Qi, C. Zhao, H. Ji, and Z. Zhang, “Fabrication, microstructure and electrocatalytic property of novel nanoporous palladium composites,” *J. Alloys Compd.*, vol. 508, no. 2, pp. 463–470, 2010.

[59] M. Hakamada, H. Nakano, T. Furukawa, M. Takahashi, and M. Mabuchi, “Hydrogen Storage Properties of Nanoporous Palladium Fabricated by Dealloying,” *J. Phys. Chem. C*, vol. 114, no. 2, pp. 868–873, Jan. 2010.

[60] W. Li and T. Balk, “Preparation and Hydrogen Absorption/Desorption of Nanoporous Palladium Thin Films,” *Materials (Basel).*, pp. 2496–2509, 2009.

[61] Z. Zhang, Y. Wang, Z. Qi, W. Zhang, J. Qin, and J. Frenzel, “Generalized Fabrication of Nanoporous Metals (Au, Pd, Pt, Ag, and Cu) through Chemical Dealloying,” *J. Phys. Chem. C*, vol. 113, no. 29, pp. 12629–12636, Jul. 2009.

[62] M. Grimwade, “The surface enrichment of carat gold alloys - depletion gilding,” *Gold Technol.*, vol. 26, no. May 1999, pp. 16–23, 1999.

[63] H. Lechtman, “Pre-Columbian Surface Metallurgy,” *Sci. Am.*, vol. 250, no. 6, pp. 56–63, Jun. 1984.

[64] J. Erlebacher, M. J. Aziz, a Karma, N. Dimitrov, and K. Sieradzki, “Evolution of nanoporosity in dealloying.,” *Nature*, vol. 410, no. 6827, pp. 450–3, Mar. 2001.

[65] J. Erlebacher, “An Atomistic Description of Dealloying,” *J. Electrochem. Soc.*, vol. 151, no. 10, p. C614, 2004.

[66] W. Thompson, M. Kaye, C. Bale, and A. Pelton, “Pourbaix Diagrams for Multielement Systems,” in *Uhlig’s Corrosion Handbook*, Second Edi., R. Winston Revie, Ed. John Wiley & Sons, Inc., 2000, pp. 103–109.

[67] L. L. Martínez, M. Segarra, M. Fernández, and F. Espiell, “Kinetics of the dissolution of pure silver and silver-gold alloys in nitric acid solution,” *Metall. Trans. B*, vol. 24, no. October, pp. 827–837, 1993.

[68] H. Okamoto, *Desk Handbook: Phase Diagrams for Binary Alloys*, Second Edi. Materials Park, OH: ASM International, 2010.

[69] Y. Sun, S. a. Burger, and T. J. Balk, “Controlled ligament coarsening in nanoporous gold by annealing in vacuum versus nitrogen,” *Philos. Mag.*, vol. 94, no. 10, pp. 1001–1011, Feb. 2014.

[70] M. Haruta, “New Generation of Gold Catalysts: Nanoporous Foams and Tubes—Is Unsupported Gold Catalytically Active?,” *ChemPhysChem*, pp. 1911–1913, 2007.

[71] M. Haruta, “Size- and support-dependency in the catalysis of gold,” *Catal. Today*, vol. 36, no. 1, pp. 153–166, Apr. 1997.

[72] M. Haruta, “Gold catalysts prepared by coprecipitation for low-temperature oxidation of hydrogen and of carbon monoxide,” *J. Catal.*, vol. 115, no. 2, pp. 301–309, Feb. 1989.

[73] M. Haruta, “Low-Temperature Oxidation of CO over Gold Supported on TiO2, α-Fe2O3, and Co3O4,” *J. Catal.*, vol. 144, no. 1, pp. 175–192, Nov. 1993.

[74] M. Haruta, “When gold is not noble: catalysis by nanoparticles.,” *Chem. Rec.*, vol. 3, no. 2, pp. 75–87, Jan. 2003.

[75] M. Haruta, “Gold as a novel catalyst in the 21st century: Preparation, working mechanism and applications,” *Gold Bull.*, vol. 37, no. 1–2, pp. 27–36, Mar. 2004.

[76] V. Zielasek, B. Jürgens, C. Schulz, J. Biener, M. M. Biener, A. V. Hamza, and M. Bäumer, “Gold catalysts: Nanoporous gold foams,” *Angew. Chem. Int. Ed.*, vol. 45, pp. 8241–8244, 2006.

[77] A. Wittstock, V. Zielasek, J. Biener, C. M. Friend, and M. Bäumer, “Nanoporous gold catalysts for selective gas-phase oxidative coupling of methanol at low temperature.,” *Science*, vol. 327, no. 5963, pp. 319–322, Jan. 2010.

[78] D. Kramer, R. Viswanath, and J. Weissmüller, “Surface-stress induced macroscopic bending of nanoporous gold cantilevers,” *Nano Lett.*, 2004.

[79] W. Li, S. Schendel, and T. Balk, “Microstructure and Hydrogen Absorption/Desorption Behavior of Nanoporous Pd Thin Films,” *MRS Proc.*, vol. 1098, 2008.

[80] E. M. Bringa, J. D. Monk, A. Caro, A. Misra, L. Zepeda-Ruiz, M. Duchaineau, F. Abraham, M. Nastasi, S. T. Picraux, Y. Q. Wang, and D. Farkas, “Are nanoporous materials radiation resistant?,” *Nano Lett.*, vol. 12, no. 7, pp. 3351–5, Jul. 2012.

[81] E. G. Fu, M. Caro, L. a. Zepeda-Ruiz, Y. Q. Wang, K. Baldwin, E. Bringa, M. Nastasi, and a. Caro, “Surface effects on the radiation response of nanoporous Au foams,” *Appl. Phys. Lett.*, vol. 101, no. 19, p. 191607, 2012.

[82] M. Caro, W. M. Mook, E. G. Fu, Y. Q. Wang, C. Sheehan, E. Martinez, J. K. Baldwin, and a. Caro, “Radiation induced effects on mechanical properties of nanoporous gold foams,” *Appl. Phys. Lett.*, vol. 104, no. 23, p. 233109, Jun. 2014.

[83] R. Li and K. Sieradzki, “Ductile-brittle transition in random porous Au,” *Phys. Rev. Lett.*, vol. 68, no. 8, pp. 1168–1172, 1992.

[84] J. Biener, A. Hodge, and A. Hamza, “Microscopic failure behavior of nanoporous gold,” *Appl. Phys. Lett.*, pp. 1–3, 2005.

[85] A. M. Hodge, J. R. Hayes, J. A. Caro, J. Biener, and A. V Hamza, “Characterization and Mechanical Behavior of Nanoporous Gold,” *Adv. Eng. Mater.*, vol. 8, no. 9, pp. 853–857, 2006.

[86] T. Balk, C. Eberl, Y. Sun, K. Hemker, and D. Gianola, “Tensile and compressive microspecimen testing of bulk nanoporous gold,” *JOM*, 2009.

[87] Y. Sun, J. Ye, A. M. Minor, and T. J. Balk, “In situ indentation of nanoporous gold thin films in the transmission electron microscope.,” *Microsc. Res. Tech.*, vol. 72, no. January, pp. 232–241, 2009.

[88] J. Biener, A. M. Hodge, A. V. Hamza, L. M. Hsiung, and J. H. Satcher, “Nanoporous Au: A high yield strength material,” *J. Appl. Phys.*, vol. 97, pp. 2–5, 2005.

[89] J. Biener, A. M. Hodge, J. R. Hayes, C. A. Volkert, L. A. Zepeda-Ruiz, A. V. Hamza, and F. F. Abraham, "Size effects on the mechanical behavior of nanoporous Au," *Nano Lett.*, vol. 6, pp. 2379–2382, 2006.

[90] A. Hodge, J. Biener, and J. Hayes, "Scaling equation for yield strength of nanoporous open-cell foams," *Acta Mater.*, vol. 55, pp. 1343–1349, 2007.

[91] E. W. Andrews, G. Gioux, P. Onck, and L. J. Gibson, "Size effects in ductile cellular solids. Part II: Experimental results," *Int. J. Mech. Sci.*, vol. 43, pp. 701–713, 2001.

[92] Y. Toivola, A. Stein, and R. F. Cook, "Depth-sensing indentation response of ordered silica foam," *J. Mater. Res.*, vol. 19, no. 01, pp. 260–271, Mar. 2011.

[93] P. Sudheer Kumar, S. Ramchandra, and U. Ramamurty, "Effect of displacement-rate on the indentation behavior of an aluminum foam," *Mater. Sci. Eng. A*, vol. 347, pp. 330–337, 2003.

[94] L. J. Gibson and M. F. Ashby, *Cellular Solids: Structure and Properties*, 2nd ed. Cambridge: Cambridge University Press, 1997.

[95] M. Hakamada and M. Mabuchi, "Mechanical strength of nanoporous gold fabricated by dealloying," *Scr. Mater.*, vol. 56, pp. 1003–1006, 2007.

[96] D. Lee, X. Wei, X. Chen, M. Zhao, and S. Jun, "Microfabrication and mechanical properties of nanoporous gold at the nanoscale," *Scr. Mater.*, vol. 56, pp. 437–440, 2007.

[97] D. Lee, X. Wei, M. Zhao, X. Chen, S. C. Jun, J. Hone, and J. W. Kysar, "Plastic deformation in nanoscale gold single crystals and open-celled nanoporous gold," *Model. Simul. Mater. Sci. Eng.*, vol. 15, no. 1, pp. S181–S192, Jan. 2007.

[98] A. M. Hodge, R. T. Doucette, M. M. Biener, J. Biener, O. Cervantes, and A. V. Hamza, "Ag effects on the elastic modulus values of nanoporous Au foams," *J. Mater. Res.*, vol. 24, no. 04, pp. 1600–1606, Jan. 2011.

[99] N. Abdolrahim, D. F. Bahr, B. Revard, C. Reilly, J. Ye, T. J. Balk, and H. M. Zbib, "The mechanical response of core-shell structures for nanoporous metallic materials," *Philos. Mag.*, vol. 93, no. 7, pp. 736–748, Mar. 2013.

[100] M. M. Biener, J. Biener, A. Wichmann, A. Wittstock, T. F. Baumann, M. Bäumer, and A. V. Hamza, "ALD functionalized nanoporous gold: Thermal stability, mechanical properties, and catalytic activity," *Nano Lett.*, vol. 11, pp. 3085–3090, 2011.

[101] C. Volkert and E. Lilleodden, "Approaching the theoretical strength in nanoporous Au," *Appl. Phys. Lett.*, pp. 3–5, 2006.

[102] A. Mathur and J. Erlebacher, “Size dependence of effective Young’s modulus of nanoporous gold,” *Appl. Phys. Lett.*, no. December 2006, pp. 2006–2008, 2007.

[103] H. Jin, L. Kurmanaeva, and J. Schmauch, “Deforming nanoporous metal: Role of lattice coherency,” *Acta Mater.*, vol. 57, pp. 2665–2672, 2009.

[104] W. E. Warren and A. M. Kraynik, “The Nonlinear Elastic Behavior of Open-Cell Foams,” *J. Appl. Mech.*, vol. 58, no. 2, p. 376, 1991.

[105] K. Gall, J. Diao, and M. Dunn, “The strength of gold nanowires,” *Nano Lett.*, no. Figure 1, 2004.

[106] C. Eberl, R. Thompson, D. S. Gianola, and K. Hemker, “Digital Image Correlation and Tracking (Matlab© functions).” 2010.

[107] W. Oliver and G. Pharr, “Measurement of hardness and elastic modulus by instrumented indentation: Advances in understanding and refinements to methodology,” *J. Mater. Res.*, 2004.

[108] W. Oliver and G. Pharr, “An improved technique for determining hardness and elastic modulus using load and displacement sensing indentation experiments,” *J. Mater. Res.*, vol. 7, no. 06, pp. 1564–1583, Jan. 1992.

[109] J. Lohmiller, C. Eberl, R. Schwaiger, O. Kraft, and T. Balk, “Mechanical spectroscopy of nanocrystalline nickel near room temperature,” *Scr. Mater.*, vol. 59, no. 4, pp. 467–470, Aug. 2008.

[110] R. . Hasiguti, N. Igata, and G. Kamoshita, “Internal friction peaks in cold-worked metals,” *Acta Metallurgica*. 1962.

[111] A. W. Sommer and D. N. Beshers, “Damping peaks in deformed nickel,” *J. Appl. Phys.*, vol. 37, no. 1966, pp. 4603–4614, 1966.

[112] J. L. Besson and P. Boch, “Identification of internal-friction peaks in cold-worked nickel,” *Nuovo Cim. B Ser. 11*, vol. 33, pp. 29–37, 1976.

[113] E. Bonetti, E. G. Campari, L. Pasquini, and E. Sampaolesi, “Microstructure-related anelastic and magnetoelastic behavior of nanocrystalline nickel,” *J. Appl. Phys.*, vol. 84, no. 1998, p. 4219, 1998.

[114] E. Bonetti, E. G. Campari, L. Del Bianco, L. Pasquini, and E. Sampaolesi, “Mechanical behaviour of nanocrystalline iron and nickel in the quasi-static and low frequency anelastic regime,” *Nanostructured Mater.*, vol. 11, no. 6, pp. 709–720, 1999.

[115] E. Bonetti and L. Pasquini, “Mechanical spectroscopy of nanocrystalline metals: Structure and anelastic behavior,” *J. Electron. Mater.*, vol. 28, no. 9, pp. 1055–1061, Sep. 1999.

[116] D.-H. Choi, “Dynamic mechanical properties of metal thin films on silicon substrates: Anelasticity, damping and internal friction,” ProQuest Dissertations And Theses, 2005.

[117] W. Benoit, B. Bays, P. A. Grandchamp, B. Vittoz, G. Fantozzi, J. Ferez, and P. Gobin, “Modulus effects and Hasiguti peaks on two coldworked fcc metals: Gold and aluminium,” *J. Phys. Chem. Solids*, vol. 31, pp. 1907–1912, 1970.

[118] S. Okuda and R. . Hasiguti, “Internal friction peaks of gold worked gold and copper at low temperatures,” *Acta Metallurgica*, vol. 11. pp. 257–265, 1963.

[119] R. R. Hasiguti, “The Structure of Defects in Solids,” *Annu. Rev. Mater. Sci.*, vol. 2, no. 1, pp. 69–92, Aug. 1972.

[120] A. Seeger, “Progress and problems in the understanding of the dislocation relaxation processes in metals,” *Mater. Sci. Eng. A*, vol. 370, no. 1–2, pp. 50–66, Apr. 2004.

[121] T. Kosugi and T. Kino, “A new low-temperature dislocation-relaxation peak in aluminum,” *J. Phys. Soc. Japan*, 1989.

[122] K. Chountas, “Influence of Neutron Irradiation at Low Temperature on Internal Friction and Bulk Modulus of Silver,” *Phys. status solidi*, vol. 219, 1972.

[123] D. O. Thompson and D. K. Holmes, “Dislocation Contribution to the Temperature Dependence of the Internal Friction and Young’s Modulus of Copper,” *J. Appl. Phys.*, vol. 30, no. 1958, pp. 525–541, 1959.

[124] H. Tanimoto, K. Mutou, Y. Hosonuma, K. Yamamoto, and H. Mizubayashi, “Anelasticity study on interfaces of nanocrystalline Au and nanoporous Au,” *Mater. Sci. Eng. A*, vol. 521–522, pp. 295–298, Sep. 2009.

[125] D. A. Porter, K. E. Easterling, and M. Y. Sherif, *Phase transformations in metals and alloys*, Third. CRC press, 2009.

[126] J. von Neumann, *Written Discussion*. Cleveland, OH, 1952.

[127] P. Beck and P. Sperry, “Effect of recrystallization texture on grain growth,” *Trans. AIME*, 1949.

[128] H.-C. Kim, C.-G. Kang, M.-Y. Huh, and O. Engler, “Effect of primary recrystallization texture on abnormal grain growth in an aluminum alloy,” *Scr. Mater.*, vol. 57, no. 4, pp. 325–327, Aug. 2007.

[129] R. W. Cahn and P. Haasen, *Physical Metallurgy (Fourth Edition)*. Elsevier Ltd, 1996.

[130] J. E. Burke and D. Turnbull, “Recrystallization and grain growth,” *Prog. Met. Phys.*, vol. 3, pp. 220–292, Jan. 1952.

[131] C. Smith, “Some elementary principles of polycrystalline microstructure,” *Metall. Rev.*, 1964.

[132] N. J. Briot, T. Kennerknecht, C. Eberl, and T. J. Balk, “Mechanical properties of bulk single crystalline nanoporous gold investigated by millimetre-scale tension and compression testing,” *Philos. Mag.*, vol. 94, no. 8, pp. 847–866, 2014.

[133] O. Okman, D. Lee, and J. W. Kysar, “Fabrication of crack-free nanoporous gold blanket thin films by potentiostatic dealloying,” *Scr. Mater.*, vol. 63, no. 10, pp. 1005–1008, Nov. 2010.

[134] O. Okman and J. W. Kysar, “Fabrication of crack-free blanket nanoporous gold thin films by galvanostatic dealloying,” *J. Alloys Compd.*, vol. 509, no. 22, pp. 6374–6381, Jun. 2011.

[135] H. Rösner, S. Parida, D. Kramer, C. A. Volkert, and J. Weissmüller, “Reconstructing a nanoporous metal in three dimensions: An electron tomography study of dealloyed gold leaf,” *Adv. Eng. Mater.*, vol. 9, no. 7, pp. 535–541, 2007.

[136] T. Fujita, L. H. Qian, K. Inoke, J. Erlebacher, and M. W. Chen, “Three-dimensional morphology of nanoporous gold,” *Appl. Phys. Lett.*, vol. 92, pp. 2008–2010, 2008.

[137] Y. Lu, J. Song, J. Y. Huang, and J. Lou, “Fracture of Sub-20nm Ultrathin Gold Nanowires,” *Adv. Funct. Mater.*, vol. 21, no. 20, pp. 3982–3989, Oct. 2011.

[138] J. Diao, K. Gall, M. Dunn, and J. Zimmerman, “Atomistic simulations of the yielding of gold nanowires,” *Acta Mater.*, vol. 54, pp. 643–653, 2006.

[139] E. Rabkin and D. J. Srolovitz, “Onset of plasticity in gold nanopillar compression.,” *Nano Lett.*, vol. 7, no. 1, pp. 101–7, Jan. 2007.

[140] C. Deng and F. Sansoz, “Size-dependent yield stress in twinned gold nanowires mediated by site-specific surface dislocation emission,” *Appl. Phys. Lett.*, vol. 95, no. 9, p. 091914, 2009.

[141] C. R. Weinberger, A. T. Jennings, K. Kang, and J. R. Greer, “Atomistic simulations and continuum modeling of dislocation nucleation and strength in gold nanowires,” *J. Mech. Phys. Solids*, vol. 60, pp. 84–103, 2012.

[142] J. R. Greer, W. C. Oliver, and W. D. Nix, “Size dependence of mechanical properties of gold at the micron scale in the absence of strain gradients,” *Acta Mater.*, vol. 53, no. 6, pp. 1821–1830, Apr. 2005.

[143] L. Y. Chen, S. Terrab, K. F. Murphy, J. P. Sullivan, X. Cheng, and D. S. Gianola, “Temperature controlled tensile testing of individual nanowires,” *Rev. Sci. Instrum.*, vol. 85, 2014.

[144] T. Zhu, J. Li, A. Samanta, A. Leach, and K. Gall, “Temperature and Strain-Rate Dependence of Surface Dislocation Nucleation,” *Phys. Rev. Lett.*, vol. 100, no. 2, p. 025502, Jan. 2008.

[145] Y. Lu, J. Song, J. Huang, and J. Lou, “Surface dislocation nucleation mediated deformation and ultrahigh strength in sub-10-nm gold nanowires,” *Nano Res.*, vol. 4, no. 12, 2011.

[146] A. Sedlmayr, E. Bitzek, D. S. Gianola, G. Richter, R. Mönig, and O. Kraft, “Existence of two twinning-mediated plastic deformation modes in Au nanowhiskers,” *Acta Mater.*, vol. 60, no. 9, pp. 3985–3993, May 2012.

[147] D. Tabor, “The hardness of solids,” *Rev. Phys. Technol.*, vol. 145, 1970.

[148] M. Wilsea, K. Johnson, and M. Ashby, “Indentation of foamed plastics,” *International Journal of Mechanical Sciences*, vol. 17. pp. 457–IN6, 1975.

[149] M. Shaw and T. Sata, “The plastic behavior of cellular materials,” *Int. J. Mech. Sci.*, vol. 8, pp. 469–478, 1966.

[150] S. Baxter and T. Jones, “Physical properties of foamed plastics and their dependence on structure,” *Plast. Polym.*, 1972.

[151] R. Miller, “A continuum plasticity model for the constitutive and indentation behaviour of foamed metals,” *Int. J. Mech. Sci.*, vol. 42, pp. 729–754, 2000.

[152] G. Gioux, T. . McCormack, and L. . Gibson, “Failure of aluminum foams under multiaxial loads,” *Int. J. Mech. Sci.*, vol. 42, no. 6, pp. 1097–1117, Jun. 2000.

[153] a. D. Brydon, S. G. Bardenhagen, E. a. Miller, and G. T. Seidler, “Simulation of the densification of real open-celled foam microstructures,” *J. Mech. Phys. Solids*, vol. 53, no. 12, pp. 2638–2660, Dec. 2005.

[154] G. Sachs and J. Weerts, “Zugversuche an Gold-Silberkristallen,” *Zeitschrift für Phys.*, vol. 473, pp. 474–484, 1930.

[155] C. Volkert and E. Lilleodden, “Size effects in the deformation of sub-micron Au columns,” *Philos. Mag.*, no. September 2012, pp. 37–41, 2006.

[156] R. Dou and B. Derby, “The strength of gold nanowire forests,” *Scr. Mater.*, vol. 59, no. 2, pp. 151–154, Jul. 2008.

[157] O. S. Leung, a. Munkholm, S. Brennan, and W. D. Nix, “A search for strain gradients in gold thin films on substrates using x-ray diffraction,” *J. Appl. Phys.*, vol. 88, no. 3, p. 1389, 2000.

[158] S. Brinckmann, J. Kim, A. Jennings, and J. R. Greer, “Effects of Sample Geometry on the Uniaxial Tensile Stress State at the Nanoscale,” *International Journal for Multiscale Computational Engineering*, vol. 7. pp. 187–194, 2009.

[159] R. Liu and A. Antoniou, “A relationship between the geometrical structure of a nanoporous metal foam and its modulus,” *Acta Mater.*, 2013.

[160] A. Giri, J. Tao, L. Wang, M. Kirca, and A. C. To, “Compressive Behavior and Deformation Mechanism of Nanoporous Open-Cell Foam with Ultrathin Ligaments,” *J. Nanomech. Miromech*, no. Special issue: Mechanics of Nanocomposites and Nanostructure, pp. 1–6, 2014.

[161] A. Roberts and E. Garboczi, “Elastic properties of model random three-dimensional open-cell solids,” *J. Mech. Phys. Solids*, vol. 50, pp. 33–55, 2002.

Vita

Nicolas Briot was born in Nancy, France and grew up in Burgundy, France. He graduated from the Le Creusot Institute of Technology with a degree in Physical Measurements (2003), from the University of Toulouse Paul Sabatier with a degree (specialized technician) in Materials Control and Treatment (2005) and from the University of Burgundy with a degree (Bachelor equivalent) in Chemistry of Interfaces and Materials (2007). He then worked for the JTEKT Corporation (automobile steering) in Dijon, Burgundy, in the Quality Control Laboratory of the manufacturing plant. He joined Dr. T. John Balk's research group at the University of Kentucky in 2009 to pursue a Ph.D. in Materials Science and Engineering.

Peer-reviewed Papers

1. **Briot, N. J.**, Kennerknecht, T., Eberl, C. & Balk, T. J. Mechanical properties of bulk single crystalline nanoporous gold investigated by millimetre-scale tension and compression testing. *Philos. Mag.* **94,** 847–866 (2014).

2. Wang, L., **Briot, N. J.**, Swartzentruber, P. D. & Balk, T. J. Magnesium Alloy Precursor Thin Films for Efficient, Practical Fabrication of Nanoporous Metals. *Metall. Mater. Trans. A* **45,** 1–5 (2013).

3. **Briot, N. J.**, & Balk, T. J. Developing scaling relations for the yield strength of nanoporous gold. *Philos. Mag.*, under review (2015).

4. Buerckert, M., **Briot, N. J.**, & Balk, T. J. Compression testing of millimeter-scale nanoporous gold., in preparation (2015).

Conferences Participations

1. Chair of the 2012 Gordon Research Seminar on Thin Film and Small-Scale Mechanical Behavior, held in conjunction with the related Gordon Research Conference in Waterville, ME.

2. Mechanical Testing of Bulk Nanoporous Metals, **N. J. Briot**, T. J. Balk, presentation at MRS Fall meeting 2015, Boston, MA.

3. Nanoporous Silicon: Ductile Deformation of Nanoscale Ligaments, X. Jiang, **N. J. Briot**, E. Tochigi, A. M. Minor, T. J. Balk, presentation at MRS Fall meeting 2015, Boston, MA.

4. Mechanical Properties and Scaling Behavior of Bulk Nanoporous Gold and Iridium, **N. J. Briot**, L. Wang and T. J. Balk, presentation at TMS 2014, San Diego, CA.

5. Microspecimen Testing of the Mechanical Properties of Nanoporous Metals, **N. J. Briot**, T. Kennerknecht, C. Eberl and T. J. Balk, presentation at TMS 2013, San Antonio, TX.

6. Mechanical Properties and Behavior of Nanoporous Gold, **N. J. Briot**, T. Kennerknecht, C. Eberl and T. J. Balk, poster presented at the Gordon Research Conference on Thin Film and Small-Scale Mechanical Behavior, Waterville, ME.

7. Internal Friction Measurements in Nanocrystalline and Nanoporous Metals, **N. J. Briot** and T. J. Balk, presentation at TMS 2011, San Diego, CA.

8. Anelastic Damping Studies of Nanocrystalline and Nanoporous Metals, **N. J. Briot**, J. Lohmiller, N. Werner, C. Eberl, O. Kraft and T. J. Balk, poster presented at the Gordon Research Conference on Thin Film and Small-Scale Mechanical Behavior, Waterville, ME.

9. Anelastic Behavior of Nanocrystalline Nickel and Nanoporous Metals, **N. J. Briot**, J. Lohmiller, C. Eberl, O. Kraft and T. J. Balk, presentation at MRS 2011 Fall, Boston, MA.